Author:
Rosenfeld, Lawrence M

Title:
Mid-infrared quantum optics in silicon

Light work with long waves

Mid-infrared quantum optics in silicon

Light work with long waves

By

Lawrence Mark Rosenfeld

Department of Physics
University of Bristol

A dissertation submitted to the University of Bristol in accordance with the requirements of the degree of Doctor of Philosophy in the Faculty of Science.

September 2019

Word count: 41924

Abstract

Integrated quantum photonics promises to fundamentally transform how we sense, transmit and process information. Applications of quantum optics in fields such as remote sensing, communications, and information technology will all be revolutionised, provided that in scaling up, performance is preserved. Silicon quantum photonics has shown complex, repeatable, and miniaturised integrated photonics circuits. These are fabricated with industry standard CMOS compatible techniques, but linear and nonlinear optical loss limit scalability. In this work, we show that translating to the mid-infrared yields a technology platform that simultaneously maximises manufacturability and large scale component integration, while reducing nonlinear loss.

Demonstrating a bright source of quantum correlated photons, suppression of the pump laser to the single photon level, efficient detection, and high visibility quantum interference are all essential ingredients for establishing the viability of any quantum optics platform. This thesis details these necessary steps for experimentally realising the generation and manipulation of photon-pairs in the 2.1 μm band in crystalline silicon waveguides.

We show integrated passive structures such as waveguides, grating couplers, edge couplers, directional couplers and multi-mode interference couplers. A sources of photon-pairs from spontaneous four-wave mixing is realised by combining these components into reconfigurable waveguide circuits. At a wavelength of 2.07 μm, a waveguided measurement of the nonlinear refraction finds $n_2 = 15.3 \times 10^{-18}$ m^2/W and the two-photon absorption coefficient $\alpha_2 = 0.557$ cm/GW, showing an improvement over the 1.55 μm telecommunication band. In various silicon waveguide photon-pair sources, we measure a maximum net coincidence rate of 896 Hz, a coincidence-to-accidental ratio of 25.7 and a net two-photon interference visibility of 99.3 %, demonstrating the first quantum interference in the mid-infrared on a silicon chip.

Dedication and acknowledgements

This thesis was the culmination of four years of my life, and I am indebted to many people.

To Fretlabs, Alex, Caterina, Euan, Jake, Jeremy, Joel, Sabine, and Will, sharing music with you was truly special.

CDT staff, Pete, Lin, Jorge, Döndü, Dara, Andrea, Becky, Sorrell and QETLabs team Holly, Belinda, Emma, Marissa, Laurent, Graham and many more; your hard work keeping the operation running smoothly behind the scenes made so much of this possible.

To my fellow CDT cohort 2 Alex, Henry, Jason, Joe, Lucio, Martin and Sam; thank you for sharing the adventure into the world of postgraduate studies with me, your friendship made these last years a wonderful experience.

Mark and John, thanks for believing in me and giving me the opportunity to nurture my research interests in this amazing environment.

Gary, thanks for all the interesting discussions and teaching me your insights.

Dom, Jake and Ben, it's been great to share this research with you and I am honoured to pass the torch into your capable hands. I know you will continue to keep on pushing the boundaries of awesome science.

Krishna, thanks for sharing your wisdom and advice. It helped guide me towards achieving my goals.

Josh, I could not be more fortunate to have such a good friend and mentor. It's been exciting diving into the world of integrated quantum optics with you. Your guidance and dedication to the project has been truly inspiring.

To Mum, Dad and Emily, your unwavering love and support to achieve my PhD was indispensable. Without you, none of this would have been possible.

Imogen, I loved sharing this roller-coaster ride of the last four years; you made it all worthwhile.

Author's declaration

I declare that the work in this dissertation was carried out in accordance with the requirements of the University's Regulations and Code of Practice for Research Degree Programmes and that it has not been submitted for any other academic award. Except where indicated by specific reference in the text, the work is the candidate's own work. Work done in collaboration with, or with the assistance of, others, is indicated as such. Any views expressed in the dissertation are those of the author.

SIGNED: ..... DATE: .....

Disclaimer

In this thesis, I use the phrase 'we' to describe guiding the reader i.e. you and I through the content. Later experiments were performed collaboratively, and involved the work of other people, the term 'we' here also applies to the collective contribution of the group to the work. However, in general, the contents of the thesis such as diagrams, simulations, and experimental data were solely performed by myself, except where indicated in the statement of work section stated at the end of each chapter.

List of publications and presentations

Lawrence Rosenfeld. (2018). "Integrated Quantum Photonics in the Short-wave Infrared" Bristol Postgraduate Conference. (Talk)

Lawrence Rosenfeld, Joshua W. Silverstone, Benjamin Slater, Döndü Sahin, Alex McMillan, and Mark G. Thompson. (2018). "A new platform for integrated quantum optics: the short-wave infrared" *20th European Conference on Integrated Optics*. (Talk, best student presentation prize)

Benjamin Slater, Mack H. Johnson, **Lawrence Rosenfeld**, Joshua Silverstone, Mark G. Thompson, Döndü Sahin. (2018) "Modelling Waveguide-Integrated Superconducting Nanowire Single Photon Detectors at Short-Wave Infrared". *2018 IEEE Photonics Society Summer Topical Meeting*. IEEE. pp. 93–94 (Conference proceeding).

Lawrence M. Rosenfeld, Dominic A. Sulway, Gary F. Sinclair, Mark G. Thompson, John G. Rarity, and Joshua W. Silverstone. (2019). "First observation of quantum correlated short-wave infrared photon pairs" Bristol Quantum Information Technologies Workshop. (Poster)

Lawrence M. Rosenfeld, Dominic A. Sulway, Mark G. Thompson, John G. Rarity and Joshua W. Silverstone. (2019). "Short-wave infrared correlated photons from silicon waveguides". *CLEO-Europe 2019*. Optical Society of America, ea_p_4. (Poster, conference proceedings)

Lawrence M. Rosenfeld, Dominic A. Sulway, Mark. G. Thompson, John G. Rarity and Joshua W. Silverstone. (2019). "The First Quantum Interference in the Mid-infrared is on a Silicon Chip" *CLEO-Europe 2019*. Optical Society of America, pd_2_2. (Talk, conference proceedings)

Joshua W. Silverstone, **Lawrence M. Rosenfeld**, *et al.* (2019). "Silicon Quantum Photonics in the Short-Wave Infrared: A New Platform for Big Quantum Optics" *CLEO-Europe 2019* Optical Society of America, ea_6_2. (Conference proceedings)

Lawrence M. Rosenfeld, Dominic A Sulway, Gary F Sinclair, Vikas Anant, Mark G. Thompson, John G. Rarity, and Joshua W. Silverstone. (2019). "Mid-infrared quantum optics in silicon" arXiv:1906.10158. (Preprint, submitted)

Yuya Yonezu, Dominic A. Sulway, **Lawrence M. Rosenfeld**, Pisu Jiang, John G. Rarity, Takao Aoki, Joshua W. Silverstone. (2020) "Ultra low-loss, high bandwidth, adiabatic fibre-chip coupling for integrated silicon photonics in the mid-infrared" (In preparation)

Table of Contents

List of Tables

List of Figures

Acronyms

AMZI	Asymmetric Mach-Zehnder interferometer.
ANT	Applied Nanotools.
AR	Anti-reflective.
BPF	Bandpass filter.
BS	Beamsplitter.
CAR	Coincidence to accidental ratio.
CORN	Cornerstone.
CW	Continuous wave.
DC	Directional coupler.
DCR	Dark count rate.
EBL	Electron beam lithography.
ER	Extinction ratio.
FCA	Free carrier absorption.
FCD	Free carrier dispersion.
FDTD	Finite-difference time-domain.
FOM	Figure of merit.
FSR	Free spectral range.
FWHM	Full width at half maximum.
FWM	Four-wave mixing.
GHZ	Greenberger-Horne-Zeilinger.
GVD	Group velocity dispersion.
HOM	Hong-Ou-Mandel.
IME	Institute of Microelectronics.
IMEC	Interuniversity Microelectronics Center.
JSI	Joint spectral intensity.
LOQC	Linear optical quantum computing.
LP	Linear polariser.
MC	Monochromator.
MFD	Mode-field diameter.
MIR	Mid-infrared.
MLL	Mode-locked laser.
MM	Multi-mode.
MMI	Multimode interference coupler.
MZI	Mach-Zehnder interferometer.
NDF	Neutral density filter.
NIR	Near infrared.
NLO	Nonlinear optics.

NLSE	Nonlinear Schrödinger equation.
OL	Optical lithography.
OSA	Optical spectrum analyser.
PC	Polarisation controller.
PCB	Printed circuit board.
PD	Photodiode.
PML	Perfectly matched layer.
PSD	Power spectral density.
QCL	Quantum cascade laser.
QIP	Quantum information processing.
SDE	System detection efficiency.
SEM	Scanning electron microscope.
SFWM	Spontaneous four-wave mixing.
SM	Single-mode.
SMF	Single-mode fibre.
SNSPDs	Superconducting nanowire single-photon detectors.
SOI	Silicon on insulator.
SPDC	Spontaneous parametric down-conversion.
SPM	Self-phase modulation.
SSFM	Split-step Fourier method.
SWIR	Short-wave infrared.
TE	Transverse electric.
TEC	Temperature controller.
TIA	Time interval analyser.
TIR	Total internal reflection.
TM	Transverse magnetic.
TOPM	Thermo-optic phase modulator.
TPA	Two-photon absorption.
VGA	V-groove array.
VGC	Vertical grating coupler.
VOA	Variable optical attenuator.
WG	Waveguide.
XPM	Cross-phase modualtion.
XTPA	Cross two-photon absorption.

CHAPTER 1

Introduction

Photonic quantum technologies promise to radically change information processing, much in the same way as the classical computing digital revolution [1]. The growth and emergence of quantum technologies in the early twenty first century exploded in functionality and in scale. The end of Moore's law is tangibly within reach with the physical size of silicon transistors nearing the atomic scale. Consequently conventional silicon integrated electronic circuits are limited from exponential growth, foreshadowing a disruptive new approach to information processing technology. Processing information using the laws of quantum mechanics offers a way forward, and optics is a strong candidate for its realisation. In crystalline silicon waveguides at telecommunication wavelengths, nonlinear loss detrimentally limits the performance. A new epoch of integrated quantum information processing technologies can be achieved by translating to the low-loss mid-infrared spectral region (2-20 μm), which curtails linear and nonlinear absorption while benefiting from an improved manufacturability and applications. This thesis shows the experimental realisation of high visibility quantum interference using mid-infrared photons generated on a chip. The first chapter outlines the background that enables integrated quantum photonics and the prerequisites for the rest of this thesis. The content of this chapter is inspired by the introductory sections of Dr. Joshua Silverstone's thesis [2], who gives an excellent and comprehensive background in the surrounding topics.

1.1 The rise of quantum information in silicon

The transfer of human knowledge from generation to generation, over thousands of years, has led to the unrivalled success of our species as the dominant life form on the rock we call Earth. As the dawn of the twentieth century approached, fundamental discoveries uncovered the mysterious shrouds of what forms the basis of all light and matter.

The first important concepts in quantum mechanics came in 1900 when Max Planck used a field quantised by restricted modes of its emitters to explain the spectrum of blackbody radiation [3]. This led to Einstein's proposal of the intrinsically quantised radiant en-

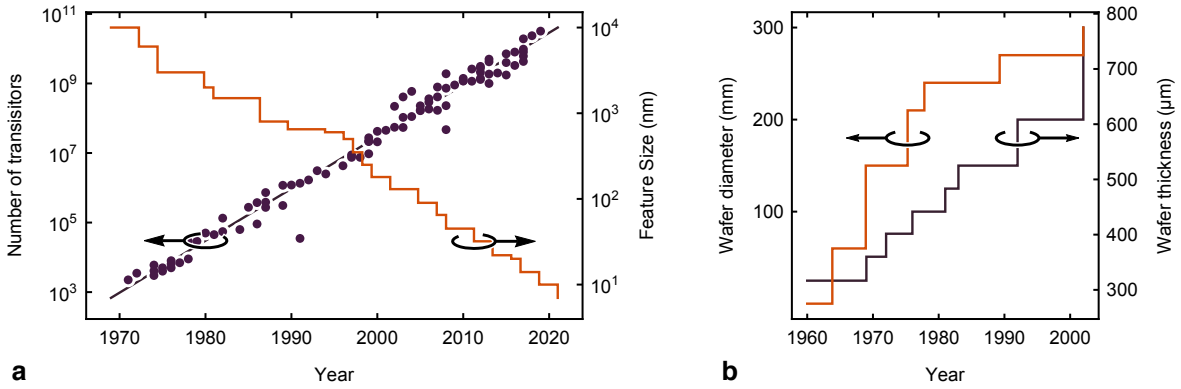

Figure 1.1: Moore's law. **a**, The number of transistors and feature size scaling of integrated circuits over time, logarithmic scale. **b**, Change in size and thickness of wafers over time[8,9].

ergy field and the photon[4] in 1905. In 1911 Rutherford's breakthrough experimental verification of the atomic nucleus[5] constituted the early foundations for our understanding of matter itself, followed shortly after by Niels Bohr's first attempt to quantise the behaviour of the electron orbiting the atomic nucleus. By the mid 1920s the modern theory of quantum mechanics[6,7], developed by Heisenberg and Schrödinger, threw out the old world conceptions and found that nature itself was ill defined and random. This was much to the displeasure of many scientists, including Einstein. The theories that were developed here would underpin much of the fundamental operation of our modern day technology. Phenomena, such as the solid state band gap, could be quantum mechanically explained through the motion of electrons through a periodic lattice of atoms, leading to a forbidden region of the electron wavefunction.

World War II led to the birth of modern computing with Alan Turing's seminal work on computation[10], developing the concept of a general purpose computer. Fast forward 23 years and discovery of the transistor, and the invention of the integrated circuit[11] by Jack Kilby, spurred a technological revolution in large scale information processing. This led to ubiquitous use of the computers and communication technology providing the backbone to modern day society.

As the need for processing information grew, so did the computing power required for larger volumes of data. Gordon Moore famously stated, in what became known as Moore's law, that the number of integrated transistors doubles roughly every two years[12], as shown in Fig. 1.1a. Wafer sizes have also increased over time (see Fig. 1.1b), but component density and therefore processing power is limited by the physical size of the fabricated transistor. Until recently, this trend of transistors doubling has been followed, with the latest era of devices containing over 10^{10} transistors on a single device, and the current processes beginning development of 5 nm transistors[13]. However, the miniaturisation of these components cannot indefinitely continue due to leakage of the electron wavefunction in the nanoscopic structures.

Photons, unlike electrons, do not dissipate heat, travel much faster, and are naturally easy to interface between interconnected remote systems[14,15]. The first integrated optical waveguides were demonstrated in lithium niobate in 1973[16], and integrated silica waveguides in 1981[17]. The field of silicon photonics has grown rapidly since its advent in the '80s pioneered by Soref and Reed[18] and Bookham Technology in the '90s. The modern

era, from the mid 2000s, saw demonstration of GHz rates of optical signals[19] by Intel. This now has large scale applications in information processing and communication[20].

The future of computing is not indefinitely doomed to plateau with the end of Moore's law. The idea for a new generation of computers was conceived by Richard Feynmann. He proposed that computers operating with the laws of quantum mechanics could simulate quantum systems more faithfully[21]. These so called 'quantum computers' are now being developed by research groups and start-ups all over the world[22,23]. Quantum algorithms are being developed to solve a range of difficult problems such as integer factorisation, unstructured search and quantum simulation, with polynomial and in some cases exponential speed up on the worst case run time[24]. The difficulty of finding integers factors of a 2048-bit number that are both large primes underpins the security of the commonly used RSA encryption protocol, and would take thousands of years to crack with classical computers. Current estimates show that with 20 million noisy qubits, this figure could be dramatically reduced to 20 hours[25] demonstrating the potential computational power of quantum devices for certain tasks.

To fully describe the state of n two-level quantum systems, 2^n states must be stored on a classical computer, whereas only n are required with a quantum processor. Clearly, for large quantum system sizes i.e. $n > 100$, this quickly becomes intractable on classical hardware. By mapping intrinsically quantum systems such as molecules to quantum hardware, simulations of quantum chemistry problems[26] that are not feasible with classical computers becomes possible.

It was previously thought that using single photons and only linear optics for quantum computing would be impossible, which the authors Knill, Laflamme and Milburn set out to confirm at the turn of the 21st century. Their work showed that it was entirely possible using linear optics[27]—beamsplitters and phase shifters. Processing quantum information requires access to quantum light, of which there are two main categories: continuous- and discrete-variable. Continuous-variable quantum optics requires a resource of squeezed states[28] which are measured with homodyne detection by beating the squeezed state against a bright local oscillator[29]. The discrete-variable approach on the other hand, is realised with a source of single photons, linear optics, and single photon counting. The rest of this discussion is concerned with the discrete-variable method to quantum information processing (QIP). This has shown to be a promising forerunner for developing a general purpose universal quantum computer[1].

Silicon has been shown to facilitate some of the most complex structures that humans have ever fabricated, and on enormous scale. Humans have fabricated more silicon transistors than seconds in the age of the universe! A photonic quantum computer built with bulk optics or fibre is in principle possible—the optical loss of these approaches is low*—in fibre attenuation for example is $\leq 0.18\,\mathrm{dB/km}$[31] at 1.55 μm wavelength. In reality, these approaches have no real hope to scale to the millions of components required for fault tolerance. Silicon's electronic properties have enabled its integration in almost all current information technology. It turns out that some of silicon's optical properties are also excellent. Silicon benefits from transparency at wavelengths greater than $\lambda > 1.13$ μm, and a large index contrast with silica facilitates high confinement and component densities. Furthermore, it possesses a large optical nonlinearity required for parametric photon-pair sources on a chip. This enables silicon as an excellent platform for large scale linear optical quantum computing (LOQC)[32].

* The largest photonic state measured with bulk optics is a 14-fold coincidence[30].

1.2 Quantum information with single photons

Before getting into the details of how single photons behave in silicon waveguides, we refer the reader to appendix B.1 on page 125 for the definitions of quantum states, and to appendix B.2 on page 126 for the action of operators on quantum states. These definitions establish the mathematical framework of quantum mechanics required to explain the following sections.

1.2.1 The quantised electromagnetic field

The electromagnetic spectrum spans a vast range of energies and utilities. At its longest wavelengths, radio waves serve as means of communication, the microwave, infrared, visible light, and ultraviolet bands all appear in everyday applications, and at the shortest of wavelengths, gamma rays cause and treat aggressive forms of cancer. While these appear to be immensely different, they are all electromagnetic fields with different energies.

The unifying theory of classical electromagnetic fields was proposed by James Clerk Maxwell in the second half of the 19th century. Maxwell's equations revolutionised our understanding of electromagnetism, combining all of the previous efforts of Faraday, Ampere and Gauss then extending it further. We show the quantisation of the single-mode field with Maxwell's equations in appendix B.3 on page 127, where an electromagnetic field is confined in a 1D cavity with perfectly conducting walls[33]. Quantising the solutions of Maxwell's equations for this system determines the Hamiltonian, which describes the total energy contained in the system. Following the derivation from Gerry and Knight[33], this can be written in terms of operators which add and remove a single quantum of energy from the system. The bosonic creation ($\hat{a}^\dagger$) and annihilation ($\hat{a}$) operators obey the commutation relation

$$[\hat{a}, \hat{a}^\dagger] = \mathbb{1}, \tag{1.1}$$

which describes the algebra of particles that are symmetric under exchange and obey Bose-Einstein statistics. The Hamiltonian, written in terms of these operators leads to

$$\hat{H} = \hbar\omega\left(\hat{a}^\dagger\hat{a} + \frac{1}{2}\right), \tag{1.2}$$

where ω is the angular frequency of the mode and $\hbar$ is the reduced Planck constant. Defining the number operator as $\hat{n} = \hat{a}^\dagger\hat{a}$, we will imminently show it is particularly important to the quantised electromagnetic field description. We now establish the set of quantum states $|n\rangle$, known as Fock states. These form an orthonormal basis are the energy eigenstates of the single-mode field Hamiltonian, with eigenvalues E_n. These states can be literally interpreted as the quantum state containing n photons with the properties

$$\langle n|m\rangle = \delta_{nm} \tag{1.3}$$

$$\hat{n}\,|n\rangle = n\,|n\rangle \tag{1.4}$$

$$\hat{H}\,|n\rangle = \hbar\omega\left(\hat{n} + \frac{1}{2}\right)|n\rangle = \hbar\omega\left(n + \frac{1}{2}\right)|n\rangle = E_n\,|n\rangle\,, \tag{1.5}$$

with energy $E_n = \hbar\omega\left(n + \frac{1}{2}\right)$ for $n \in \mathbb{N}_0$ and δ_{nm} as the Kronecker delta. The creation and annihilation operators then have the following effect on the energy eigenstates $|n\rangle$,

$$\hat{a}^\dagger |n\rangle = \sqrt{n+1}\,|n+1\rangle \tag{1.6}$$

$$\hat{a}\,|n\rangle = \sqrt{n}\,|n-1\rangle \tag{1.7}$$

$$\hat{a}\,|0\rangle = 0. \tag{1.8}$$

In this form we can then define $|n\rangle$ in terms of creation operators acting on the vacuum

$$|n\rangle = \frac{(\hat{a}^\dagger)^n}{\sqrt{n!}}\,|0\rangle\,. \tag{1.9}$$

So far we have only dealt with a single-mode field, however the results from the single-mode case can be generalised to the multi-mode field. We omit the details for this derivation* and state its main result; the Hamiltonian takes a similar form to Eqn. (1.2)

$$\hat{H} = \sum_{\mathbf{k}s} \hbar\omega_k \left(\hat{a}^\dagger_{\mathbf{k}s}\hat{a}_{\mathbf{k}s} + \frac{1}{2}\right), \tag{1.10}$$

where the summation is over photons with wavevectors $\mathbf{k}$ and independent orthogonal polarisations s. Each of these mode operators is independent of the others, so we can relabel $\hat{a}_{\mathbf{k}s} \mapsto \hat{a}_i$, and the commutators are found to be

$$[\hat{a}_i, \hat{a}_j] = [\hat{a}_i^\dagger, \hat{a}_j^\dagger] = 0 \tag{1.11}$$

$$[\hat{a}_i, \hat{a}_j^\dagger] = \delta_{ij}. \tag{1.12}$$

Consequently, the multimode photon state forms an orthonormal basis that is the tensor product of the number states for all the different modes. The creation and annihilation operators act on the respective subspace

$$|n_1\rangle\,|n_2\rangle\,|n_3\rangle = |n_1, n_2, n_3\rangle \tag{1.13}$$

$$\langle n_1, n_2, \ldots | n_1', n_2' \ldots\rangle = \delta_{n_1 n_1'}\delta_{n_2 n_2'}\ldots \tag{1.14}$$

$$\hat{a}_i^\dagger\,|n_1, n_2, \ldots, n_i, \ldots, n_N\rangle = \sqrt{n_i+1}\,|n_1, n_2, \ldots, n_i+1, \ldots, n_N\rangle\,. \tag{1.15}$$

1.3 Encoding information on photons

A photon can encode information in many of its degrees of freedom; these include polarisation[34] (Fig. 1.2a), time of arrival[35] (Fig. 1.2b), frequency[36] (Fig. 1.2c), and spatial location[37] (Fig. 1.2d). .

The main encoding we will use is 'dual-rail' or 'path' encoding, where the spatial location of a single photon encodes the information. Here we define two distinct waveguides as 'rails'. This encoding is a natural choice for integrated optics as the quantum state is manipulated with beamsplitters and phase-shifters; these components are simple to implement on a chip. A photon in the top rail encodes a $|0\rangle$ and in the bottom rail encodes a $|1\rangle$ (see Fig. 1.2d). Formally we can define the logical dual-rail basis in terms of Fock states

$$|10\rangle \equiv |0\rangle_{\mathbf{L}} \tag{1.16}$$

$$|01\rangle \equiv |1\rangle_{\mathbf{L}}\,, \tag{1.17}$$

*See Sec. 2.4 in Ref. 33

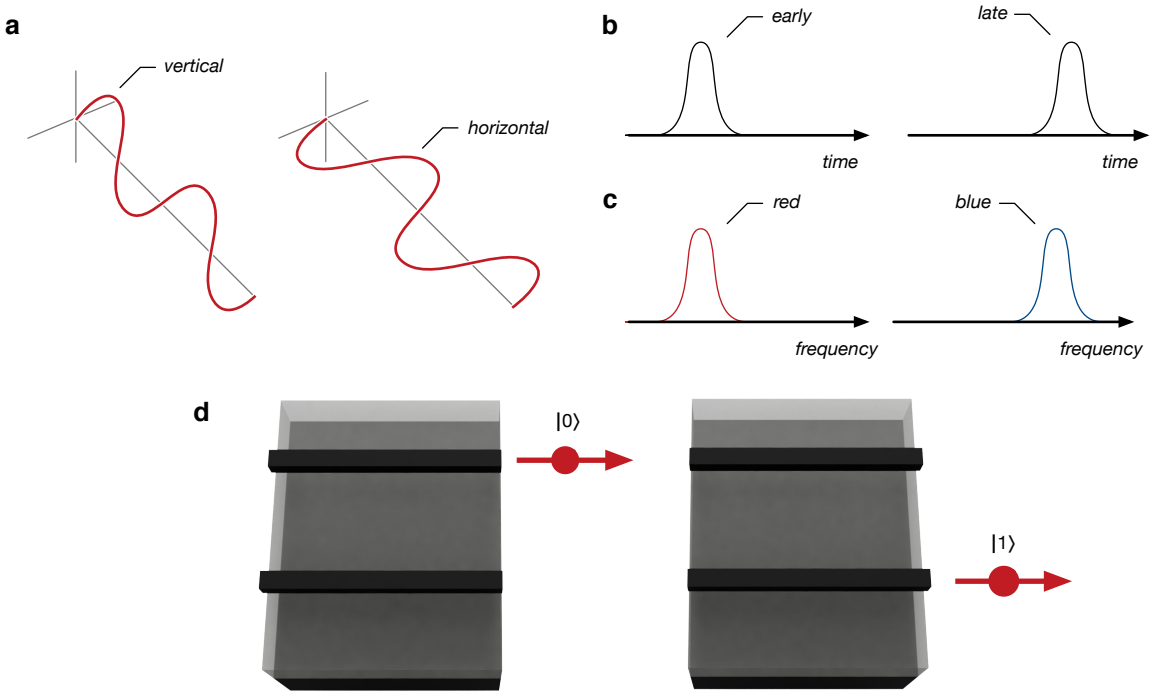

Figure 1.2: Encoding quantum information on a photon. **a**, Polarisation encoding. **b**, Time-bin encoding. **c**, Frequency encoding. **d**, Path encoding.

where the left hand sides defines the occupation in the Fock basis, and term on the right hand side subscript **L** denotes the logical state. For the remainder of this work, we will drop the **L** notation and explicitly state when we describe the photons in the logical or Fock basis. Superposition of the logical states is simply done by injecting a photon into the port of a 50/50 beamsplitter, creating a superposition of the two output modes

$$|0\rangle \xrightarrow{BS} \frac{1}{\sqrt{2}}(|0\rangle + i\,|1\rangle). \tag{1.18}$$

This naturally leads us to the next section, where we describe the quantum analogue of the bit, the qubit.

1.3.1 Qubits

Qubits reside in two dimensional complex Hilbert spaces, with the set of states mapped onto vectors in $\mathbb{C}^2$, shown in Fig. 1.3. The z-basis states of the qubit are $|0\rangle = (1,0)^T$ and $|1\rangle = (0,1)^T$, and the other states are superpositions of these basis states: $|\pm\rangle = (|0\rangle \pm |1\rangle)/\sqrt{2}$ and $|\pm i\rangle = (|0\rangle \pm i\,|1\rangle)/\sqrt{2}$. Pure qubits have norm 1 and can be represented on the surface of the unit sphere, also known as the Bloch sphere[38]. Note that classical bits are encoded exclusively on the poles of the Bloch sphere, while qubits can exist in any state on the surface. The qubit is the fundamental representation unit of binary information, encoding the classical bit in a subset of the possible states it can occupy. An arbitrary pure qubit state can be described by

$$|\psi\rangle = \alpha\,|0\rangle + \beta\,|1\rangle = \cos\left(\frac{\theta}{2}\right)|0\rangle + e^{i\phi}\sin\left(\frac{\theta}{2}\right)|1\rangle, \tag{1.19}$$

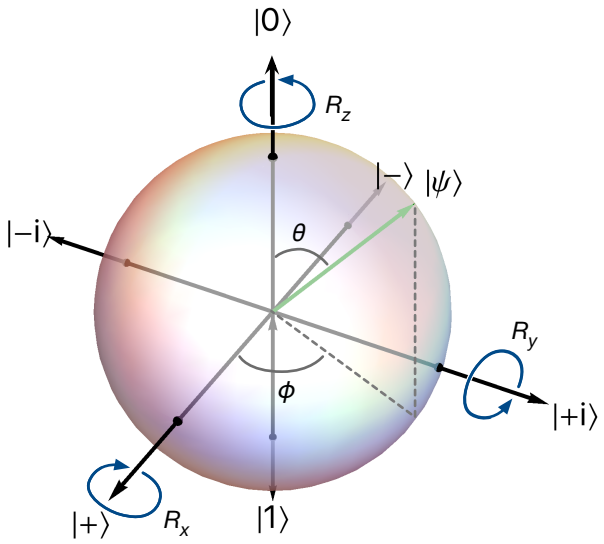

Figure 1.3: Bloch sphere representation of a qubit.

where $|\alpha|^2+|\beta|^2=1$. We show a diagram of the Bloch sphere in Fig. 1.3, with a pure quantum state $|\psi\rangle$ on the surface. Counter-intuitively, antipodal points on the sphere correspond to orthogonal states. The axes of the Bloch sphere correspond to the eigenstates of the Hermitian Pauli (spin) operators

$$\sigma_x=\begin{pmatrix}0&1\\1&0\end{pmatrix}\qquad\sigma_y=\begin{pmatrix}0&-i\\i&1\end{pmatrix}\qquad\sigma_z=\begin{pmatrix}1&0\\0&-1\end{pmatrix}, \tag{1.20}$$

which have eigenvalues $\lambda_\pm=\pm1$ and eigenvectors $\{|+\rangle,|-\rangle\}$ $\{|+i\rangle,|-i\rangle\}$ and $\{|0\rangle,|1\rangle\}$ for the operators $\sigma_x,\sigma_y,\sigma_z$, respectively. Furthermore, these operators are connected by the relation

$$[\sigma_a,\sigma_b]=2i\epsilon_{abc}\sigma_c, \tag{1.21}$$

where ϵ_{abc} is the Levi-Civita permutation symbol. Rotations around the Bloch sphere are then generated with these Pauli operators

$$R_x(\theta)=e^{i\theta\sigma_x/2}\qquad R_y(\theta)=e^{i\theta\sigma_y/2}\qquad R_z(\theta)=e^{i\theta\sigma_z/2}. \tag{1.22}$$

An arbitrary single qubit operation is performed with three single qubit rotations. This is sufficient to generate all of the states on the surface of the Bloch sphere with

$$R_\psi(\alpha,\beta,\gamma)\,|\psi_{\text{out}}\rangle=R_z(\alpha)R_x(\beta)R_z(\gamma)\,|\psi_{\text{in}}\rangle\,. \tag{1.23}$$

This can be understood with a geometric argument. The first z-rotation aligns an arbitrary state with $|\pm i\rangle$ axes, rotation around the x-axis then moves the state about $|0\rangle,|1\rangle,|+i\rangle,|-i\rangle$, and the final z-rotation varies the complex phase, thus mapping any pure state to another. In a dual-rail system, a Mach-Zehnder interferometer (MZI) with an additional, external phase shifters before and after facilitates arbitrary rotation. Schematics of bulk and integrated MZIs are shown in Fig. 1.4.

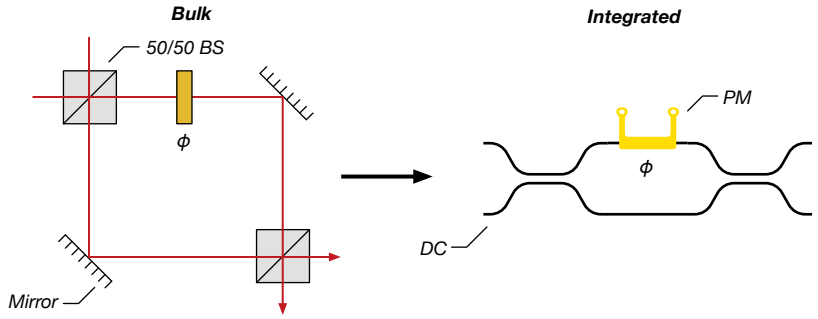

Figure 1.4: Bulk and integrated realisation of the Mach-Zehnder interferometer (MZI). A bulk MZI is implement with two 50/50 beamsplitters (BS), reflective mirrors, and a phase retarder. An integrated MZI is accomplished with an integrated beamsplitter such as a directional coupler (DC), and a phase shift is facilitated by refractive index modification with an eletro- or thermo-optic phase modulator (PM).

The phase shift applied to one rail is a unitary transformation applying a phase ϕ to one of the mode operators $\hat{b}^\dagger \mapsto e^{-i\phi}\hat{b}^\dagger$. This describes a rotation about the z-axis of the Bloch sphere

$$\hat{U}_\phi = \begin{pmatrix} 1 & 0 \\ 0 & e^{-i\phi} \end{pmatrix} = e^{-i\phi/2}\begin{pmatrix} e^{i\phi/2} & 0 \\ 0 & e^{-i\phi/2} \end{pmatrix}, \tag{1.24}$$

is equivalent to the rotation operator $\hat{R}_z$ with a global phase of $e^{-i\phi/2}$ which can be ignored since it is unobservable*. To show the rotation property of the MZI, we sandwich a phase shifter operation between two beamsplitter transformations

$$\hat{U}_{\mathrm{MZI}}(\phi) = \hat{U}_{\mathrm{BS}}\hat{U}_\phi\hat{U}_{\mathrm{BS}} = \frac{1}{\sqrt{2}}\begin{pmatrix} 1 & i \\ i & 1 \end{pmatrix}\begin{pmatrix} e^{i\phi/2} & 0 \\ 0 & e^{-i\phi/2} \end{pmatrix}\frac{1}{\sqrt{2}}\begin{pmatrix} 1 & i \\ i & 1 \end{pmatrix} = i\begin{pmatrix} \sin(\phi/2) & \cos(\phi/2) \\ \cos(\phi/2) & -\sin(\phi/2) \end{pmatrix}, \tag{1.25}$$

again the global phase of i can be neglected. Finally, we see that the rotation $R_x(\phi)$ is equivalent (up to a global phase) to a z-rotation of $\pi/2$ before and after the MZI

$$\hat{R}_x(\phi) = -\hat{R}_z(\pi/2)\hat{U}_{\mathrm{MZI}}(\phi+\pi)\hat{R}_z(\pi/2). \tag{1.26}$$

Therefore an MZI with two external phase-shifters can produce arbitrary single-qubit transformations up to a global phase

$$\begin{aligned} R_\psi(\alpha,\beta,\gamma) = R_z(\alpha)R_x(\beta)R_z(\gamma) &\to -R_z(\alpha)R_z(\pi/2)U_{\mathrm{MZI}}(\beta+\pi)R_z(\pi/2)R_z(\gamma) \\ &= -R_z(\alpha+\pi/2)U_{\mathrm{MZI}}(\beta+\pi)R_z(\gamma+\pi/2). \end{aligned} \tag{1.27}$$

1.3.2 Entanglement

A multipartite system is given by the tensor product of the qubit states

$$|\Psi\rangle = |\psi_1\rangle|\psi_2\rangle\ldots|\psi_N\rangle. \tag{1.28}$$

*This is from the fact that only relative phases can be observed in quantum mechanics. Projection onto a state requires taking the modulus squared of a state for the probability to be a real number—if a state $|\psi\rangle$ has a global phase $e^{i\theta}$, the probability of measuring it in state $|\phi\rangle$ is $|\langle\phi|e^{i\theta}|\psi\rangle|^2 = |e^{i\theta}\langle\phi|\psi\rangle|^2 = e^{i\theta}e^{-i\theta}\langle\phi|\psi\rangle\langle\psi|\phi\rangle = \langle\phi|\psi\rangle\langle\psi|\phi\rangle = |\langle\phi|\psi\rangle|^2$ therefore $|\psi\rangle$ is indistinguishable from $e^{i\theta}|\psi\rangle$ and global phases are unobservable.

Arbitrary N qubit states can be written as a superposition over all qubit bitstring permutations

$$|\Psi\rangle = c_{00\ldots0}|00\ldots0\rangle + c_{10\ldots0}|10\ldots0\rangle + \ldots + c_{11\ldots1}|11\ldots1\rangle\,. \tag{1.29}$$

The two qubit state

$$|{+}{+}\rangle = \frac{1}{2}(|00\rangle + |01\rangle + |10\rangle + |11\rangle), \tag{1.30}$$

has an equal superposition of the two qubit z-basis states. This system is said to be a product state as it can be factorised into two qubit states i.e. it can be written $|\psi_1\rangle|\psi_2\rangle$. When a system is not able to be factored into a product of its constituents, it is said to be *entangled*. For example, if $c_{01} = c_{10} = 0$ in the two qubit equal superposition state, it cannot be factorised. The four Bell states form the class of maximally entangled two-qubit states and are written

$$|\Phi^+\rangle = \frac{|00\rangle + |11\rangle}{\sqrt{2}} \qquad |\Psi^+\rangle = \frac{|01\rangle + |10\rangle}{\sqrt{2}}$$
$$|\Phi^-\rangle = \frac{|00\rangle - |11\rangle}{\sqrt{2}} \qquad |\Psi^-\rangle = \frac{|01\rangle - |10\rangle}{\sqrt{2}}.$$

These entangled states lie at the heart of what is deemed strange about quantum mechanics. The first of the four Bell states shows that if we measure the first qubit as $|0\rangle$ or $|1\rangle$, then we will always measure the other qubit in the same state, regardless of their spatial separation.

To generate entanglement, two-qubit controlled gates are required. In general, the controlled-gates will apply an operator if the first qubit is in the state $|1\rangle$. Typically in optics, the controlled phase or CZ gate creates this entanglement[39] with the relationship

$$\mathrm{CZ}|00\rangle \mapsto |00\rangle \qquad \mathrm{CZ}|01\rangle \mapsto |01\rangle$$
$$\mathrm{CZ}|10\rangle \mapsto |10\rangle \qquad \mathrm{CZ}|11\rangle \mapsto -|11\rangle\,.$$

If we apply the CZ gate to qubits in the state $|{+}{+}\rangle$ we get

$$\mathrm{CZ}|{+}{+}\rangle = \frac{1}{2}(|00\rangle + |01\rangle + |10\rangle - |11\rangle) \tag{1.31}$$
$$= \frac{|0{+}\rangle + |1{-}\rangle}{\sqrt{2}}, \tag{1.32}$$

which is the smallest possible graph state, and is a maximally entangled state locally equivalent to $|\Phi^+\rangle$.

Another important entangled state is the $N00N$ state[40] which is given by

$$|N00N\rangle = \frac{|N0\rangle + |0N\rangle}{\sqrt{2}}, \tag{1.33}$$

here N is the number of photons occupying a mode. This implies if we measure a photon in one mode, all N photons also occupy this mode. In the next section, we show that two-photon interference forms the path entangled two-photon $N00N$ state. Later in chapter 5, we demonstrate the measurement of path entangled states of two mid-infrared (MIR) photons on a silicon chip.

The third important type of entanglement extends the notion of maximally entangled states to multipartite systems. The Greenberger-Horne-Zeilinger (GHZ) states[41] are described by

$$|\mathrm{GHZ}\rangle = \frac{|0\rangle^{\otimes N} + |1\rangle^{\otimes N}}{\sqrt{2}}, \tag{1.34}$$

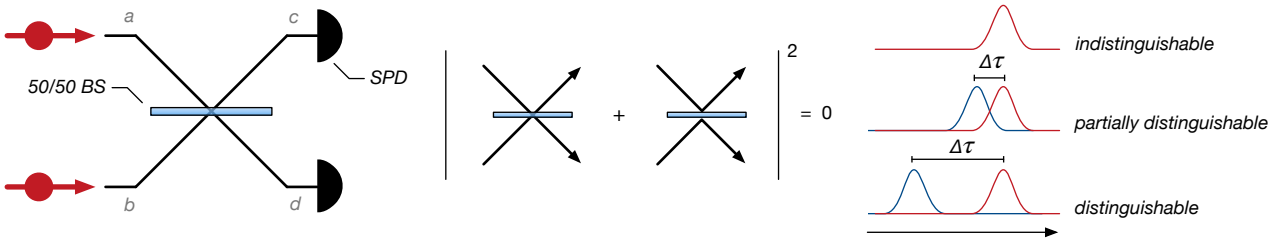

Figure 1.5: Schematic showing the Hong-Ou-Mandel effect of two photon interference. The probability amplitude of detecting a single photons at each output port of a 50/50 beamsplitter (BS) destructively interferes when the photon arrival time delay is zero, i.e. $\Delta\tau = 0$. Figure re-adapted from Ref. 1.

with $N > 2$. Simply put, this is in an equal quantum superposition of all N qubits existing simultaneously in the $|0\rangle$ and $|1\rangle$ state. Here, loss of a single qubit is represented by the partial trace over one of the subsystems, leaving an unentangled mixed state. Measuring one of the qubits in the computational z-basis results in the other qubits existing in the same pure, but unentangled states. In a three particle GHZ state, a measurement of a single qubit in the X basis yields a maximally entangled Bell state. The GHZ state turns out to be a key building block for generating resources required for one-way optical quantum computing[42].

1.3.3 Two-photon interference

Two-photon interference was first demonstrated in 1987 by Hong, Ou and Mandel[43]. Hong-Ou-Mandel (HOM) interference is particularly challenging since the photons that interact must be essentially identical in all degrees of freedom such as frequency, polarisation and time. The measurement of HOM interference was enabled by the discovery of spontaneous parametric down-conversion (SPDC). Here, a pump photon is annihilated in a nonlinear crystal, creating two photons at new frequencies conserving energy and momentum[44]. Here, we show the mechanism of two-photon interference at a balanced beamsplitter[45,46]. Consider two identical photons incident at the two input ports of a 50/50 beamsplitter (see Fig. 1.5)

$$|11\rangle = \hat{a}^\dagger \hat{b}^\dagger |00\rangle . \tag{1.35}$$

The beamsplitter applies the transformation $\hat{a}^\dagger \mapsto (\hat{c}^\dagger + i\hat{d}^\dagger)/\sqrt{2}$ and $\hat{b}^\dagger \mapsto (i\hat{c}^\dagger + \hat{d}^\dagger)/\sqrt{2}$, so

$$\hat{a}^\dagger \hat{b}^\dagger |00\rangle \xrightarrow{\text{BS}} \frac{1}{2}(\hat{c}^\dagger + i\hat{d}^\dagger)(i\hat{c}^\dagger + \hat{d}^\dagger)|00\rangle \tag{1.36}$$

$$= \frac{1}{2}(i\hat{c}^{\dagger 2} + \hat{c}^\dagger \hat{d}^\dagger - \hat{d}^\dagger \hat{c}^\dagger + i\hat{d}^{\dagger 2})|00\rangle \tag{1.37}$$

$$= \frac{1}{2}(i\hat{c}^{\dagger 2} + i\hat{d}^{\dagger 2})|00\rangle \tag{1.38}$$

where in the last line, the two terms with one photon in each output mode cancel since $\hat{c}^\dagger$ and $\hat{d}^\dagger$ commute. Finally, applying the mode operators gives the state

$$|\psi_{\text{out}}\rangle = i\frac{|20\rangle + |02\rangle}{\sqrt{2}}. \tag{1.39}$$

We see that the output is a path entangled two-photon $N00N$ state, where both of the single photons occupy the same output mode. The probability that two detectors at the output ports simultaneous click is therefore zero i.e. $P(|11\rangle) = |\langle 11|\psi_{\text{out}}\rangle|^2 = 0$.

In the original measurement, a path delay was used to modify the arrival time of two photons at the beamsplitter, varying the distinguishability with the temporal degree of freedom. When the time delay $\Delta\tau \to 0$ the photons become indistinguishable causing the coincidence counts drop to zero. This led to the notion of the 'HOM dip'. The visibility (or depth) of the HOM dip is defined as[47]

$$V = \frac{X_{\text{max}} - X_{\text{min}}}{X_{\text{max}}}, \tag{1.40}$$

where $X_{\text{min}}, X_{\text{max}}$ are the minimum and maximum number of coincidence counts. The visibility determines the indistinguishably and the photon-number purity, with the classical or completely distinguishable bound of $V = 50\%$[48]. Thus, true two-photon interference has occurred if the visibility exceeds 50%.

The effect of two-photon interference was observed shortly after in a MZI[49]. The results presented in this thesis performed two-photon interference with an interferometer configuration[47], shown in Sec. 5.1.3. To make fair comparisons between interferometers and 'traditional' HOM interference visibilities, another metric is used[49]

$$V_{\text{MZI}} = \frac{X_{\text{max}} - X_{\text{min}}}{X_{\text{max}} + X_{\text{min}}}. \tag{1.41}$$

The phenomenon of the two-photon interference and path entanglement gave rise to the whole field of quantum optics. From a humble beginning of two-photons, to date the largest measured photonic state is a 14-fold coincidence from a demultiplexed quantum dot source[30].

1.3.4 Quantum computing

This thesis mainly focuses on integrated quantum optics technology. Quantum computing is however an important application which drives the evolution of the technology, motivating this brief summary. Quantum computing promises to solve some of the hardest computational problems, such as simulating quantum chemistry[26]. Quantum computers can be realised in a number of different physical platforms such as photonics, ion traps[50], and superconducting circuits[51]. Each of these approaches has its own strengths and weaknesses, and the race is on to demonstrate a device operating at the large* scales required to solve useful problems. However, for the remainder of this discussion, we will exclusively focus on the approach employing photonic qubits.

Photonic quantum computers are a forerunner for realising a fully fault tolerant device[32]. In general, an arbitrary N-mode unitary operation transforms any of the input modes to any of the output modes with a large interferometer. Here, it is convenient to think in the Heisenberg picture, where the evolution of a system is mapped onto the operators. An arbitrary N-mode evolution, describes the transformation from the input mode operator vector $\{\hat{a}_0, \hat{a}_1 \dots \hat{a}_N\}$ to the output mode operators $\{\hat{b}_0, \hat{b}_1 \dots \hat{b}_N\}$ with the

*Current estimates show that an error corrected universal quantum computer needs hundreds of millions of physical qubits to solve physics and chemistry problems faster than classical computers[52].

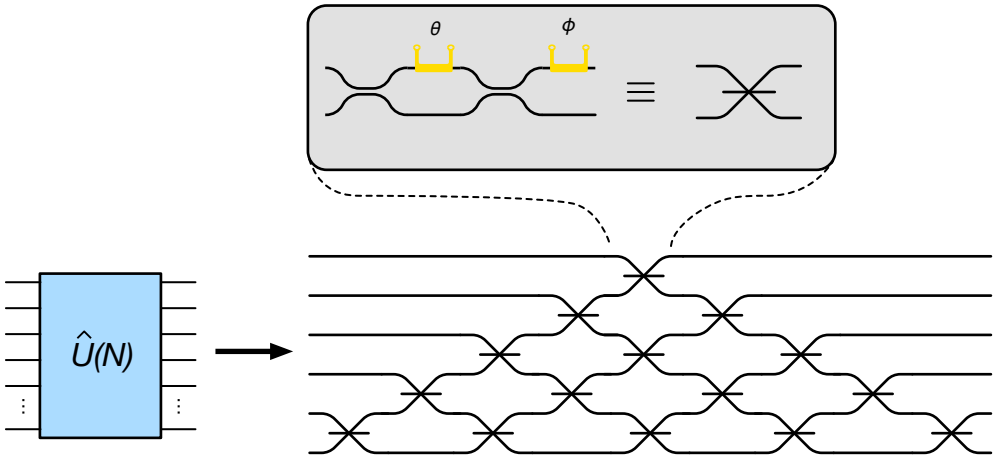

Figure 1.6: Reck scheme of a arbitrary unitary N-mode transformation where each of the input modes can be mapped to any of the outputs. The unit cell is a Mach-Zehnder interferometer with a single external phase shifter.

unitary $\hat{U}(N)$

$$\begin{bmatrix} \hat{b}_1 \\ \hat{b}_2 \\ \vdots \\ \hat{b}_N \end{bmatrix} = \hat{U}(N) \begin{bmatrix} \hat{a}_1 \\ \hat{a}_2 \\ \vdots \\ \hat{a}_N \end{bmatrix}. \tag{1.42}$$

The experimental realisation of a universal N-mode unitary operator using linear optics was first described by Reck and Zeilinger in 1994, now known as the 'Reck scheme'[53]. Experimentally, the Reck scheme transformation is performed with a triangular array of beamsplitters and phase shifters which we show in Fig. 1.6. A notable landmark experiment demonstrated universal linear optics with a six-mode Reck scheme in silica waveguides[54].

The original model of quantum computing uses the 'gate' model, where in analogy to a classical computer, manipulation of bits of data is done with a series of logic gates. In classical computers the NAND gate is universal for computation, such that a series of NAND gates can compute any output from any input bit string. In a quantum device, there are many realisations of discrete set of quantum gates that lead to universal quantum computing. All of these include a two-qubit gate such as the CZ described in the previous section[55]. The current primary contender for universal quantum computation uses the measurement based approach[32]. The resource for this model of computing are large entangled graph states. Qubits are photons initialised in the $|+\rangle$ state, forming the nodes, and CZ entanglement between qubits form the edges.

This is a different paradigm of quantum computing, also known as one-way quantum computing. All gates are implemented with single-qubit measurements, and the choice of one- or two-qubit gates is made via choice of local measurement bases[56,57]. The measurement and feedforward of the entangled states corresponds to a phenomenon of quantum teleportation. The precise measurement bases used depends on the (random) result of previous measurements, hence feedforward must be employed to ensure the correct operation is performed. This model can elegantly be thought of an initial super-

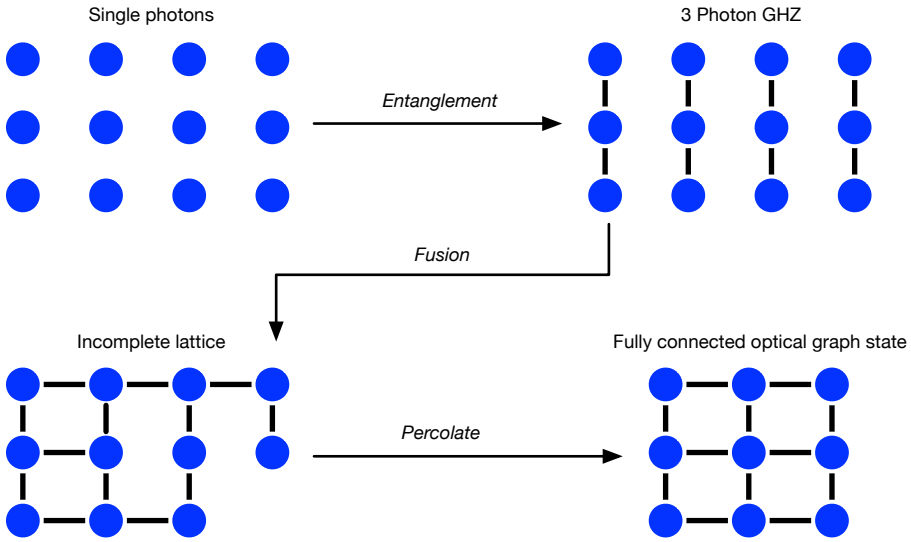

Figure 1.7: Construction of optical graph states for measurement based quantum computing. Single photons are entangled into GHZ states, before being fused together into a large incomplete optical lattice. Finally, bond deletion through measurement yields a fully connected optical graph state.

position over all possible output solutions, that is collapsed into the desired output state with measurement and feedforward.

In the gate model of quantum computing, the main challenge is to preserve the quantum state from decohering while the quantum logic gates are applied. In the measurement based approach, the main overhead comes from constructing the initial optical graph state. Photons naturally have long coherence times*, and so optical loss dominates the error mechanisms. Once the graph state is created, the overhead of the measurements and feedforward is comparatively easy.

Figure 1.7 shows how to generate the optical graph state; a source of single photons or Bell pairs and a method to entangle them into three-photon GHZ states is required. Once a source of three-photon GHZ states is achieved, a fusion operation is used to join the clusters together[58] to construct a larger, incomplete optical lattice. The qubits with missing edges can be deleted with Z-basis measurements, leaving a complete lattice state suitable for universal quantum computation[42].

For fault tolerant quantum computing the optical loss dominates the probability of success. Furthermore, an estimated 10^6 single photons are required to encode sufficient physical qubits for solving useful problems[32]. To achieve quantum technologies with millions of photons, an approach that has high performance and ultra-low optical loss is essential. Clearly, to achieve the scale required, implementations using fibre and bulk optics are rendered unfeasible. This leaves the only remaining candidate as mass manufacturable integrated optics.

*Light from the Lyman-α blobs have remained polarised for over 11 billion years in transit to earth[32]!

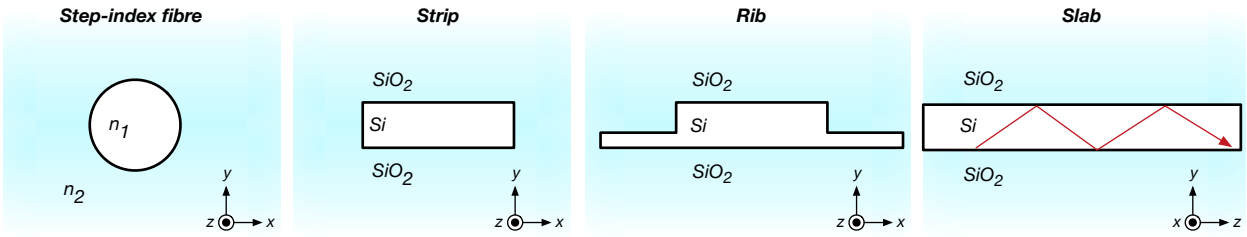

Figure 1.8: Types of optical waveguide

1.4 Integrated optics

We now review the set of integrated optics components that constitute the building blocks used in the measurements presented in this thesis. The growth of silicon as an optical material has led to the explosion of silicon photonics. Applications range from optical interconnects in data centres[20], to compact environmental sensors[59]. Recent years have seen the emergence of the first reprogrammable optical informational processing devices[54,60], albeit on smaller scales than required for full blown universal quantum computing. We refer the reader to appendices C (page 133) and E (page 151) for more background detail of the integrated optics and the wave equation, respectively.

1.4.1 Waveguides

Optical waveguides are structures that are spatially inhomogeneous, providing a refractive index contrast that confines and guides light. Commonplace waveguides are optical fibres, allowing low-loss transmission of signals over vast distances facilitating communication—a diagram of a typical circular core step-index fibre is shown in Fig. 1.8. All total internal reflection (TIR) waveguides have a region of high refractive index (n_1), usually referred to as the core, surrounded by a material of lower refractive (n_2) index called the cladding i.e. $n_1 > n_2$. Waveguides that support a single-mode are known as single-mode (SM) waveguides, while waveguides that support more than one waveguide mode are known as multi-mode waveguides. The speed that light propagates through a waveguiding structure is governed by the effective refractive index, or more succinctly, the effective index $n_{\text{eff}} = c/v$, where c is the speed of light in vacuum and v is the phase velocity in the guiding medium.

Dispersion in bulk materials is the phenomenon where the refractive index of a material depends on the optical frequency. The effective index is determined by the bulk refractive index and the waveguide dispersion, where the phase velocity of light depends on the physical geometry of the confining structure. The effective index of a waveguide lies somewhere between the value of bulk index of the core and cladding i.e. $n_{\text{clad}} < n_{\text{eff}} < n_{\text{core}}$. If a waveguide supports a mode, it will continue to propagate with the same transverse mode profile in the absence of external perturbations.

For light propagating in a waveguide with effective index n_{eff}, it has a propagation constant proportional to the wavenumber $\beta = k_0 n_{\text{eff}} = \omega n_{\text{eff}}/c$, where ω is the angular frequency. For most dielectric media, the magnetic susceptibility is approximately 1, leading

to the wave equation* for plane electric and magnetic waves

$$\nabla^2 \mathbf{F} = \mu_0 \epsilon \frac{\partial^2 \mathbf{F}}{\partial t^2}, \tag{1.43}$$

with $\mathbf{F} \in \{\mathbf{E}, \mathbf{B}\}$, $\epsilon = \epsilon_0 \epsilon_r$ and $\epsilon_r \approx n^2$ is the relative permittivity, relating directly to the dielectric refractive index. The transmitted waves in optical waveguides are not plane waves; they propagate with a phase velocity $v = c/n_{\text{eff}}$. Since the definition of a guided optical mode profile remains constant (without perturbation), the field can be separated into the profile $\mathcal{F}$ in x and y and propagation in z, eliciting a solution of the form

$$\mathbf{F} = \mathcal{F}(x, y) e^{-i(\omega t - \beta z)}. \tag{1.44}$$

Taking Eqn. (1.44) and plugging this into Eqn. (1.43) gives

$$\nabla^2 \mathcal{F}(x, y) = \left(\beta^2 - \frac{\omega^2}{c^2} n(x, y)\right) \mathcal{F}(x, y) \tag{1.45}$$

$$= (\beta^2 - k^2) \mathcal{F}(x, y). \tag{1.46}$$

Equation (1.46) is a vector formula of the Helmholtz flavour, with eigenvalue β, and is useful in simulating the waveguide dispersion. In general this equation can only be solved analytically when the confinement is in one dimension. For fully vectoral solutions in two dimensions, numerical techniques are often required using what is known as a 'mode solver'. Mode solving simulations will be used extensively in the following chapters to model the propagation constant, dispersion and effective modal area of waveguides.

In integrated optics there are three main types of waveguide which we now discuss—slab, strip and rib. It is worth noting that more exotic types exist: suspended [61], subwavelength [61] and photonic crystal waveguides [62] have all been demonstrated, but are not part of experiments described in this thesis.

Slab waveguides

In a slab waveguide (see Fig. 1.8), also known as planar waveguide, the light is free to propagate in the plane of the optical material. This is in contrast to the strip and rib waveguides where the optical mode is confined in two dimensions. We can construct an optical mode that can be assumed to be propagating in the z-direction, and polarised in the $\hat{x}$ direction so that $\mathcal{F}(x, y) = \mathcal{F}(y)\hat{x}$. Since the field is transverse and polarised, if the electric field lies along $\hat{x}$ then there must be zero electric field component in the propagating z direction; this polarisation is known as transverse electric (TE). Similarly if the magnetic field is aligned with the $\hat{x}$ axis, the field is called transverse magnetic (TM). See appendix C.1 on page 133 for more details on the symmetric slab waveguide. The cutoff condition of a slab waveguide mode occurs when the propagation angle of the mode undergoing TIR propagates at the critical angle; beyond this angle it becomes an unguided radiation mode. In a symmetric slab waveguide (where the top and bottom cladding are the same), the cutoff for the fundamental mode occurs at zero thickness and therefore any symmetric waveguide supports at least one TE and one TM mode. Conversely, the asymmetric waveguide (different upper and lower cladding) fundamental mode cutoff

*See appendix E.1 on page 151 for derivation.

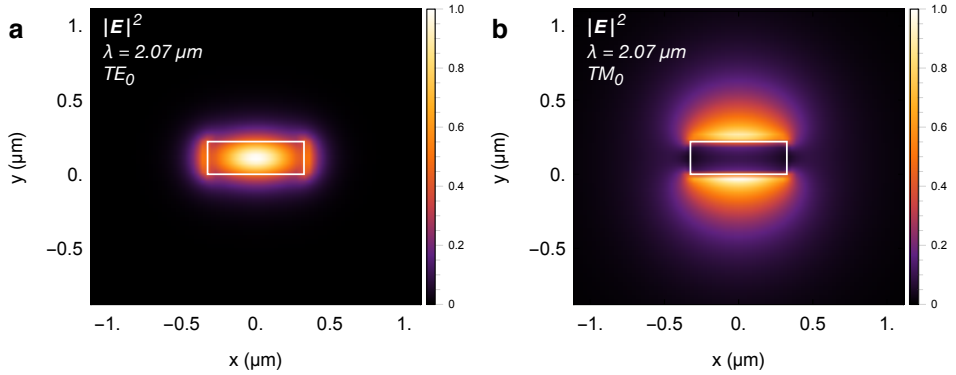

Figure 1.9: Mode solved strip waveguide normalised electric field magnitude $|E|^2 = |E_x|^2 + |E_y|^2 + |E_z|^2$. **a**, Fundamental transverse electric (TE) waveguide mode. **b**, Fundamental transverse magnetic (TM) waveguide mode.

does not occur at zero thickness and therefore gives rise to true single-mode operation when the fundamental TM mode is cutoff and the TE mode is not. While none of the propagation waveguides used in this thesis are planar, the guiding region of grating couplers can be treated as a slab waveguide. Calculation of the fundamental slab mode effective index with Eqn. (C.6) is used to design grating couplers and this approximate method is presented in appendix C.2 on page 134.

Strip waveguides

Strip waveguides have a huge number of names in the literature, but here we define the type of waveguides that are rectangular as seen in Fig. 1.8. These types of waveguide provide high confinement in two dimensions and are typically used in waveguide photon-pair sources. The height of the waveguide is usually fixed by the wafer manufacturer, since the silicon film across a wafer has uniform thickness. The height of waveguide determines the width where higher order modes can propagate. It is also important for photon-pair generation—for some waveguide heights no waveguide width exists with the dispersion that gives rise to efficient phase-matching in the fundamental mode (see Sec. 1.7.3). The waveguide width degree of freedom allows for tuning of the dispersion which can produce a bright, phase-matched photon-pair source.

Generally, the Helmholtz equation (Eqn. (1.46)) cannot be solved analytically for these structures*; numerical solutions with a mode solver are often required. Predominantly in this thesis, strip waveguides are used for sources, symmetric and asymmetric Mach-Zehnder interferometers, delay lines and routing light around waveguide circuits. The field intensity of a strip waveguide supporting one TE and one TM optical mode is presented in Figs. 1.9a and 1.9b, respectively. Due to this higher confinement of this TE mode, all the designs presented are exclusively for the TE mode. Furthermore, the minimum low-loss bending radius of these waveguides is also substantially smaller than the TM mode, making it superior for higher density component integration.

In general, fully TE and TM modes do not physically exist, with some small but non-zero component of the electric or magnetic field in the direction of propagation; these

*Although approximate solutions exist such as Marcatili's method[63]

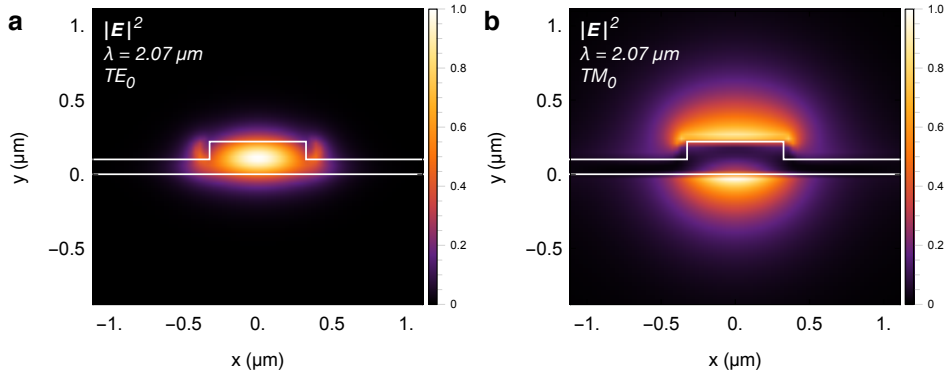

Figure 1.10: Mode solved rib waveguide normalised electric field magnitude $|E|^2 = |E_x|^2 + |E_y|^2 + |E_z|^2$. **a**, Fundamental transverse electric (TE) waveguide mode. **b**, Fundamental transverse magnetic (TM) waveguide mode.

modes are actually quasi-TE and -TM. For brevity, we will drop the 'quasi' nomenclature and implicitly recognise that these modes are not fully transverse.

The dominant loss mechanism of these waveguides arises from overlap of the optical mode with the sidewalls. In bulk, scattering losses from features that are much smaller than the wavelength scale as λ^{-4} [64]. For guided waves with a correlation length of the defects shorter than the wavelength, this has been shown to reduce the scattering to a λ^{-3} dependence [65,66] which is also due to the reduction in confinement at longer wavelengths [66].

Rib waveguides

Rib waveguides can have lower loss than strip waveguides, since the overlap of the waveguide walls is reduced due to the optical mode propagating in the slab region of the waveguide. Single-mode rib waveguides can also support a TE (Fig. 1.10a) and TM (Fig. 1.10b) mode, and require the use of a mode solver to obtain a numerical solution to the vectoral Helmholtz equation.

One main application of rib waveguides is in electro-optic modulators. Here, the rib waveguide core has positive and negative dopants, and the slab regions provide an area for metallic contacts for applying voltages to modify the refractive index [15]. Rib waveguides were not used for a photon-pair source due to the lower optical confinement and incorrect dispersion for phase-matching. A multi-mode rib waveguide was tested as a delay line, presented in Sec. 3.5.1 with a reasonably low optical loss of 0.38 dB/cm.

1.4.2 Modal properties of waveguides

The effective modal area of a waveguide determines the size of the waveguide mode. For nonlinear optics, this parameter is of great importance as it determines the confinement (and intensity) of the optical field, and subsequently the effective nonlinearity of the waveguide. Several definitions exist for the waveguide modal area exist with the most

common being[67]

$$A_{\text{eff}} = \left(\iint_{-\infty}^{\infty} S_z dxdy\right)^2 \Big/ \iint_{-\infty}^{\infty} S_z^2 dxdy \tag{1.47}$$

$$\approx \left(\iint_{-\infty}^{\infty} |F(x,y)| dxdy\right)^2 \Big/ \iint_{-\infty}^{\infty} |F(x,y)|^4 dxdy, \tag{1.48}$$

where $S_z = (\mathbf{E} \times \mathbf{H}) \cdot \hat{z}$ is the time-averaged Poynting vector in the propagation direction. In Eqn. (1.48), the approximation is that the refractive index varies slowly in the transverse direction. This definition is mostly used for the results presented in chapter 3. However, when we attempt to precisely measure the waveguide nonlinear parameters in chapter 4, we use an alternate definition that is more representative, weighting the modal area by nonlinear core of the waveguide[67].

A crucial building block for any quantum photonic platform is low-loss waveguides. The majority of linear propagation losses arise from scattering off the side wall roughness[64] and free carrier absorption from background doping[68]. Typically single-mode strip waveguides in the near infrared (NIR) have linear scattering losses of around 1 – 3 dB/cm[69,70]. An advantage of working in the MIR means that simply by translating the wavelength from 1.55 μm to around 2.1 μm, results in a $> 2\times$ reduction of linear propagation loss from reduced sidewall scattering[64].

Reducing waveguide losses can also be achieved by minimising overlap of the waveguide modes and the sidewalls. In a strip waveguide this is attained by increasing the waveguide width at the cost of using multi-mode waveguides. In Sec. 3.2, we use multi-mode waveguide structures to reduce loss. Other fabrication approaches have improved[71] or almost entirely eliminate[72] the sidewall roughness, thus decreasing the strength of the scattering perturbation.

Dispersion is another key parameter of the waveguide. The dispersion in a waveguide has a contribution the from bulk value, but also from the physical geometry of the waveguide. The waveguide dimensions determine the value of the propagation constant, and other important properties that are fundamental to photon-pair generation—discussed in more detail in Sec. 1.7.3. In general the exact form of the waveguide propagation constant is not known, so a common approach is to take the Taylor expansion about a central frequency[73]

$$\beta(\omega) = \beta_0 + \beta_1(\omega - \omega_0) + \frac{\beta_2}{2}(\omega - \omega_0)^2 + \frac{\beta_3}{6}(\omega - \omega_0)^3 + \dots \tag{1.49}$$

where

$$\beta_n = \left.\frac{d^n \beta}{d\omega^n}\right|_{\omega=\omega_0} \qquad \text{where } n \in \mathbb{Z}^+. \tag{1.50}$$

The constants $\beta_1 = 1/v_g$, is related to the group velocity at which the centre of a pulse propagates, and β_2 is the group velocity dispersion (GVD) which determines how fast a pulse spreads out or contracts. In fibre optic communications, the GVD is usually defined using the derivative with respect to wavelength i.e. $D = \frac{d}{d\lambda}\frac{1}{v_g} = -\frac{2\pi c}{\lambda^2}\beta_2$ which has a negative sign with respect to β_2. To avoid confusion between calling these positive and negative dispersion due to the different sign conventions, these are often referred to normal ($\beta_2 > 0$) and anomalous ($\beta_2 < 0$) GVD.

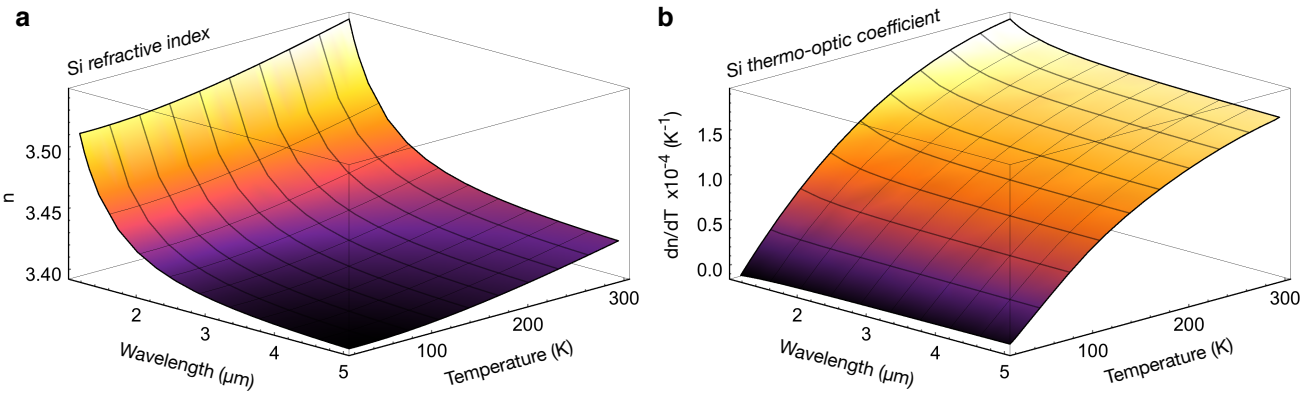

Figure 1.11: Thermo-optic coefficient and dispersion with varying temperature of silicon using Sellmeier model from Ref. 74. **a**, Dispersion of silicons refractive index with varying temperature. **b**, Dispersion of silicons thermo-optic coefficient with varying temperature.

1.4.3 Themo-optic phase modulation

Silicon posses a thermo-optic coefficient that changes the refractive index with variations in temperature. We use this effect in chapter 5 to manipulate the quantum state on-chip. The phase change is given by

$$\Delta\phi = \frac{2\pi L}{\lambda}\Delta n, \tag{1.51}$$

where L is the length travelled in the medium, λ is the wavelength and Δn is the change in refractive index due to the thermo-optic effect. In silicon in the 2.1 μm band, the thermo-optic coefficient is approximately $\partial n/\partial T = 1.7 \times 10^{-4}$ K^{-1} [74]. A plot showing the variation of the refractive index and thermo-optic coefficient of silicon is shown in Figs. 1.11a and 1.11b. Modifying the temperature of the waveguide locally varies the refractive index and the phase of light with low loss. This mechanism of exploiting the thermo-optic effect can be used to implement Mach-Zehnder interferometers, with the temperature difference imparting the phase shift. This mechanism is however relatively slow* with a maximum speeds of hundreds of kHz [76], and proves to be completely impossible to scale at cryogenic temperatures†. Furthermore, at cryogenic temperatures the thermo-optic coefficient of silicon is reduced (see Fig. 1.11b), meaning additional power dissipation is required to impart the same phase change [74]. Finally, the effects of thermal cross-talk make running large scale experiments challenging, as the effect of driving one thermo-optic phase modulator (TOPM) in one part of a chip may affect the phase on a proximal waveguide. While future large scale optical quantum information processing will need high speed modulation for multiplexing, this effect is easy to implement and useful for small scale, proof of concept room temperature experiments (such as ours) that do not require fast modulation and long integration times for each measurement setting.

*For comparison, silicon Mach-Zehnder intensity modulators have been shown to operate at >50 GHz [75].
†The maximum cooling power of big cryostats are around 230 mW at 1.0 K [77].

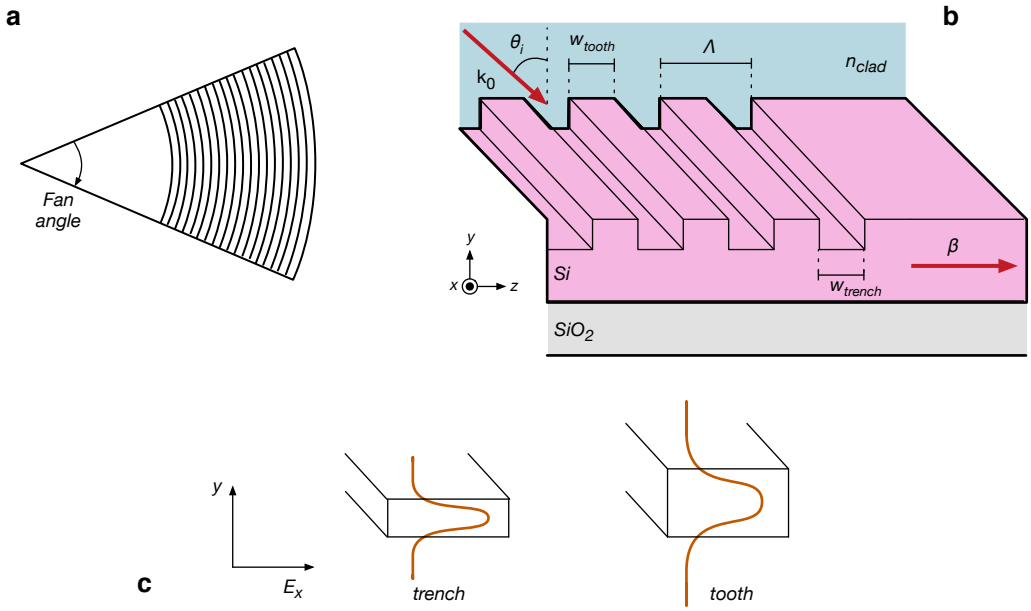

Figure 1.12: Grating couplers overview. **a**, Birds eye view schematic of a focusing grating coupler. **b**, In plane isometric view of the grating, with incident light at angle θ_i, period Λ, tooth and trench widths w_{tooth}, w_{trench} and top cladding with index n_{clad}. **c**, Schematic of the x-component of the electric field for the slab modes of the tooth and trench.

1.4.4 Fibre-chip couplers

Fibre-chip coupling facilitates the transmission of light from an optical fibre into a waveguide mode. For reference, the mode-field diameter (MFD) of typical single-mode fibre (SMF) at 2.1 μm wavelength is around 15 μm[78], while the waveguide is of order 0.5 μm. This clearly highlights the disparity between the scales of the two, differing by almost an order of magnitude, and the challenge of facilitating efficient coupling. We now review the two main types of coupler used for experiments in the following chapters—the grating coupler and edge coupler.

Grating couplers and edge couplers have their own strengths and weaknesses. Grating couplers are frequency bandwidth limited due to a finite range of the phase-matching condition and are lossy. Gratings are convenient for long-term coupling stability and simultaneously addressing multiple optical inputs and outputs with a fibre array. They also allow for a large number of devices to be tested as the form factor can be small and coupling can be achieved at any location on the chip surface.

Edge couplers have a far broader coupling frequency response and low losses. Long term coupling stability of edge coupling is reduced, and the total number of optical inputs and outputs is limited due to practical challenges with aligning multiple lensed fibres into an array. Since coupling must be achieved at the facets, the total number of devices that can be accessed is reduced compared to gratings due to limited space on the chip edge.

Grating couplers

Grating couplers are periodic structures that diffract light from above the plane of the chip, typically at some incident angle θ_i to the chip surface normal, into the waveguide for a specific polarisation. The main design parameters of a grating are the etch depth, period, and fill factor—the ratio of tooth to grating period. Additionally, compact focusing grating couplers have the fan angle (Fig. 1.12a), and the eccentricity[79] e—a measure of difference between the major (a) and minor (b) axes of an ellipse—as additional design parameters*. We show an in plane schematic of a grating in Fig. 1.12b. Typical figures of merit for these structures are the 3 dB coupling bandwidth and peak insertion loss.

Grating couplers usually have a partial etch to break the symmetry of a slab waveguide, causing light to be preferentially scattered in the upwards direction. Phase-matching occurs when the waves scattered by the grating have the same phase and constructively add together. Grating couplers are bandwidth limited due to a finite range of the phase-matching condition. Gratings benefit from long term stability, easy alignment of multiple inputs and outputs waveguide circuits and the convenience of wafer scale testing from top coupling with a V-groove array (VGA). In this thesis, we predominantly work with uniform grating couplers. We outline the theory of their operation and a robust design strategy in appendix C.2 on page 134. When the phase-match condition is satisfied, solving for the first diffraction order gives an expression in terms of the grating period[66] Λ

$$\Lambda = \frac{\lambda}{n_{\text{eff}} - n_{\text{clad}} \sin\theta_i}, \tag{1.52}$$

where λ is the central wavelength of emission from the grating, n_{eff} is the weighted effective index for the tooth and trench slab modes (Fig. 1.12c), n_{clad} is the top cladding index and θ_i is the angle of incidence from the chip surface normal.

Uniform grating couplers cause an exponential decay of the field intensity along the length of the grating, which is often poorly matched to the input/output fibre mode. Techniques such as apodisation† can help improve the mode overlap[80,81]. Furthermore, other techniques employing blazed gratings[82], subwavelength structures[83,84] and back mirrors[84] have been shown to improve coupling efficiencies to sub-decibel levels.

Edge couplers

Edge couplers directly overlap the fibre and waveguide modes at the facet of the chip. Edge couplers benefit from broadband transmission which is essential for generating photon pairs over large frequency detunings. Waveguide modes have a cross sectional area of around ~ 0.1 μm^2 while a fibre core is around ~ 200 μm^2. Lensed fibres are required to focus a Gaussian beam to a MFD that is comparable to a waveguide.

Edge couplers come in two different flavours: expanded and inverted tapers. The expanded edge coupler tapers adiabatically from a single-mode waveguide to a large multi-mode strip waveguide to increase the modal area. Design of expanded edge couplers involves mode overlap integrals between the lensed fibre Gaussian mode and the

*Here, $e = \sqrt{1 - b^2/a^2}$, where the equation for an ellipse is $(x/a)^2 + (y/b)^2 = 1$.

†Varying the fill factor along the length of grating.

expanded taper using[85],

$$\eta_c = \frac{\left| \iint E_i^* E_m dxdy \right|^2}{\left(\iint |E_i|^2 dxdy\right)\left(\iint |E_m|^2 dxdy\right)}, \tag{1.53}$$

where η_c is the coupling efficiency, x, y are the spatial coordinates across the modal cross section, E_i and E_m are the electric fields of the input fibre and the edge coupler modes, respectively. The optimal width of the expanded taper is chosen for the greatest overlap. These couplers are typically used when the chip facet position is not well known due to uncertainty on a cleave.

The inverted edge couplers taper a waveguide down to a small size. As the geometry of the inverted edge coupler becomes reduced, the optical mode becomes less confined, with the majority mode now delocalised and propagating in the cladding[86]. The minimum edge coupler taper geometry is then again chosen when the size of the optical mode becomes comparable with the fibre mode, increasing the power coupling between the two. Inverted edge couplers are used when the exact position of the optical facet is known. This is to reduce the larger delocalised mode from leaking into the silicon substrate, calling for short distances for when optical mode is large.

Other more fancy edge couplers have also been demonstrated, using subwavelength designs[87], and adiabatic mode transfer between a nano-tapered fibre evanescently coupling into a nano-tapered optical waveguide[88].

1.4.5 Integrated beamsplitters

Beamsplitters are a fundamental building block of linear optics. A generic lossless beamsplitter is described by the unitary matrix[89]

$$\hat{U}_{\mathrm{BS}} = \begin{pmatrix} \sqrt{\eta} & i\sqrt{1-\eta} \\ i\sqrt{1-\eta} & \sqrt{\eta} \end{pmatrix}, \tag{1.54}$$

where η is the beamsplitter reflectivity. We now discuss two main methods of integrated beamsplitters for coupling light between different waveguides.

Directional coupler

Directional couplers (DCs) are an almost lossless method of coupling light between waveguides. Two identical waveguides are brought into proximity, and the evanescent field of from one waveguide leaks into the adjacent one forming superpositions of the individual waveguide modes called supermodes. Two possible configurations are excited: the symmetric (Fig. 1.13a) and antisymmetric (Fig. 1.13b) supermode of the waveguide pair. The supermodes have slightly different effective indices, the difference of these is $\Delta n = |n_{\mathrm{odd}} - n_{\mathrm{even}}|$. Due to the slight difference in phase velocities between the two modes, a beating effect occurs; if light is injected in one of the DC inputs, the power oscillates between the two waveguides. Correctly choosing the length of the coupling region achieves a 50/50 beamsplitter. The crossover length L_{x} at wavelength λ, where optical power is completely transferred from one waveguide to another, is given by[90]

$$L_{\mathrm{x}} = \frac{\lambda}{2\Delta n}. \tag{1.55}$$

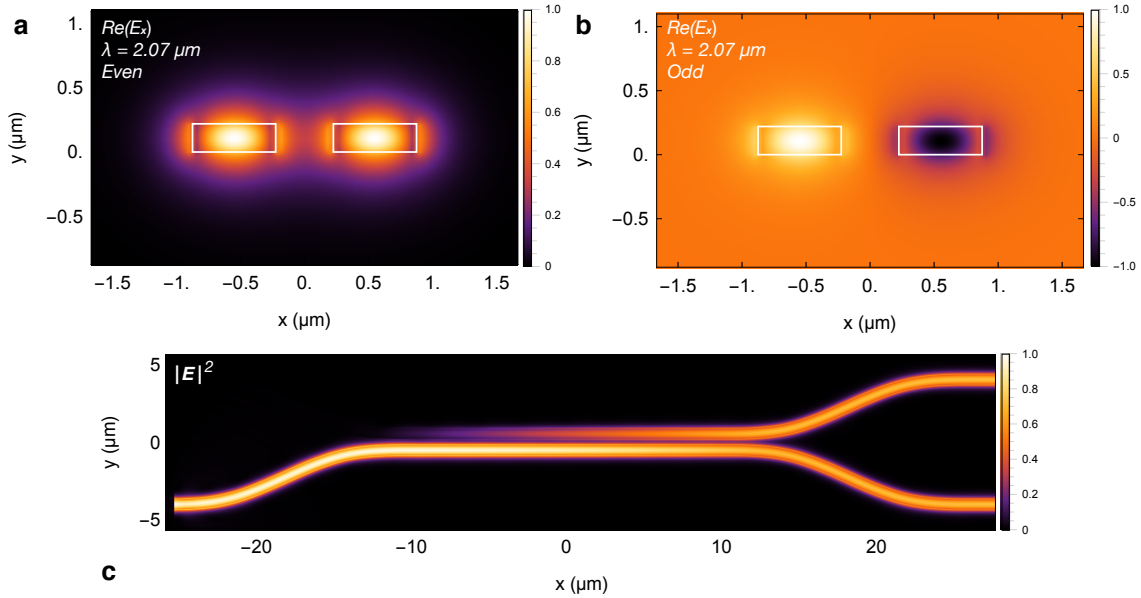

Figure 1.13: Directional couplers. **a**, Normalised real x component of the electric field of the even supermode. **b**, Normalised real x component of the electric field of the odd supermode. **c**, Normalised electric field magnitude $|E|^2 = |E_x|^2 + |E_y|^2 + |E_z|^2$ for a 3D FDTD simulation of a balanced directional coupler.

We may rewrite the beamsplitter matrix in Eqn. (1.54) in terms of trigonometric functions

$$\hat{U}_{\mathrm{DC}} = \begin{pmatrix} \cos(\pi z/(2L_{\mathrm{x}})) & i\sin(\pi z/(2L_{\mathrm{x}})) \\ i\sin(\pi z/(2L_{\mathrm{x}})) & \cos(\pi z/(2L_{\mathrm{x}})) \end{pmatrix}, \tag{1.56}$$

with z as the length propagated in the coupling region. For a realistic coupler however, there will be some non-zero coupling from the bending before a coupling region. This means for a 50/50 beamsplitter operation $\eta = 0.5 = \cos^2(\pi(L_{50/50} + L_{\mathrm{bend}})/(2L_{\mathrm{x}}))$, where L_{bend} is the effective extra length from the bending region and $L_{50/50}$ is defined in Eqn. (1.57). Figure 1.13c shows the electric field from a finite-difference time-domain (FDTD) simulation of a balanced DC.

To design a 50/50 beamsplitter, standard mode solving for the odd and even supermode will determine the crossover length. The DC with a zero length coupling region should be simulated with FDTD method to estimate the effective length of the bends—see Appendix C.6 on page 140 for more details. Finally, the balanced directional length is given by

$$L_{50/50} = \frac{L_{\mathrm{x}}}{2} - L_{\mathrm{bend}}. \tag{1.57}$$

To illustrate the coupling between these supermodes, an in-plane electric field for a 3D FDTD simulation of a balanced directional coupler is given in Fig. 1.13c. The directional coupler is prone to fabrication variations as small changes in the gap or waveguide widths lead to deviations in the directional coupler reflectively. Techniques using curved [91] or tapering to asymmetric waveguides [92] in the coupling region, have improved the 3 dB coupling bandwidth in excess of 100 nm.

Asymmetric directional couplers have also recently become of great interest; transverse mode order conversion [93,94] has applications in mode-division multiplexing [95] and dispersion engineering for photon pair sources.

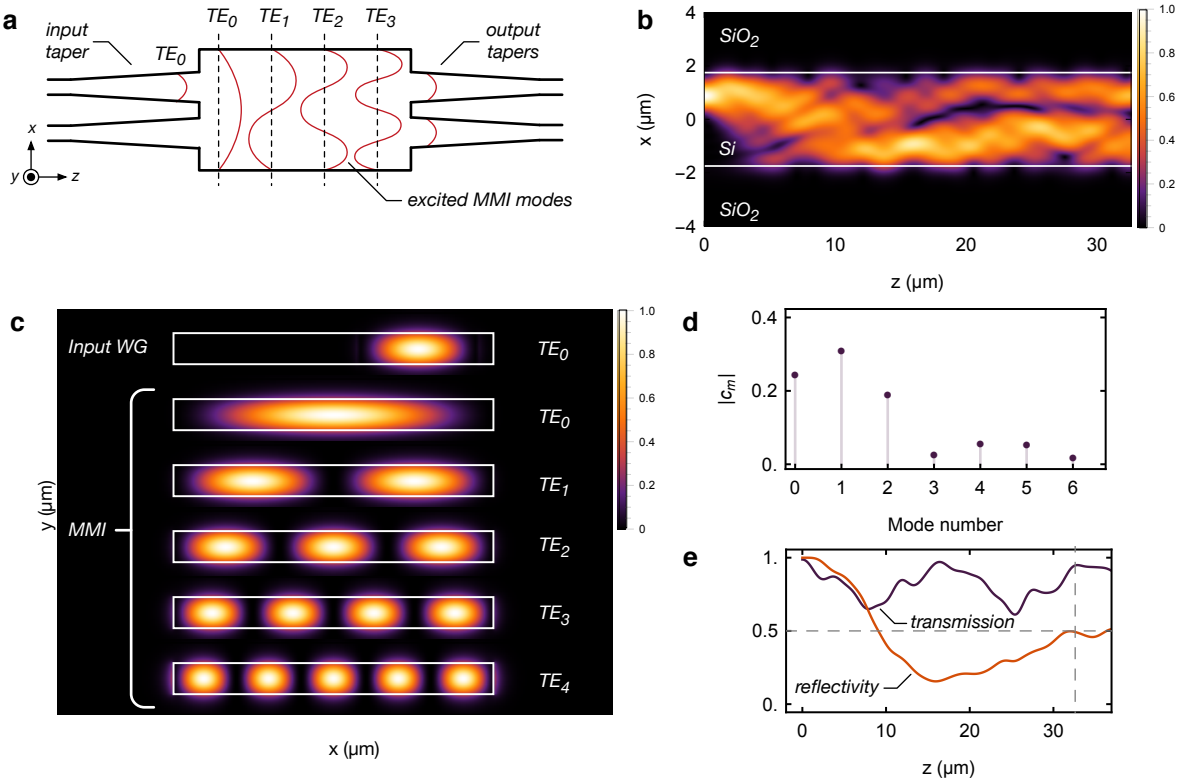

Figure 1.14: Multimode interference couplers (MMI). **a**, Schematic showing the plan view of a 2×2 MMI. **b**, Normalised in plane electric field amplitude with propagation using mode solving field excitation calculations at $\lambda = 2.07$ μm. **c**, Normalised electric field magnitude $|E|^2 = |E_x|^2 + |E_y|^2 + |E_z|^2$ of the input waveguide and excited modes in the multimode region. **d**, Magnitude of the field excitation coefficients between the input and MMI modes. **e**, Transmission into the output waveguide, and reflectivity along the coupler length.

Multimode interference coupler

Multimode interference couplers (MMIs) interfere multiple copropagating modes, each with different propagation constants. In general, a MMI can have an arbitrary number of inputs and outputs. For our waveguide circuits, we only use power splitters with one input and two outputs, and beamsplitters with two inputs and outputs. The MMI typically has higher insertion loss than the DC, but is more robust to fabrication imperfections, and has a wider 3 dB coupling bandwidth.

MMIs usually consists of a taper up from a single mode waveguide before a wide multimode region where several modes are supported, a schematic of a typical MMI device and the excited modes electric fields are shown in Figs. 1.14a and 1.14c respectively. The input waveguide mode excites a set of these modes with varying amplitudes, depending on the overlap between the electric fields (Fig. 1.14d), described by[96]

$$c_m = \frac{\iint E_i E_m dxdy}{\sqrt{\iint E_i^2 dxdy}} \tag{1.58}$$

where c_m are the field excitation coefficients of each mode, x, y are the spatial coordinates across the modal cross section, E_i and E_m are the electric fields of the input and m^{th}

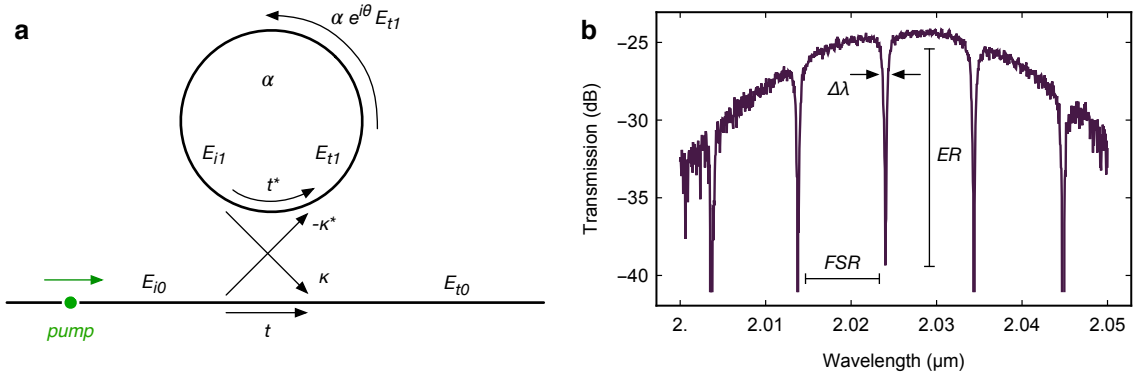

Figure 1.15: Ring resonators. **a**, Schematic of the single bus ring resonator. **b**, Transmission spectra of a single bus ring resonator with 100 μm cavity length. We label the extinction ratio (ER), free spectral range (FSR) and linewidth ($\Delta\lambda$).

mode* in the MMI multimode region, respectively. The beat length of the lowest two order modes in the MMI region is then computed[96]

$$L_\pi = \frac{\pi}{\beta_0 - \beta_1}, \tag{1.59}$$

where $\beta_m = 2\pi n_{\text{eff}}/\lambda$ is the propagation constant of mode m. The evolution of the field from the superposition of all of the copropagating modes is given by[96]

$$\Psi(z) = \sum_m c_m \psi_m e^{i\beta_m z} \approx \sum_m c_m \psi_m e^{i\frac{m(m+2)\pi}{3L_\pi} z}, \tag{1.60}$$

where Ψ is the propagated waveguide mode (as shown in Fig. 1.14b) in the MMI region and ψ_m is the m^{th} modes electric field. The MMI length is then selected when the integrated fields over the positions of the output tapers is balanced and maximised, as shown in Fig. 1.14e.

Other notable designs facilitate polarising beamsplitters with asymmetric designs[97], and improve the 3 dB coupling bandwidth employing subwavelength grating structures[98].

Exotic couplers

Other more innovative couplers exist, none of which are used in this thesis, but they are worth highlighting. Exotic couplers usually differ from traditional MMI and DC types of components, often relying on machine learning, and genetic algorithms.

Particular examples include an ultra-compact polarising beamsplitter, with the appearance of a QR code, allowing pixels to be etched or unetched[99]. Another paper uses genetic algorithms—particle swarm optimisation—to design a small, low-loss 1×2 Y-junction splitter with a continuous spline curvature[100]. Plenty of other examples using computational methods to design new components and widgets exist, promising to push the limits of integrated photonics.

1.4.6 Ring resonators

Ring resonators are a type of optical cavity, with a coupling region often enabled by a directional coupler—we schematically show a single-bus ring resonator in Fig. 1.15a.

*m is labelled from zero i.e. $m \in \{0, 1, 2, \ldots\}$

Ring resonators with a single bus are frequently used for parametric frequency conversion[101] and photon-pair sources[102] by pumping a resonance of the ring and collecting photons inside resonances equally spaced in energy*. These structures benefit from cavity enhancements effects, which lead to orders of magnitude increased pair generation rates[103], but suffer from sensitivity to environmental fluctuations therefore requiring stabilisation. Ring resonators can also be used for applications such as modulation[104], filtering[105] and gas sensing[106]. For the ring filter a secondary coupling region is added, known as the drop channel, which couples light back out of the resonator and into a different waveguide.

We give a detailed background of a single bus ring resonator operation in appendix C.3 on page 136. Here we state the end result: when light in the ring completes an integer number of wavelengths i.e. $\theta+\phi = 2m\pi$, the power at the output waveguide reduces to[107]

$$P_{t1} = \frac{(\alpha - |t|)^2}{(1-\alpha|t|)^2}, \tag{1.61}$$

where α is the round trip transmission, and t is the reflectivity (or coupling loss) of the ring. In the case where $|t| = \alpha$, i.e. the coupling losses of the ring balance the round trip losses, the transmitted power at the output waveguide drops to zero. This phenomenon, known as critical coupling, is due to destructive interference. When a ring is critically coupled, the light propagates inside the ring until its field has decayed from scattering and propagation losses.

The figures of merit of ring resonators are the extinction ratio (ER), which is the ratio between the maximum and the minimum transmission of resonance linewidth; typically measured in dB and labelled in Fig. 1.15b. Additionally, the spacing between adjacent resonances is known as the free spectral range (FSR). The FSR of a resonator is given by†

$$\mathrm{FSR}_\lambda = \frac{\lambda^2}{n_g \Delta L} \tag{1.62}$$

$$\mathrm{FSR}_\nu = \frac{c}{n_g \Delta L}, \tag{1.63}$$

where c is the speed of light, $n_g(\lambda) = n - \lambda(dn/d\lambda)$ is the group index ΔL is the cavity length, λ is the wavelength and $\mathrm{FSR}_{\nu,\lambda}$ are the free spectral range in frequency and wavelength units, respectively.

In Sec. 3.4.3, we use an add-drop configuration with four cascaded ring resonators to demonstrate an integrated filter. Here, a second waveguide bus is placed on the other side of the resonator to couple light back out of the structure. If the coupler has two scattering matrices with parameters κ_1, κ_2 and t_1, t_2, the power at the drop port on resonance is then given by[107]

$$P_{\mathrm{drop}} = \frac{(1-|t_1|^2)(1-|t_2|^2)\cdot\alpha}{(1-\alpha|t_1 t_2|)^2}, \tag{1.64}$$

where maximum coupling at the drop port is achieved when the ring is lossless and the couplers are symmetric i.e. $\alpha = 1$ and $t_1 = t_2$.

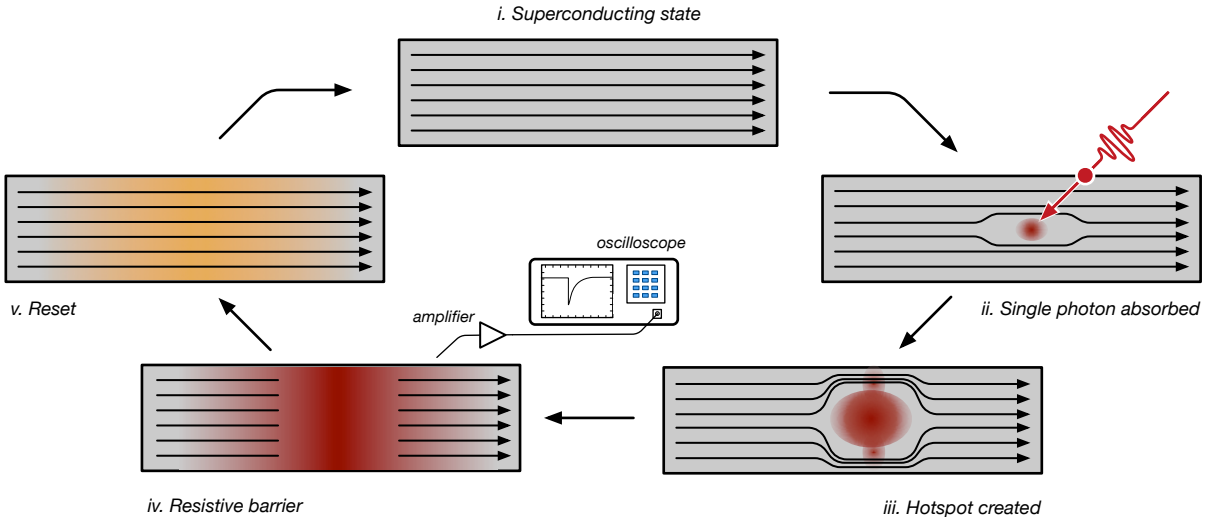

Figure 1.16: Operation of superconducting detectors. *i*. Nanowire is in superconducting state, *ii*. An incident photon is absorbed by the material, *iii*. This creates a resistive hotspot region, *iv*. The hotspot grows in size until a resistive barrier forms, which directs the current towards the amplification electronics. *v*, The nanowire returns to the superconducting state. Figure re-adapted from Ref. 108.

1.5 Superconducting detectors

Single photon detectors are necessary for single photon experiments. These come in two broad categories: single-photon avalanche photodiodes and superconducting nanowire single-photon detectors (SNSPDs); in our experiments, we exclusively use SNSPDs. The physics of these devices is relatively complex, with photon-detection mechanisms attributed to hotspots and vortices in different photon energy regimes[109]. We now briefly review a high-level description of the SNSPDs hotspot mechanism.

Superconducting nanowires detectors typically run at cold temperatures below 4 K, and rely on the superconductivity of cold metal alloys. At low temperatures, known as the critical temperature T_c, the electrical characteristics change, and the resistance of the material drops to zero. An electrical current in a superconductor below the critical temperature can flow indefinitely with no external power source. In this state, pairs of electrons are bound together in a phenomenon known as Cooper pairs. These pairs of electrons behave like Bosons since the total spin of a pair is an integer, which allows many of them to exist in the same quantum (ground) state and ultimately leads to the superconductivity[110].

To use this phenomenon to detect photons, the superconducting nanowire detector is initially in the superconducting phase. An incident photon with an energy much higher than Cooper pair binding energy illuminates the superconducting material, breaking the bond between the Cooper pairs. This creates an area known as a 'hotspot' where the electron pairs have been broken which leads to an increase in resistance. Since the resistance suddenly becomes non-zero, this causes a spike in the voltage detector output which, when amplified, is measurable on an oscilloscope or time interval analyser

*which is equal in resonant mode number spacing if the dispersion of the group index is flat.
†For the origin of this result see Sec. C.4.1 on page 137.

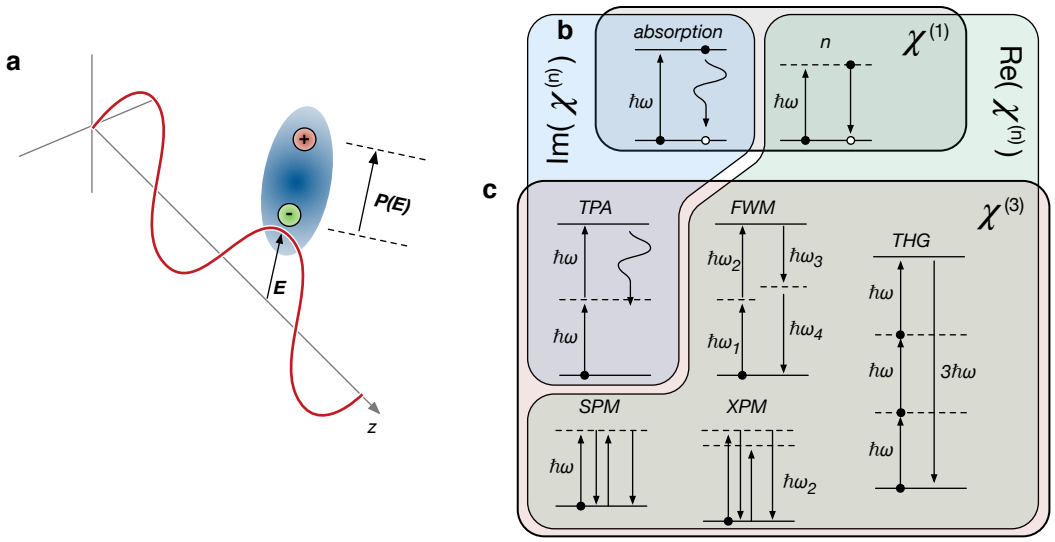

Figure 1.17: Optical nonlinearities in silicon, figure adapted from Ref 113. **a**, Illustration of the interaction of an electric field wave interacting locally, inducing a dipole moment and polarising the dielectric material. **b**, Linear susceptibility energy level diagrams, the interaction of a photon with dielectric determines the linear refractive index, and absorption by free electrons gives rise to absorption. **c**, Third-order susceptibility nonlinear effects energy level diagrams. The nonlinear interaction with electrons is responsible for self-phase modulation (SPM), cross-phase modulation (XPM), third-harmonic generation (THG), two-photon absorption (TPA) and four-wave mixing (FWM).

(TIA)[108]—see Fig. 1.16.

Typical figures of merit of a superconducting detector are the system detection efficiency (SDE), dark count rate (DCR), timing jitter (uncertainty of arrival time), afterpulsing and reset time back to the superconducting state. Superconducting nanowires have been shown to demonstrate state-of-the-art in all of these metrics with efficiencies greater than 93%[111]. Additionally, SNSPDs have been shown to be sensitive up to 5 μm[112], but moving to longer wavelengths in the MIR results in more significant contributions from black-body radiation on the DCR.

1.6 Nonlinear optics in silicon

1.6.1 Nonlinear polarisation

Optical nonlinearities are responsible for a whole host of phenomena, which are illustrated in Fig. 1.17c, ranging from the optical Kerr effect, single photon production from spontaneous four-wave mixing (SFWM)[46] to third harmonic generation[113]. We refer the reader to appendix E on page 151 for further discussion of the nonlinear wave equation. In dielectric media, an electric field causes the bound charges in the material to separate creating a local electric dipole moment—see Fig. 1.17a. The electric displacement field is defined as[73]

$$\mathbf{D} = \epsilon_0 \mathbf{E} + \mathbf{P} = \epsilon_0 (1 + \chi) \mathbf{E}, \tag{1.65}$$

where $\mathbf{P}$ is the polarisation density, $\mathbf{E}$ is the electric field, ϵ_0 is the permittivity of free space, and χ is the electric susceptibility of the dielectric. This polarisation field is then

naturally related back to the electric field

$$\mathbf{P} = \epsilon_0 \chi \mathbf{E}. \tag{1.66}$$

The microscopic origin of optical nonlinearities arises from anharmonic motion of bound electrons with an applied field[73]. The polarisation **P** of a nonlinear material therefore does not respond linearly with the electric field. The polarisation is often expressed as a power series in the field strength **E**

$$\mathbf{P} = \epsilon_0 \left(\chi^{(1)} \cdot \mathbf{E} + \chi^{(2)} \cdot \mathbf{EE} + \chi^{(3)} \cdot \mathbf{EEE} + \ldots \right), \tag{1.67}$$

here, $\chi^{(n)}$ is the n^{th} order electric susceptibility, which are $n+1$ rank tensors with units of $(\text{m/V})^{n-1}$. The first term in the expansion $\chi^{(1)}$, called the linear susceptibility, gives rise to the linear refractive index of dielectric materials (see Fig. 1.17b). The higher order polarisation terms ($n > 1$), are responsible for optical nonlinearities. Optical nonlinearities arise in two types of crystals—second- and third-order. Second-order nonlinear materials lack inversion symmetry at the molecular level, and silicon does not have a $\chi^{(2)}$ nonlinearity. Silicon does however have a third-order nonlinearity and therefore has this so called crystalline inversion symmetry, where for a crystal with a lattice site centred at $\vec{r}_0 = (0,0,0)$, every point in the crystal unit cell has an indistinguishable point under the transformation $\vec{r} \mapsto -\vec{r}$.

1.6.2 Nonlinear refraction and phase

Silicon has a relatively large third-order nonlinearity, which can also be predicted[114] from the high linear refractive index $n \sim 3.45$*. The majority of the third-order nonlinear effects originate from the nonlinear refractive index n_2. The total refractive index of a third order nonlinear material is[73]

$$\tilde{n}(I) = n_0 + n_2 I, \tag{1.68}$$

where n_0 is the linear refractive index and I is the optical intensity. The nonlinear refraction is directly related to the third order susceptibility tensor by[73]

$$n_2 = \frac{3}{8n} \text{Re}(\chi^{(3)}_{xxxx}), \tag{1.69}$$

where the field is assumed to be linearly polarised such that there is only contribution to the refractive index from one element of the rank-four tensor. Since the refractive index is now intensity dependent, so is the phase of light propagating in the medium

$$\phi = k_0 \tilde{n}(I) L = k_0 n_0 L + k_0 n_2 I L = \phi_0 + \Phi_{\text{NL}}, \tag{1.70}$$

where $k_0 = 2\pi/\lambda$, λ is the wavelength, and L is the length propagated in the medium. We can rewrite the nonlinear phase†

$$\Phi_{\text{NL}} = k_0 n_2 I L = k_0 n_2 \frac{P}{A_{\text{eff}}} L = \gamma P L, \tag{1.71}$$

*$\chi^{(3)} \propto \chi^{(1)}/E_{\text{at}}^2$ where $E_{\text{at}} = e/(4\pi\epsilon_0 a_0^2)$, where e is the elementary charge and a_0 is the Bohr radius.
†Here we use $I = P/A_{\text{eff}}$.

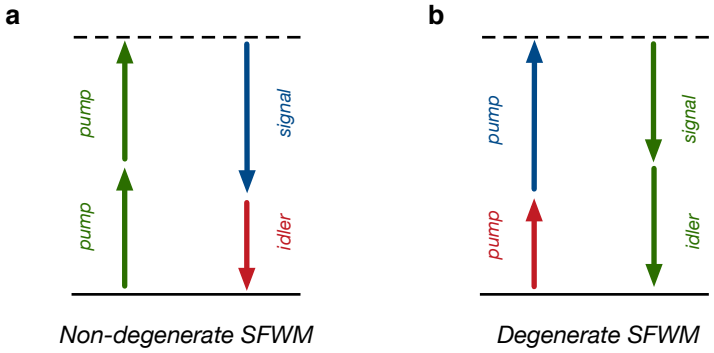

Figure 1.18: Degenerate and non-degenerate spontaneous four-wave mixing (SFWM).

where P is the peak power, A_{eff} is the effective area of the waveguide, and we define the waveguide nonlinear parameter

$$\gamma = \frac{k_0 n_2}{A_{\text{eff}}}. \tag{1.72}$$

The nonlinear phase Φ_{NL} is an intensity dependent phase that an optical pulse acquires propagating through nonlinear $\chi^{(3)}$ media. This is also commonly known as self-phase modulation (SPM)—see appendix E.4 on page 155 for the origin of this. Another closely related phenomenon is cross-phase modualtion (XPM), where one optical pulse induces a phase shift on another pulse of a different frequency, polarisation or direction. Self-phase modulation has applications in generation of optical solitons in waveguides with anomalous GVD[115], production of squeezed light[116] and supercontinuum generation[117]. Cross-phase modulation, has applications in fast all-optical switching of single photons[118].

1.6.3 Four-wave mixing

Generation of new optical frequencies with four-wave mixing (FWM) is also enabled by the $\chi^{(3)}$ nonlinearity[101,119]. While SPM and XPM effects are always phase-matched, great care must be taken when designing a source for generating parametric fluorescence. In silicon quantum photonics, photon-pairs are generated via SFWM in a silicon waveguide. In SFWM, two pump photons are elastically scattered off of the nonlinear $\chi^{(3)}$ material through an intermediate virtual energy level. The single photons produced are referred to as the signal ($\omega + \Delta\omega$) and idler ($\omega - \Delta\omega$) frequencies.

The two main types of FWM used in integrated quantum optics are *1*, when the two pump photons are the same, generating non-degenerate new frequencies at sidebands $\Delta\omega$ from the pump (Fig. 1.18a), or when *2*, two pumps are $\Delta\omega$ either side of the degenerate signal and idler frequencies generated (Fig. 1.18b). The frequencies of the signal and idler photons are constrained by energy and momentum conservation[73]

$$\omega_{p1} + \omega_{p2} - \omega_s - \omega_i = 0 \tag{1.73}$$

$$\Delta k = k_{p1} + k_{p2} - k_s - k_i \to 0, \tag{1.74}$$

where $k = 2\pi n/\lambda$. Providing energy matching is satisfied, the momentum conservation condition of $\Delta k = 0$ is also known as 'phase-matching', and is determined by the effective index of the waveguide at the new frequencies generated. In a waveguide, the additional degree of freedom from the waveguide geometry allows the dispersion to be modified.

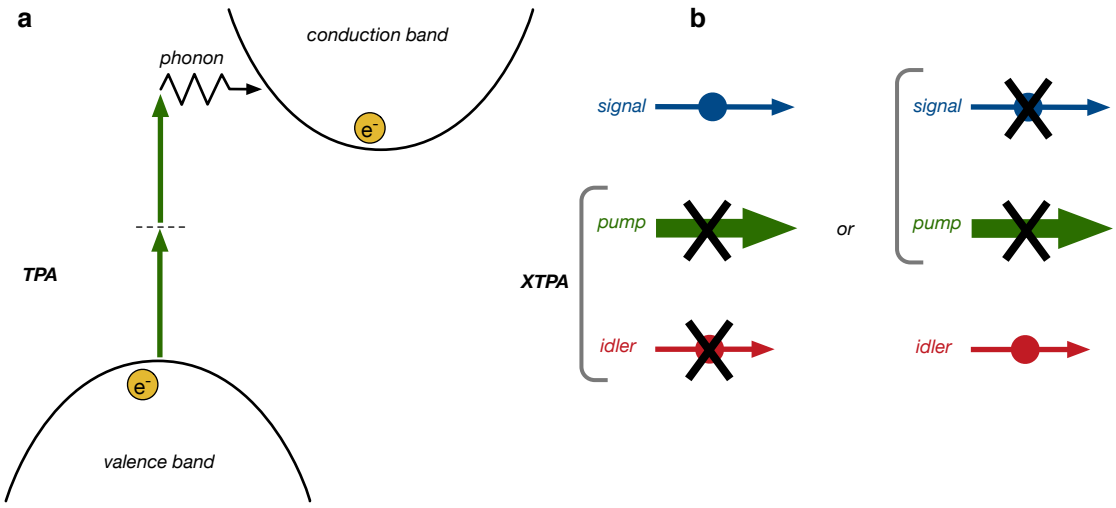

Figure 1.19: Two-photon absorption (TPA) and cross two-photon absorption (XTPA) in an indirect band gap semiconductor.

Another approach for phase-matching is with different transverse mode orders[120]. The phase-matching for a waveguide photon-pair source is discussed in more detail in Sec. 1.7.3.

1.6.4 Two-photon absorption

Two-photon absorption (TPA) is nonlinear absorption, where an electron in the valence band is excited to the conduction band by two photons via a virtual energy level (see Fig. 1.19a), growing quadratically with optical intensity. Due to silicon's indirect band gap, this process must be mediated by a phonon, to provide the momentum for the transition to take place. At low temperature, it has been shown that the TPA drops significantly at NIR wavelengths[121]. However, electrons may also emit a phonon to facilitate this process, meaning that TPA still occurs when phonons freeze out at low temperatures.

The decay of optical intensity I due to linear losses and TPA is described by the differential equation[121,122]

$$\frac{\partial I}{\partial z} = -\alpha_0 I - \beta_{\mathrm{TPA}} I^2 \tag{1.75}$$

$$\frac{\partial P}{\partial z} = -\alpha_0 P - \alpha_{\mathrm{TPA}} P^2, \tag{1.76}$$

where $\alpha_0, \beta_{\mathrm{TPA}}, \alpha_{\mathrm{TPA}}$ are the linear, bulk and waveguide nonlinear absorption coefficients, respectively. In this process, free carriers are also generated leading to increased free carrier absorption (FCA), as well as modification of the refractive index due to free carriers, also known as free carrier dispersion (FCD). Modification of the refractive index and absorption by free carriers can be explained with a Drude model[123]

$$\Delta n_{\mathrm{FCD}} = \frac{-e^2}{2\epsilon_0 n m^*} \frac{N_c}{\omega^2} \tag{1.77}$$

$$\Delta \alpha_{\mathrm{FCA}} = \frac{-e^3}{2\epsilon_0 c n m^{*2}} \frac{N_c}{\omega^2}, \tag{1.78}$$

where e, m^* and N_c are the elementary electronic charge, free-carrier effective mass and the free carrier concentration, respectively. The concentration of carriers generated from TPA is approximately given by [124]

$$N_c \approx \frac{\beta_{\mathrm{TPA}}\tau}{2\hbar\omega} I^2 = \frac{\alpha_{\mathrm{TPA}}\tau}{2\hbar\omega}\frac{P^2}{A_{\mathrm{eff}}^2}, \qquad \begin{cases} \tau = \tau_c & \text{if CW} \\ \tau = \Delta t / a & \text{if pulsed} \end{cases} \tag{1.79}$$

where τ_c is the free carrier lifetime and Δt is the pulse duration and a is a shape factor*.

TPA and the carrier effects it induces reduce the performance of integrated optics, leading to saturation of power in nonlinear waveguide sources [124], inducing optical bistability in rings [125] and reducing the accuracy of MZIs [126]. The phenomenon of cross two-photon absorption (XTPA), shown in Fig. 1.19b, stimulates nonlinear loss with photons from the pump pulse on single photons generated from parametric fluorescence [127,128], limiting the heralding efficiency. To mitigate FCA effects generated from TPA, the usual approach employs biased PN or PIN diodes to sweep out the free carriers [103,129].

1.7 Photon-pair sources

We refer the reader to appendix B on page 125 for background on quantum optics operators and two-mode squeezing. Single-photon and photon-pair sources have been demonstrated in a number of platforms: Quantum dots [30], nitrogen vacancy colour centres in diamond [130], bulk crystals [131], silica fibre [132], lithium niobate [133], silicon nitride [134], and silicon [46] to name just a few! Quantum dots have been used to measure the largest simultaneous (14-fold) photon coincidence from one quantum dot, multiplexed in time with Pockles cells [30]. Variations in quantum dot structure and therefore spectrum means that high visibility HOM interference from different emitters is yet to be demonstrated. Diamond colour centre single-photon sources have recently been embedded in silicon nitride [130], illuminating one path for mass integration. However, work still remains to produce arrays of indistinguishable colour centres on large scales. Integrated lithium niobate SPDC pair-sources are another promising route for large-scale quantum optics, benefiting from integration of high speed low-loss modulators based on the Pockels effect [133], but commercial availability is limited. Silicon and silicon nitride SFWM sources have been shown to produce some of the most complex quantum circuits [37], but low-loss (recent models [135] estimate < 0.01 dB/switch are needed), high-speed modulators (GHz) for multiplexing these platform's probabilistic sources to make them suitable for universal LOQC have remained elusive.

Three key requirements for a photon-pair source are brightness, indistinguishability and separability [2]. Brightness means the source must produce many photons for a given pump power. Once a bright source is achieved, indistinguishability in all degrees of freedom i.e. the photons are identical in frequency, polarisation, time etc., is required for high quality quantum interference to occur (recall two-photon interference Sec. 1.3.3). Finally, the separability matters for interfering multiple photon-pair sources. This means that the measurement of one half of the photon-pair reveals no information about the other half. Otherwise if a photon-pair is inseparable the source is entangled and measurement collapses the state which adversely affects interference with subsequent photons from

*$a \approx 3$ for Gaussian pulses, and $a = 1$ for square. Valid for low repetition rates f with short pulses $\Delta t \ll \tau_c$ and $\tau_c f \ll 1$ [2]

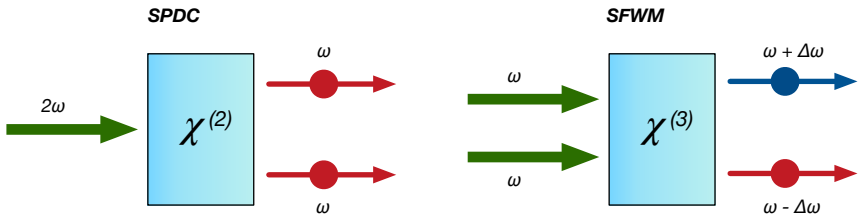

Figure 1.20: Parametric sources. A $\chi^{(2)}$ nonlinear medium uses spontaneous parametric down conversion (SPDC), to scatter one pump photon of frequency 2ω into two single photons of frequency ω. A $\chi^{(3)}$ nonlinear medium uses spontaneous four-wave mixing (SFWM) to scatter two pump photons into sidebands with detuning $\Delta\omega$.

other pairs. Inseparability of a biphoton state renders it useless for multi-photon quantum information applications.

Parametric photon-pair sources take a bright pump laser coherent state* $|\alpha\rangle$ and scatter pump photons off the nonlinear crystal to produce photon pairs which is depicted in Fig. 1.20. In non-degenerate FWM processes, these photons are scattered in sidebands $\Delta\omega$ symmetrically away from the pump. In general, SFWM implements the two-mode squeezing operator. The Heisenberg uncertainty principle states that two non-commuting operators, such as position and momentum, cannot be known to infinite precision i.e. $\Delta x \Delta p \geq \hbar/2$, where $\Delta x, \Delta p$ are the standard deviations of the position and momentum, respectively. A state is said to be squeezed when the uncertainty of the operators are not symmetric i.e. $\Delta x \neq \Delta p$, resulting in some noise component below the standard quantum limit. Spontaneous four-wave mixing results in a 'squeezed vacuum' state from which the photon-pairs can be postselected. The two-mode squeezing operator is defined as[33]

$$\hat{S}_{II}(\xi) = \exp(\xi \hat{a}^\dagger \hat{b}^\dagger - \xi^* \hat{a}\hat{b}) \tag{1.80}$$

$$\hat{S}_{II}(\xi)\,|\text{vac}\rangle = |\xi_{II}\rangle\,. \tag{1.81}$$

With some algebra (see appendix B.5 on page 130), we can show that the probability of producing exactly n-pairs of photons with this model is then given by

$$\Xi_n^{\text{thermal}} = |\,\langle nn|\xi_{II}\rangle\,|^2 = \text{sech}^2|\xi|\tanh^{2n}|\xi|. \tag{1.82}$$

When the squeezing is into a low number of modes (i.e. two modes), the probability of producing n photons is described by Eqn. (1.82). However, when squeezing into many modes, we can approximate the probability as a Poissonian distribution. In the case where the number of modes is large $|\xi| \to 0$ for the state $|\xi_{II}\rangle$ to remain normalised. In this scenario $\tanh|\xi| \approx |\xi|$ then Eqn. (1.82) becomes[136†]

$$= \frac{1}{\cosh^2|\xi|}\tanh^{2n}|\xi| = \frac{1}{e^{2\ln(\cosh|\xi|)}}\tanh^{2n}|\xi| \tag{1.83}$$

$$\approx \frac{1}{e^{|\xi|^2}}|\xi|^{2n} = e^{-\mu}\mu^n = \Xi_n^{\text{Poisson}}, \tag{1.84}$$

where μ is the mean number of photon pairs per pulse. In the small signal regime, the parameter $|\xi|^2$ represents the probability of producing a pair of photons per unit pulse duration and collection bandwidth. Depending on the experimental regime, the value of $|\xi|$ can take on different values, described in table 1.1.

*See appendix B.4 (page 129) for the origin of this state.

†The approximation is from the Taylor expansion where $2\ln(\cosh|\xi|) \approx |\xi|^2 + \mathcal{O}(|\xi|^3)$ for $|\xi| \ll 1$.

Squeeze parameter, $\lvert\xi\rvert$	Case	Notes	Reference
γPL	lossless	γ from Eqn. (1.72)	-
γPL_{eff}	linear loss	$L_{\text{eff}} = (1 - e^{-\alpha L})/\alpha$	127
$\gamma PL_{\text{eff}}\Theta$	phase-mismatch	$\Theta = \text{sinc}(igL)$, g from Eqn. (1.98)	137
$\gamma\alpha_{\text{TPA}}^{-1}\ln(1+\alpha_{\text{TPA}}PL_{\text{eff}})\Theta$	nonlinear loss	$\alpha_{\text{TPA}} = \partial\alpha/\partial P$	127,138

Table 1.1: Expressions for the squeeze parameter $\lvert\xi\rvert$ under different experimental conditions. P is the pulse peak power, which is equal to the average power for continuous wave (CW) operation.

Table 1.1 shows several realistic situations of the squeeze parameter for generating photons on-chip that include the effects of phase-matching, loss, and nonlinear loss. The phase-matching contribution to generating SFWM is critical, and is discussed in the following section 1.7.3.

1.7.1 Joint spectrum

The two-dimensional probability distribution with the associated signal and idler frequencies are succinctly mapped to an energy and phase-matching function known as the joint spectral amplitude (JSA)[139]

$$f(\omega_s, \omega_i) = \alpha(\omega_s + \omega_i)\Theta(\omega_s, \omega_i), \tag{1.85}$$

where α is the pump envelope function, and Θ is the phase-matching function which for simple crystals is a sinc function, parameterised by the dispersion and hence phase-mismatch Δk. More details of the phase-matching are given in Sec. 1.7.3. The joint spectrum may not be separable into two functions that individually describe the single photons; the degree of spectral correlation between the signal and idler determines the amount of spectral entanglement. The joint spectrum describes the bi-photon state so it must be normalised

$$\int d\omega_s d\omega_i f(\omega_s, \omega_i)\,|1_s, 1_i\rangle \rightarrow \int d\omega_s d\omega_i |f(\omega_s, \omega_i)|^2 = 1. \tag{1.86}$$

Filtering, applied to a source, can be used to reduce the spectral correlations and make an unentangled separable state at the cost of heralding efficiency. The spectral purity is determined by the number of Schmidt modes, under the decomposition of the state into the form $|\Psi\rangle = \sum_i \sqrt{\lambda_i}\,|\phi_i\rangle\,|\chi_i\rangle$, then[139]:

$$K = \frac{1}{\sum_i \lambda_i^2} = \frac{1}{\mathcal{P}}, \tag{1.87}$$

which shows that the purity $\mathcal{P} = 1$ when there is only a single Schmidt mode with $\lambda_i = 1$. A fast way to characterise the joint spectral intensity of a source, is with stimulated emission tomography[140]. Here, a stimulating beam combined with the pump elucidates the relative intensity of the spectral correlations. These are directly proportional to the spontaneous single-photon measurement, but are orders of magnitude brighter.

1.7.2 Coincidence measurements

Quantum correlated photons are measured with time of arrival, or coincidence measurements. A coincidence is when a time interval analyser (TIA) time correlates the output from two detectors, simultaneously registering a click. Building up statistics over

many measurements, a peak at zero relative time delay is a 'smoking gun' signature that photon-pairs are being generated in the same event, since the emission (and detection) of the SFWM pair is correlated in time. The rate of coincidence R from a source will be modified by the compound of effective transmission η, corresponding to the lumped loss from the point of the pair generation, up to and including the effective detector losses. The rate of detection events is given by[141]

$$C_s = \eta_s R \tag{1.88}$$
$$C_i = \eta_i R \tag{1.89}$$
$$X_{\text{net}} = \eta_s \eta_i R, \tag{1.90}$$

where C_s, C_i are the singles count rate on the individual detector channels, and X_{net} is the net coincidence rate with the accidental counts subtracted i.e. $X_{\text{net}} = X_{\text{raw}} - X_{\text{acc}}$, here $X_{\text{raw}}, X_{\text{acc}}$ are the gross (uncorrected) and accidental count rates. Note that since the rate of the coincidences is conditional on both photons being detected, the scaling in the presence of loss is very unfavourable.

Accidental counts make the analysis more complicated. These occur when linear noise processes corresponding to leaked pump laser and dark-single photon events are measured. The detection rates then become[103]

$$C_s = \eta_s \left[\Pi(P) f + \mathcal{L} f P\right] + \mathcal{D}_s \tag{1.91}$$
$$C_s = \eta_i \left[\Pi(P) f + \mathcal{L} f P\right] + \mathcal{D}_i \tag{1.92}$$
$$X_{\text{raw}} = \eta_s \eta_i \Pi(P) f + X_{\text{acc}}, \tag{1.93}$$

where f is the laser repetition rate, $\Pi(P)$ is the power dependent probability of producing a photon-pair, $\mathcal{L}$ is a linear noise coefficient and $\mathcal{D}$ is the dark count rate of the detectors. Finally, including the effects of multi-pair emission in the high squeezing limit must also be taken into account. Given a photon-pair is emitted, the probability of losing a signal photon is given by $(1-\eta_s)$, meaning that the probability of *not* losing a that photon is $1-(1-\eta_s)$. For n photon-pairs produced, the probability that at least one of n photons survives is $1-(1-\eta_s)^n$. This leads to the expression that at least one signal and one idler from n pairs survive is[2]

$$\eta = (1-(1-\eta_s)^n)(1-(1-\eta_i)^n). \tag{1.94}$$

A key performance metric of a photon-pair source is the ratio of true coincidence events triggered by a pair of photons, to the total number of false-positives, known as the coincidence to accidental ratio (CAR)

$$\text{CAR} = \frac{X_{\text{net}}}{X_{\text{acc}}}. \tag{1.95}$$

A CAR > 1 means that there is a measurable photon-pair signal, but ideally this should be as large as possible. The currently the highest CAR measured on a silicon chip is over 12000[142].

1.7.3 Phase-matching

Phase-matching is essential when designing a photon-pair source. A significant fraction of time in my PhD was spent trying to solve this problem! The dispersion must be chosen

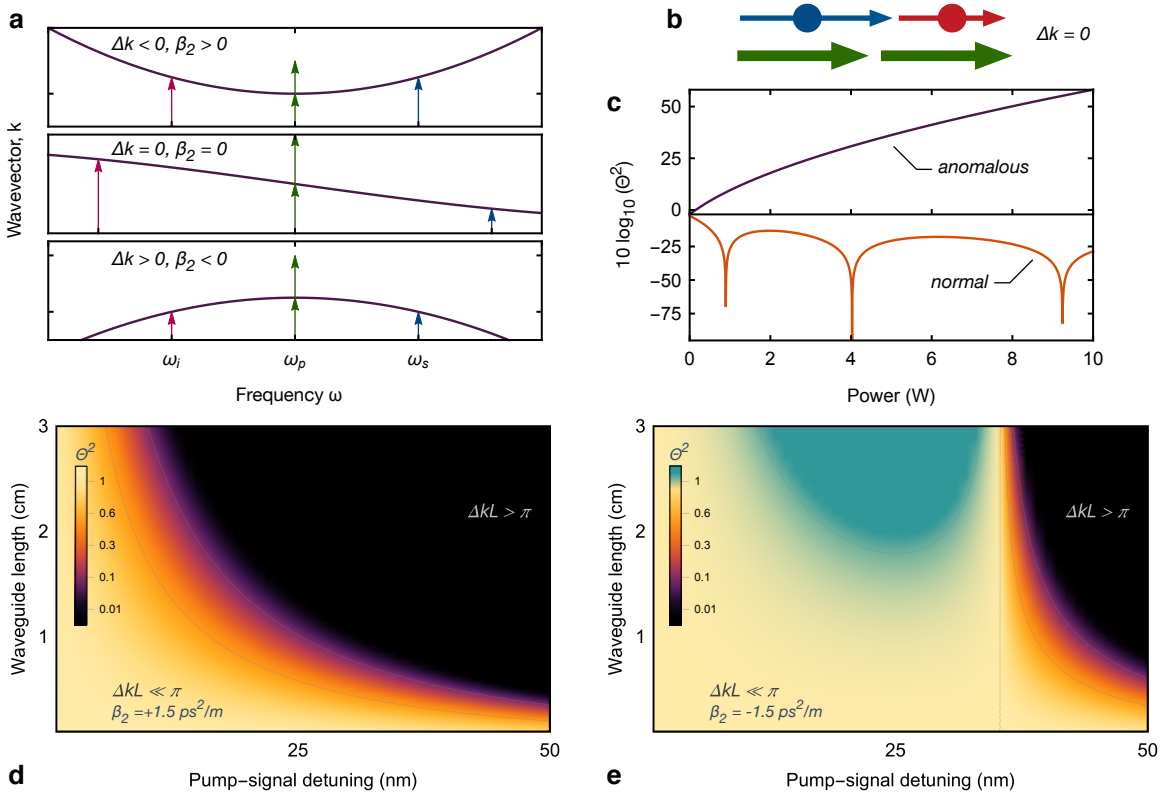

Figure 1.21: Phase-matching. **a**, Normal, zero and anomalous group-velocity dispersion (β_2), pictorial representation of degenerate FWM wavevectors for pump, signal and idler. **b**, Linear phase matching where the wavevectors of the signal and idler photons match the two pump photons. **c**, Phase matching function with varying peak power for normal and anomalous group-velocity dispersion (GVD). **d**, Normal GVD for different pump-signal detunings and waveguide lengths, $\beta_2 = +1.5$ ps^2/m and $P = 0.5$ W. **d**, Anomalous GVD for different pump-signal detunings and waveguide lengths, $\beta_2 = -1.5$ ps^2/m and $P = 0.5$ W. The region of $\Theta \gg 1$ corresponds to modulation instability.

so that the wavevectors of the generated signal and idler matches the annihilated pump photons. Microscopically, the emitted fields of the dipoles in the material are in phase, and coherently add in the forward direction[114].

The linear momentum mismatch between the four fields in the case of non-degenerate FWM can be described by

$$\Delta k \approx -\beta_2(\omega_p - \omega_s)^2. \tag{1.96}$$

See appendix C.5 (page 140) for the derivation of this result. A pictorial representation of linear phase-matching in the normal, phase-matched and anomalous dispersion regimes are shown in Figs. 1.21a and 1.21b. Usually for phase-matching close to the pump, the effects of the fourth-order dispersion (β_4) are much smaller than β_2 and are neglected. For efficient FWM, the momentum matching can be achieved with $\beta_2 \approx 0$. In a nonlinear source however, there is a contribution to the phase-matching from the nonlinear phase of the pump so the net phase mismatch is given by[73,127]

$$\Delta\kappa = \Delta k - \Delta k_{\mathrm{NL}} = \Delta k - 2\gamma P. \tag{1.97}$$

Since $\gamma P \geq 0$, for efficient FWM phase-matching $\Delta k > 0$, implying that $\beta_2 < 0$, which is

referred to as anomalous group-velocity dispersion. The parametric gain[73,127] of a source is given by*

$$g = \sqrt{\left(\frac{\Phi_{\mathrm{NL}}}{L}\right)^2 - \left(\frac{\Phi_{\mathrm{NL}}}{L} - \frac{\Delta k}{2}\right)^2} \approx \frac{i}{2}(2\gamma P - \Delta k), \tag{1.98}$$

and the phase-matching efficiency is[127]

$$\Theta = \mathrm{sinc}(igL). \tag{1.99}$$

In the case where g is imaginary, i.e. normal dispersion, the phase-matching efficiency decays with increasing pump power (Figs. 1.21c) or pump-signal detuning (Figs. 1.21d). In the case where g is real i.e. anomalous dispersion, leads to exponential growth in the gain. The large growth of the gain in the anomalous dispersion regime is also known as modulation instability. This phenomenon leads to spontaneous temporal modulation of a CW beam into a pulse train[73].

In Figs. 1.21c and 1.21d, we see that if the dispersion is normal, the phase matching efficiency rapidly drops. A waveguide source with normal dispersion can produce photon-pairs, but only if β_2, pump power, waveguide length and frequency detuning are small. For our initial attempts at producing a photon-pair source in chapter 3, this detail led to unsuccessful first generations of integrated pair sources. The source design was constrained by the accessibility of silicon films for waveguides that could only produce normal dispersion for the fundamental TE_0 mode. In the anomalous dispersion regime however (Figs. 1.21c and 1.21e), the phase-matching efficiency and bandwidth is significantly improved from the normal dispersion regime. Anomalous GVD is therefore a necessary requirement for an efficient, bright photon-pair source with large spectral detuning. Only in retrospect did we realise that the dispersion of the TE_1 mode was anomalous—an important note for future source designers is not to forget about using high order transverse modes for phase-matching!

1.8 Mid-infrared optics

The 'fingerprint' region, spanning the mid-infrared from 2-20 μm, is resonant with a multitude of molecular transitions, corresponding to vibrational modes that uniquely identify species with characteristic absorption lines. Exploiting this, lab-on-a-chip sensors are able to distinguish and identify molecules from gaseous and liquid analytes[143]. Atmospheric transparency windows and diminished scintillation are utilised in MIR lidar systems[144], while optical phased arrays in the MIR benefit from alleviated phase error and high-power handling, thus optimising system performance and reliability[145]. Great progress has been made to achieve integration of MIR optics in silicon. In the short wavelength end of the MIR band (the short-wave infrared (SWIR)), integrated implementations are accomplished with silicon on insulator (SOI), up to around 4 μm[146–149], where silica's transparency region ends. A picture to illustrate the transparency window of silicon and silica in MIR are shown in Fig. 1.22. At these wavelengths, two-photon absorption in silicon is reduced or entirely eliminated, thereby enabling applications in nonlinear optics[150]: frequency combs[151], optical parametric oscillators and amplifiers[119], all have been realised.

*The approximation here is from the binomial expansion of $(1-x)^{\frac{1}{2}} \approx 1 - x/2$ when $x < 1$.

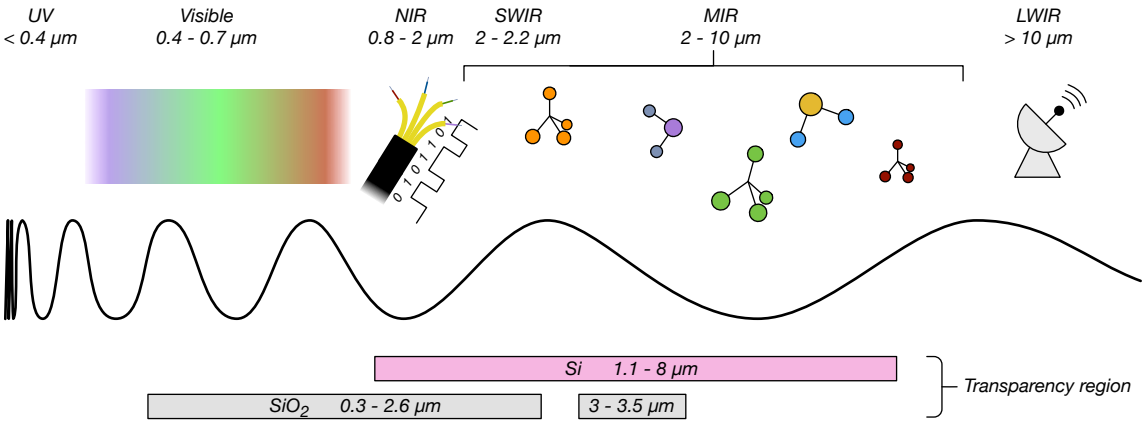

Figure 1.22: The electromagnetic spectrum. Not to scale.

Utilising quantum entanglement and superposition, optical quantum technologies are expected to transform communication, measurement, and ultimately information processing[1]. Quantum states are tremendously fragile, and are easily perturbed by the environment. This sensitivity means for real-world deployment, high performance is required to expand the platform for useful, large-scale applications. Classical optics has taken the first steps advancing into the MIR and quantum optics is not far behind. Photon-pair sources using SPDC in bulk crystals have been modelled[152], and experimental demonstrations have been established with one[153], and two[131] MIR photons. Room-temperature avalanche photodiodes and up-conversion were used for detection in these experiments, but these are limited by thermal noise and low efficiency.

To date, silicon photonics, which takes advantage from proficient mass manufacturability, has generally operated in the near-infrared telecommunications bands around 1.31 and 1.55 μm. Applications of the technology in data centres have dramatically increased in extent and capacity. Quantum optics in silicon has also emerged alongside[128]. Quantum experiments have been showing progressively larger interferometers with parametric sources of photon-pairs[37,60,154], but remarkably low optical loss will be necessary to significantly increase photon numbers.

Waveguide, component and fibre-chip coupling losses have all been gradually improving[72,84,155–157], but intrinsic nonlinear loss is ineradicable. TPA, while limiting the pump power, also detrimentally reduces the heralding efficiency of integrated photon-pair sources, and therefore places a foundational cordon on silicon quantum photonics scalability.

Wide band gap materials, such as silicon nitride, are a commonly used method for alleviating TPA[134,158] at telecom wavelengths. However, silicon nitrides intrinsically smaller nonlinear refraction and lower optical confinement means far higher pump powers are required to generate the same nonlinearity. Furthermore, variations in fabrication of silicon nitride films makes within wafer-scale refractive index uniformity a challenge for large scale identical photon-pair sources[159].

Figure 1.23 shows the dispersion of nonlinear TPA coefficient β_{TPA}, nonlinear refractive index n_2, and Rayleigh scattering cross-section. We see that at room temperature around 2.2 μm, at the two-photon band edge of silicon, the energy of two photons is insufficient to promote a valance band electron, thus extinguishing TPA. The nonlinear

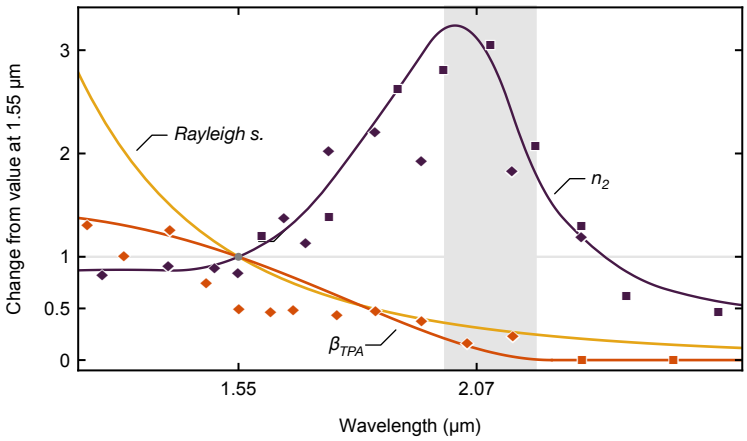

Figure 1.23: Dispersion of nonlinear refraction (n_2), nonlinear absorption (β_{TPA}) at room temperature, and simple Rayleigh scattering in silicon, normalised to the values at 1.55 μm. The diamonds and squares are data taken from Z-scan measurements in Refs. 160 and 161. The lines for n_2 is a guide for the eye, and β_{TPA} a model for two-photon absorption[162]. The side-by-side comparison for this plot was originally conceived by Dr. Joshua Silverstone.

refraction simultaneously has a resonant spike, increasing the efficiency of photon-pair generation. This wavelength band is also comfortably within the transparency range of SOI silica cladding, enabling standard manufacturing processes.

At long wavelengths propagation losses are diminished[64,163] due to reduced Rayleigh scattering from waveguide side-wall roughness , and constraints on fabricating subwavelength devices become relaxed[157,164]. A nonlinear figure of merit, such as the ratio of n_2/β_{TPA}, shows that at longer wavelengths in silicon the performance is improved.

The optimum room temperature wavelength for improving nonlinear optics in silicons, is at around 2.2 μm since TPA has dropped to zero, and there is still an enhancement of the nonlinear refraction from the resonant spike. At low temperature, where future experiments integrating sources and detectors on the same chip would need to operate, this is expected to blue shift to around 2.15 μm due to the increase in silicon's band gap[165]. Due to practical constraints for obtaining a pulsed mode-locked pump laser, we operated our experiments at 2.07 μm and were unable to reach the completely TPA free region beyond 2.2 μm. However, a wavelength shift of 80 nm from 2.07 μm to the low temperature two-photon band edge at 2.15 μm is a far less of a challenge than translating from 1.55 μm to the 2.1 μm. Therefore this will be significantly easier to implement with the framework developed from this thesis when a pulsed laser light source at this wavelength becomes readily available.

For large scale quantum optics applications such as LOQC, high brightness and low-loss waveguide sources are essential. Simply by translating from 1.48 μm to 2.1 μm, at an average 0.1 pairs per pulse, yields an estimated improvement from 72% to 96% in the heralding efficiency due to reduced XTPA*. When the improvement of linear losses from Rayleigh scattering is also included from this wavelength translation, this becomes a significant boost in platform performance. This illuminates the necessity of implementing a TPA free, low-loss and scalable platform to enable photonic quantum technologies. The MIR in silicon offers one such route to achieve this end goal. Hence, we will explore

*Calculated with the Eqn. (4) from Ref. 128 and β_{TPA},n_2 values from Refs. 160,161.

the potential of the 2.1-μm band as a platform for low-loss quantum optics in crystalline silicon.

1.9 Thesis aims and outline

The aim of this thesis is to establish the viability 2.1 μm band for single-photon quantum information applications. To realise a quantum optics platform in the MIR, there are several necessary requirements. The fundamental objective for any single-photon quantum optics platform must be to show quantum interference, which leads to several other prerequisites that must be achieved to reach this main goal. For quantum interference to occur on a chip, a method for coupling light into the chip, waveguides, balanced beamsplitters which can be connected together into reconfigurable waveguide circuits must be all developed. With this aim established, we must generate a source of indistinguishable photon-pairs. To produce indistinguishable photon-pairs, the waveguide geometry must be adjusted so the dispersion enables efficient phase-matching, and the distinct sources should be identical. If the required photon-pairs are generated and interfered, demultiplexing them from the bright pump laser and a method to detect them is also essential. By showing quantum interference, all of these aims and objective are necessarily fulfilled. Finally to demonstrate the benefits of the 2.1 μm platform in silicon waveguides, new applications that are not possible with existing technology should be enabled or an improved nonlinear performance metric, such as the ratio of nonlinear refraction to two-photon absorption (n_2/β_{TPA}) must be shown.

This thesis is concerned with developing all of the necessary infrastructure for demonstrating MIR silicon quantum photonics; we do this by showing an integrated source of quantum correlated photons, with high visibility quantum interference in the 2.1 μm band. In chapters 2 and 3, we develop the integrated optics toolkit and laboratory infrastructure for measuring quantum correlated photons. Chapter 4 is concerned with the measurements of quantum correlated photon-pairs, sensitive detectors and a plethora of nonlinear optics to verify our claims of the MIR performance gains. Chapter 5 shows two such integrated photon-pair sources configured in an experiment proving high visibility quantum interference on-chip. Finally, we state the conclusions and future outlook in chapter 6.

CHAPTER 2

Off-chip infrastructure

The instrumentation required for generating and measuring quantum correlated photon-pairs in the mid-infrared (MIR) poses a significant challenge. Off-the-shelf apparatus available in the near infrared (NIR), is truly phenomenal with exceedingly high performance at low costs. In the MIR, challenges in bulk optics filtering, and detection had to be addressed to enable the measurement of photon-pairs. At the start of the project the instrumentation for performing measurements was limited. As time progressed, a plethora of experimental methods and equipment enabled the first MIR photon-pair generation. This chapter summarises the development of the bulk optics and detection infrastructure in the first two years of this project. In the following chapter, we describe how this instrumentation was used to build experiments that led to the generation of new optical frequencies with stimulated four-wave mixing (FWM). The contents of the chapters 2 and 3 in isolation are mostly chronological, but occurred in parallel. The structure for these chapters are logically grouped into the off- and on-chip infrastructure. We refer the reader to see Fig. G.1 for the timeline.

2.1 The starting lineup

Starting research into quantum optics in the MIR had a humble beginning. Equipped with one breadboard, a continuous wave (CW) laser, a monochromator and a photodiode, the adventure into the unknown started in a dark (and somewhat dusty) corner of the 'Wetlab'.

We now briefly review the instrumentation at the outset of the project. For the initial characterisation of the integrated optics, we used an CW Eblana photonics intersubband quantum cascade laser (QCL)[166] centred at 2.049 μm, with a linewidth of < 2 MHz, maximum output power of 1.5 mW, and was packaged into a butterfly mount. The laser had a temperature controller (TEC) allowing for a modest tuning range of around 3 nm (see Fig. 2.1a), and a current source to vary the output power of the diode shown in Fig. 2.1b. This laser was invaluable for bulk and integrated optics alignment, linear characterisation of waveguides and grating couplers, estimating the splitting ratios of integrated

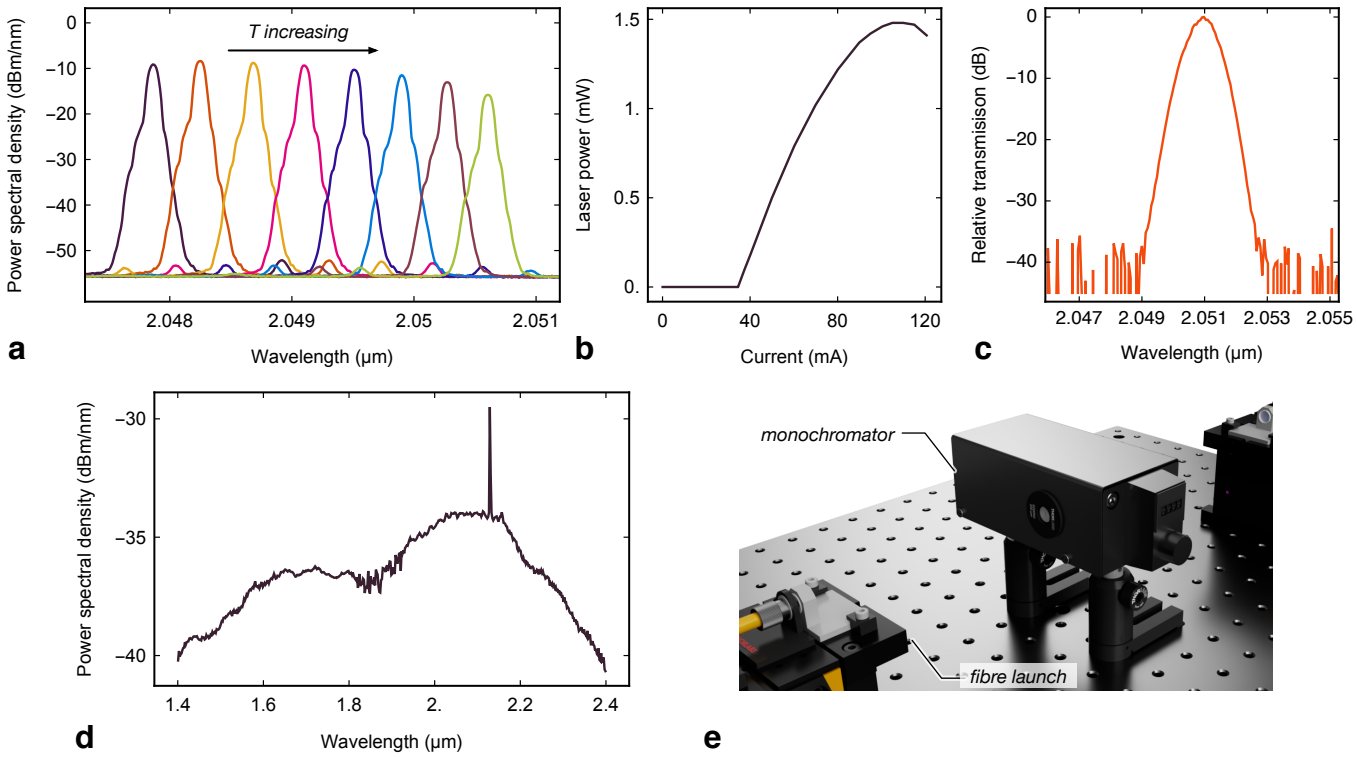

Figure 2.1: Characterisation of the starting equipment. **a**, Varying the temperature of the quantum cascade laser showed a maximum tuning of 3 nm over 30°C. **b**, The laser diode output power vs. current, the lasing threshold is approximately 37 mA. **c**, Relative transmission of the tuneable bulk monochromator filter. **d**, Spectrum of the supercontinuum laser source with no bandpass filters. **e**, The free-space fibre launch method for coupling light into the monochromator.

beamsplitters, and as a stimulating seed for observing stimulated four-wave mixing.

We were also lucky share to a supercontinuum[117] light source—a NKT SuperK Compact—with our colleagues. We show the output spectrum of the laser in Fig. 2.1d. The source spanned the wavelength range 500-2400 nm and was also completely indispensable for this work, providing important spectral information about our integrated and bulk devices. The total output power across its full spectral range is specified by the manufacturer at around 100 mW, but we usually applied a 500 nm wide bandpass filter centred at 2000 nm, reducing the total maximum optical power to around 1 mW.

An Optometrics Czerny–Turner monochromator[167] with bulk free space fibre couplers complemented the supercontinuum source in the spectral characterisation measurements. The monochromator had a full width at half maximum (FWHM) of 1 nm (Fig. 2.1c), insertion loss of 10 dB (subsequently reduced to 4 dB with many rounds of optimising the design, described in Sec. 2.4), and an extinction of around 55 dB at an offset of 20 nm. We present a schematic of the original monochromator configuration before optimisation in Fig. 2.1e.

For bright light detection, we had a Thorlabs InGaAs[168] integrating sphere photodiode, sensitive from 1200-2500 nm. Finally, NIR (c.a. 1.55 μm) superconducting nanowire detectors (with the MIR fibre loop filters removed) gave us a chance to measure signals in the single-photon regime, albeit with low efficiency of order 1%.

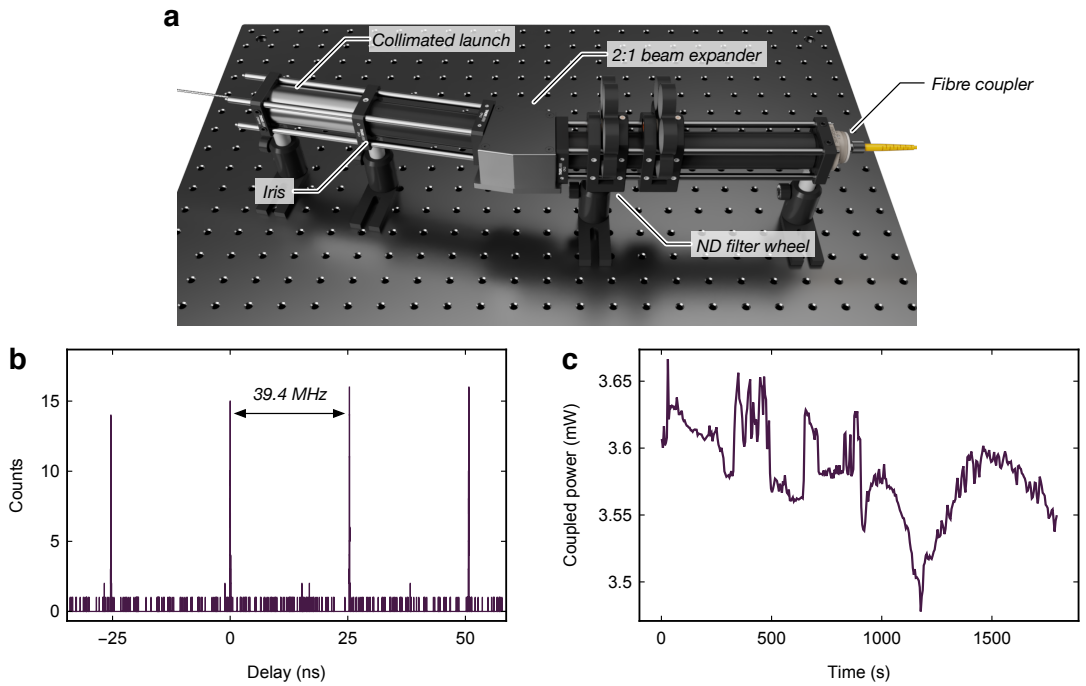

Figure 2.2: Mode locked laser assembly and characterisation. **a**, Model of the bulk optics laser cage system to fibre couple the free space collimated launch of the mode locked laser (MLL). **b**, Autocorrelation of attenuated laser pulses measured with superconducting detectors and a time interval analyser. **c**, Stability measurement of the MLLs optical power coupled into fibre.

A figure with select technical specifications of this instrumentation is shown in Fig. 2.1. Later on in the project a mode-locked laser, tuneable CW laser, an optical spectrum analyser (OSA), autocorrelator, bespoke single-photon detectors, and more monochromators were obtained which enabled the measurement of quantum correlated photon pairs—these will be mentioned in the body of the thesis when they were acquired. However, these were not at our disposal at the start of this research and meant that the initial learning experience took substantially longer.

2.2 Mode-locked laser

Eight months into the project, we acquired a 2 μm mode-locked laser (MLL) from AdValue photonics. This laser would be the work horse of this research activity, providing us with many invaluable nonlinear optical measurements and ultimately would lead to first observation of single-photons from spontaneous four-wave mixing (SFWM).

The MLL was a Thulium seed fibre laser that pumps a Holmium fibre laser, emitting up to 300 mW of average optical power into free space[78]. The output pulses from the laser were specified as 2.8 ps at a 39.4 MHz repetition rate corresponding to a peak power of > 10 kW*.

*Or in more tangible units, this is > 13 horse power!

2.2.1 Cage design

The output of the laser was emitted into free space through a collimating lens. However to be useful for the experiments, it needed to be fibre coupled. The first initial characterisation launched light from the armoured output head directly into a thermal power meter to verify the device was working. The next step was to design a robust cage system to fibre couple the laser from free space, while also protecting the user from the highly dangerous unfiltered beam.

The design started by clamping the output free space launch into a cage mount. The cage has lens tubing along its length to block lab users from the beam. The first optic was a 2:1 beam expander, which we ran in reverse, reducing the beam waist to improve the collection efficiency into fibre. The second optic was a variable filter wheel, which we installed 10, 20 and 30 dB neutral density filters for reduced power free space optical alignment. Finally at the end of the cage, an anti-reflective (AR) coated lensed fibre coupling port was added. The optimised coupling reached > 140 mW which was sufficient for some serious nonlinear optics. The majority of the excess loss of the cage system is due to incorrect mode-matching between the fibre-lens coupling port and the collimated beam. A model of the cage system is depicted in Fig. 2.2a.

We verified the repetition rate of the laser by performing an autocorrelation of the attenuated laser using the superconducting detectors which we show in Fig. 2.2b. The measured repetition rate agreed well with the manufacturers specification. Stability of the MLL and cage system was also assessed by directly connecting the output fibre into a photodiode (see Fig. 2.2c). We found that the cage system showed good long term coupling stability necessary for running long experiments.

2.3 Bulk variable optical attenuator

It was not clear if changing the maximum output of the mode-locked laser with the power dial on the front panel of the laser would impart a polarisation rotation, thereby inducing polarisation dependent loss from grating couplers. In absence of a variable optical attenuator (VOA) in the 2 μm region, we had to build one using bulk optics instead. To control the optical transmission while keeping the gain of the laser constant, we used a free space design with a knife edge to facilitate single-mode attenuation from blocking the beam.

The final design used two collimated fibre launches with NIR single mode fibre (SMF-28) directly facing each other with a ~ 15 cm separation, shown in Fig. 2.3a. The long span between them, allows for multiple flip mount optics to be inserted into the beam path. Multiple 25 dB neutral density filters (NDFs) were used to add baseline attenuation down to the single photon level (see Fig. 2.3c. for transmission spectra)—and were employed in Secs. 2.5.1 and 4.3 for single photon detector characterisation. Dynamic attenuation was achieved with a linear translation stage attached to a stepper motor (Zaber T-LA28A). This controlled the position of the razorblade that blocked the free space beam. The stepper motor could be directly controlled from a computer, enabling measurements involving varying the optical power. This setup would prove invaluable in later experiments. The total coupling loss from fibre-to-fibre, in absence of NDFs, was approximately 4 dB.

We can model the optical attenuation as a function of knife edge position with the following treatment. Assuming that the free space beam is a symmetric two dimensional

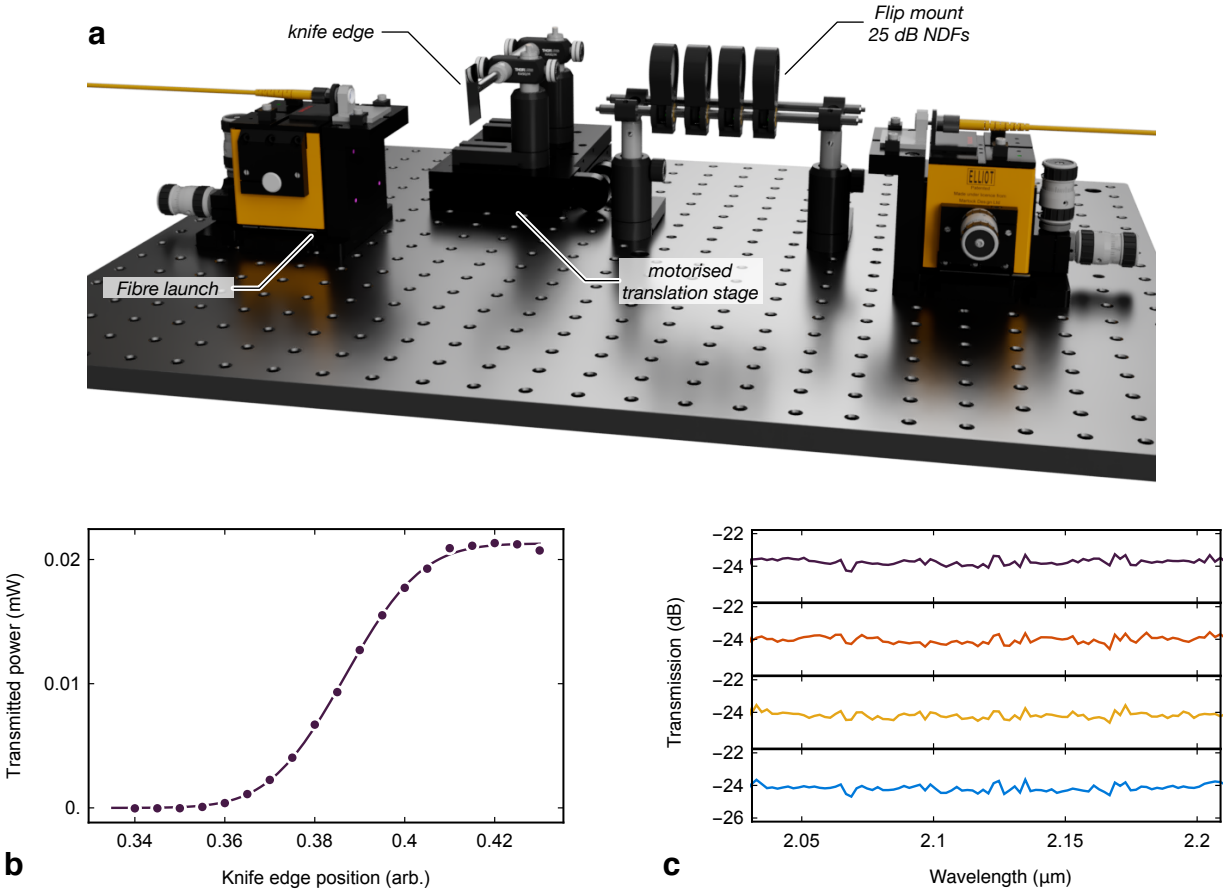

Figure 2.3: Bulk variable optical attenuator. **a**, Layout of the bulk variable optical attenuator. A knife edge provides variable attenuation, while four neutral density filters (NDFs) provide an additional 100 dB of baseline attenuation. **b**, Optical transmission with varying knife edge position. **c**, Transmission spectrum of four NDFs.

normalised Gaussian centred at the origin

$$G(x,y) = \frac{1}{2\pi\sigma^2} e^{-\frac{x^2+y^2}{2\sigma^2}}, \tag{2.1}$$

where σ relates to the collimated beam diameter. The razorblade blocking function of the beam is then simply the Heaviside step function in one dimension $\Theta(x_k - x)$ where x_k is the knife edge position. To model the transmitted power as a function of knife edge position, we take the integral over all space

$$\begin{aligned} P(x_k) &= P_0 \iint_{-\infty}^{\infty} G(x,y)\Theta(x_k - x)\,dx\,dy, \\ &= \frac{P_0}{2}\left(1 - \mathrm{erf}\left(\frac{-x_k}{\sqrt{2}\sigma}\right)\right), \end{aligned} \tag{2.2}$$

where P_0 is the transmitted maximum power and erf is the Gaussian error function. A fit of Eqn. (2.2) to experimental transmission data is shown in Fig. 2.3b.

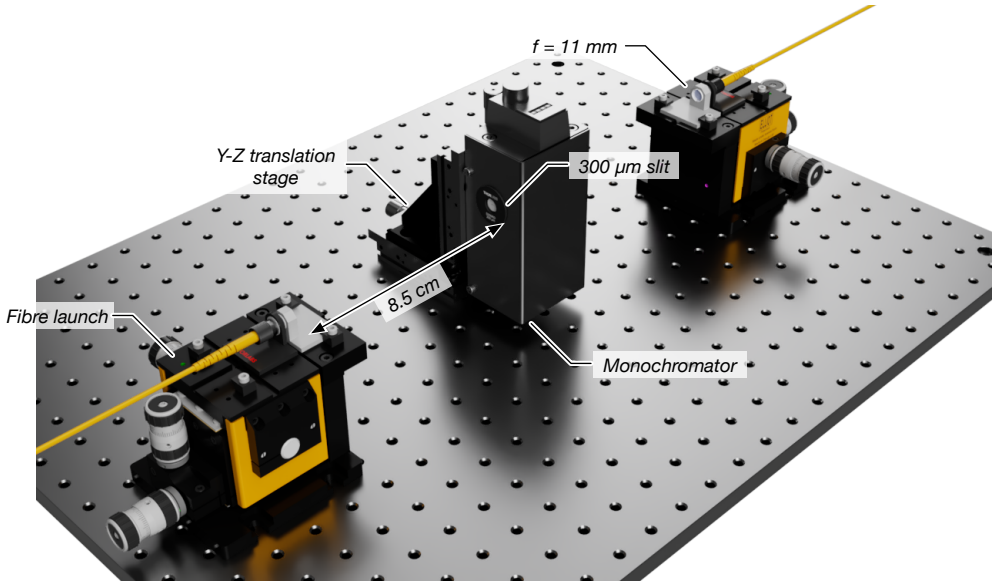

Figure 2.4: Optimised monochromator filter layout.

2.4 Monochromator filter optimisation

The free-space fibre coupled monochromator at the project start had a transmission of roughly -10 dB. The loss from this filter was unsatisfactory, so an approach to optimise the coupling further was developed. The final design of the monochromator launch setup is shown in Fig. 2.4. To increase the coupling, the orientation of the monochromator was changed to be in the upright position and extra degrees of freedom added with two linear translation stages in the Y-Z plane of the setup. An efficient methodology for achieving the global optimum of coupling for this configuration of monochromator is presented in appendix D.5 on page 149.

Using the strategy outlined in appendix D.5 it was possible to achieve a peak transmission of -4 dB, approximately four times more than the previous method yielded. Later in chapters 4 and 5, four of these monochromators would be used back-to-back on the single photon signal and idler output channels. The improved alignment strategy developed here led to a total improvement of more than 200 times in the coincidence count rates over the previous alignment strategies.

2.4.1 Cleaning the pump spectrum

In the measurements described in Sec. 3.3, we attributed the majority of the saturation in the input output power relationships to the spectral broadening of the pump. With the addition of the OSA to the equipment, we were able to measure the pump spectrum which is shown in Fig. 2.5a , and the experimental setup in Fig. 2.5b. The measured output spectrum of the laser was remarkably broad, with sideband peaks that would inevitably drown out any single photons produced from spontaneous four-wave mixing.

To address this problem, we initially used two monochromators in series to filter the pump spectrum—see Fig. 2.5d. Figure 2.5c shows the pump laser spectrum after filtering, which is clearly far more suitable for producing and detecting single photons centred on

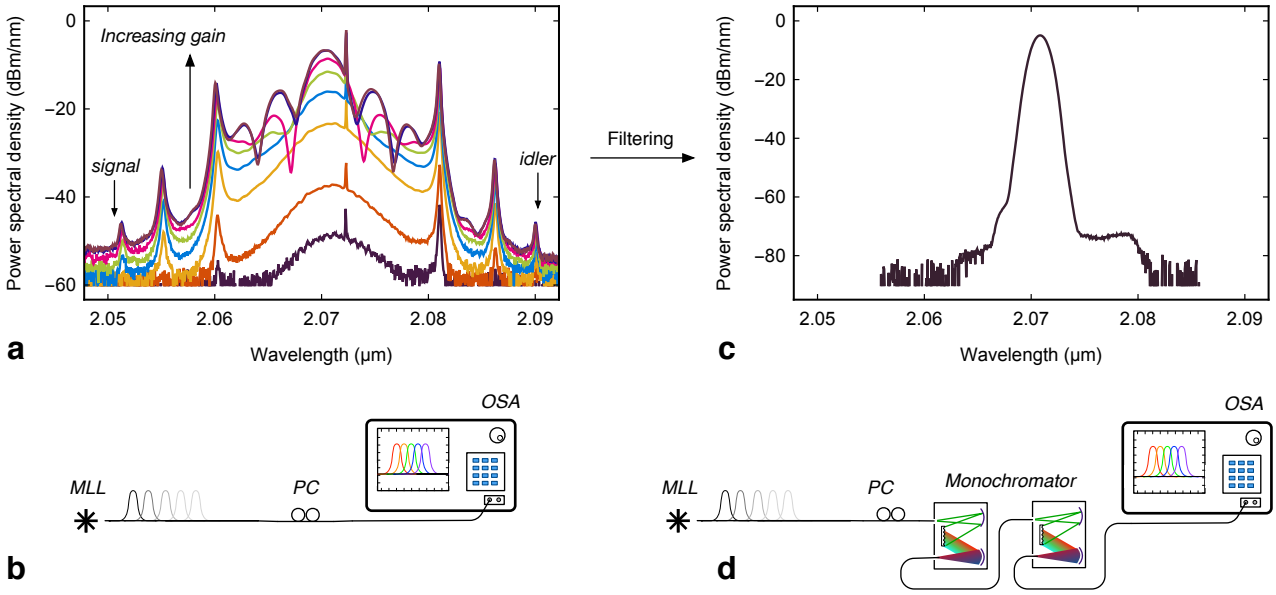

Figure 2.5: Mode-locked laser spectrum and filtering. **a**, Pump laser spectra with increasing gain varying the potentiometer on the front panel. As the gain is increased the power and sidebands also increase. The target signal and idler wavelengths are highlighted demonstrating that the unfiltered pump sidebands would drown out any single photons produced. **b**, Experimental scheme for the spectras measured in part a. **c**, Mode-locked laser pulse spectrum after filtering with grating monochromators. **d**, Experimental scheme for the spectras measured in part c.

2.05 μm and 2.09 μm.

2.4.2 Measuring the pulse duration

To verify the manufacturer-stated pulse duration, we repurposed a derelict Femtochrome FR-103PD autocorrelator and installed a MIR photodiode for measuring the mode-locked laser. The unfiltered pulse in the frequency domain was extremely broad; spectral filtering to reduce its width leads to broadening in the time domain. Using an anti-parallel rotating mirror assembly [169], one arm of a Michelson interferometer is then swept across a fixed arm. The autocorrelation intensity is detected with two-photon conductivity in the photodetectors [170]. The electrical output is then read with an oscilloscope. Given a path length of the two arms and rotation speed of the mirror assembly, the oscilloscope trace width is related to the intensity autocorrelation by [169]

$$\kappa = \frac{4\pi f d}{c}, \tag{2.3}$$

where κ is the conversion factor between oscilloscope units and pulse duration, f is the rotation frequency of the mirrors, d is the distance between the mirrors and c is the speed of light in vacuum.

Since our laser is mode-locked, we assume an hyperbolic secant pulse ansatz of the form $\mathrm{sech}^2(\tau/t_p)$, where t_p is the characteristic time of the pulse. To calculate the actual pulse duration from our oscilloscope, we must find the deconvolution factor. The auto-

correlation trace width is then related to the full width at half maximum FWHM by

$$\Delta\tau = 2t_p \text{arccosh}(\sqrt{2}). \tag{2.4}$$

The deconvolution factor for secant shaped pulses is $\Delta\tau \approx 0.648\Delta t'$, where $\Delta\tau$ is the actual pulse duration and $\Delta t'$ is the FWHM measured on the oscilloscope trace. For a derivation of this result see appendix D.6 on page 150.

We measured the unfiltered pulse duration to be 2.9 ps, which is in good agreement with the manufacturer specified value of 2.8 ps. A typical intensity autocorrelation trace is shown in Fig. 2.6c. We are now able to measure the pulse duration for any filtered pulse, and can more accurately estimate the peak power coupled into the waveguide which is essential to accurately measure the waveguide nonlinearity.

To convert the average power from a photodiode the following conversion can be used. Given a pulse FWHM, $\Delta\tau$, the duty cycle d_c of the laser is given by

$$\mathrm{d}_c = f\ \Delta\tau, \tag{2.5}$$

where f is the repetition rate in frequency units and $\Delta\tau$ is the pulse duration for a *rectangular* pulse. Since we must find the normalisation such that the area of a secant shaped pulse is preserved relative to a rectangular function with the same width FWHM, we find that

$$\int_{-\infty}^{\infty} \text{sech}^2\left(\frac{\tau}{t_p}\right) d\tau\ = 2t_p. \tag{2.6}$$

Finally putting this all together, the peak power P_p is calculated as

$$P_p = \frac{P_{\text{avg}}}{\mathrm{d}_c} = \frac{P_{\text{avg}}}{2t_p f} = \frac{\text{arccosh}(\sqrt{2})}{f\ \Delta\tau} \approx \frac{0.88}{f\ \Delta\tau} P_{\text{avg}} \tag{2.7}$$

where P_{avg} is the average power.

2.4.3 Double-pass monochromator filter

In November 2018, we acquired another two monochromators (bringing our total to five) to facilitate off-chip filtering. It was clear from the measurement described in Sec. 3.4.2 that at least two monochromators on the output of the chip would be required to suppress the pump down to the single-photon level. However, to measure coincidences, a total of four monochromators would be needed on the signal and idler output arms of the integrated light source, therefore motivating the need to reduce the number of filters on the input pump laser to just one.

In an attempt to enable this measurement, we set out to design a monochromator in a double-pass configuration to achieve greater extinction on the laser sidebands and create sufficient experimental resources for measuring SFWM. The double-pass design simply places a concave reflecting mirror close to the output aperture of the monochromator to reflect the light back in the incident direction, but with a slightly deflected angle. The beam then hits the grating in the reverse direction and after the exit slit reflects from a mirror at $\sim 45°$ angle, which is then directed to another fibre coupling stage—shown in Fig. 2.6a.

This technique worked well; the insertion loss of the double-pass was 6 dB compared to 4 dB for the single-pass, but the extinction of the double-pass was greater than a single-pass. Due to the limits of our detection equipment, it was not possible to exactly quantify

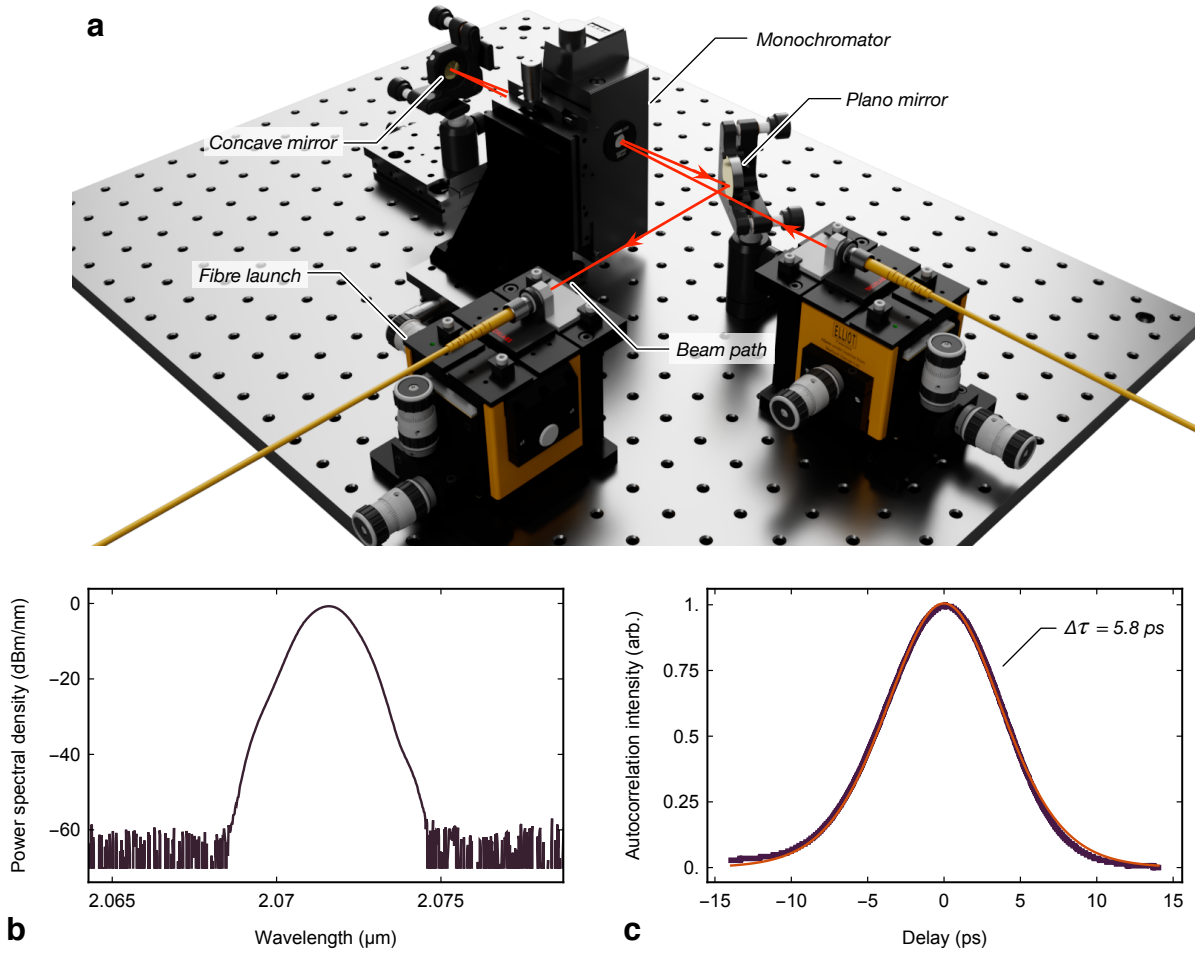

Figure 2.6: Double-pass monochromator filter for the pump laser. **a**, Layout and beam path of the double-pass monochomator configuration. **b**, Frequency dependent power for the double-pass filtered spectrum of the MLL. **c**, Measured intensity autocorrelation (purple) and hyperbolic secant autocorrelation (orange) fit of the double-pass filtered MLL pulse.

the absolute level of extra extinction and whether this was greater than two single-pass monochromators in series, since it was below the noise floor of our detectors.

A characterisation of the MLL after the spectrum was cleaned with a double-pass monochromator in time and frequency domains is shown in Figs. 2.6a and 2.6b. The double-pass filter reduced the broad frequency response of the laser to a FWHM of around 1 nm making it suitable for photon-pair experiments. The tight frequency filtering was at the expense of broadening the pulse duration in the time domain to around 5.8 ps, leading to reduced peak power. This double-pass configuration was sufficient to suppress the bright laser sidebands down to the single-photon level when combined with signal/idler pump rejection monochromators detuned 20 nm from the pump.

2.5 Towards mid-infrared superconducting detectors

The initial pair of detectors we worked with were tungsten silicide (WSi) nanowires from PhotonSpot, optimised for operation at $\lambda = 1.55$ μm. In an attempt to improve our detec-

tion efficiencies, we reached out to Prof. Robert Hadfield from the University of Glasgow. His group specialises in the development of superconducting nanowire single-photon detectors (SNSPDs), with active research in MIR nanowire fabrication. We acquired a research cryostat with four NIR band SNSPDs, and swapped out two of these for MIR nanowires that we characterised.

Understanding the efficiency of the detectors is important; it identifies effective loss from detection in the coincidence rates, and therefore is critical for evaluating photon-pair source performance. The following sections are concerned with a measurement strategy for quantifying this metric, and recognising the optimal bias and threshold settings for a detector. We outline our method for characterising the both telecom and mid-infrared single-photon detectors at MIR wavelengths, and summarise the measured efficiencies in table 2.1. Primarily these characterisations were used to identify the most sensitive pair of detectors with the best chance to measure SFWM photon-pairs.

2.5.1 Characterisation

Monochromatic characterisation

We now outline the measurement strategy used to estimate the efficiency of a nanowire detector at a single wavelength. The measurement starts with taking the monochromatic CW QCL laser centred at $\lambda = 2.049$ μm, and passing it through a polarisation controller and the bulk VOA. The optical power is monitored on a calibrated InGaAs Thorlabs photodiode (S148C) at a fibre leading to the cryostat input fibres. The reason for placing the photodiode here is to calibrate out any effective fibre losses from the single-mode fibre up to the point of the cryostat.

The first step measures the transmitted power on the photodiode as a function of knife edge position on the bulk VOA, where we show a typical measured transmission curve in Fig. 2.7b. Second, the transmission of four 25 dB neutral density filters (NDFs) built into the VOA with flip mounts are sequentially measured. Third, all four NDFs are placed in the beam path attenuating the laser down to the single photon regime, and the input fibre to the photodiode is connected the cryostat. Finally, optimising the polarisation of the light, the electrical output of the detectors are amplified and connected to a time-tagger which integrates the measured singles counts—See Fig. 2.7c for a diagram of the experimental setup.

We quantify the input photon flux arriving at the detector by estimating the power transmitted after the four NDFs, and then calculate the expected flux dividing by the photon energy ($E = hc/\lambda$). The ratio of launched input photon flux to the measured count rate is fit with a linear slope, as shown in Fig. 2.7a, determining the system detection efficiency of the nanowire detectors.

In table 2.1, we present our estimates of several different nanowires at different bias settings. Since the peak detection efficiency is strongly dependent on bias, these measurements are hard to directly compare and are mostly responsible for the observed discrepancy in measured efficiency—this is especially clear between the measurements of PhotonSpot channels 5 and 6.

We found the most efficient detector was the PhotonSpot WSi nanowire (channel 6) at around 6.6% (see Fig. 2.7a), however its counterpart in the same cryostat only registered a peak efficiency of 0.05% albeit at a far lower bias setting which greatly affects the

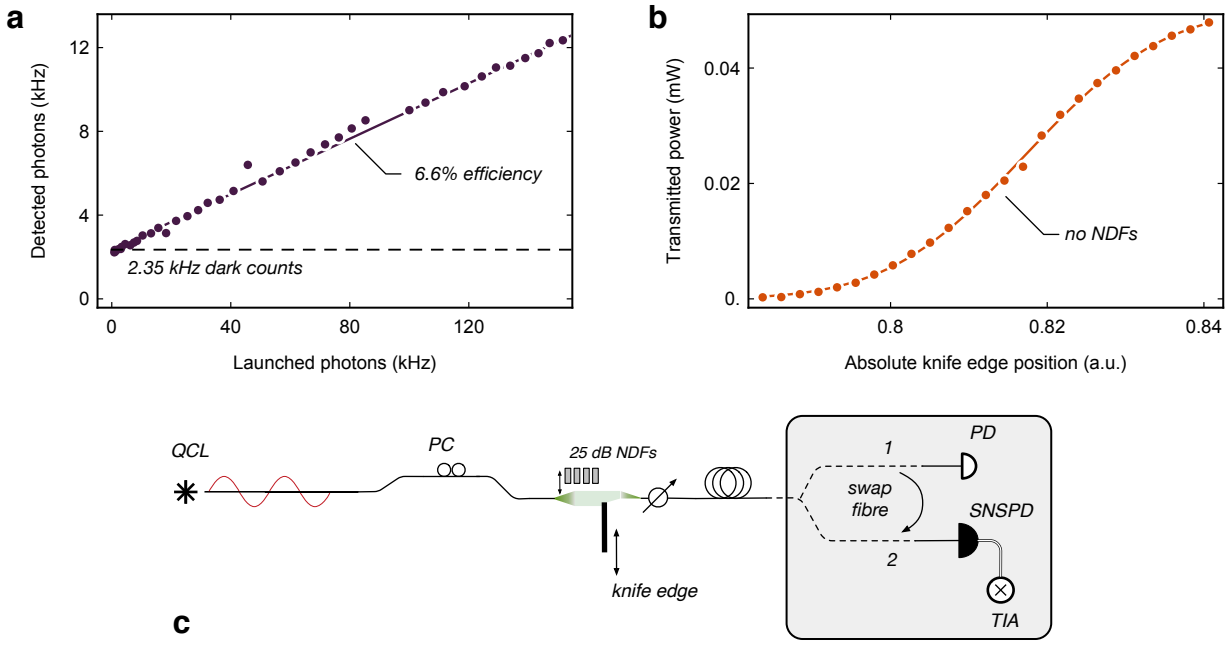

Figure 2.7: Single wavelength superconducting detector characterisation. **a**, Efficiency measurement of a PhotonSpot superconducting detector with the MIR fibre loop removed. **b**, Bright light power measured on a calibrated photodiode as a function of knife edge position used to estimate the number of launched photons. **c**, Experimental scheme to measure the superconducting detector efficiency. Bright light transmission of a knife edge attenuator is measured, along with four 25 dB neutral density filters (NDF) on a photodiode (PD). The NDFs are then placed in the beam path and the fibre is connected to the superconducting detector.

efficiency*. A possible but unverified explanation for this discrepancy could be due to the fibre in the cryostat being wound to different radii†.

The PhotonSpot channels 7 and 8 had tightly wound MIR fibre loop filters, leading to an orders of magnitude reduction in the detection efficiency, clearly seen in the measured values in table 2.1. The Hadfield niobium nitride detectors channels 1-4 were also optimised for telecommunication-band operation and were in a different cryostat. This cryostats temperature went down to around 2.8 K in contrast to the 0.8 K of the PhotonSpot system. The different superconducting detector material and operating temperature of the cryostat‡, also contributes to some of the observed difference in measured system detection efficiency (SDE) values. Furthermore, the importance of removing the MIR fibre loops is clear. The best detector from the Hadfield system peaked at around 2% efficiency. The first and second best Hadfield detectors (3 and MIR, respectively) had a difference in the estimated efficiencies by a factor of 3.

Since not detecting either half of a photon-pair results in no coincidence detection, the effective reduction in count rate scales as the addition (product) of the transmission in logarithmic (linear) units. The optimal pair of the Hadfield detectors had comparable effective detector losses on the coincidences of $10\log_{10}(0.021) + 10\log_{10}(0.01) =$

*Later experiments with much larger bias voltage increased this estimate to around 0.5%

†This cryostat was in 24/7 operation so we never had the opportunity to open it up and to check and change this.

‡Superconducting detector efficiency is temperature dependent[171]

−36.5 dB, which is similar to the effective loss of the commercial 1.55 μm detectors of $10\log_{10}(0.06) + 10\log_{10}(0.005) = -34.8$ dB. From these measurements, we identified that using PhotonSpot channels 5 and 6 would give us the best chance to detect a signature of SFWM.

Detector name	Bias (V)	Threshold (mV)	Dark count rate (kHz)	Efficiency (%)
PhotonSpot 5*	0.2	200	0.083	0.05
PhotonSpot 6*	0.7	100	2.4	6.6
PhotonSpot 7	1.13	200	0.24	1.8×10^{-3}
PhotonSpot 8	0.94	200	0.21	2.0×10^{-3}
Hadfield 1	1.11	130	1.9	0.60
Hadfield 2	1.5	100	0.73	0.36
Hadfield 3	0.44	75	4.4	2.1
Hadfield 4	0.8	75	1.2	0.078
Hadfield MIR	0.45	35	1.7	1.0

Table 2.1: A table summarising the monochromatic efficiency measurement for several NIR and a MIR SNSPDs. $*$ denotes the MIR filter removed. This table serves as a guideline for the approximate performance of the detectors and was used to identify the pair of detectors with the greatest likelihood of registering MIR photon-pairs. Since all the detectors are measured at fairly different bias settings, a direct comparison of performance is not possible.

Bias and threshold sweeps

The next set of measurements were to quantify the effect of sweeping the bias and discrimination voltages on the detected count rates. To do this, we set up the experiment in a similar fashion to the previous section. However, in these measurements we fixed the launched power and looked at the behaviour of the detectors with, and without illumination. This would help us determine the optimal measurement setting regions for detecting single photons. The QCL laser was again attenuated with four NDFs and launched directly at the SNSPDs. The discrimination and bias voltage were then swept by remotely controlling the biasing electronics from the computer. Finally, the singles counts were again processed with a time-tagger and collected on a computer.

Figure 2.8a and 2.8b shows side-by-side comparisons of the dark and light counts versus the set bias and measurement discrimination voltage, measured for a NIR detector. We see that the region in the top corner of Fig. 2.8a has a small plateau where the single-photons are being registered—corresponding to the optimal bias settings.

Statement of work

The laser cage system, bulk variable optical attenuator, single- and double-pass monochromator bulk optics setup were designed, built and characterised by me. Ben Sayers and I repaired and aligned the optical pulse autocorrelator. The monochromatic measurements of the PhotonSpot superconducting nanowires were performed by myself and Dr. Joshua Silverstone. The telecommunication band detectors were made by Dr. Vikas Anant. The mid-infrared detectors were designed, fabricated and packaged by Dr. Kleanthis Erotokritou. Gregor Taylor, Dr. Kleanthis Erotokritou, and Prof. Robert Hadfield in-

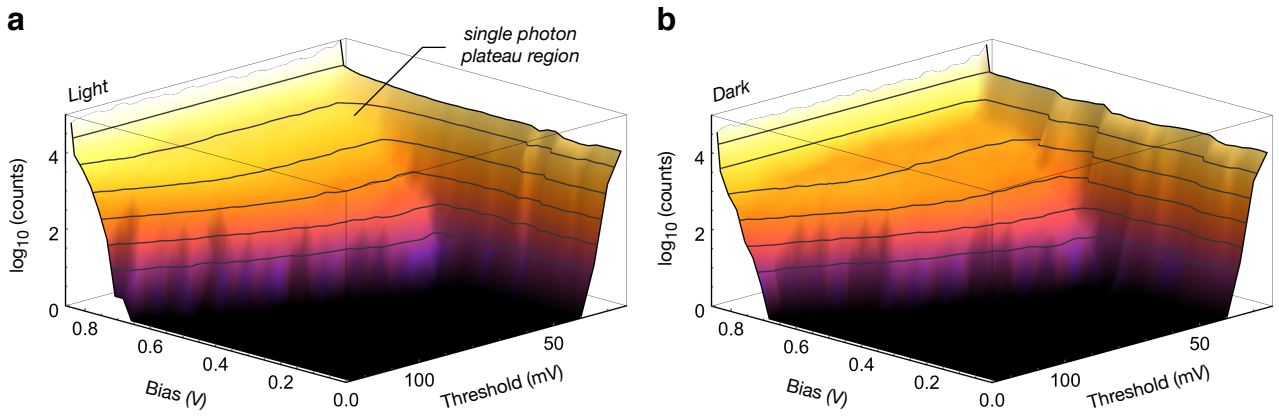

Figure 2.8: Bias and threshold characterisation of SNSPDs. Since the detectors are inefficient, the dark and light counts plots look similar. The optimal bias and threshold setting for sensitivity is in the plateau region where the light counts are registered, but before the exponential increase from latching or a discrimination level that triggers from electronic noise. **a**, Light counts with varying detector bias and discrimination threshold voltage, logarithmic scale. **b**, Dark counts with varying detector bias and discrimination threshold voltage, logarithmic scale.

stalled these detectors into the cryostat. Myself and Dr. Kleanthis Erotokritou characterised the efficiency of mid-infrared detector.

Chapter 3

On-chip infrastructure

To observe mid-infrared (MIR) photon-pairs from a silicon waveguide source, integrated filtering, optics and phase-matching problems were solved. An arsenal of component designs, experimental methods and equipment enabled MIR photon-pair generation.

Before we can demonstrate on-chip quantum interference, the following experimental requirements are necessary. *1*, A bright source of photon-pairs. For this, a method of efficiently coupling in and out of the chip and a phase-matched waveguide is essential. *2*, A way to filter out the pump, down to the single-photon level. When bright pump laser, which is more than 13 orders of magnitude brighter than single photons, is incident on the detectors, the single-photons are effectively drowned out in noise. *3*, Efficient single photon-detection—a bright source of single-photons is rendered useless if they can't be measured. *4*, High performance Mach-Zehnder interferometers (MZIs). In a time-reversed Hong-Ou-Mandel (HOM) measurement, low-loss waveguides, balanced beamsplitters, and phase modulation are imperative for good fringe visibilities.

This chapter elucidates the necessary technical developments including; initial characterisation of integrated optics, the evolution of waveguide sources, design and measurement of waveguide circuits, and finally the observation of stimulated four-wave mixing. Here, we set the stage for pushing the boundary from classical to quantum photonics in the MIR. In the following sections, we perform measurements on five generations of chips. Before diving into these details, we summarise their performance in table 3.1

Parts of this work were given as an oral presentation at the international conference '2018 European Conference on Integrated Optics' (ECIO) in Valencia, and was awarded the best student presentation prize[172].

3.1 Passive structures: Generation 1

The first integrated optics we measured were waveguide chips fabricated on 220 nm silicon on insulator (SOI) by the Institute of Microelectronics (IME). On the first itera-

Gen	Name	t (nm)	Clad	η_{GC} (dB)	η_{WG} (dB/cm)	Experiments	Comments
1	IME02	220	SiO_2	7	-	Gs, BS	-
2	IME03	220	SiO_2	8	0.2	Gs, BS, WG	MM WG
3	IMEC390	390	Air	7	0.2	WG	Loss from 173
4	IME05	220	SiO_2	8	1.2	Gs, BS, WG, SRC, RG	low η_{WG} contrast
5	CORN05	340	SiO_2	3.5	3	Gs, BS, WG, SRC, RG	Optical lithograph chip

Table 3.1: Chip design summary. Columns titles; generation, internal chip name, SOI thickness t, top cladding material, grating transmission (η_{GC}), propagation loss (η_{WG}), experiment keys: gratings (Gs), beamsplitters (beamsplitter (BS)), waveguides (WG), sources (SRC), rings (RG).

tion of chips, the main components that were investigated were vertical grating couplers, and integrated beamsplitters. These components are the nuts and bolts of any integrated waveguide circuit and are a necessary first step in establishing MIR integrated optics.

Multi project wafer runs facilitate an efficient usage of silicon photonics design space, combining the work of several separate parties onto a single wafer to reduce the cost. Work started on our research group's second iteration of the IME chips: IME02 (see Fig. F.2 on page 161 for design area), henceforth referred to as 'generation 1'. Using the experimental scheme showed in Fig. 3.1f and optimising the polarisation for maximum transmission, the optimal uniform grating coupler pitch for our quantum cascade laser (QCL) laser was found to be $\Lambda = 960$ nm for a 12 degrees incident coupling angle, which is in excellent agreement with the theory value predicted from the uniform grating equation of $\Lambda = 957$ nm[83] (see Eqn. (1.52)). This also confirmed that the modelling and design methodology could be relied on. The results of the coupling against grating pitch are summarised in Fig. 3.1c.

We measured the reflectivity* of 2×2 multimode interference couplers (MMIs)[61,96] and directional couplers (DCs), using a channel loss independent measurement technique described in appendix D.1 on page 145. The main result of the derivation gives

$$R = \frac{b \pm \sqrt{b}}{1 - b}, \tag{3.1}$$

where R is the beamsplitter reflectivity, and $b = (t_{13}\, t_{24})/(t_{14}\, t_{23})$ is a dimensionless ratio of input to output coupling transmissions that eliminates losses up to the integrated coupler. Here t_{ij} is the optical transmission from input port i to output port j. See labelled ports on Fig. 3.1d. The results of these loss independent measurements are shown in Figs. 3.1a and 3.1b. Note for nominally the same design, the reflectivity of the MMI is approximately constant, while the DC (Fig. 3.1e) has significant variation for the same beamsplitter design—clearly showing the difference in fabrication tolerance between the MMI and DC.

*The reflectivity, which is equivalent to the splitting ratio, is a measure of how balanced the outputs of a beamsplitter is. This term which has generally been adopted by the quantum optics community over the term splitting ratio.

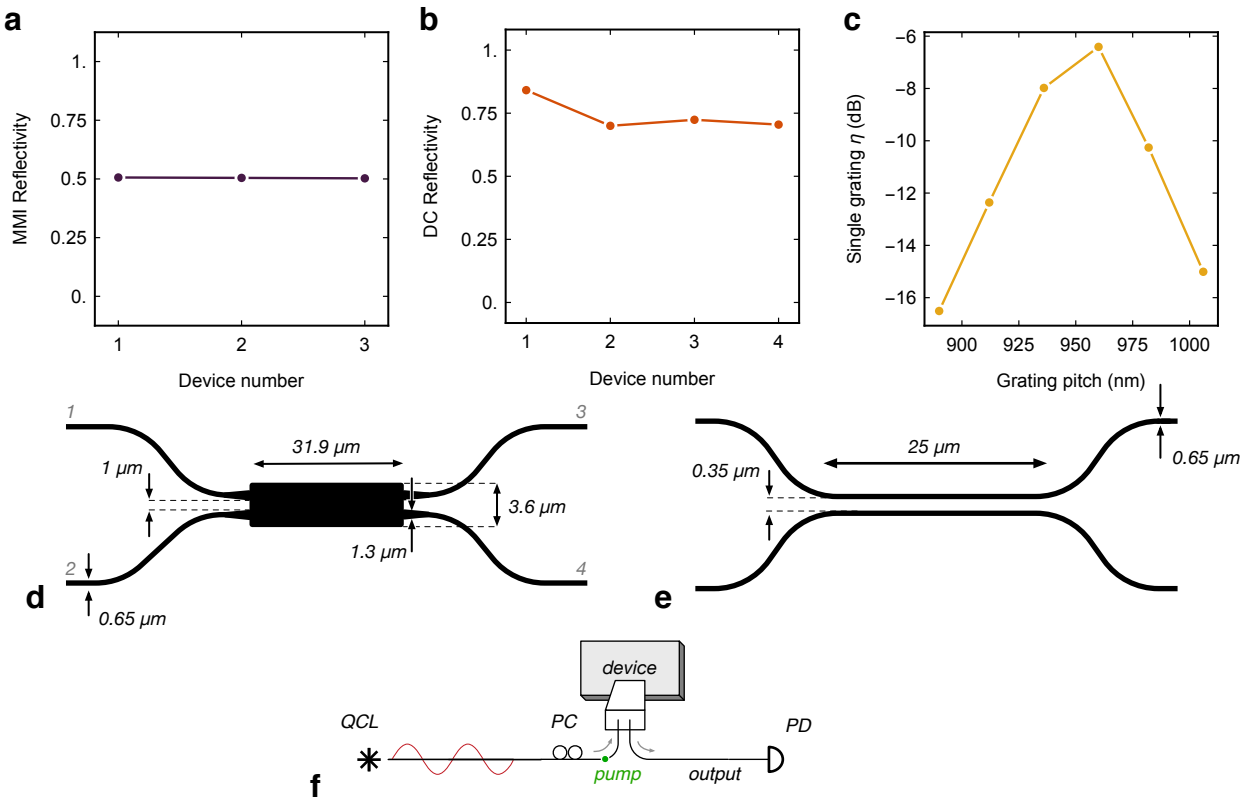

Figure 3.1: Characterisation of generation 1 integrated optics. Each data point in these plots is a single sample. **a**, Reflectivity of the multiple 2 × 2 MMI devices with the same design parameters. **b**, Reflectivity of the multiple directional coupler (DC) devices with the same design parameters. **c**, Single grating transmission with varying grating pitch. **d**, Schematic showing the 2 × 2 MMI geometry. **e**, Schematic showing the DC geometry. **f**, Experimental setup: Laser is polarisation controlled (PC), coupled into the device, and detected with a photodiode (PD).

3.2 Parametric sweep of integrated optics: Generation 2

Developing a complete integrated optics toolbox in the MIR required searching a large parameter design space for key optical components: waveguides, grating couplers, MMIs DCs, and ring resonators. In the second chip we tested from IME on 220 nm SOI (IME03), henceforth 'generation 2', a substantial design study swept across the various integrated optics design parameters—see Fig. F.3 (page 162) for layout. This informed us of a reliable set of integrated components that would work in the MIR band for future experiments. The following sections show these measurements.

Grating couplers

Honing a design for good fibre-chip coupling of the pump, on and off the chip was necessary for MIR photon-pair generation. This chip had a total of 60 uniform grating coupler designs arranged in a layout with three rows of twenty gratings, and we show a subset of these in Fig. 3.2e. The following design variations comprised the grating array: *1*, Deep etch grating pitch. *2*, Eccentricity. *3*, Fan angle. *4*, Broken tooth* [82]

*These are gratings with two etch steps—full and partial, see Fig. 3.2b inset for grating structure.

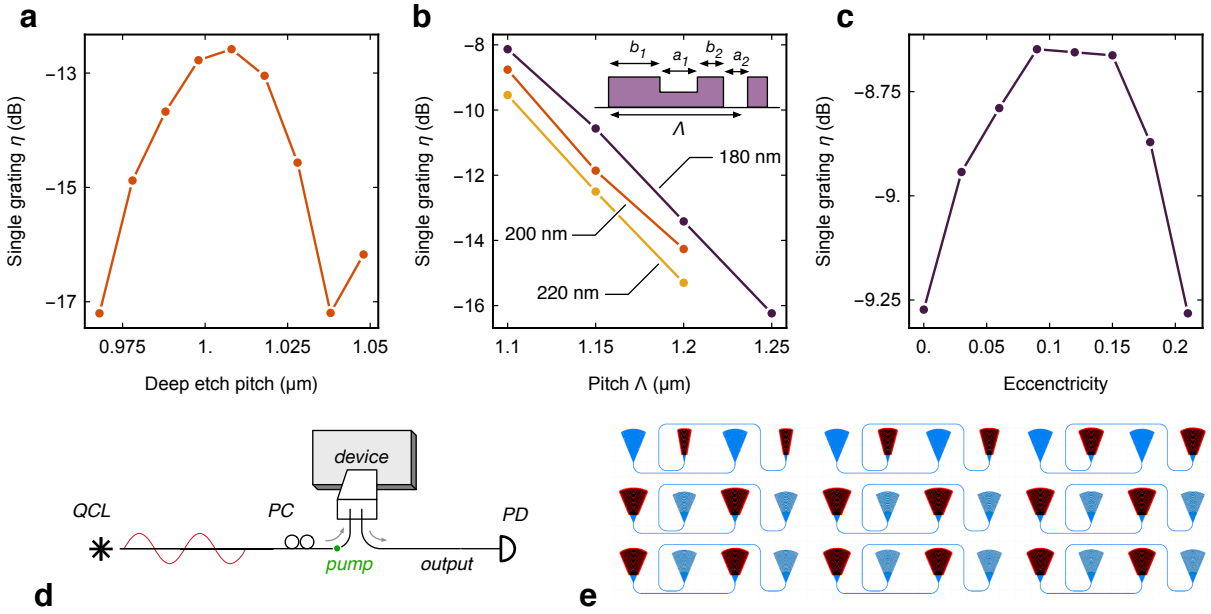

Figure 3.2: Generation 2 grating coupler parameter sweep. **a**, Single grating transmission, varying the deep etch uniform grating pitch. **b**, Single broken tooth grating transmission, varying the full pitch Λ, with $b_1 = 0.4$ μm, $a_1 = 0.288$ μm, for three fixed widths b_2 of 180 nm, 200 nm and 220 nm. Inset: side view schematic of the broken tooth grating structure. **c**, Single grating transmission with a shallow etch, varying the eccentricity. **d**, Experimental scheme for the grating efficiency measurements. **e**, Subsection of the grating coupler array, plan view.

To measure all of these structures was a large task. We worked with a six-axis nanopositioning stage (Thorlabs Nanomax), with stepper motors to automate positioning in the x-y plane. The automated alignment measurement strategy is outlined in appendix D.2 (page 146), and experimental scheme shown in Fig. 3.2d.

The single grating transmission measured with a a 10° V-groove array (VGA) varying the grating pitch of uniformand broken tooth grating couplers[82] are summarised in Figs. 3.2a and 3.2b. We see that, as expected, the grating coupler pitch determines the coupling efficiency, as the optimum pitch changes with wavelength. The measurements were taken with a continuous wave (CW) laser fixed at $\lambda = 2.049$ μm. The peak coupling efficiency (-12.6 dB) with a grating deep etch (130 nm) grating pitch of $\Lambda = 1.008$ μm (See Fig. D.3b for spectral response shape and appendix D.3 on page 147 for corresponding measurement strategy) agrees reasonably with the simulated optimal pitch $\Lambda = 1.028$ μm.

However, we find that the deep etch process for the grating couplers reduces the coupling efficiency significantly (cf. the shallow etch (70 nm) grating results with peak transmission of -8.6 dB Fig. 3.2c). Unfortunately, no light was transmitted from the fan angle sweep. We relied on simulation instead, implying the optimal aperture diffraction angle of 45°. From the best eccentricity measured we compile the optimal uniform grating coupler parameter set in 220 nm SOI in table 3.2. From the generation 2 chip, we were

Parameter	Pitch (μm)	Eccentricity	Fill factor	Fan angle (°)	Etch depth (nm)
Value	0.936	0.135	0.5	45	70

Table 3.2: Optimal 220 nm uniform grating coupler parameters, with 10° coupling angle.

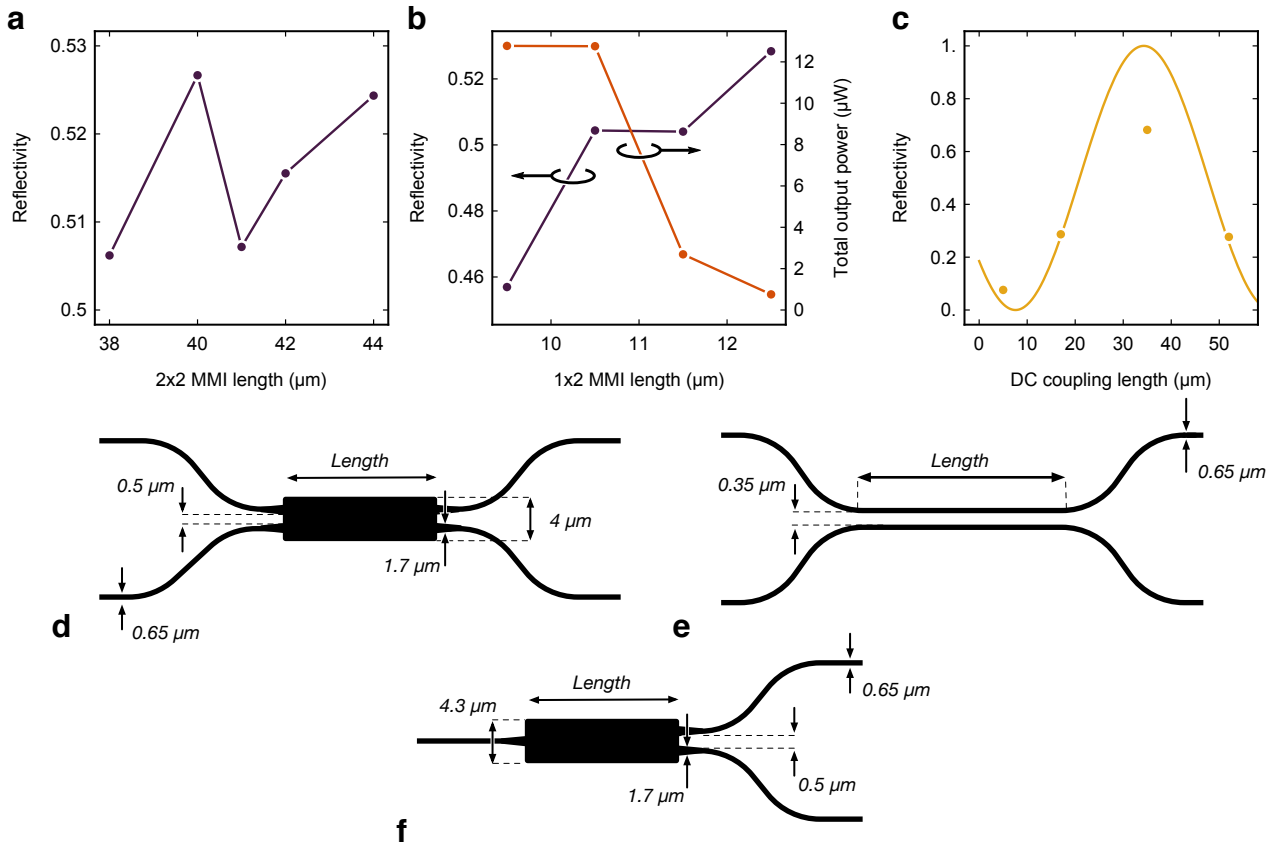

Figure 3.3: Generation 2 waveguide couplers characterisation. **a**, 2 × 2 MMI reflectivity measurement with varying MMI length. **b**, 1 × 2 MMI reflectivity measurement and total transmitted power at output ports with varying MMI length. **c**, Directional coupler reflectivity with varying coupling length, line is a fit of a sinusoid. **d**, Schematic of the 2 × 2 MMI geometry. **e**, Schematic of the directional coupler geometry. **f**, Schematic of the 1 × 2 MMI geometry.

able to verify that the grating couplers were indeed centred on the target wavelengths that we designed them for. We show a few sample spectra collected in Fig. D.3b. The devices are modest in their performance when compared to the efficiency of telecom band grating couplers which have a transmission of around -3 dB on this same chip.

Integrated beamsplitters

The beamsplitters on this chip were a set of five 2 × 2 MMIs, five DCs and four 1 × 2 MMIs, with varying lengths. The geometric design parameters for these beamsplitters are shown in Figs. 3.3d, 3.3e, and 3.3f. The measurement, described in Sec. D.1, was used on all the four port devices to determine the loss independent reflectivity and the results are shown in Figs. 3.3a and 3.3c.

Channel loss independent measurements of the 1 × 2 MMI[147] structures are not possible, as one can not ratiometrically eliminate the unknown channel losses. The symmetry of these structures means that they should be balanced, but there is significant wavelength dependent loss due to the positions of self images in the MMI region not aligning with the output waveguide tapers. The reflectivity of the design shown in Fig. 3.3f as a function of 1 × 2 MMI length were calculated as the ratio of the power at the two output

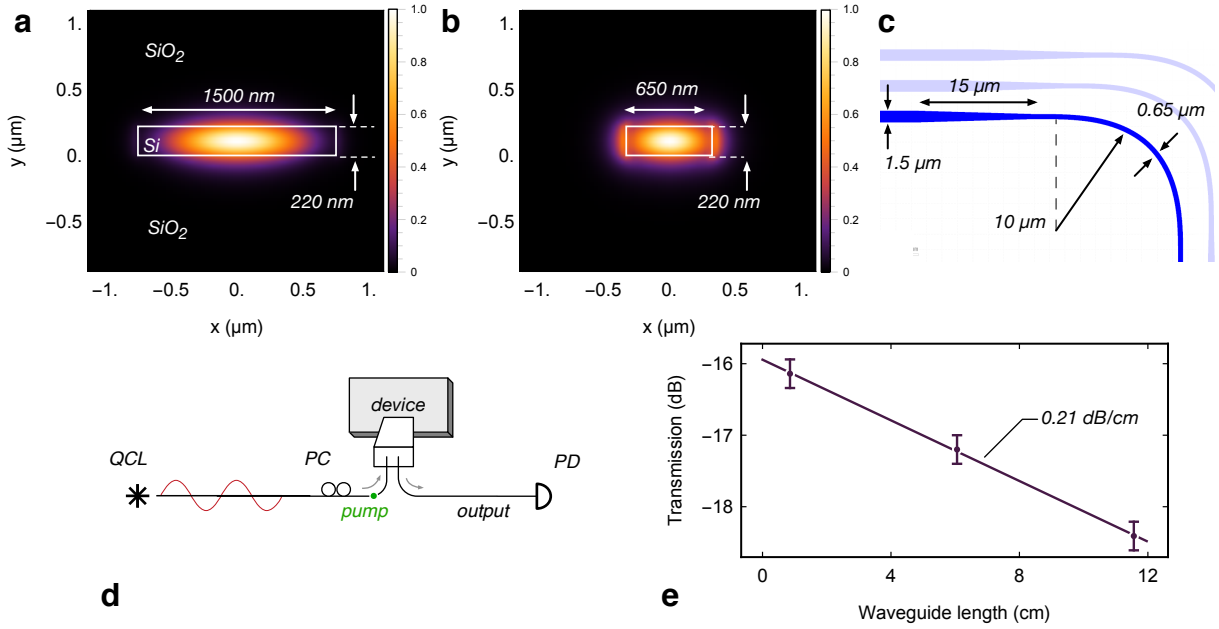

Figure 3.4: Design and measurement of a low-loss waveguide on generation 2. **a**, Mode solved normalised electric field magnitude $|E|^2 = |E_x|^2 + |E_y|^2 + |E_z|^2$ of the expanded waveguide section. **b**, Mode solved normalised electric field magnitude of the bending region single-mode waveguide. **c**, Top down view of the square spiral, annotated with geometry for the bending regions. **d**, Experimental setup for the measurement shown in d. **e**, Linear cutback measurement of the waveguide with a linear fit indicating propagation loss of 0.21 dB/cm.

ports. The results are shown in Fig. 3.3b, with the measurement configuration seen in Fig. 3.2d.

These measurements were useful for informing the next set of components that were used in the next chip design. These had substantially more complex experiments comprised of circuits using the best beamsplitters and grating couplers from these measurements.

Low-loss multimode waveguide

The low-loss waveguides on this chip were strip waveguides, wrapped into square spirals to reduce the scattering losses from the curved waveguide sections*. The waveguide had a cross sectional geometry of 1500×220 nm^2 in the straight sections, with 15 µm tapers down to single mode waveguides of width $w = 650$ nm for the bending regions—see Fig. 3.4c and Fig. F.9 for magnified view of the layout. The bends were $R_{\text{min}} = 10$ µm ($R_{\text{eff}} = 18.7$ µm) Euler bends[175], which adiabatically change the radius of curvature continuously to reduce loss. In principle, these waveguides could have performed the bending at the multi-mode waveguide width, however very large bends > 50 µm would have been needed to minimise coupling into higher order modes. Each spiral of the three spirals in this experiment had 8 loops, and therefore a constant number of a tapers and bends. Figures 3.4a and 3.4b shows the mode solved electric field intensity profile of the multi- and single-mode waveguides used for the low-loss spirals, respectively. Upon in-

*Dr. Euan Allen from our research group measured an excess of 7 dB/cm on spirals with continuous curvature at 1.55 µm[174].

spection, it is obvious that the electric field overlap with the waveguide walls is far higher in the single mode waveguide which would lead to larger propagation losses. While the multi-mode waveguide sources are lower loss, the large effective area requires long interaction lengths for use as a photon-pair source, since the waveguide nonlinearity scales $\propto 1/A_{\text{eff}}$.

To characterise the linear transmission, the QCL laser, centred at $\lambda = 2.049$ μm, was passed through a polarisation controller and then measured on a Thorlabs InGaAs photodiode. Controlling polarisation, the light was then coupled into the fundamental transverse electric (TE) mode of the silicon delay line with grating couplers, finally recording the output power on the photodiode. Measuring a single device for each waveguide length, the transmission of the waveguides as a function of waveguide length estimates the propagation loss in a measurement known as a 'cutback'. The cutback measurement scheme and results are shown in Figs. 3.4d and 3.4e, finding a linear propagation loss of 0.21 ± 0.03 dB/cm and a grating loss of 7.97 dB/grating. Here, the error bars on each data point are assumed to be ±0.2 dB due to uncertainty on the photodiode reading, and the error on the propagation loss is the standard error from calculated linear fit.

This result compares well to a result at $\lambda = 1.55$ μm in 220-nm SOI[176] employing a similar approach. Here, they report a propagation loss of 0.27 ± 0.01 dB/cm with a multi-mode 700 nm width rib waveguide with a 70 nm partial etch, and 470 nm width single-mode strip waveguide bends.

To summarise, in Secs. 3.1 and 3.2 we characterised a set of integrated components in 220-nm SOI: grating couplers, integrated beamsplitters, low-loss waveguides and ring resonators. With this set of components, we could now start developing waveguide circuits that combine these building blocks into something more complex. The next step towards achieving photon-pairs was to demonstrate waveguided optical nonlinearities.

3.3 Nonlinear optics in MIR silicon waveguides: Generation 3

This section describes our first nonlinear optics measurements on a chip manufactured by Interuniversity Microelectronics Center (IMEC), henceforth 'generation 3', from the silicon photonics research group in Belgium. The samples were sent to us by a collaborator—Prof. Bart Kuyken—who designed the chip and had published a MIR supercontinuum and frequency comb generation spanning an octave with these devices[173].

The structures of interest on this chip were 1 cm straight waveguides with the target waveguide having a cross sectional geometry of 1000×390 nm^2. These air-clad silicon waveguides were dispersion engineered to have anomalous group-velocity dispersion in the 2 μm wavelength band. The waveguide dimensions, electric field intensity and the dispersion of key parameters are shown in Figs. 3.5a, 3.5b and 3.5c.

The strategy to couple light into the waveguide used a pair of reference grating couplers, with a much lower propagation loss and a short enough waveguide to observe both fibres in the same microscope image. The alignment strategy for two independent fibres is outlined in appendix D.4 on page 149. An optimal angle of $\theta = 11°$ was found from testing different coupling angles, corresponding to a single grating transmission of approximately 7 dB at $\lambda = 2.05$ μm. It was now possible to pump the 1 cm waveguide with the newly equipped mode-locked laser enabling our first nonlinear optical characterisation in silicon.

Measurement of optical nonlinearity

Armed with the newly built variable optical attenuator (VOA), the first measurement of optical nonlinearity was performed, with the experimental setup shown in Fig. 3.5d. In this measurement, the pulsed mode-locked laser was passed through the bulk optical attenuator and launched into the 1-cm straight waveguide via the grating couplers. A 90:10 optical tap and photodiode monitored the input power. An output fibre then collected light from the chip and the transmitted power was then monitored on a second photodiode.

We show the results of this measurement in Fig. 3.5e, where we plot the inverse transmission as a function of launched power. In the absence of nonlinearity, the line should be flat as the transmission does not depend on power. Here, it is clear that there is a non-zero gradient of the line, implying that at higher powers coupled into the waveguide the output power begins to saturate. A strong motivation for working in the 2.1 μm band is the large reduction of two-photon absorption (TPA) along with the resonant spike in the nonlinear refraction[160,161]. Our experimental data showed saturation of the output optical power and a sudden deviation from the inverse transmission linear fit at high power. Was the behaviour predominantly due to TPA or nonlinear broadening from self-phase modulation (SPM)*? In absence of an optical spectrum analyser (OSA) to directly measure the waveguide output pulses, we relied on numerical modelling instead.

Split-step Fourier method analysis

The nonlinear Schrödinger equation (NLSE), is a nonlinear pulse propagation equation[177]. For further details of how this result is derived see appendix E.1 and E.2 on pages 151 and 153, respectively. An approximate formula for pulse propagation is given by[73]

$$\frac{\partial A}{\partial z}+\frac{\alpha}{2}A+\frac{i\beta_2}{2}\frac{\partial^2 A}{\partial T^2}-\frac{\beta_3}{6}\frac{\partial^3 A}{\partial T^3}=i\gamma\left(|A|^2A+\frac{i}{\omega_0}\frac{\partial}{\partial T}(|A|^2A)-T_RA\frac{\partial|A|^2}{\partial T}\right), \tag{3.2}$$

where z is the propagation distance in the waveguide, T is the time in the frame of reference moving with the pulse at the group velocity, A is a slowly varying pulse envelope, β_i is the i^{th} derivative of the propagation constant $\beta(\omega)$ in the Taylor series expansion about carrier frequency ω_0, α is linear propagation loss, $\gamma = k_0 n_2 / A_{\text{eff}}$ is the effective waveguide nonlinear parameter and T_R is a Raman response function to the optical pulse.

In most cases, the NLSE equation does not have an analytical solution, thus numerical solutions are required to obtain information of the nonlinear effects from the silicon waveguides. Two broad categories of numerical methods that can be used to solve the NLSE are *1*, finite difference methods and *2*, pseudospectral methods. A common pseudospectral method for solving a nonlinear dispersive propagation medium is the split-step Fourier method. The run time of these algorithms is often an order of magnitude faster due to the computationally efficient discrete fast Fourier transform (FFT) algorithm–see appendix E.3 (page 155).

We implemented our simulations of the NLSE with Python. We took experimentally measured parameters such as the propagation loss, laser repetition rate, in-waveguide peak power estimated from the reference grating transmission, and the manufacturer specified pulse duration, and fed these as input to the algorithm. Additionally, we used

*see appendix E.4 (page 155) for origin of SPM.

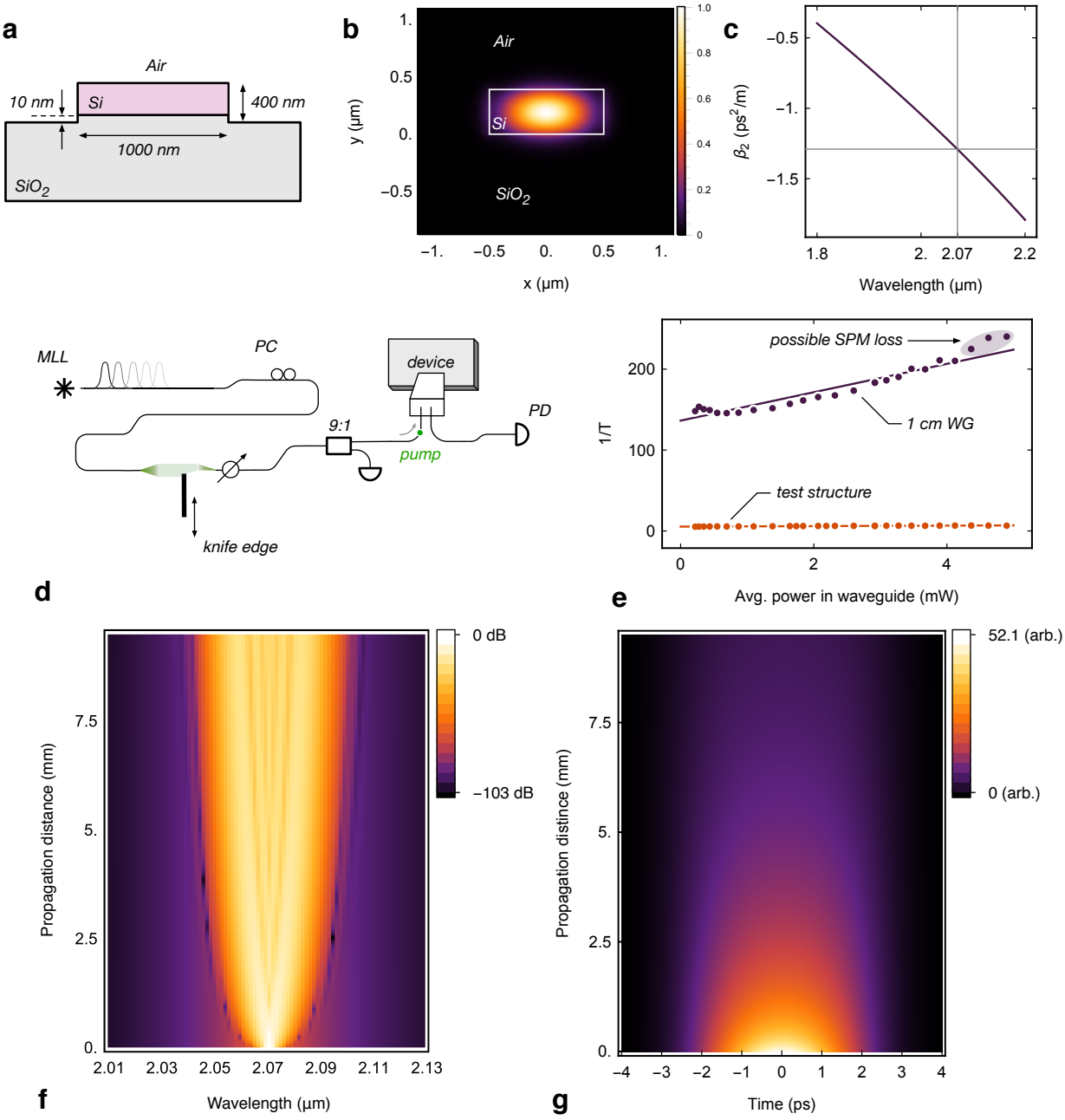

Figure 3.5: Generation 3 modelling and experimental nonlinearity. **a**, Waveguide cross section dimensions. **b**, Simulated waveguide electric field magnitude $|E|^2 = |E_x|^2 + |E_y|^2 + |E_z|^2$ of the fundamental TE mode. **c**, Simulated waveguide mode group velocity dispersion (β_2) with varying wavelength. **d**, Experimental scheme used for measuring the nonlinear transmission of the waveguide. **e**, Experimentally measured inverse transmission with varying input power coupled to the waveguide. **f**, Split-step Fourier method simulations in the frequency domain for the highest power optical pulse intensity as it propagates through the waveguide, log scale normalised to peak input pulse intensity at $z = 0$. Self-phase modulation is a possible cause of broadening outside of the grating coupler bandwidth, leading to nonlinear behaviour in the inverse transmission. **g**, Split-step Fourier method simulations of the propagating pulse intensity in the time domain, linear scale.

literature values for the dispersive[161] and absorptive[160] nonlinearity at $\lambda = 2.07$ μm. We chose the step size as 10 μm and temporal domain of the simulation to be 4 times the pulse full width at half maximum (FWHM), which eliminated numerical instabilities from the pulse spreading to the simulation boundaries.

In Fig. 3.5e, the data points at high power deviate suddenly away from the inverse transmission curve. Performing split-step Fourier method (SSFM) simulations at the highest power that is launched in our experiment, we observe significant nonlinear broadening due to SPM, possibly causing the optical pulse to broaden beyond the grating coupler bandwidth. The results of the SSFM in the time and frequency domains are shown in Figs. 3.5f and 3.5g. Without an OSA we could not directly verify this, but the simulations could help explain the origin of this effect. Furthermore, in retrospect, the actual input spectrum (without filtering) of the mode-locked laser was significantly broader than our initial estimate (see Fig. 2.5a). The waveguide design was originally for supercontinuum generation, and given the large spectral width of input pulse, made the possibility of broadening beyond the grating coupler bandwidth a plausible hypothesis. The modelling confirmed that the combinations of residual nonlinear TPA and SPM broadening, could explain the observed saturation in the input-output power relationship shown in Fig. 3.5e.

The generation 3 chip was a useful test bed to start investigations of the classical nonlinear optics in the MIR. The two independent single fibres had a long distance from the point they were fixed, combined with a set of optomechanics that were constructed from what was available at the time made the setup unstable and required recoupling every few minutes. The lengthy integrations required for measuring photon-pairs from spontaneous four-wave mixing (SFWM), in the presence of high loss and low efficiency detectors, indicated the experiment would be challenging*.

We had now confirmed the optical nonlinearity of the waveguides in the MIR. To continue progress towards a MIR photon-pair source, larger waveguide circuits, single photon measurements, and filtering now had to be addressed.

3.4 Waveguide circuits: Generation 4

In January 2017 we began working on designing the first integrated circuits. The chip was to be fabricated by Institute of Microelectronics (IME05), henceforth 'generation 4', on a 220-nm SOI platform. The final designs were submitted in March and received late in the summer of the same year. This chip had several experiments including photon-pair sources, and integrated filtering in the MIR.

An overview image of the design can be found in Fig. F.4 (page 163). This was the first opportunity to start building larger integrated quantum circuits, based of the atomic blocks measured on the generation 1 and 2 chips discussed in Secs. 3.1 and 3.2.

The following sections 3.4.1, 3.4.3, 3.4.4 and 2.5.1 formed the basis of an oral presentation that was given at the European Conference on Integrated Optics in Valencia, June 2018[172].

Before describing the experiments in the next section, it is worth highlighting the acquisition of a new experimental tool that would be completely invaluable. We were fortunate to acquire a long wavelength OSA: Yokogawa AQ6375. This piece of equipment

*The first successful correlated photon-pair measurement integrated for nearly 12 hours!

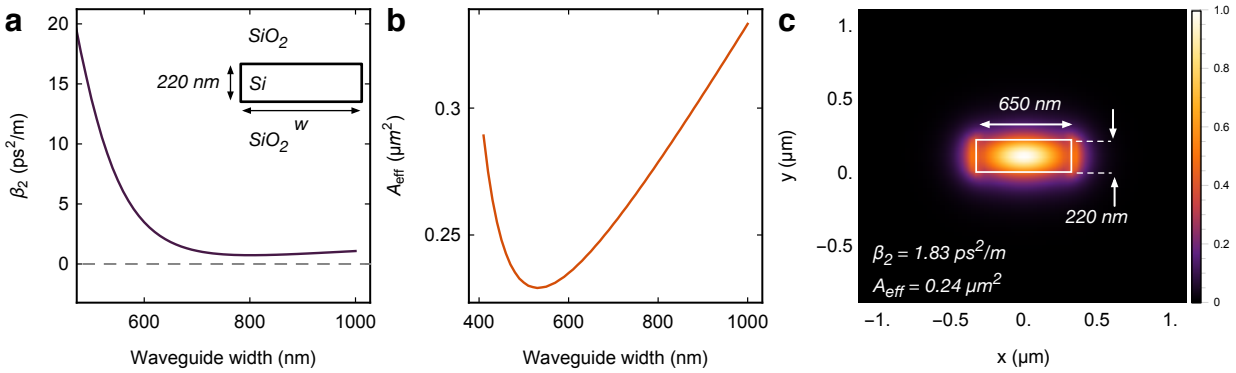

Figure 3.6: Generation 4 single-mode waveguide simulations. **a**, Group velocity dispersion (β_2), with fixed height of 220 nm and varying waveguide width. **b**, Effective modal area (A_{eff}) with varying waveguide width. **c**, Normalised electric field magnitude $|E|^2 = |E_x|^2 + |E_y|^2 + |E_z|^2$ profile for the standard source waveguide.

was critical for the test, measurement and spectral characterisation of integrated devices. This ultimately assisted with the observation of photon-pairs in the MIR.

3.4.1 Waveguides and passive components

Waveguides

The standard single-mode strip waveguide for this chip had a geometry of 650×220 nm^2. An image showing the waveguide mode-solved electric field intensity, effective modal area, and group-velocity dispersion are shown in Figs. 3.6a, 3.6b, and 3.6c. We see that the group-velocity dispersion does not become zero or negative, therefore a phase-matching efficiency of unity is not possible with any TE_0 waveguide design.

Grating couplers

Three focusing grating couplers were designed for an 8° fibre array polish angle, with central wavelengths of 2.05, 2.07 and 2.09 μm (pitch of 0.916, 0.9283, 0.9410 μm, respectively), corresponding to the expected collection wavelengths of the four-wave mixing fluorescence*. The uniform grating couplers were designed using the grating equation, Eqn. (C.9)[83], and the methodology described in appendix C.2 on page 134.

To measure the spectral transmission, the supercontinuum source was linearly polarised and the polarisation controlled with a half-wave plate, before being recorded on the OSA. The laser was then connected into the reference grating structures on the chip, connected together with a shunt waveguide, which is assumed to have negligible loss ($L \approx 127$ μm). Finally, the light was then coupled back off chip and measured on the OSA—the experimental scheme is shown in Fig. 3.7c. The subtraction of the input to output trace determines the spectral transmission, plotted in Fig. 3.7a. We saw that the central wavelengths of the three designs were very close to the target designs.

*other uniform grating parameters are from table 3.2.

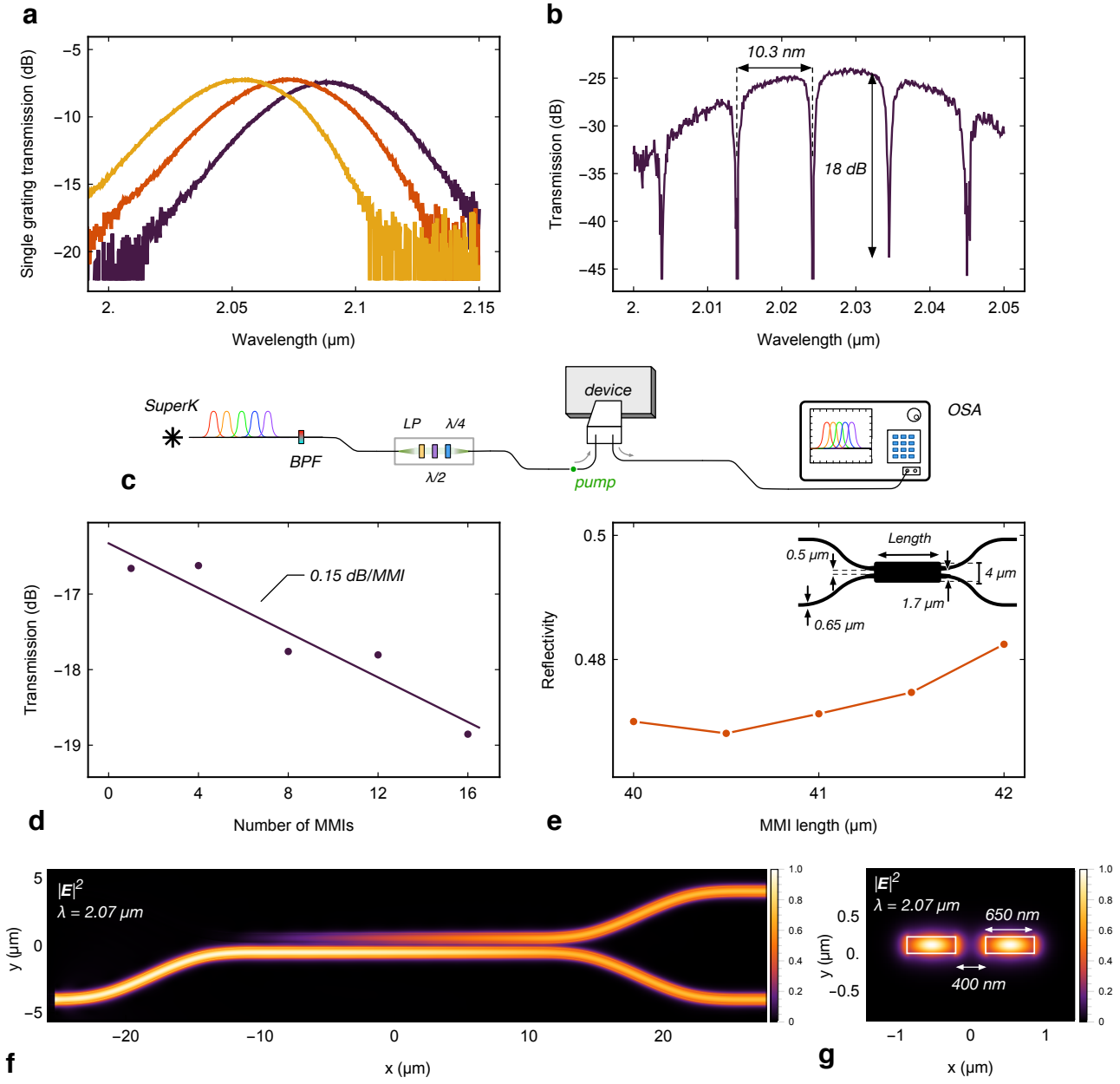

Figure 3.7: Generation 4 passive structure summary. **a**, Grating coupler transmission spectra for the signal, pump, and idler gratings centred on 2.05, 2.07, 2.09 μm, respectively. **b**, Transmission spectra of the ring resonator with a 10 μm bus coupling region. **c**, Experimental scheme for the measurements in plots a and b. Supercontinuum (SuperK) is bandpass filtered (BPF), and linearly polarised (LP) coupled into the device before being detected with the OSA. **d**, 2 × 2 MMI cutback measurement, varying the MMI length. **e**, Loss independent MMI reflectivity measurement as a function of MMI length. **f**, 3D FDTD electric field magnitude $|E|^2 = |E_x|^2 + |E_y|^2 + |E_z|^2$ for the directional coupler. **g**, Mode solved cross section normalised electric field magnitude for the directional coupler.

Directional couplers

The initial cross over length was estimated with mode solving, and the final design verified with the 3D finite-difference time-domain (FDTD) method. After several iterations of 3D FDTD, a balanced coupler was designed with the final design parameters: coupling length $L = 20$ μm, gap $g = 0.4$ μm. An electric field intensity cross section from mode solving, and the in-plane field from FDTD are shown in Figs. 3.7f and 3.7g. The experimental measurement of the reflectivity was performed using the methods outlined in appendix D.1 and was determined to be $R = 0.58$. The measurement setup employed the QCL laser centred at $\lambda = 2.049$ μm, 20 nm away from the designed central wavelength of this coupler. The discrepancy between the simulated and measured reflectivities could possibly be explained by the dispersion of the supermode beat length—this effect is apparent in our FDTD simulations of a separate device shown in Fig. C.8c.

MMIs

The design of the 1×2 and 2×2 MMIs used on this chip were taken from the previously measured optimal design from generation 2. In addition to the reflectivity measurement of the coupler ($R = 0.48$) at $\lambda = 2.05$ μm, a coupler cutback was also designed for the 2×2 MMI, with an estimated transmission of 0.15 dB/coupler—see Fig. 3.7d. A sweep of MMI length against the reflectivity is shown in Fig. 3.7e, which are all within 0.01 of the simulated mode solved and propagated reflectivity at this wavelength.

Ring resonators

The ring resonators on this chip were not used as a photon-pair source. These rings constituted a part of a cascaded on-chip filter described in the following Sec. 3.4.3. The key design parameters are the ring length (100 μm), bus gap and length of the coupling region. Two ring designs had a gap of 0.35 μm and coupling lengths of 10 and 15 μm. The exact loss of the device is not known before it is fabricated. Furthermore, the sensitivity of the directional coupler to fabrication tolerances means performance can be varied. Assuming 3 dB/cm loss (corresponding to $\alpha = 0.993$) and symmetric couplers, the simulated fraction of the power at the drop port on resonance was estimated as 0.96 (extinction ratio (ER) = 14 dB) and 0.98 (ER = 17 dB) for the 10 and 15 μm bus lengths respectively. Recall that the maximum power coupling at the drop-port of an add-drop resonators occurs for lossless rings with symmetric couplers (cf. Eqn. (1.64)).

The ring resonator test structures were spectrally characterised using the same methodology as the grating couplers described before. The transmission spectra of the ring with a 15 μm coupling length is shown in Fig. 3.7b. The group index of these structures can be determined from the free spectral range (FSR)—the distance between adjacent resonances in frequency—using Eqn. (1.63).

The FSR of the two rings was measured as 10.3 nm, corresponding to a group index of $n_g = 3.98$ at $\lambda = 2.03$ μm, which is in excellent agreement with the simulated group index of $n_g = 3.98$. As expected, the difference between these two designs was the ER of the devices, with a maximum ER of 15 and 18 dB for the 10 and 15 μm bus lengths, respectively. Clearly, the device with the 15 μm coupling length is more suitable for filtering due to its higher ER. This circuit variant was therefore characterised in Sec. 3.4.3.

3.4.2 The search for single photons

Single-photon measurements have stringent requirements; a bright source of photons, efficient single-photon detection and high extinction filtering. The detectors that were available were two near infrared (NIR) nanowires with the MIR filters removed*. The challenge of effective pump rejection after the chip, down to the single-photon level, remained. To satisfy this condition, more than 100 dB of pump rejection is required[178–180]. This is to attenuate the laser to the single-photon level, to not drown out photon-pairs from SFWM with bright pump. This measurement succumbed to insufficient off-chip filtering from the monochromators.

Waveguide source measurement

The waveguide was 1 cm long and had a 650×220 nm^2 cross sectional area. We attempted stimulated four-wave mixing (FWM) using the CW QCL laser as the stimulating seed and the mode-locked laser as the other pump[119]. The group-velocity dispersion (see Fig. 3.6a) of this source does not become zero or negative—a requirement for efficient phase-matching. However, we originally hoped that the mismatch would not be too large for the experiment to produce a detectable fluorescence signal. In absence of any bright light signature from stimulated FWM on the OSA, we attempted to looked at the output on superconducting nanowire detectors. Unfortunately, there was insufficient off-chip filters to clean the mode-locked laser (MLL) spectrum, the CW lasers sideband noise, and the output of the chip, so we resorted to looking at just singles counts of SFWM.

In the attempt to measure the SFWM singles counts, we varied the power using the bulk VOA while sweeping the output wavelength monochromator across a range of wavelengths using the experimental configuration seen in Fig. 3.8c. A typical set of singles counts versus wavelength is shown in Fig. 3.8a. A slice of data for different powers at single wavelengths of 2.049 and 2.054 μm is shown in Fig. 3.8b. We see that as the power linearly increases, so do the singles counts—corresponding to typical linear noise processes such as leaked pump. The Hamiltonian of SFWM is quadratic, so doubling the power in a phase-matched waveguide should yield four times increase in the number of photon-pairs produced. This was clearly not the case for this measurement. With the benefit of hindsight, the combination of a poorly phase-matched waveguide, insufficient off-chip filtering and inefficient detectors meant that this experiment was sure to fail. One experiment on the chip remained: the cascaded ring filter, which is now presented in the following section.

3.4.3 Ring filtering experiment

The filtering experiment had a 1-cm single mode waveguide source, attached to the grating coupler input. Four 100 μm cascaded ring resonators[181] at the output of the source had the drop port of each ring connected to the input bus of the next ring. An integrated circuit layout of the device is shown in Fig. 3.9e.

Each ring resonator had a 100 μm long thermo-optic phase modulator (TOPM), driven with a heater driver and dissipated heat through a resistive filament. The heat transferred to the waveguide induces a refractive index change, controlling the position of the resonances—see Fig. 3.9a. Fabrication imperfection led all of four rings to have slight

*See Sec. 2.5.1 for efficiency characterisation.

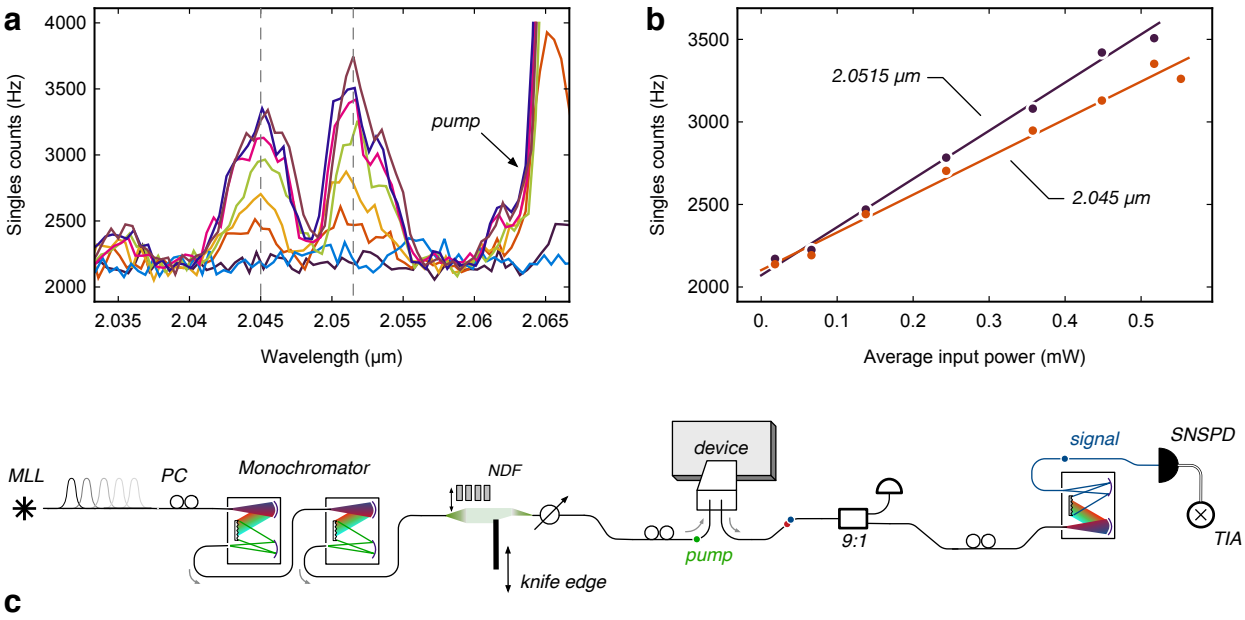

Figure 3.8: Generation 4 singles counts measurement from a source waveguide. **a**, Wavelength dependent single counts measured. The vertical grey lines indicate the slice of data used in the power versus counts plot in b. **b**, Singles counts with varying launched laser power for two different wavelengths. The rate of singles counts is linear with the input power indicating that the signal is linear noise such as leaked pump laser. **c**, Experimental scheme used for attempted single photon measurement. A mode-locked laser (MLL) is filtered with monochromators and attenuated with a knife edge. Controlling polarisation (PC), the pump is launched into the chip. An optical tap (9:1) monitors power at the chip output, and the other arm is filtered before being detected with a superconducting detector (SNSPDs) and time interval analyser (TIA).

variations in the resonance position, requiring alignment with thermal tuning. To electrically and optically characterise the ring response, we launch the CW QCL laser into a ring and simultaneously measure the electrical current to the TOPM and optical output of the drop port on a photodiode as a function of applied voltage which is plotted in Figs. 3.9c and 3.9d, respectively. We show a typical spectral response of the resonance shift of a ring as a function of applied voltage in Fig. 3.9b and 3.9c.

To facilitate temperature stabilisation of the ring resonators, a thermoelectric Peltier cooler was placed underneath the surface of the printed circuit board (PCB). The PCB was made of aluminium, increasing the thermal conductivity between Peltier, thermistor and the silicon waveguide chip. To stabilise the on-chip temperature, the resistance of a 10 kΩ thermistor was monitored with an Arroyo temperature controller (TEC). The current flowing to the TEC was then automatically set by a proportional-integral (PI) control loop in the TEC with the gain parameters set to optimise stabilisation.

We aligned the resonances of the device using the supercontinuum laser, OSA and a 20 V heater driver board. The experimental diagram is shown in Figs. 3.9e and 3.9f (see Fig. F.10 for magnified view of structure). The laser was linearly polarised, and a $\lambda/2$ waveplate controlled the polarisation launched into the chip. The alignment strategy was to couple the source waveguide with the laser, and observe the transmitted light at the through port of the first resonator (grating port and spectrum labelled 1 on Figs. 3.9e and 3.9g, respectively) on the OSA. Setting the voltage to around 10 V—approximately

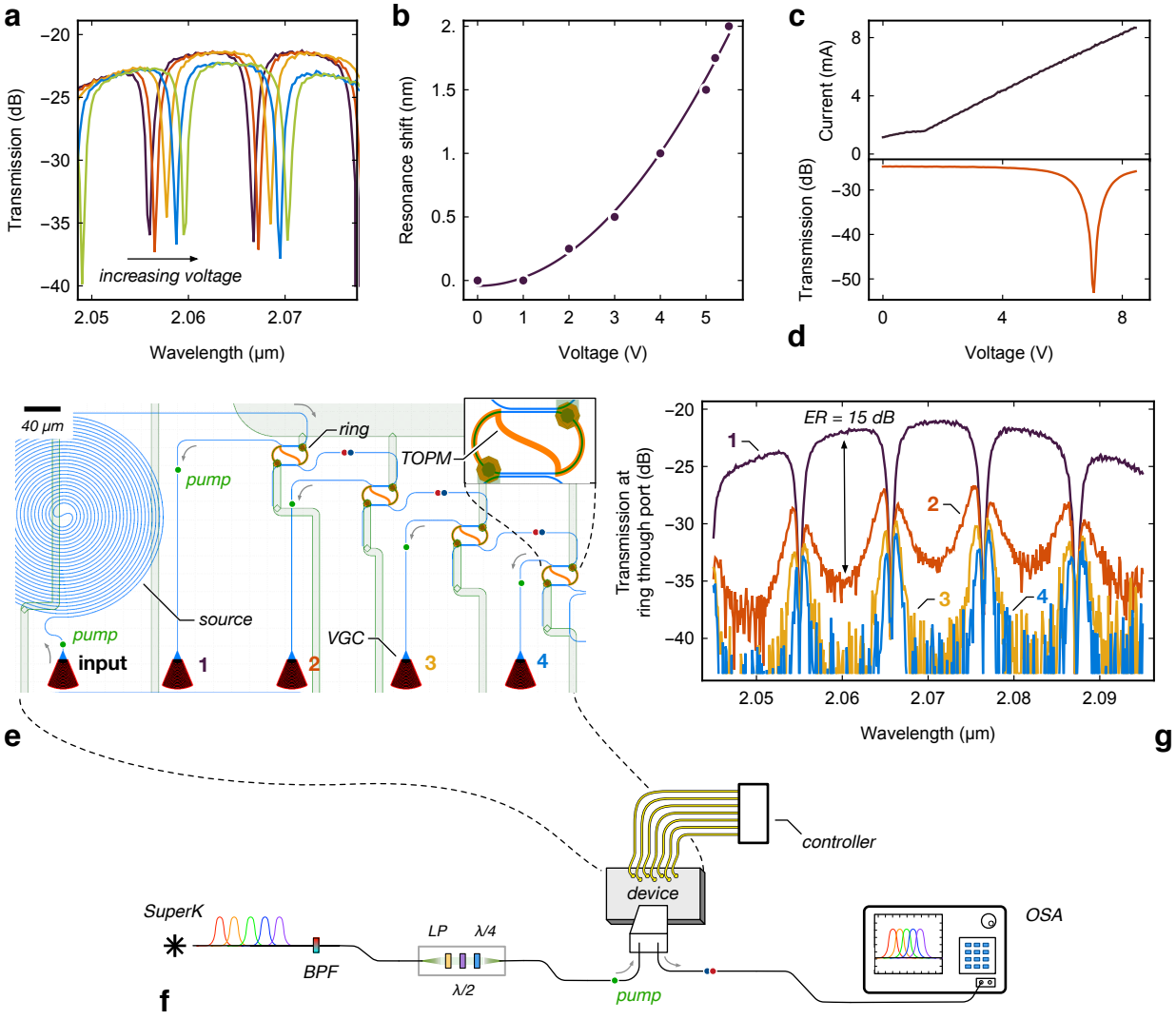

Figure 3.9: Generation 4 integrated source and ring filtering experiment. **a**, Thermal tuning of ring resonances. **b**, Relative position of the ring resonance with applied TOPM voltage. **c**, Current voltage characterisation of a ring resonators TOPM. **d**, Optical transmission with varying applied TOPM voltage at $\lambda = 2.049$ μm. **e**, Plan view of the source and cascaded ring filter. The pump laser is coupled into the first VGC (input). After the source, using thermal tuning with a TOPM, the pump laser frequencies are transmitted from the through port and off the chip (1). The signal/idler frequencies are transmitted from the drop port to the input of next ring. This scheme is cascaded four times to implement the filter. Inset: magnified view of the ring resonator waveguides in blue, and the thermo-optic phase shifter in orange. **f**, Experimental setup for characterisation of the integrated ring filter. The supercontinuum laser (SuperK) is bandpass filtered (BPF), and linearly polarised (LP). Controlling polarisation with waveplates ($\lambda/2, \lambda/4$), the light is launched into the chip and is transmitted through the filter and monitored at outputs 1-4. A computer controls the ring TOPMs. Finally, the chip output is measured on the OSA. **g**, Optical transmission spectrum as measured at grating couplers 1,2,3,4 labelled on part **e**, at the through ports of the four ring resonators. A maximum of 15 dB extinction is observed between adjacent ring filters, implying but not demonstrating a maximum of 60 dB on-chip pump rejection.

half of the maximum voltage of the driver—allowed shifting of the ring's resonances in either direction. The chip output was then coupled to the second resonator through port (grating port labelled 2 on Fig. 3.9e). Controlling the power dissipated in the second ring aligned the resonance with the first ring (spectrum labelled 2 on Fig. 3.9g). This was then repeated for the third and fourth rings, aligning all the resonances. A plot of the transmission spectra through the four rings labelled 1-4 is shown in Fig. 3.9g, with the corresponding grating couplers that were monitored in Fig. 3.9e. This filtering strategy shows increasing off-resonance rejection of the supercontinuum laser by the cascaded rings, demonstrating the potential for using this to suppress the mode-locked pump laser in a photon-pair experiment.

We see a maximum of 15 dB of extinction is achieved between each stage of the cascaded filter, implying but not demnonstrating an upper limit of 60 dB of on-chip filtering. This on its own is insufficient to extinguish the pump laser (~ 0 dBm) down to the single photon level (~ −130 dBm). Combined with additional a single off-chip monochromator filter, would satisfy the single photon pump rejection requirements for observing single photons. Previous studies have shown that the noise floor of pump rejection in a single chip is around 70 dB[178,180]. This is predominantly due to the laser scattering and coupling into the silicon substrate, which cannot be removed with filtering structures confined to the plane of the silicon waveguide layer.

3.4.4 Nonlinear optics in a delay line

We now revisited the low loss delay lines from the generation 2 chip, described in Sec. 3.2, previously characterising the linear transmission. Now equipped with a filtered pulsed laser and an OSA, we were able to perform nonlinearity measurements on these devices.

Self-phase modulation is a good measure of the waveguide dispersive nonlinearity as the process is always phase-matched regardless of the waveguide dispersion. Furthermore, from visually inspecting an output pulse spectrum, it is quick to estimate the amount of nonlinear phase. This is approximately proportional to the number of lobes in the spectrum. In this measurement, we filter the pump laser with a single monochromator and vary the optical power with the bulk VOA. Controlling polarisation, pump is launched into the fundamental TE mode of the delay line via vertical grating couplers, and monitored at the output with the OSA—See Fig. 3.10c for the experimental diagram.

An approximate formula for the maximum nonlinear phase is given by[182]

$$\Phi_{\max} \approx \left(m - \frac{1}{2}\right)\pi, \qquad \text{for } m > 1 \tag{3.3}$$

where m is the number of peaks in the broadened spectrum. From inspecting the output and observing the maximum number of lobes, we found that around 3π of SPM from propagation in the 11.6 cm delay line, shown in Fig. 3.10a. While this confirmed the presence of the dispersive nonlinearity in the waveguide, it was an imprecise method for actually measuring it. It would only be in a later measurement—outlined in Sec. 4.2.2—we would accurately quantify the nonlinear refraction coefficient of silicon at $\lambda = 2.07$ µm.

Using the input-output power relationship, we observe nonlinear transmission of the laser. A plot of the normalised transmission against launched peak power is shown in Fig. 3.10b, giving further evidence for the residual TPA at this wavelength. Later in Sec. 4.2.2, we accurately measure the TPA coefficient in silicon waveguides.

(3.4)

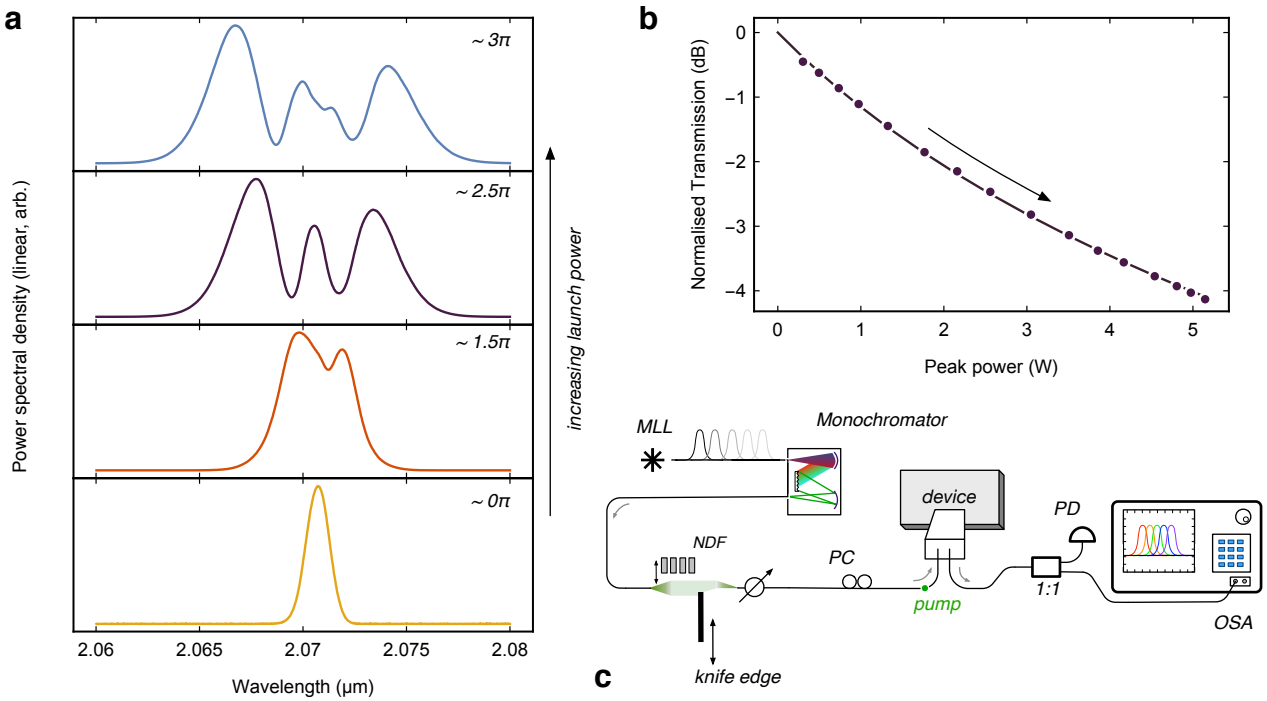

Figure 3.10: Nonlinear self-phase modulation and two photon absorption measurements in a 11.6 cm low loss delay line in the generation 2 chip. **a**, Spectral broadening with increasing power due to nonlinear SPM. **b**, Normalised transmission with varying peak power launched. The nonlinear transmission is due to residual two-photon absorption. **c**, Experimental setup for the optical nonlinearity measurement. A mode-locked laser (MLL) is filtered with a monochromator with the optical intensity controlled with a knife edge. The light is launched into the chip, and the output is monitored with a fibre beamsplitter (1:1), photodiode (PD) and OSA.

This section established stronger evidence for the large dispersive nonlinearity of silicon in the MIR, and generated a successful design for removing an appreciable fraction of the pump with an integrated ring filter.

3.5 Phase-matched mid-infrared optics: Generation 5

Until now progress had been made into developing the integrated optics infrastructure necessary for quantum optics in the MIR. However, the search for photon-pairs had been fruitless. From the start of the project, we were aware that the group velocity dispersion (GVD) in 220 nm SOI (See Fig. 3.11a) would be normal, leading to non-unity phase-matching efficiency.The Cornerstone foundry based in Southampton offered a 340 nm SOI platform. The 340 nm waveguides for CORN05, henceforth generation 5, were capable of producing a phase-matched waveguide. We show mode solved GVD and effective area plots of rectangular strip waveguides (with geometry from Fig. 3.11b) in Fig. 3.11d, indicating the possibility of $\beta_2 < 0$.

This was a big step out into the unknown as we had developed no passive devices for this technology platform before. We developed an entirely new set of waveguides sources, DCs, MMIs, vertical grating couplers (VGCs), TOPMs, and complex designs

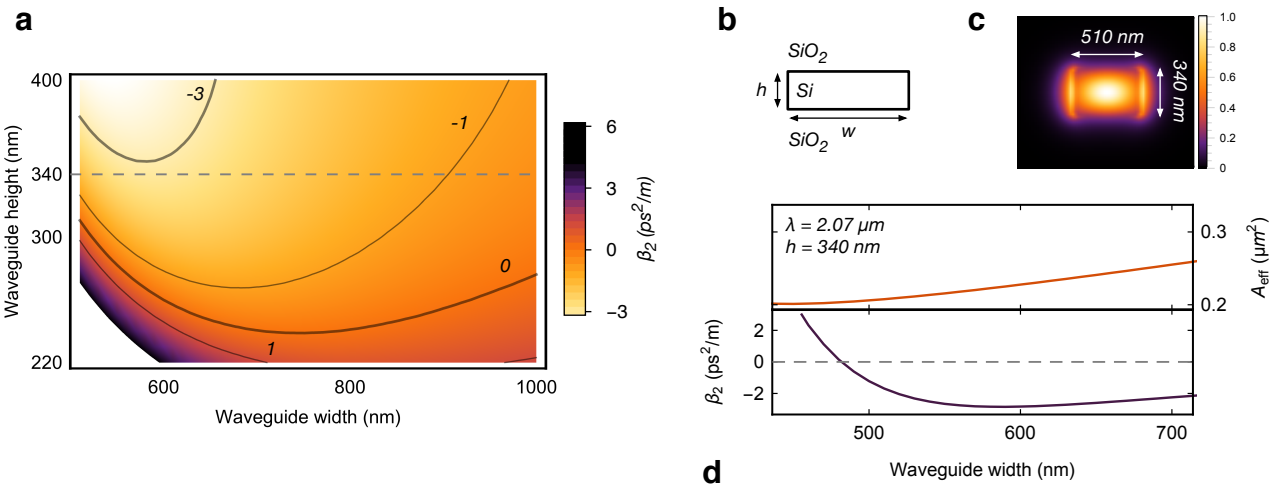

Figure 3.11: Generation 5 mode solving simulations. **a**, Waveguide group velocity dispersion (GVD) with varying width and height, simulated for a wavelength of 2.07 µm. **b**, Schematic for the mode solving simulations. **c**, Waveguide normalised electric field magnitude $|E|^2 = |E_x|^2 + |E_y|^2 + |E_z|^2$ of the selected single-mode waveguide. **d**, Group velocity dispersion and effective area varying the waveguide width for a fixed height of $h = 340$ nm. We see that for this waveguide height, anomalous GVD is possible.

combining these passive blocks into tuneable integrated circuits. In addition to creating a passive device ensemble, a set of low loss waveguide cutbacks, broadband dispersion measurement structures, Bragg filters, squeezing structures and quantum interference circuits were also designed. Armed with FDTD and mode solvers, the development of these devices would eventually lead to the first quantum interference in the MIR. The layout of the chip is shown in Fig. F.7 on page 166.

In the following sections we show a set of integrated optics in the new silicon platform, and a waveguide source design that is sufficiently phase-matched to observe stimulated FWM with (inefficient) single-photon detectors.

3.5.1 Passive components

We will now review some design, simulation and measurement of components that went onto the die. Cornerstone sent us five versions of this chip—electron beam lithography (EBL) and optical lithography (OL) fully passive, EBL with nickle chromium (NiCr) heaters and OL with NiCr and titanium nitride (TiN) heaters. The results presented in this section are from a fully passive OL device, fabricated with 248 nm deep-UV lithography, delivered in September 2018.

Waveguides

From the dispersion simulations as a function of rectangular waveguide width seen in Fig. 3.11d, two single-mode waveguide source designs were chosen with 490 and 510 nm widths both with $\beta_2 \leqslant 0$ to mitigate the possibility of fabrication variation in the designs (discussed further in Sec. 3.5.2). We show a mode-solved electric field intensity of the 510×340 nm^2 rectangular waveguide cross section in Fig. 3.11c. A cutback measurement

yielded a propagation loss of 3.19 ± 0.14 dB/cm, shown in Fig. 3.12g. Additional low-loss waveguide structures employing the same tapering between single- and multi-mode waveguides for delay lines (presented in Sec. 3.2) were included in this chip. Figure 3.12g also shows a multi-mode strip and rib low loss delay lines measurements, with propagation losses of 0.28 ± 0.03 and 0.38 ± 0.03 dB/cm, respectively. The uncertainty quoted for these three waveguide cutbacks measurements is the standard error from an ordinary least squares fit of the gradient assuming ± 0.2 dB error on each transmission measurement from the photodiode uncertainty.

Grating couplers

Using the technique described in appendix C.2 (page 134), we designed focusing uniform grating couplers. The performance of these devices outperformed expectations, and beat all previous transmission records from our VGCs from 220 nm SOI platforms. The design of these grating couplers utilised a two etch step, for an incident angle of 8 degrees. The uniform gratings are centred on 2.037, 2.052 and 2.091 μm (period 812, 822 and 833 nm, duty cycle 1/2, etch depth 140 nm, fan angle 30° and eccentricity 0.068) for the pump, signal and idler gratings, respectively (see appendix C.6 and Fig. C.6 for 2D FDTD design validation). Transmission spectra of our three designs, with target central wavelengths of $\lambda = 2.05$, 2.07 and 2.09 μm are shown in Fig. 3.12a.

In addition to these uniform gratings, we also collaborated with Xia Chen from the University of Southampton to design some apodised grating couplers. Typically uniform gratings cause exponential decay of the electric field at the desired wavelength. However the emission profile of the field is not well matched to the Gaussian mode of the single-mode fibre (SMF). In this type of design, the period and fill factor are varied as a function along the length of grating. Here, the grating strength is weak at the start, thereby improving the mode matching between the fibre and grating coupler. We used the linearly chirping approach[80,81] to implement the apodisation of the VGC, in a straight grating coupler with a 500 μm long adiabatic taper. We show the transmission spectrum of the measured device in Fig. 3.12b. This grating compared very similarly in performance to the uniform gratings. The linear chirping apodisation minimum feature size was close to the uniform grating pitch, leading to a very small change in the coupling efficiency. The central wavelength deviation, however, was more accurate than the uniform grating counterparts.

Edge couplers

The Cornerstone foundry offered cleaving of an optical facet on two edges of the chip. We designed and measured an expanded taper edge coupler design, since the exact position of the cleave was only known with a 0.5-mm uncertainty. We had to estimate the mode-field diameter (MFD) of a lensed fibre SMF-28 which is only specified by OZ Optics in the NIR frequency band. Using the specified MFD = 2.5 μm at $\lambda = 1.55$ μm, we estimate that the MFD scales approximately linearly with wavelength, therefore at $\lambda = 2.1$ μm, the MFD $\approx \frac{2.1}{1.55} \cdot 2.5 = 3.39$ μm. With this appraisal, we used the overlap integral between a Gaussian field with this MFD and the rectangular expanded taper to determine the optimal width. The simulation results are shown in Fig. 3.12b, with a peak mode overlap of 33% at 4.2 μm waveguide width. In retrospect de-risking the edge coupler design with many widths would have been sensible since the MFD was not exactly known—this was

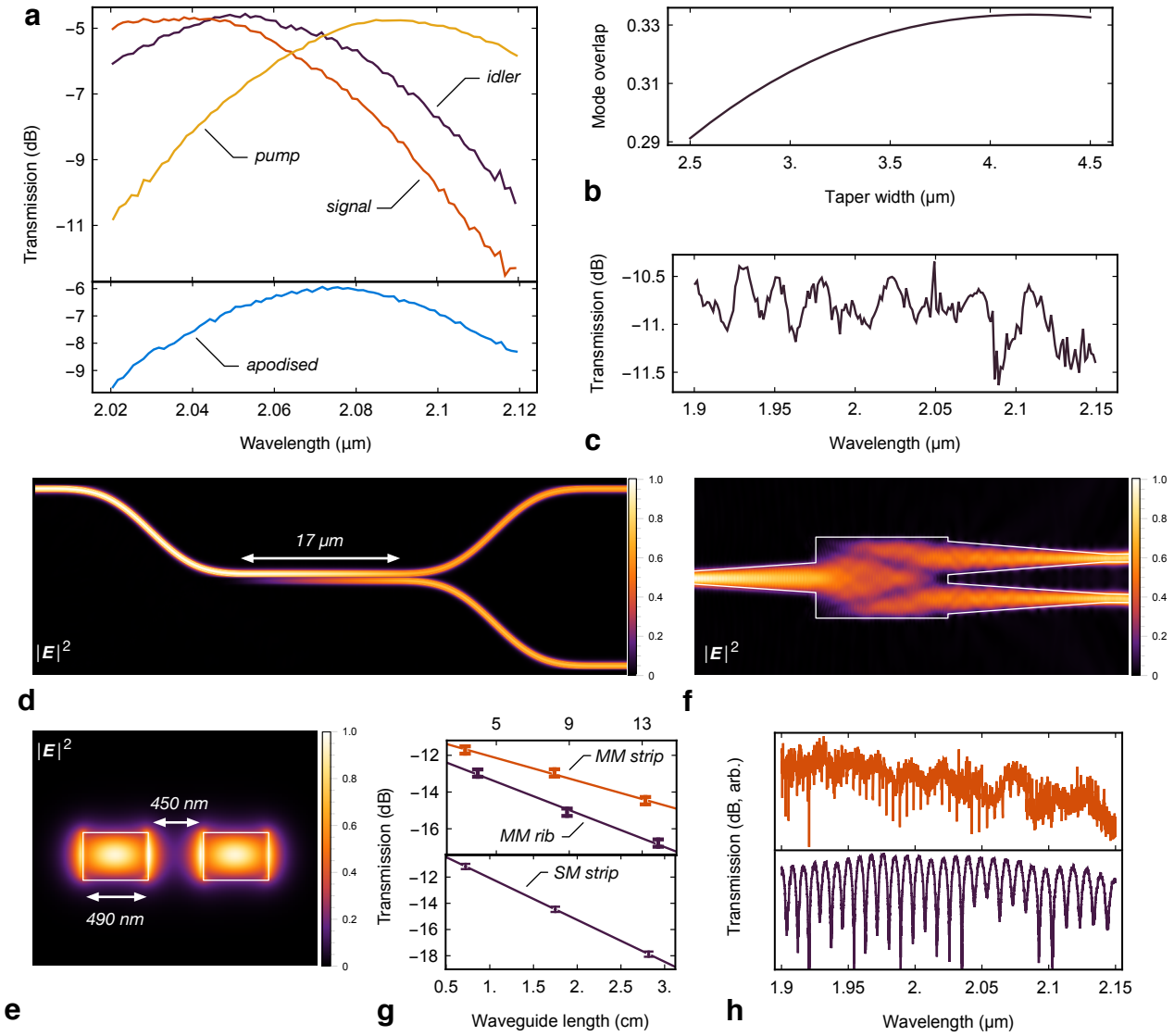

Figure 3.12: Generation 5 design and measurement summary. **a**, Transmission spectra of the pump, signal, idler and apodised grating coupler. **b**, Simulated mode overlap of expanded waveguide taper edge coupler with the lensed fibre, varying the waveguide width. **c**, Measured transmission spectra of a single expanded edge coupler. **d**, FDTD simulations of the normalised electric field magnitude $|E|^2 = |E_x|^2 + |E_y|^2 + |E_z|^2$ for the directional coupler. **e**, Mode solved cross section of the normalised electric field magnitude for directional couplers even supermode. **f**, FDTD simulations of the electric field intensity for the 1×2 MMI. **g**, Cutback measurements of the single-mode (SM) strip source waveguide, multi-mode (MM) strip waveguide and multi-mode rib waveguide. **h**, Broadband transmission spectra of the (top) edge coupled ring resonator and (bottom) asymmetric MZI, logarithmic scale.

implemented on the next chip design we submitted to Cornerstone. We measured the transmission spectra of these devices seen in Fig. 3.12c. The measured transmission is less than simulated—which is to be expected with fibre and polarisation misalignment. Furthermore, a rough estimate of the Fresnel reflection from the air to silicon interface gives approximately 3.4 dB loss per facet at normal incidence*.

Integrated beamsplitters

We designed the 1×2 MMI using a mode overlap calculation described in Sec. 1.4.5. First, the input waveguide taper fundamental TE mode is simulated, and the field overlap is calculated with each supported TE mode in the multimode region, to find the relative amplitudes of the modes excited in the MMI. The propagation through the structure is determined by the weighted superposition calculated from the simulated field excitation coefficients. Using this design method, we find that the optimal 1×2 MMI design has geometry: 17.4 μm length, 5 μm width, 2 μm taper width and 0.5 μm gap. The final design was then verified with 3D FDTD, with the electric field profile shown in Fig. 3.12f. Appendix C.6 on page 143 and Fig. C.7 gives extra details on the FDTD simulation method.

The directional coupler was simulated in two parts. The first step was to perform mode solving for the waveguide odd and even (Fig. 3.12e) supermodes refractive indices in order to compute the expected crossover length. Secondly, the effective coupling length from the Euler S-bending regions into the coupler were simulated with 3D FDTD. Finally, we subtract the effective coupling from the bends from the expected mode solved result, the final design was verified with 3D FDTD and is shown in Fig. 3.12d—see appendix C.6 on page 144 and Fig. C.8 for some more details on the FDTD design method. At $\lambda = 2.049$ μm, we experimentally measure the reflectivity to be $R = 0.49 \pm 0.02$. Here, the reflectivity value and uncertainty are evaluated from a sinusoidal fit and the associated standard error of a transfer matrix to an MZI fringe with a 1×2 MMI on the input. We assume that the input 1×2 MMI is balanced and the fringe visibility determines the coupler reflectivity.

The impact of wafer variation on these designs can be quantified by mode solving simulations. Directional couplers are almost lossless to within waveguide propagation loss, so the main parameter affected by thickness variation is the supermode crossover length of the DC (i.e. without subtraction of the bend coupling). This varies by $\Delta L_x = 4.6$ μm (or ~ 11% of the designed DC length) with a wafer thickness variation of 340 ± 20 nm. Due to the symmetry of the 1×2 MMI structure, the reflectivity is expected to be constant, with the loss of the device being modified from the self-images not aligning with the output tapers. From mode solving we estimate a negligible difference in the optimal MMI length of $\Delta L = 0.2$ μm (corresponding to a simulated 0.001 dB change in the loss) of the device from ±20 nm wafer thickness variations.

Group index structures

Using the edge couplers we designed, a range of broadband group index structures were measured—asymmetric Mach-Zehnder interferometers (AMZIs) and rings. Light from the supercontinuum source was coupled to the chip with the output measured on the

*calculated from $r_F \approx \frac{3.4-1}{3.4+1} = 0.54$

OSA. For both the AMZI and the ring resonator, the single-mode (SM) waveguide with dimensions 490×340 nm^2 was used. The AMZI had a path imbalance of $\Delta L = 100$ μm, and the ring had a cavity length $L = 182$ μm. Two transmission spectra measured over a bandwidth of 250-nm are presented in Fig 3.12h. We simulated the group index across the range of measured wavelengths. The measured FSR for the AMZI give values a mean value of $n_g = 4.42$ that is in good agreement with the simulated value of $n_g = 4.38$ at $\lambda = 2.07$ μm, shown in Fig. 3.12h (bottom). The ring data (Fig. 3.12h top) was too noisy to extract an accurate group index value.

Comparison of dies

We now give a brief comparison of the performance of several of the Cornerstone chips, identifying key metrics such as the propagation loss, grating loss and deviation of the grating coupler from the designed wavelength. All propagation loss measurements were performed with the QCL and photodiode, and the grating coupler wavelength deviation with the supercontinuum and OSA.

Lithography	TOPM	Received	η_{GC} (dB)	η_{WG} (dB/cm)	$\Delta\lambda_{GC}$ (nm)
EBL	×	06/18	12.6	5.51	100
EBL	✓	08/18	10.0	11.6	-
OL	×	10/18	3.52	2.97	10
OL	✓	02/19	4.31	3.19	15

Table 3.3: Comparison of performance for Cornerstone dies. The grating coupler loss η_{GC} is the peak transmission measured from all grating couplers, the propagation loss η_{WG} is from a single mode waveguide cutback measurement, and the central wavelength offset $\Delta\lambda$ is the largest measured offset from the target designs.

From inspecting table 3.3, we can immediately see that the devices fabricated with EBL are performing poorly. For the EBL devices, the loss and deviation of the central wavelength from the design meant that these chips were unlikely to produce correlated photon pairs. The OL devices on the other hand performed very well and ultimately led to our observation of FWM in the following sections.

3.5.2 Stimulated four-wave mixing

Measuring photons from stimulated FWM would be easier than SFWM, since the amplified photon counts are orders of magnitude brighter. With five monochromators, there would be sufficient off chip filtering with one filter on each input, and two on the single-photon channel.

Stimulated four-wave mixing is a process whereby two pump photons are scattered off of a virtual energy level to sidebands around the pump fields. The second laser acts as the stimulating field on one of the photons and leads to amplification in the outputs[119,183]. This technique is often used in nonlinear optical generation of bright new frequencies and measuring the joint spectral amplitude of a source[140].To broadly illustrate the effect of the stimulating seed we allude to its behaviour with the following analysis. The interaction Hamiltonian of the stimulated and spontaneous FWM process is proportional to

$$\hat{H} \propto \chi_0 \Theta \hat{a}_s^\dagger \hat{a}_i^\dagger \hat{a}_{p1} \hat{a}_{p2} + H.c., \tag{3.5}$$

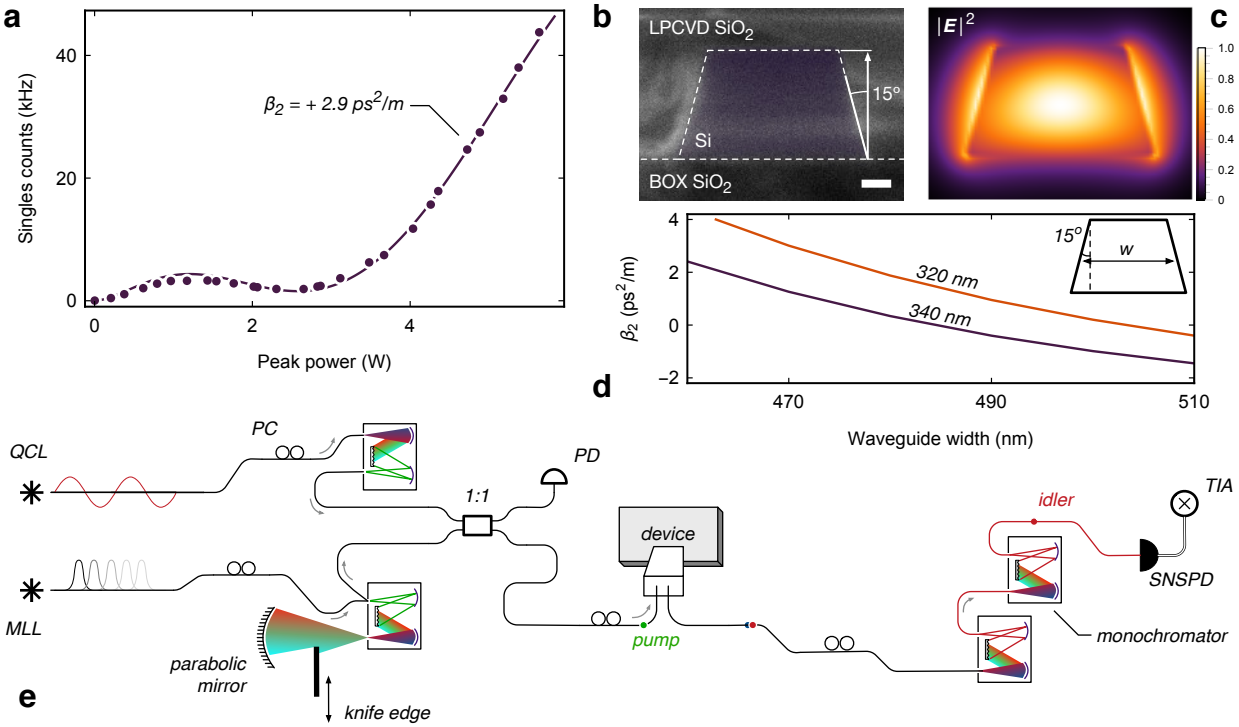

Figure 3.13: Stimulated four wave mixing with a silicon waveguide and understanding the phase mismatch. **a**, Singles counts varying the launched peak power, a nonlinear model fit to the data estimates that the GVD is normal with $\beta_2 = +2.9$ ps^2/m. **b**, Scanning electron microscope image of a reference waveguide structure in the cleave region of the chip. A side wall angle of 15° is measured. **c**, Normalised electric field magnitude $|E|^2 = |E_x|^2 + |E_y|^2 + |E_z|^2$ of a waveguide with the 15° angled walls, 340 nm height and 510 nm across the middle of the waveguide. **d**, Group velocity dispersion β_2, with a 15° sidewall angle for two fixed waveguide heights of 340 nm and 320 nm. **e**, Experimental layout for the stimulated four-wave mixing measurement. The mode-locked laser (MLL) and CW QCL lasers are filtered and combined on a beamsplitter (1:1). The pumps are launched into an 8.8-mm spiral with a designed width of 490 nm. Light is coupled off the chip and the pump is suppressed, finally detected with superconducting nanowire single-photon detectors (SNSPDs).

where χ_0 is an effective nonlinear coupling coefficient related to the gain by $g = i\chi_0\Theta t/\hbar$, here Θ is the phase-matching biphoton wavefunction. To simplify the maths, we make the undepleted pump approximation* where $\hat{a}|\alpha\rangle = \hat{a}^\dagger|\alpha\rangle = \alpha|\alpha\rangle$. Applying the four-wave mixing unitary operator to the input state with both pump and signal coherent states gives

$$\hat{U}|\alpha_p\alpha_p\alpha_s 0_i\rangle = \left(\mathbb{1} + g\hat{a}_s^\dagger\hat{a}_i^\dagger\hat{a}_{p1}\hat{a}_{p2} + \ldots\right)|\alpha_p\alpha_p\alpha_s 0_i\rangle \tag{3.6}$$

$$= |\alpha_p\alpha_p\alpha_s 0_i\rangle + g\alpha_p^2\alpha_s|\alpha_p\alpha_p\alpha_s 1_i\rangle + \ldots, \tag{3.7}$$

where we see that terms in the expansion now contain an additional coefficient α_s, proportional to amplitude of the stimulating coherent state, therefore amplifying the rate of idler photon production.

*This approximation is valid in low conversion efficiencies—in this section we are generating on average ~ 1.5 pairs per pulse at maximum power, but each pump laser pulse has order 10^5 photons.

In this experiment, we take the mode-locked laser as the pump field centred at λ = 2.071 μm and the QCL as the stimulating field on the signal frequency mode at λ = 2.049 μm. Both the pump and seed are filtered to remove sidebands that would drown out any photons produced from the waveguide source. The lasers are then combined on a beamsplitter and, controlling polarisation, launched into the fundamental TE mode of an 8.8-mm waveguide with a cross section of 490×340 nm^2, via vertical grating couplers. Light is then coupled back off-chip, and filtered with two back-to-back monochromators centred at an idler wavelength of 2.0915 μm. Finally, the idler photons are detected with a single superconducting detector and the counts registered on a time interval analyser (TIA). The experimental diagram for this measurements is shown in Fig. 3.13e (see Fig. F.11c for magnified view of structure).

We show the results of the singles counts against the launched peak power in Fig. 3.13a. We see that in the low power regime, there is an oscillation of increasing counts which then has a null again at around 3 W. This behaviour is a signature of a phase-matching function with normal dispersion, leading to a sinc-like behaviour in the singles counts versus power. Using a nonlinear fitting procedure of the formula

$$C = \mathcal{L} f P + f \Delta t \Delta \nu_c \sum_{n=1}^{\infty} \Xi_n^{\text{thermal}} (1 - (1 - \eta)^n), \tag{3.8}$$

where $\mathcal{L}$ is a linear noise term, f is the repetition rate of the laser, P is the power, Ξ_p^{thermal} is the power dependent probability of producing a photon pair with the thermal distribution (Eqn. (1.82)). Here, the squeeze parameter includes phase matching and linear loss (See. table 1.1), and η is the compound transmission including detection efficiency. From the nonlinear model fitting of Eqn. (3.8), we estimated that the GVD was normal with a value of $\beta_2 = +2.9$ ps^2/m.

However, the waveguide was designed with mode solving for $\beta_2 \approx 0$. In an attempt to better understand the origin of this discrepancy, we measured a scanning electron microscope image of a waveguide that extended into the cleaved region of the die—shown in Fig. 3.13b. It was immediately clear that the waveguide walls had a far steeper angle than the originally simulated vertical sidewalls. In absence of this information from the foundry a rectangular geometry was used for our modelling. We also found that the foundry SOI silicon film specified the uncertainty ±20 nm. We resimulated the mode-solved cross section with these details (see Figs. 3.13c and 3.13d). The simulated dispersion of the device with reduced film thickness of 320 nm shows that with waveguide widths in the neighbourhood of 490 nm, the dispersion is normal. This gives evidence to support the observed oscillations in the singles counts from the waveguide source due the normal GVD induced phase-mismatch.

This was our first measurement which unambiguously demonstrated MIR frequency conversion using stimulated FWM in silicon. This result, combined with the new filtering strategy for the pump (outlined in Sec. 2.4.3) meant we had all of the tools at our disposal to produce correlated photon-pairs with SFWM.

3.5.3 Attempts to measure spontaneous four-wave mixing

We now attempted to measure SFWM, using a similar experimental setup to the previous section. Initially, we chose an output wavelength of $\lambda = 2.091$ μm since we had observed the stimulated FWM fluorescence there. Despite having measured stimulated counts at

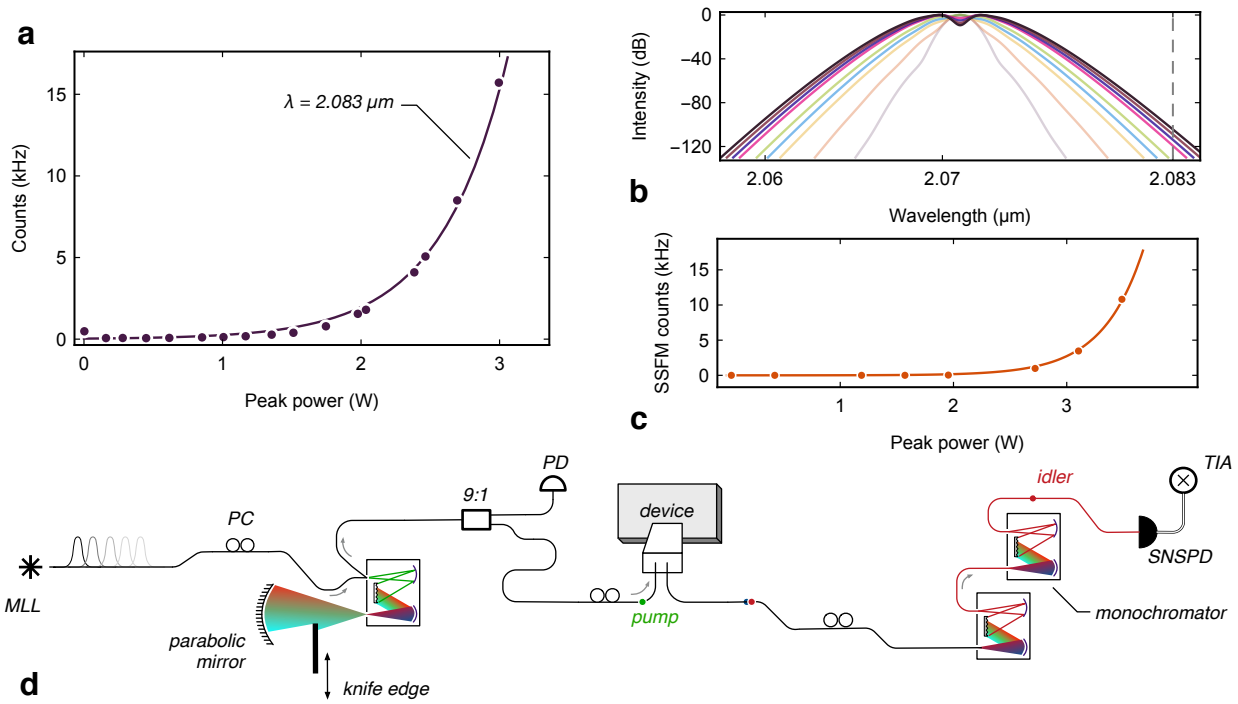

Figure 3.14: Attempting to measure SFWM, and verifying the false result with SSFM. **a**, Singles counts measured through an 8.8-mm spiral, with varying peak power. The nonlinear response with power indicates photons generated from the chip, however this false positive signature is actually leaked, broadened pump laser. **b**, Split-step Fourier method (SSFM) modelling of the laser pulse broadening in the test waveguide structure due to self-phase modulation. The grey dashed indicates the measurement wavelength. **c**, Estimated counts that would be measured by SNSPDs, from SSFM modelling the pulse power at a frequency of 2.083 μm (grey dashed line in b). **d**, Experimental setup used in the attempt to measure SFWM from the 8.8-mm generation 5 waveguide.

a pump-idler detuning of 21 nm, no SFWM singles counts were seen varying the input power. Our previous stimulated measurements indicated that the dispersion was normal, so we attempted to reduce the pump-signal detuning. In doing so, we observed what seemed to be an apparent signature of SFWM, which is shown in Fig. 3.14a.

At first, we were convinced that this was indeed SFWM, since the signature completely disappeared when the nonlinear waveguide replaced with an attenuator with the same loss. However, the fit of the singles counts implied anomalous GVD, given the exponential number of counts with launched power, contradicting our previous stimulated FWM results. Further investigations revealed rapid decay of the singles count rates with increasing pump-idler detuning. This opposed the previous outcome that the phase-matching was sufficient to observe stimulated FWM at larger frequency detunings.

Eventually, we concluded that the exponential increase in singles counts with increasing launched power was not a signature of SFWM. Recall that singles counts from leaked pump laser typically should be linear with the pump power. We verified that this analysis was (unfortunately) not always correct.

As the power of the pump laser was increased, nonlinear broadening of the pump pulse into the monochromator passband was responsible for the singles counts exponen-

tial behaviour. To confirm this, we ran SSFM simulations and found wavelengths close to the pump, had a similar exponential singles counts profile with increasing power—shown in Figs. 3.14b and 3.14c. This result was the last in a series of experimental frustrations. The measurement of MIR single photons produced from our waveguide sources remained elusive, for now.

3.6 Summary and conclusions

The search for photon-pairs from a waveguide chip in the MIR was a long endurance test, consuming nearly two years of my PhD, yielding no 'smoking gun' of correlated photon-pairs. In doing so the infrastructure for an entire lab had been setup along with an extensive set of passive integrated components for developing larger, and more complex integrated waveguide circuits. Several avenues for producing photon-pairs had been explored on different SOI platforms. Towards the end of this saga, a key milestone of producing stimulated four-wave mixing was achieved. This demonstrated that, in principle, the waveguide source designed for the 340 nm SOI would, with more efficient detectors, be suitable for observing quantum correlated photons. As it happened, within a month of achieving the stimulated FWM result the first experimental signature of SFWM was observed. The next chapter is concerned with illuminating this.

Statement of work

The generation 1 and 2 integrated optics were designed by Dr. Joshua Silverstone and fabricated by IME. I performed all the measurement and data analysis of these devices. The generation 3 chip was designed by Prof. Bart Kuyken at the Ghent photonics research group at IMEC. I performed all measurements and data analysis of these results. The Python code used to implement the split-step Fourier method was based off of Matlab code from Dr. Nobuyuki Matsuda at NTT. The generation 4 chip layout and integrated optics design was done by myself and fabricated by IME. All measurements and data analysis of the generation 4 chip were performed by me. The generation 5 uniform chip grating coupler, edge couplers, directional couplers, source, and circuit layout was designed by me and fabricated by Cornerstone. Dr. Joshua Silverstone also contributed to the layout, designed the 1×2 MMI, and the TOPMs length from the sheet resistance data, and I verified the MMI design with FDTD simulation. Dr. Xia Chen designed the apodised grating coupler parameters in the generation 5 device with analysis of FDTD simulations that I performed. All measurements and data analysis of the generation 5 devices were performed by myself. Dominic Sulway took the scanning electron microscope (SEM) image of the waveguide and also assisted with the stimulated four-wave mixing experiment.

Chapter 4

Quantum correlated photons in the mid-infrared

Quantum correlated photon-pairs are essential for any quantum optics platform, providing the primitive resource for performing experiments. Without access to ultra-high performance off-the-shelf instrumentation, satisfying the stringent criterion for generating, filtering and efficiently detecting single-photons is remarkably difficult. Exquisitely precise control is necessary for producing photon-pairs, and then differentiating them from the 10^{16} photons in the pump pulse that generated them!

To create these phenomenally delicate quantum states, the parametric source must be phase-matched and possess a substantial nonlinearity. Photon-pair rates also benefit from small nonlinear absorption. Finally, high efficiency detectors are needed to facilitate the measurement.

The first observation of quantum correlated photons produced from a silicon chip, where all four fields have wavelengths beyond 2 μm, forms the basis of this chapter. In addition to this, classical nonlinear optical characterisation of our source determined broadband stimulated four-wave mixing, the effective waveguide nonlinearity and the waveguided two-photon absorption coefficients. Finally, we benchmark the detector efficiency of mid-infrared (MIR) optimised superconducting nanowire detectors. These were instrumental to achieving vastly improved photon-pair coincidence rates.

The results in this chapter were presented in the Bristol Quantum Information Technologies Workshop 2019, and the 2019 Conference on Lasers and Electro-Optics Europe and European Quantum Electronics Conference (CLEO Europe). These generated published peer reviewed conference papers [184,185] and formed a significant part of the article of Ref. 186.

4.1 Introduction

Moving away from the industry standards at 1.55 μm is not an easy task as the basic underpinning infrastructure must all be redeveloped. While the performance of instrumentation at 1.55 μm is excellent, the viability of large scale quantum optics in crys-

talline silicon is fundamentally limited by the reduced heralding efficiency from cross two-photon absorption (XTPA). The MIR presents an opportunity to quench this nonlinear absorption, and unlock the full potential of silicon quantum photonics. We will go on to show that our MIR waveguide source produces a peak coincidence count rate of 896 Hz and a peak coincidence to accidental ratio (CAR) of 25.7. For context, this result is still much less the state-of-the-art silicon photon pair sources in a ring resonator which have shown a peak CAR of 12000 and a peak of 4.9 kHz measured coincidence count rates[142]. However, since to the best of our knowledge this is the first mid-infrared silicon photon-pair source, like-for-like comparisons at this wavelength band are difficult. However, a comparison with bulk crystal spontaneous parametric down-conversion (SPDC) implementations is possible. Coincidences measured at MIR wavelengths beyond 2 μm in bulk had a peak CAR of 15.7 with a corresponding rate of 105 Hz[131], in contrast we measured a rate of 4.4 Hz at our peak CAR.

In early January 2019 we awaited the arrival of MIR optimised superconducting nanowire single-photon detectors (SNSPDs), and the final batch of the Cornerstone (CORN) chips presented in the previous chapter (see Sec. 3.5). These were fabricated with optical lithography and with heaters for thermo-optic phase modulators (TOPMs). This 340 nm waveguide platform had the capability for waveguide designs that are phase-matched for the fundamental transverse electric (TE) mode. The realisation of this source design led to a signature of stimulated four-wave mixing (FWM) in Sec. 3.5.2. As the CLEO Europe submission deadline grew closer, an attempt to observe correlated photons with the low efficiency detectors with an overnight time correlation histogram measurement.

Upon arrival to the lab the following morning an irrefutable experimental signature had been acquired. The rates were extremely low, in the millihertz regime, but with several loss budget optimisations, this was increased to a maximum rate of 1 Hz. This work formed the basis of an accepted poster to CLEO Europe. In February 2019 the arrival of the generation 5 chip with heaters yielded orders of magnitude improvement in the phase-matching. The truly phase-matched waveguide enabled our coincidence count rates to reach near kHz rates, and allowed for stimulated FWM to have sufficient optical power to be measured on the optical spectrum analyser (OSA).

The final addition of a tuneable continuous wave (CW) laser completed our arsenal of experimental tools. The Sacher Lion enabled a broadband measurement of the stimulated FWM[187]. This laser has a tuning range over 1.98-2.09 μm, with a maximum output power of around 4 mW, and sideband suppression of around 55 dB.

4.2 Classical nonlinear optics

4.2.1 Stimulated four-wave mixing

To measure stimulated FWM, the pulsed mode-locked laser and the tuneable CW seed lasers are combined on a fibre beamsplitter before the chip. Both lasers are then launched into a 7.2-mm waveguide with a cross section of 510×340 nm^2 and sidewall angle of 15°. The wavelength of the tuneable laser is swept on one side ($\lambda \leq 2.071$ μm) of the pulsed pump, producing amplified FWM at longer wavelengths ($\lambda \geq 2.071$ μm) that is classically measurable on the OSA—for an experimental scheme see Fig. 4.1e. In this measurement, verified the broadband phase-matching of the device, showing stimulated emission from the waveguide over a bandwidth greater than 60 nm (Fig. 4.1b). In fact the device is

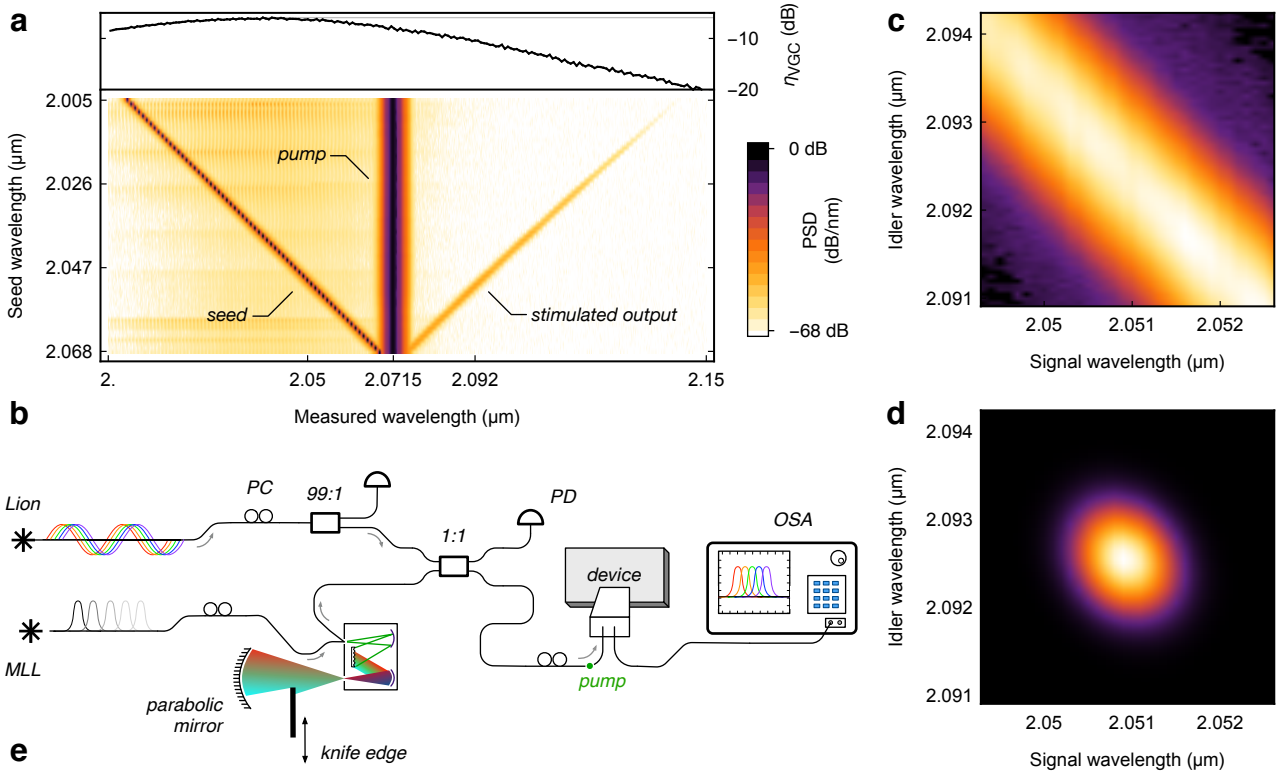

Figure 4.1: Bright stimulated four-wave mixing measurement. **a**, Single grating coupler transmission (η_{VGC}) spectra of the waveguide source. **b**, Measured normalised power spectral density (PSD) of broadband stimulated four-wave mixing. A stimulating seed laser (CW, tuneable, $\lambda \leq 2.071$ μm) is swept on one side of the pulsed pump at 2.071 μm, while spectra are collected from an optical spectrum analyser, showing the stimulated output on the other side ($\lambda \geq 2.071$ μm). **c**, Unfiltered joint spectral intensity (JSI) of the waveguide source using stimulated emission tomography. Lighter colours correspond to higher probability density. **d**, Approximate analysis for the JSI of the biphoton wavefunction by post-processing the stimulated emission profile with the monochromators filter shape. The stimulated four-wave mixing data acquired in part c is superimposed with the measured transmission spectra of the filters, estimating the expected JSI. Lighter colours correspond to higher probability density. **e**, Experimental configuration used to measure stimulated four-wave mixing. A tuneable CW laser (Lion) and pulsed mode-locked laser (MLL) are combined on a beamsplitter (1:1) and with input monitoring optical taps (99:1). The lasers pump a 7.2-mm waveguide with 510×340 nm^2 cross section, and the chip output measured on an optical spectrum analyser (OSA).

expected to be phase-matched at larger pump detunings; the decay of the stimulated FWM is predominantly due to the finite grating coupler bandwidth, shown in Fig. 4.1a.

We attempted to measure the joint spectral intensity (JSI) of the waveguide source using stimulated emission tomography [140,188]. This measurement places the single-photon spectral filters before the chip and sweeping the stimulating laser across them, to characterise the intensity and correlations between the signal and idler photons. The extra loss induced by the free space monochromator filters made the seed too low power to observe stimulated FWM at the output of the waveguide source. Instead, an approximate analysis of the expected JSI was performed. The wavelength dependent transmission functions of the monochromators were characterised with the supercontinuum source, and fit with a Gaussian function. The stimulated output measurement taken in Figs. 4.1b

and 4.1c, were then post-processed with the two fitted transmission functions of the filters. The results of this analysis are shown in Fig. 4.1d and gives an approximate analysis of the source JSI.

4.2.2 Nonlinear absorption

To measure the two-photon absorption (TPA), we look at the nonlinear transmission with varying power from the knife edge attenuator. For the experimental scheme, see Fig. 4.2d. In this measurement we simultaneously acquire the data for the estimation of the nonlinear refraction presented in Sec. 4.2.3. The picosecond pulsed mode-locked laser is filtered with a single monochromator giving a pulse width full width at half maximum (FWHM) of $\Delta\tau = 4.82$ ps—the reason for this is to increase the total amount of optical power coupled to the chip. The filtering requirements are less stringent than in the single-photon measurement regime, where any leaked pump will drown out spontaneous four-wave mixing (SFWM) fluorescence. Before the chip the optical power of the pump laser is measured with a 9:1 optical tap and a photodiode. The light is then coupled into the 17.5-mm source waveguide (510×340 nm^2 cross-sectional area and 15° sidewall angle) via grating couplers. After propagation, the light is coupled back off-chip and measured on the OSA. To extract the normalised transmission of the device, we perform numerical integration on the optical spectra at the output of the chip to estimate the total transmitted power.

As the power of the pump is increased, we see a decrease in the normalised transmission (Fig. 4.2b). While TPA is significantly reduced at $\lambda = 2.07$ μm, there is still sufficient energy for two photons to promote an electron across the band gap. In fact the cutoff wavelength at room temperature indicates that wavelengths greater than 2.25 μm are necessary to entirely eliminate TPA. Due to practical limitations at the start of the project, we were only able to acquire a 2.07 μm mode-locked laser, and therefore were unable to completely benefit from completely extinguishing the TPA. We see that, as expected, the nonlinear transmission grows with optical intensity indicating that residual TPA is occurring in the waveguide. To estimate the waveguide TPA coefficient we follow the fitting procedures described in Refs. 121,189. We start with the expression for the power as a function of propagation distance[121]

$$\frac{\partial P}{\partial z} = -\alpha P(z,t) - \alpha_{\mathrm{TPA}} P(z,t)^2 - \sigma_{\mathrm{FCA}} \bar{N}_c(z,t) P(z,t), \tag{4.1}$$

where P is the power, integrated over the entire mode cross-section, α is the linear losses, σ_{FCA} is the is the total free carrier cross section, $\bar{N}_c$ is the total carrier density averaged over the mode cross-section. Since the carrier concentration varies as the laser pulse generates free carriers from TPA, the rate equation is given by[121]

$$\frac{\partial \bar{N}_c(z,t)}{\partial t} = \frac{\bar{\beta}_{\mathrm{TPA}}}{2\hbar\omega} P(z,t)^2 - \frac{\bar{N}_c(z,t)}{\tau_c}, \tag{4.2}$$

where $\bar{\beta}_{\mathrm{TPA}}$ is now also weighted to the mode distribution, and $\tau_c \sim 1.9$ ns is the free carrier lifetime[190–192]. Values of the carrier lifetime have been shown to vary in the literature[151,193]. However, the lifetime here is not too sensitive for our case since we are operating in the regime where the pulse duration is much shorter than the lifetime i.e. 5 ps $\ll \tau_c$. Therefore the majority of the carriers generated by TPA will not have relaxed to the valence band within the pulse duration, and residual free carrier absorption (FCA)

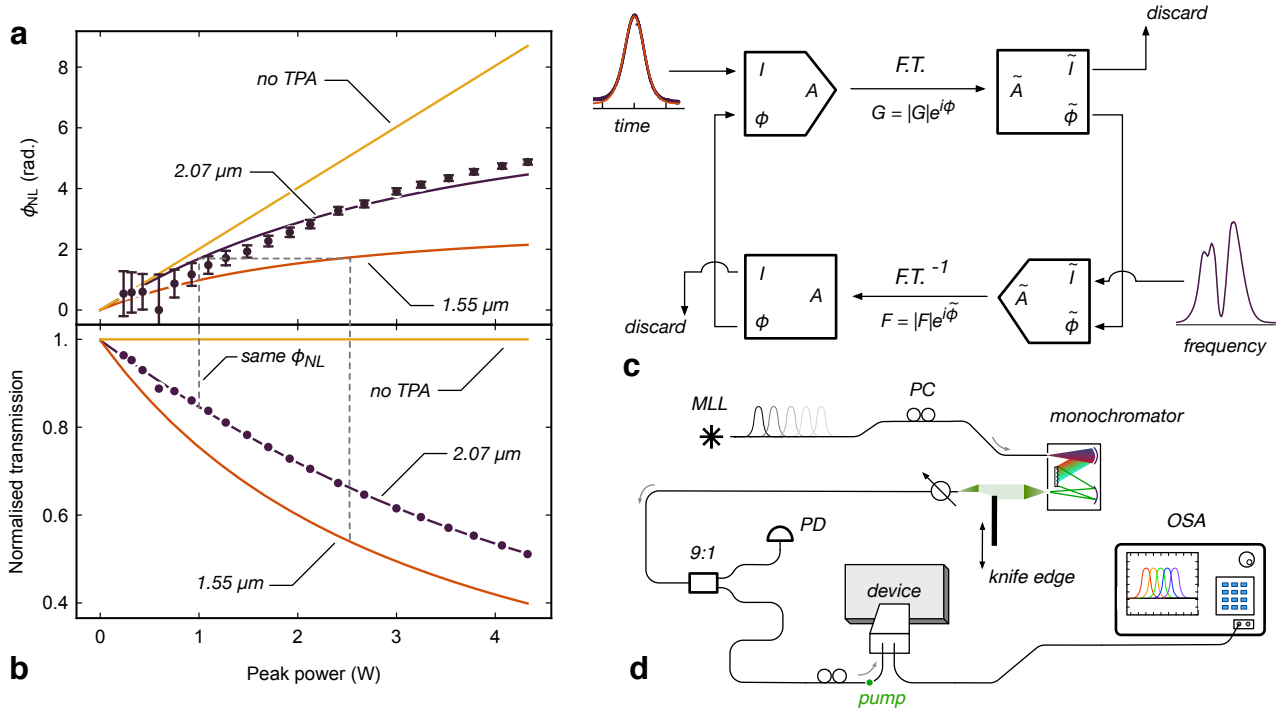

Figure 4.2: Waveguide nonlinear parameter characterisation. The grey dashed line shows line of equivalent nonlinear phase ϕ_{NL} highlighting the benefits of our approach. **a**, Nonlinear phase from the waveguide source, with varying launched peak pump power. The phase is retrieved using the Gerchberg-Saxton algorithm shown in part c. A model for the NIR and completely TPA free is also included for reference. **b**, Normalised transmission with increasing launched pump power, showing the presence of residual TPA. For comparison, a model for completely TPA free and the NIR is included. **c**, Block diagram outlining the Gerchberg-Saxton phase retrieval algorithm. The input pulse in the time domain undergoes the Fourier transform operation (F.T.) and the intensity is discarded. The intensity is then replaced with the envelope measured in the frequency domain, and is inverse Fourier transformed (F.T.$^{-1}$). Replacing the intensity information with the time domain envelope completes one iteration of the algorithm. **d**, Experimental layout for the measurement of nonlinear phase and transmission. The mode-locked laser (MLL) is filtered and the optical power monitored with a tap (9:1). Light is launched into the device and the output monitored on the OSA.

from carriers generated from the previous pulse will be negligible since the repetition period of the laser (25 ns) is much greater than the carrier lifetime. Since Eqn. (4.1) has a free carrier concentration that also depends on intensity, an analytical solution is difficult to obtain. Thus to estimate the carrier concentration, we generate a grid of points for different intensities, TPA coefficients and free carrier densities using the nonlinear Schrödinger equation (NLSE)[121,138]. Assuming that the function is smooth, we then apply an interpolation function between our discretised grid of numerically calculated points. We use this to extract the fit values of the coefficients from the transmission data. In the model, we take in the predetermined propagation loss from the cutback measurement, the autocorrelation pulse duration, and allow the TPA and FCA to be free fit parameters. We determine that our fitted parameters to be $\alpha_{\mathrm{TPA}} = 24.4 \pm 3.1\,\mathrm{W^{-1}m^{-1}}$, $\sigma_{\mathrm{FCA}} = 4.31 \times 10^{-21}\mathrm{m^2}$, and we use the dimensionless parameter $\mu = 7.5$ from Ref. 138, which governs the impact of free carrier dispersion (FCD). We estimate the effective modal area using mode solving

calculations, computing it using the formula[67]

$$A_{\text{eff}} = A_{\text{NL}} \iint_{-\infty}^{\infty} S_z dx dy \Big/ \iint_{\text{NL}} S_z dx dy, \tag{4.3}$$

where A_{NL} is the cross sectional area of the nonlinear region, $S_z = (\mathbf{E} \times \mathbf{H}) \cdot \hat{z}$ is the time-averaged Poynting vector z-component in the waveguide propagation direction. Using this model for the effective area we find $A_{\text{eff}} = 0.228\ \mu\text{m}^2$ and compute the bulk TPA coefficient to be $\beta_{\text{TPA}} = 0.557 \pm 0.07\ \text{cm} \cdot \text{GW}^{-1}$, which are consistent within experimental error of measurements from the literature in bulk silicon[160] of $0.3 \pm 0.4\ \text{cm} \cdot \text{GW}^{-1}$ at $\lambda = 2.05\ \mu\text{m}$. We plot our measured value with the literature values of β_{TPA} in Fig. 4.3.

A comparison between a TPA-free model and for the near infrared (NIR) at $\lambda = 1.55\ \mu\text{m}$ is given in Fig. 4.2b, where we assume a typical single-mode (SM) waveguide cross sectional area of $500 \times 220\ \text{nm}^2$ and the FCA and FCD parameters taken from Ref. 138, and the room temperature TPA values are taken from Ref. 121.

4.2.3 Nonlinear refraction

To estimate the nonlinear refraction n_2, and waveguide nonlinearity coefficient γ, we configure our experiment as shown in Fig. 4.2d. The data is collected synchronously with the nonlinear transmission measurement described previously. Here, we now analyse the spectral broadening from self-phase modulation (SPM) to estimate the nonlinear phase from the waveguide. We start by recording the input pulse autocorrelation to estimate the pulse duration in the time domain, where we assume a hyperbolic secant envelope. Varying the incident optical power into the waveguide, the broadened pulses in the frequency domain are then measured on the OSA.

The optical phase of the pulses are estimated with the Gerchberg-Saxton phase retrieval algorithm[121,194]—we show a simplified block diagram of the algorithm in Fig. 4.2c. We measure the amplitude of the pulse in the time domain with an intensity autocorrelation, and in the frequency domain with the optical spectrum analyser. In the first step, we start with a hyperbolic secant phase ansatz* with the same profile as the time domain intensity autocorrelation. From this point on at each step in the algorithm we take the Fourier transform (F.T.), retaining the estimated phase profile while replacing the intensity information with the measured values. Finally, the inverse Fourier transform is taken (F.T.$^{-1}$), discarding the intensity and again retaining the phase thus completing one iteration of the algorithm. The algorithm is iterated until the convergence on a steady state solution and then terminated. The phase profile across the pulse is the final output.

The phase profile is then fit with a model[121]

$$\phi(L,t) = \gamma \int_0^L P(z,t) dz - \frac{\sigma_{\text{FCA}} \mu}{2} \int_0^L \bar{N}_c(z,t) dz, \tag{4.4}$$

where P is the power, $\bar{N}_c$ is the free carrier density averaged across the waveguide mode cross section and μ is governs the impact of FCD[138]. The phase integrals are numerically evaluated for each launched pump power inputting the TPA and FCA values from the transmission measurement in Sec. 4.2.2. The waveguide nonlinearity γ is the free parameter that we extract from the reconstructed phase profiles. We show the results from

*As long as we start with a smooth pulse-like shape, the algorithm should converge; the final reconstructed phase is not too sensitive to the initial guess.

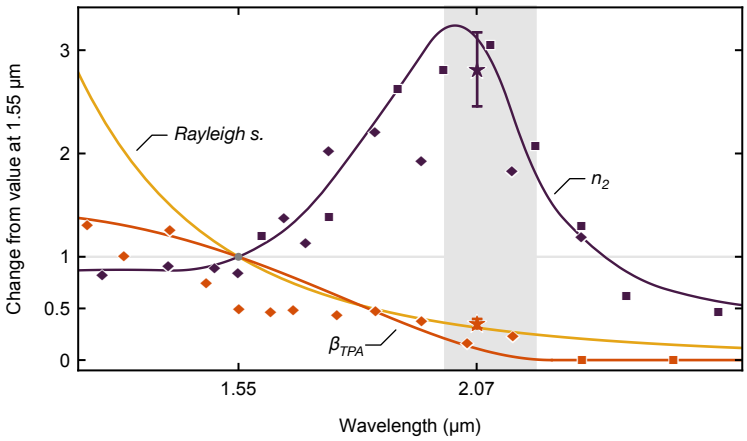

Figure 4.3: Dispersion of key optical phenomena in silicon, normalised to the NIR values at 1.55 μm. The intensity-dependent refractive index (n_2), bulk two-photon absorption coefficient (β_{TPA}) and the Rayleigh scattering efficiency are shown. The diamonds and squares are measured using bulk Z-scan techniques from Refs. 160,161, respectively. Our waveguided measurement values are shown as stars. The line for n_2 is a spline to guide the eye, and for β_{TPA} a model for two-photon absorption[162].

the retrieved nonlinear phase versus launched waveguide peak power in Fig. 4.2b. We determine the average γ for each power, weighting the average to spectra with greater broadening since the retrieved phase signal is stronger in these data sets. We find that the waveguide nonlinear coefficient is $\gamma = 203 \pm 26\ \mathrm{W^{-1}m^{-1}}$. To extract the bulk TPA coefficient, we again use the effective area from mode solving, integrating over the nonlinear region from Eqn. (4.3). We find $n_2 = 15.3 \pm 1.8 \times 10^{-18}\ \mathrm{m^2W^{-1}}$, which is in within experimental error for values from the literature[160,161]. We plot our measured and literature values of n_2 in Fig. 4.3. In Fig. 4.2a for comparison, we also include models of the TPA-free and NIR values of the nonlinear phase versus power. Here, we assume the room temperature value of n_2 and $\alpha_{\mathrm{TPA}} = 48.5\ \mathrm{W^{-1}m^{-1}}$ are from Ref. 121, computing $\gamma = 134\ \mathrm{W^{-1}m^{-1}}$ from a typical NIR waveguide with dimensions $500 \times 220\ \mathrm{nm^2}$. We plot our measured value of n_2 with the literature values in Fig. 4.3.

From our measurements of n_2 and β_{TPA} in the previous two subsections, we now plot these data points at 2.07 μm along with the literature values of silicon's nonlinearities in Fig. 4.3. We see that the waveguided values are broadly consistent with the measured values in bulk. The error bars of the TPA coefficient were calculated using a Monte-Carlo analysis with 10^4 samples and a normal probability distribution. The assumed uncertainties are 0.2 dB for the 90:10 input tap, 0.5 dB on the input chip coupling, and 5% of the measured pulse duration. For the nonlinear refraction, the errors are calculated so that the mean error is equal to the statistical spread of the data, and the relative uncertainty of each point is proportional to the amount of spectral broadening. A notable source of uncertainty here is due to the large aperture size (0.5 nm bandwidth) in measurement of the spectra with the OSA.

4.3 Detector characterisation

We had now confirmed the significant waveguide nonlinearity and reduced TPA of our source, that was also phase-matched—verified by stimulated FWM measurements. The final piece of the puzzle for generating photon-pairs was to show efficient single-photon detectors.

Prior to receiving the detectors, we installed three SM2000 MIR fibres, each approximately 30 m in length* to the detectors. The previous link with NIR (SMF-28) fibre, induced up to 10 dB loss per channel. The new fibre infrastructure reduced this number to around 1.9 dB, increasing our coincidence count rates by around 200 times.

In February 2019 we acquired two superconducting detectors optimised for operation in the MIR, which were designed by Dr. Vikas Anant from PhotonSpot. These two nanowire detectors were different—detectors A and B are non-latching and latching designs, respectively. The nanowires were adapted from a batch of NIR nanowires. The key optimisation was that the dielectric cavity surrounding the detector, increased absorption into the nanowire at $\lambda = 2.1$ μm. Furthermore, the nanowires were packaged with MIR fibre, to improve transmission from the cryostat input fibre to the 780 mK stage. The SNSPDs were fabricated from 4-nm thick niobium nitride film, deposited using magnetron sputtering and patterned using electron beam lithography (EBL) into a superconducting 100-nm wide meander.

These detectors were designed and fabricated by Vikas, but he did not have the tools to characterise their efficiency around the target wavelength. The next step was to perform a detailed characterisation of the performance, enabling us to back out the pair-generation rates.

4.3.1 Efficiency and dark counts

The efficiency measurements performed were similar to the method presented in Sec. 2.5.1. However, with the acquisition of a tuneable CW laser, we could spectrally characterise the efficiency. Prior to starting the measurement, the output electrical traces from the two detectors A and B† were recorded varying the detector bias current. A typical amplified trace, as measured on the oscilloscope, is presented in Fig. 4.4d. The peak voltage of the amplified electrical output varies roughly linearly with applied bias, we fit a straight line model to the maximum pulse heights—shown in Fig. 4.4e—corresponding to 7.46 and 10.84 $\mathrm{mV\mu A^{-1}}$ for detectors A and B, respectively. We use this linear fit model with a constant offset to adaptively set the discrimination voltage for each bias setting.

Following this one time calibration, the bright light of the tuneable CW laser is recorded on a Thorlabs InGaAs photodiode (S148C), using the bulk knife edge attenuator for each wavelength in the sweep. The transmission of four neutral density filters (NDFs) (Thorlabs NENIR30B) in the bulk variable optical attenuator (VOA) was then recorded 10 times at each wavelength point to obtain random error statistics of the attenuated laser power in the measurement‡. Inserting all four NDFs into the beam path reduces the photon flux

*Our lab was in a side room of a larger lab, so we had to route 30m of SM2000 fibre to optically interface our experiment to the cryostat with the detectors.

†The labels A and B correspond to internally connected cryostat ports D4 and D3, respectively

‡Statistical analysis in previous measurements of the detector efficiencies were not as rigorous as the primary purpose was to identify the most likely superconducting detector pair to register a signature of SFWM photon-pairs—statistics of the uncertainty were not essential to identify this, just the mean value.

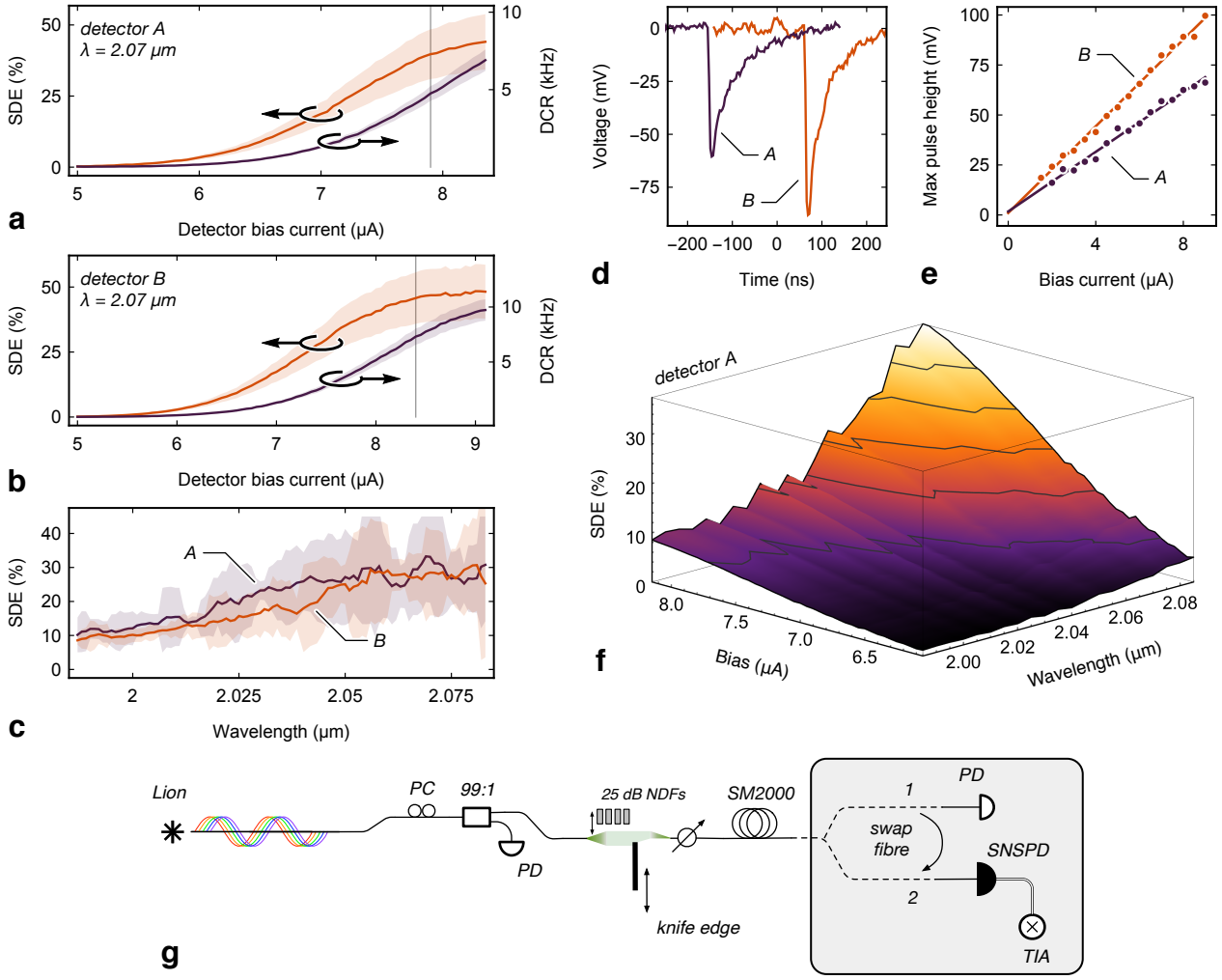

Figure 4.4: MIR optimised SNSPDs characterisation. **a**, System detection efficiency (SDE) and dark count rate (DCR) of detector *A*, with varying bias current measured using the method from part g. **b**, SDE and DCR of detector *B*, with varying bias current. **c**, Wavelength dependence of the SDE at fixed bias currents of 8.4 and 7.9 μA for detectors *A* and *B*, respectively. A moving average window of five points is applied to the data, with the shaded regions indicating one standard deviation in the sample window. The vertical grey lines on plots a, b identify this bias setting for this graph. **d**, Typical amplified output electrical pulse of the two detectors, both at a bias current of 8 μA, and measured on an oscilloscope. **e**, The peak electrical pulse height for the two detectors as a function of the bias current, fit with a linear slope model. **f**, A system detector efficiency surface plot, sweeping both the wavelength and the bias current of detector *A*. **g**, Experimental layout diagram of the technique used for characterising the superconducting detector efficiency.

down to the single-photon regime. The input fibre of the photodiode is then connected to the SNSPDs—the experimental scheme is shown in Fig. 4.4g.

Before the efficiency measurement starts, the knife edge is positioned in the fully blocking position, and the bias is swept to estimate the detector dark counts. Finally, the knife edge is moved to the calibrated positions from the bright light measurement. The estimated launched and measured photon fluxes are fit with a linear slope model for each bias setting to obtain the system detection efficiency (SDE) with varying bias, seen

in Figs. 4.4a and 4.4b. We find that the SDE plateaus for both detectors at around 8 μA, with peak values of 44±10 % and 48±10 % for detectors *A* and *B*, respectively. The shaded region is one standard deviation using the error analysis presented in Sec. 4.3.2. We find from performing cross-correlation coincidence measurements that the FWHM timing jitter of the two detectors is ~ 215 ps, which can be seen in the inset to Fig. 4.5c.

The observed sigmoidal shape in the dark count rate with increasing bias is typically seen when black-body radiation couples into the fibre. At room temperature, the black-body emission spectra peaks at around 10 μm. Translating to longer wavelengths below the 10 μm apex increases the spectral intensity of this background noise. Our MIR fibre supports wavelengths up to 2.3 μm leading to an order of magnitude more 'dark' counts than NIR fibre (see Fig. 4.7c)—a draw back of working at longer wavelengths at room temperature.

In another measurement we follow the procedure described above, but this time fix the bias at a constant value for both detectors (identified by the vertical grey lines in Figs. 4.4a, 4.4b.) and sweep the wavelength of our tuneable laser to characterise the spectral response. We plot the spectral dependence of the two SNSPDs in Fig. 4.4c. In this graph, a moving average window of five points has been applied to the estimated detector efficiency to reduce the noise in the spread of measured values*. The error bars are the standard deviation of the points in the sampled moving average window. Finally, we perform a measurement sweeping both the wavelength and bias and present results from a typical SDE measurement for nanowire *A* in Fig. 4.4f. The wavelength dependence of the measured efficiency in both Figs. 4.4c and 4.4f show a general trend of increasing efficiency as the wavelengths increases towards 2.08 μm.

4.3.2 Errors in the estimated efficiency

To estimate the errors, we first outline the uncertainties of the measurement. Losses from fibre are calibrated out by placing the photodiode at the output fibre next to the cryostat. The predominant error however in the measurement is the uncertainty on the absolute power reading from the photodiode. The relative uncertainty is estimated to be ±10 %. The four NDFs were measured 10 times to estimate the random error in the transmitted power. Furthermore, due to cavity interference effects that occur between multiple parallel optics, we assume an extra uncertainty of 1 dB on the total NDF transmission, estimated by evaluating the difference between the sum of two individually measured transmissions, and then simultaneously measured NDF transmissions.

At each bias setting, 16 optical powers are launched and integrated for 0.5 s, a total of 5 count rate polls, to average over the random error in the single-photon counting. We take the count rate error as the Poissonian error, given by the square root of the counts. Since the laser is susceptible to mode hopping, the recorded input power is measured on a 99:1 optical tap before the VOA. During the single-photon efficiency characterisation stage, we take the ratio of the launched power measured on the 99:1 during the bright light calibration, to the launched power while measuring attenuated laser on the SNSPDs. We use this to scale our estimated number of launched photons accordingly.

To fit each input-output photon flux, we use ordinary least squares regression. The

*This effect can predominantly be attributed to power fluctuations from the mode hopping of the tuneable CW laser as the wavelength is swept.

gradient of this can be calculated by

$$\hat{\beta} = \frac{\sum_{i=1}^{n} (x_i - \bar{x})(y_i - \bar{y})}{\sum_{i=1}^{n} (x_i - \bar{x})^2}, \tag{4.5}$$

where $\bar{x}, \bar{y}$ are the means of the data set, $\hat{\beta}$ is the slope and hence the estimated SDE of the detector. Here, we take the error on $\bar{x}, \bar{y}$ as the standard error of the mean. In the regression and calculation of slope, we treat the errors as Gaussian and calculate the uncertainty by propagating them in quadrature to calculate the standard error of the fit. This leads to the final error estimate and error bars in Figs. 4.4a and 4.4b.

4.4 Quantum correlated photons

The first key milestone in establishing the MIR as a platform for integrated quantum optics was to produce quantum correlated photon pairs. Fully equipped with sufficient off-chip filters, sensitive detectors and a phase-matched waveguide source, the measurement of correlated photons was now within reach.

We refer the reader to Secs. 1.6.3, 1.7 and 1.7.3 for the discussion of four-wave mixing, pair generation and phase-matching. To describe the pair generation process a common approximation to make is where the pump remains undepleted[195]. Creation of a single photon leaves the coherent state unchanged $\hat{a}|\alpha\rangle = \hat{a}^\dagger|\alpha\rangle = \alpha|\alpha\rangle$, which in the case of low FWM conversion efficiency is valid. Since we are generating a pair of non-degenerate photons at different frequencies, the pair generation Hamiltonian can be described by a two-mode squeezed vacuum[33]

$$\hat{H} = \hbar\Omega \hat{a}^\dagger \hat{b}^\dagger + \hbar\Omega^* \hat{a}\hat{b}, \tag{4.6}$$

where $\hat{a}, \hat{b}$ are the annihilation operators for the signal and idler photons. The interaction strength $\hbar\Omega \propto \alpha^2$ depends on the pump laser power. When the nonlinear coupling is weak i.e. $\hbar\Omega \ll 1$, we can expand the unitary operator $\hat{U} = \exp(-i\hat{H}t/\hbar)$ to first order

$$\hat{U}_{\text{SFWM}} \approx \mathbb{1} - it(\Omega \hat{a}^\dagger \hat{b}^\dagger + \Omega^* \hat{a}\hat{b}) + \mathcal{O}(\Omega^2). \tag{4.7}$$

When this operator is applied to the vacuum,

$$\hat{U}_{\text{SFWM}}|00\rangle = |00\rangle - \zeta|11\rangle, \tag{4.8}$$

where $\zeta \equiv i\Omega t$, and $|\zeta|^2$ can be thought of the small signal probability of generating a pair of photons.

4.4.1 Pair generation experiment

The source waveguide used for this experiment was a 7.2-mm strip waveguide with dimensions 510×340 nm^2. To measure quantum correlated photon-pairs, we configured our experiment as follows: the mode-locked pump laser is filtered with a double-pass monochromator, producing pulses with a FWHM $\Delta\tau = 5.78$ ps, and a peak power of 24.4 W. Controlling the polarisation, the filtered pump is coupled into the fundamental

TE mode of the waveguide via vertical grating couplers (VGC), with a loss of 7.4 dB*, estimated from the fit of the transmission data in Sec. 4.2.2.

After propagating through the waveguide, the pump, signal and idler all are copropagating and are coupled back off chip with a second vertical grating coupler (VGC). We passively demultiplex the photons with a 1:1 fibre beamsplitter, and filter each single photon channel with two back-to-back single pass monochromators, providing > 100 dB pump suppression required to attenuate it to the single photon level [178,196]. The passband for the signal and idler photon collection filters are separated ± 1.46 THz (± 20.8 nm) from the pump. Finally, we detect the photon-pairs with superconducting detectors A and B (see Sec. 4.3) biased at 7.9 and 8.1 μA, respectively. These biases were chosen as the efficiencies are almost plateaued, the chances of the detectors latching is minimised, and corresponding dark count rates not too large. The amplified electrical detector output pulses are time correlated using a time interval analyser (TIA) (PicoQuant PicoHarp 300) with a 4 ps bin resolution. In the low and high power regimes, we integrate a time correlation histogram for 540 and 180 seconds, respectively. A optical micrograph of the device and the experimental scheme are shown in Figs. 4.5a and 4.5b (see Figs. F.11a and F.11b for magnified layout of the device).

4.4.2 Analysis and results

Time of arrival correlation measurements are the gold standard for validating quantum correlated photons. To extract the coincidence count rates from the measured histograms, we use the following analysis procedure. For each optical power launched, we fit each peak in the correlation histogram with a Gaussian function and estimate the standard deviation σ for each peak. We then integrate $3\sigma \sim 389$ ps about each peak to obtain an estimate of the total counts. The peak at zero relative delay (see Fig. 4.5c) corresponds to photon-pairs generated in the same SFWM event (yellow curve in 4.5c). We identify this as the main correlation peak since it contains data from true coincident events, and then take the average of the counts in the side accidental peaks—generated by leaked pump laser, multi-pair events and other noise processes. Subtracting the averaged accidental counts from the uncorrected main coincidence peak yields the net coincidence count rate.

Our analysis gives a maximum net coincidence count rate of 112 ± 3 Hz (orange curve in 4.5c), and a peak CAR using Eqn. (1.95) of 25.7 ± 1.1 corresponding to a coincidence count rate of 1.1 Hz. For context, the state-of-the-art in a silicon ring resonator has measured [142] a peak CAR of 12000 and a peak measured pair-rate of 4.9 kHz. This highlights the challenge still required by the MIR platform to engineer reduced linear, filtering and effective detector losses to match this performance. For the fitting procedure of these curves see Sec. 4.4.3. On a longer 17.5-mm waveguide, we measure a peak net coincidence rate of 224 Hz see Fig. 4.7. Here, the quoted errors on the count rates are treated as Poissonian, and the error in the CAR is due to the random uncertainty, taken as the standard deviation of the measured coincidence count rates and propagated in quadrature. Due to the passive demultiplexing of our signal and idler photons, the actual net coincidence count rates produced by the waveguide are 4× the measured values (for justification see the next subsection). Therefore, for these two coincidence measurements we observe true rates of 448 Hz and 896 Hz.

*This loss is higher than the peak of 5.1 dB at $\lambda = 2.035\mu$m since the pulsed laser is centred on $\lambda = 2.071\mu$m

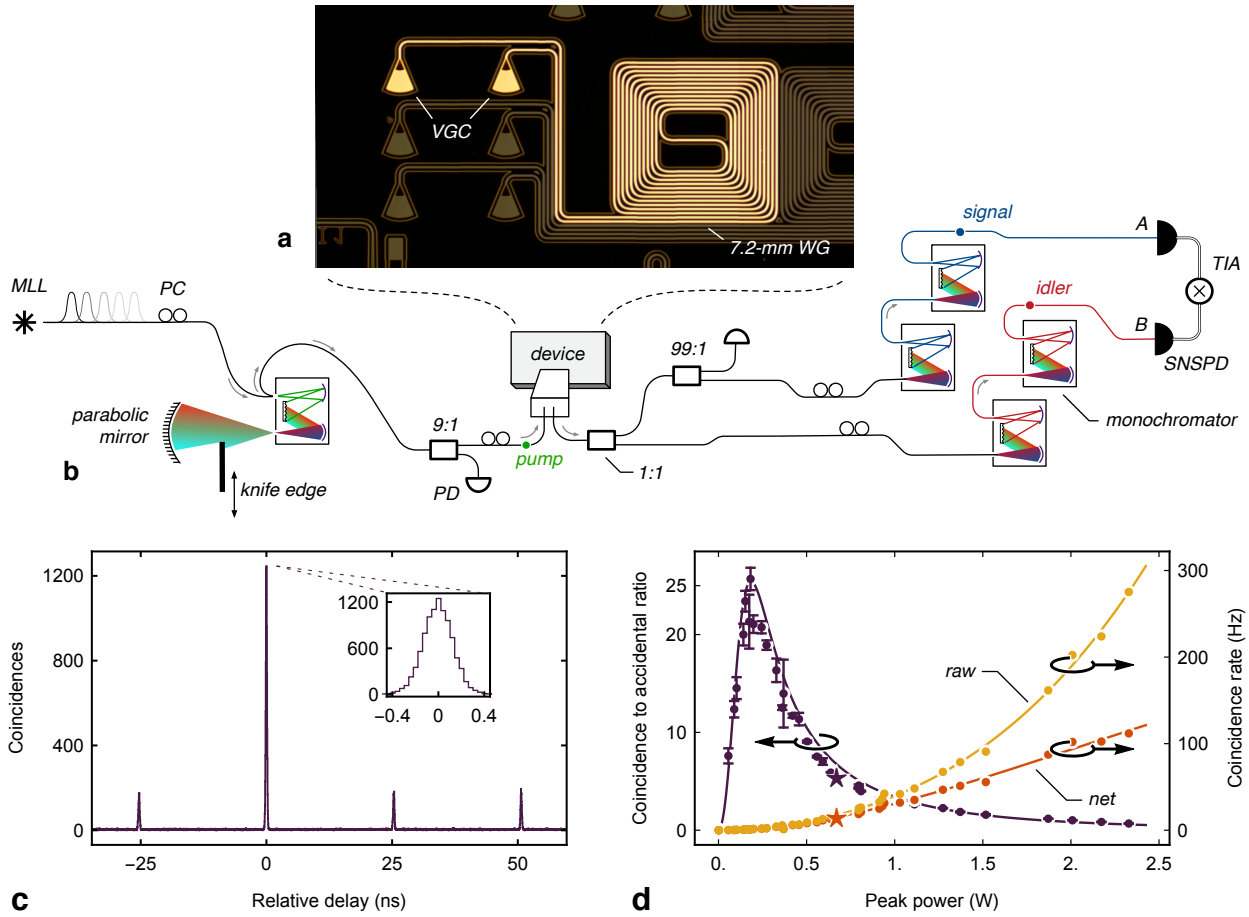

Figure 4.5: Quantum correlated photon-pairs. **a**, Dark field micrograph of the waveguide source that produced the correlated photons. **b**, Experimental scheme to measure quantum correlated photon-pairs. The pump laser is filtered and coupled into the device. At the output, photon-pairs are passively demultiplexed with a beamsplitter (1:1) and two back-to-back monochromators suppress the pump, finally detecting the photons with superconducting nanowire (SNSPDs). **c**, Typical time correlation histogram for correlated photon pair emission from SFWM, integrated for 540 s. The peak at zero delay corresponds to photon-pairs generated in the same SFWM event. Inset: magnified view of the main coincidence correlation peak; the temporal distribution of values is due to the SNSPDs timing jitter. The data point that corresponds to this histogram is shown as a star in plot d. **d**, Coincidence to accidental ratio, raw and net (accidental-subtracted) coincidence count rates with varying launched peak pump power in the waveguide. Fit to the data uses the methods described in Sec. 4.4.3.

Quantum treatment of the beamsplitter and filters

Due to the passive demulitplexing of signal and idler photons, we only register a fraction of the events in our measurement of correlated photon-pairs. We now justify this claim with the following analysis.

When a single photon-pair is produced from SFWM, the pump signal and idler are all copropagating at the output of the chip. The photons are incident on one port of a 50/50 beamsplitter with vacuum at the other port, the total initial quantum state is given by

$$|\psi_{\text{in}}\rangle = |1_s, 1_i\rangle_A |\text{vac}\rangle_B = \hat{a}_s^\dagger \hat{a}_i^\dagger |0_s, 0_i\rangle_A |\text{vac}\rangle_B \,, \tag{4.9}$$

where $|\text{vac}\rangle$ is the vacuum state, subscripts s, i are the signal and idler occupation number and A, B denote the beamsplitter input ports. Assuming the beamsplitter is balanced and lossless[89], the creation operators transform according to $\hat{a}^\dagger \mapsto \frac{1}{\sqrt{2}}(\hat{c}^\dagger + i\hat{d}^\dagger)$, where $\hat{c}^\dagger$ and $\hat{d}^\dagger$ are the creation operators at the beamsplitter output ports. After the beamsplitter the state is

$$|\psi_{\text{out}}\rangle = \frac{1}{2}\left(\hat{c}_s^\dagger \hat{c}_i^\dagger - \hat{d}_s^\dagger \hat{d}_i^\dagger + i\hat{c}_s^\dagger \hat{d}_i^\dagger + i\hat{c}_i^\dagger \hat{d}_s^\dagger\right)|0_s, 0_i\rangle_C\,|0_s, 0_i\rangle_D\,. \tag{4.10}$$

Applying the creation operators to the vacuum gives

$$|\psi_{\text{out}}\rangle = \frac{1}{2}\left(|1_s, 1_i\rangle_C\,|0_s, 0_i\rangle_D - |0_s, 0_i\rangle_C\,|1_s, 1_i\rangle_D + i\,|1_s, 0_i\rangle_C\,|0_s, 1_i\rangle_D + i\,|0_s, 1_i\rangle_C\,|1_s, 0_i\rangle_D\right). \tag{4.11}$$

A coincidence event only occurs when single photons occupy both modes C and D. Dropping the C, D and s, i notation, the probability of getting a exactly one photon at each output port is given by

$$P_{\text{coincidence}} = P(|1001\rangle) + P(|0110\rangle). \tag{4.12}$$

However, our back-to-back monochromator filters only transmit exclusively the signal *or* idler photon thus, we have to also apply a postselection operator $|1001\rangle\langle 1001|$. This demonstrates that in the low squeeze limit, the detection count rate is reduced by a factor $P_{\text{click}} = |i/2|^2 = 1/4$ in the case where there are no losses after the beamsplitter. In higher number photon-pair regime the treatment is more complicated as the photon statistics at the beamsplitter output become binomially distributed.

To understand the beamsplitter behaviour in the general case, we must now treat arbitrary numbers of photon pairs with a corresponding probability distribution Ξ_n^d, with $d \in \{\text{thermal}, \text{Poisson}\}$—see Sec. 1.7 for the photon-pair distributions. In Fig. 4.6c, we show the probability of producing one or more pairs for a given squeeze parameter—the two distributions are similar in the high- and low-power limits, and deviate from each other intermediate squeezing regime. The following derivation finds the likelihood of a beamsplitter output state that can give rise to a coincidence event. Exactly n-pairs of photons incident on the beamsplitter input port is given by

$$|nn\rangle = \frac{1}{n!}(\hat{a}_s^\dagger)^n(\hat{a}_i^\dagger)^n\,|00\rangle\,. \tag{4.13}$$

Each input mode creation operators transforms according to $\hat{a}^\dagger \mapsto (\hat{c}^\dagger + i\hat{d}^\dagger)/\sqrt{2}$, therefore after the beamsplitter the state is

$$\frac{1}{n!}\left(\frac{1}{\sqrt{2}}(\hat{c}_s^\dagger + i\hat{d}_s)\right)^n\left(\frac{1}{\sqrt{2}}(\hat{c}_i^\dagger + i\hat{d}_i)\right)^n|0000\rangle\,, \tag{4.14}$$

which we can express as the sum of the product of two binomial expressions

$$\frac{1}{2^n n!}\sum_{k,m=0}^{n} i^{(k+m)}\binom{n}{k}\binom{n}{m}(\hat{c}_s^\dagger)^{n-k}(\hat{d}_s^\dagger)^k(\hat{c}_i^\dagger)^{n-m}(\hat{d}_i^\dagger)^m\,|0000\rangle\,. \tag{4.15}$$

Again, due to the monochromators transmission of only either the signal *or* the idler, the projection operator where there is *at least* one signal photon in mode C and one idler photon in mode D, i.e. $|\alpha\beta\gamma\delta\rangle\langle\alpha\beta\gamma\delta|$ where $\alpha, \delta \geq 1$ is given by

$$\hat{P}_{km} = \sum_{k=0}^{n-1}\sum_{m=1}^{n}|n-k, n-m, k, m\rangle\langle n-k, n-m, k, m|\,. \tag{4.16}$$

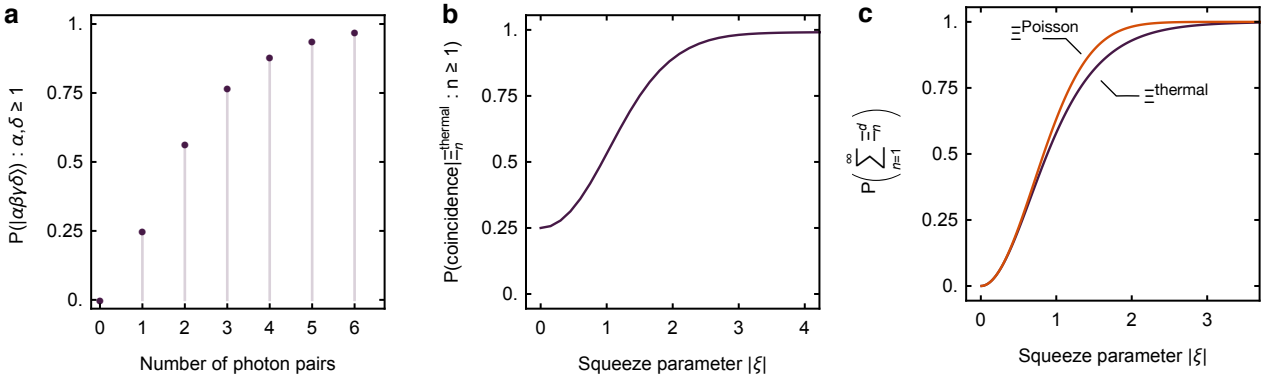

Figure 4.6: Statistics of photon-pairs incident on a beamsplitter. **a**, Probability of at least one signal photon in output mode C and one idler photon in mode D for exactly n pairs incident on a beamsplitter. **b**, Probability of at least one signal photon in mode C and one idler in mode D at the beamsplitter output, when at least one pair is generated with thermal statistics. **c**, Comparison of the Poisson and thermal distribution that at least one photon-pair is produced. In the low and high squeezing limit, the distributions converge and deviate from each other only in the intermediate regime.

Applying $\hat{P}_{km}$ operator to the state in Eqn. (4.15) results in the probability of a coincidence*

$$P_{\mathrm{c}}(n) = \frac{1}{(2^n n!)^2} \sum_{k=0}^{n-1} \sum_{m=1}^{n} \left| i^{(k+m)} \binom{n}{k} \binom{n}{m} \prod_{x \in \{k,m\}} \sqrt{(n-x)!}\sqrt{x!} \right|^2 . \tag{4.17}$$

We now use a result from conditional probability†

$$\begin{aligned} P_{\mathrm{BS}}(\text{coincidence}|\Xi_n^d : n \geq 1) &= \frac{P(P_c(n) \wedge \Xi_n^d : n \geq 1)}{P(\Xi_n^d : n \geq 1)} \\ &= \frac{\sum_{n=1}^{\infty} \Xi_n^d P_c(n)}{\sum_{n=1}^{\infty} \Xi_n^d}, \end{aligned} \tag{4.18}$$

which is the conditional probability that we have an coincidence event at the beamsplitter output given at least one pair was generated from SFWM in the absence of optical loss and unit efficiency detectors. The results of Eqns. (4.17) and (4.18) are summarised in Figs. 4.6a and 4.6b, respectively.

4.4.3 Coincidence to accidental ratio model

To fit a model to the coincidence count rate curves and CAR in Fig. 4.5d, we use the following treatment. We start by defining the probability of producing exactly n-pairs of photons with a thermal distribution

$$\Xi_n^{\mathrm{thermal}} = \mathrm{sech}^2|\xi| \tanh^{2p}|\xi| \tag{4.19}$$

where $|\xi|^2$ is the average number of photon-pairs per pulse. Defining the squeezing parameter[127,138]

$$\xi = \Delta\nu\Delta\tau \left| \frac{\gamma}{\alpha_{\mathrm{TPA}}} \ln(1 + \alpha_{\mathrm{TPA}} P L_{\mathrm{eff}}) \mathrm{sinc}(igL) \right|, \tag{4.20}$$

*For verbosity, the $\prod$ symbol here denotes the product, and not the Poisson probability distribution.
†Usually formulated as $P(A|B) = \frac{P(A \wedge B)}{P(B)}$

where $\Delta\nu$ is the collection bandwidth of the filters (70 GHz), $\Delta\tau$ is the FWHM pulse duration (5.78 ps), and the other parameters are described in table 1.1. To get the rate, we multiply the pair per pulse probability by the laser repetition f, the total channel losses (a combination of grating coupler, propagation, filter, fibre and detector effective losses) $\eta_{s,i}$, and the beamsplitter and monochromator postselection penalty,

$$R = \mathcal{D} + f\mathcal{L}P + f\sum_{n=1}^{\infty} P_{\mathrm{BS}}(\xi)\Xi_n^{\mathrm{thermal}}(1-(1-\eta_s)^n)(1-(1-\eta_i)^n). \tag{4.21}$$

Here, $\mathcal{D}$ is the SNSPDs dark count rate, $\mathcal{L}$ is linear noise such as leaked pump laser and $P_{\mathrm{BS}}(\xi)$ is defined in Eqn. (4.18). Equation (4.21) describes the *raw* coincidence count rate, given that at least one of the p-pairs produced from SFWM or linear noise caused a detection event. True coincidence events occur when a single pair are generated in a laser pulse given by

$$R_1 = f\eta_s\eta_i\Xi_1^{\mathrm{thermal}}. \tag{4.22}$$

We use a nonlinear fitting procedure to simultaneously minimise the squared distance of the curve for Eqns. (4.21) and (4.22) to the measured net and raw coincidence count rate. We find our fit estimates the parameters $\gamma = 50\ \mathrm{W^{-1}m^{-1}}$, $\Delta k = 6.5\ \mathrm{m^{-1}}$, $\alpha_{\mathrm{TPA}} = 25.2\ \mathrm{W^{-1}m^{-1}}$, $\eta_{s,i} = 0.0111$, $\mathcal{D} = 1\times10^{-6}$ Hz and $\mathcal{L} = 3.1\times10^{-8}\ \mathrm{W^{-1}}$. We find for a pump-signal detuning of 20.8 nm, the linear phase mismatch corresponds to a group velocity dispersion (GVD) of $\beta_2 = -0.08\ \mathrm{ps^2/m}$. Finally, to get the CAR model, we fit the averaged accidental peaks rate with a fourth order polynomial, constraining all of the fit coefficients to be greater than zero. The resulting CAR model fit in Fig. 4.5d is simply the ratio of these fitted models

$$\mathrm{CAR} = \frac{R_1}{R_{\mathrm{acc}}}. \tag{4.23}$$

4.5 Discussion

MIR pair generation experiments with one[153], and two[131] MIR photons from bulk spontaneous parametric down-conversion sources have been shown. To the best of our knowledge, this experiment was the first to demonstrate SFWM on-chip with all four fields having wavelengths beyond 2 μm, and in turn two key milestones of sensitive detectors and photon-pair generation in the MIR. This work opens up exciting new opportunities for MIR quantum optics for applications like quantum enhanced sensing, where the fingerprint region for gas molecules begins. There is still significant work to bridge the gap of total system performance between the state-of-the-art in the NIR, which boasts detection efficiencies[112] upwards of 93% and crystalline silicon waveguide photon-pair sources have shown[197] a peak CAR = 673.

An appreciable part of the discrepancy between the performance of the MIR and NIR approaches are due to the losses from pump rejection filtering, high dark count rate and efficiency in detection. These are not a fundamental limitation and can be engineered to achieve similar performance. In crystalline silicon TPA is intrinsic and therefore cannot be solved without modifying either the wavelength or the material system. Furthermore, challenges that have been solved along the way, such as filtering and detection, are still useful for MIR quantum gas sensing of molecular fingerprints applications that are not possible at NIR wavelengths.

The TPA we measured in this chapter is reduced from the NIR, but is still non-zero. The bandgap and hence the cutoff wavelength blue shifts with temperature[165,198]—plotted

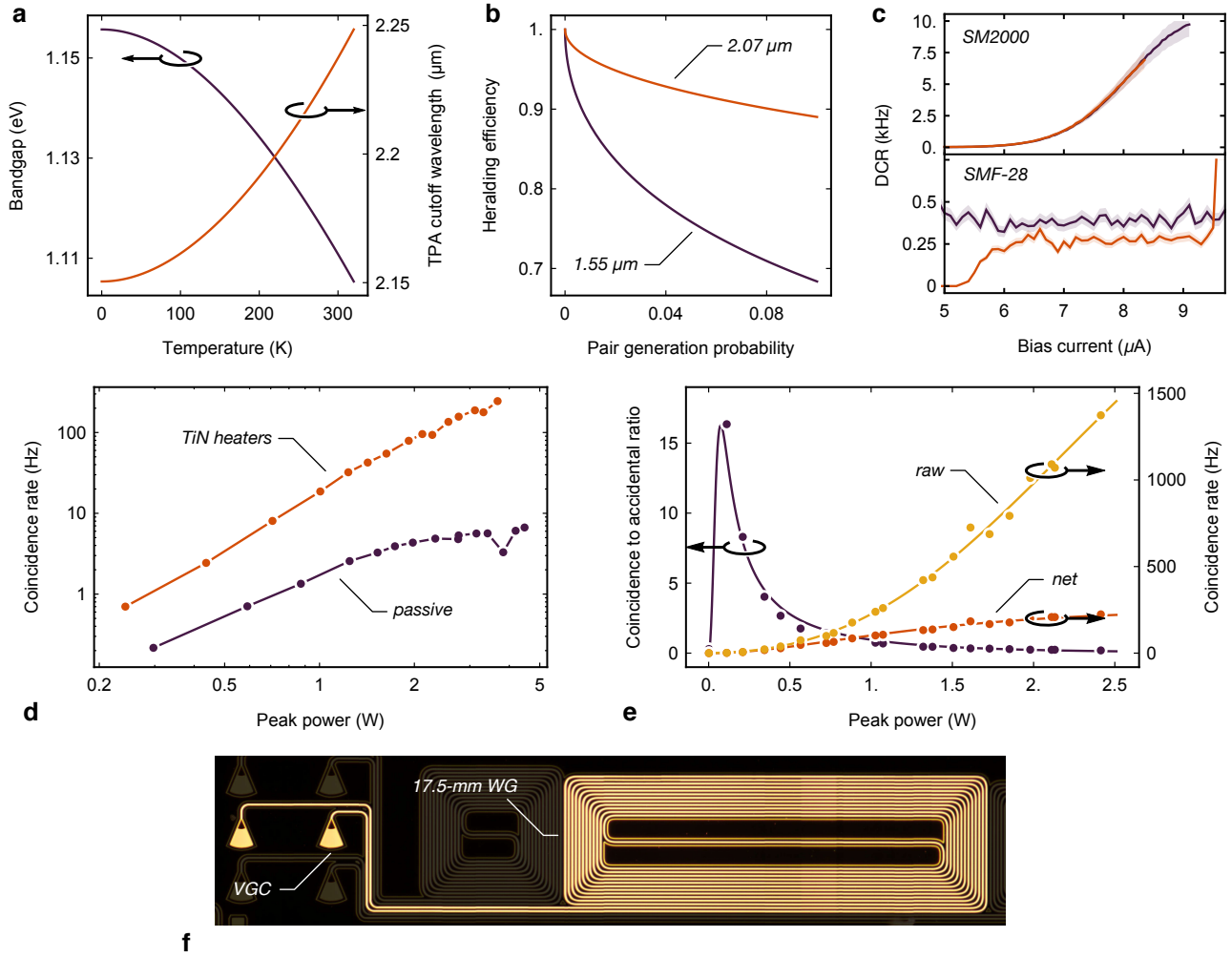

Figure 4.7: General details about the experiment and analysis **a**, Band gap and TPA cutoff wavelength with varying temperature, model from Ref. 165. **b**, Heralding efficiency of a source with increasing pump power. The model is described in Ref. 128, with the NIR TPA and n_2 values from Ref. 121, the MIR values are from our analysis in this chapter. **c**, Dark count rate (DCR) with varying bias current for the superconducting detectors, fibre coupled with no fibre (SMF-28) and MIR fibre (SM2000). The sigmoidal shape of the MIR fibre is due to black-body radiation. **d**, Log-log plot comparison of on-chip pair production rates between the fully passive and metallised (phase-matched) devices from Cornerstone. **e**, Raw and net (accidental-subtracted) pair production rates, and coincidence to accidental ratio as a function of coupled peak pump power in the long 17.5-mm device. **f**, Dark field optical micrograph of the long source waveguide (WG) and grating couplers (VGC) used for the measurement in plot e.

in Fig. 4.7a. Previous experiments on the temperature dependence of silicon have demonstrated that the low temperature TPA coefficient is significantly reduced[121]. This also motivates cryogenic integration of these sources, along with the development of longer wavelength lasers around the 2.2 μm region that will completely eliminate residual TPA and enable quantum nonlinear-optics. Regardless of this, we see that the increased nonlinear refraction and reduced nonlinear absorption already imply a large improvement

of the heralding efficiency due to XTPA. We use a model from Ref. 128

$$\eta_{\mathrm{XTPA}} \approx \frac{1}{\left(1+\frac{\beta_{\mathrm{TPA}}}{k_0 n_2}\sqrt{\frac{p}{\Delta t \Delta \nu_c}}\right)}, \tag{4.24}$$

where p is the pair-generation probability, Δt is the pulse duration and $\Delta \nu_c$ is the collection bandwidth, along with our measured and literature[160] values to show the expected heralding efficiency improvement, and plot this in Fig. 4.7b. We see that at 0.1 pairs per pulse, that the heralding efficiencies are 68% and 89% for the NIR and MIR, respectively. This illustrates the benefits of our approach to quantum silicon photonics.

A key limiting factor of the improving the CAR for future MIR single photon experiments will be to suppress the effects of "dark" counts. In this experiment the dark count rate (DCR) ~ 6 kHz, is an order of magnitude larger than in typical telecommunication nanowires. We plot the DCR of our SNSPDs as a function of bias packaged with telecom and MIR fibres in Fig. 4.7c. The long-wavelength cutoff of the MIR fibre leads to excess black-body noise coupled into our detectors and is responsible for the measured high DCR in our experiments and the observed sigmodal behaviour shape with increasing bias. This fact presents itself with a new motivations for use of a cold-filter and even full cryogenic integration of sources and detectors in the cryostat to reduce the black-body radiation noise.

The longer source waveguide (17.5-mm)—seen in Fig. 4.7f—proved to have higher count rates (Fig. 4.7e) than the 7.2-mm source. The results presented in Sec. 4.4.2 were chosen over the 17.5-mm source due to the similarity in length to the photon-pair sources in the time-reversed Hong-Ou-Mandel circuit, described in chapter 5.

The advent of a new chip, efficient detectors and a dedicated MIR fibre link, improved the coincidence rate by almost six orders of magnitude from millihertz to kilohertz. In Fig. 4.7d we show a comparison of the coincidence count rates of the passive and phase-matched metallised optical lithography chips. Clearly, the performance of the later batch made the previous versions of the die obsolete, but also crucially highlights the importance of fabrication tolerant design.

All of the pieces of the puzzle were complete to finally demonstrate the overarching goal of this project; provable on-chip quantum interference, which is the content of the next chapter.

Statement of work

I performed the measurements of the stimulated four-wave mixing, nonlinear refraction and absorption, detector efficiency, quantum correlated photon-pairs and the associated auxiliary measurements. Myself and Dominic Sulway installed the mid-infrared fibre from the lab to the cryostat. Dr. Vikas Anant fabricated the superconducting nanowires and measured the dark count rate of the detectors packaged with SMF-28. Dr. Gary Sinclair analysed the data for the measurement of the waveguide nonlinear refraction and absorption parameters. Dominic Sulway assisted with the spontaneous four-wave mixing coincidences measurement. Myself and Dr. Joshua Silverstone performed the data analysis of the detector efficiency and the coincidence measurements.

Chapter 5

On-chip quantum interference and entanglement

High visibility quantum interference is essential for showing the viability of any quantum optics platform. Hong-Ou-Mandel (HOM) interference, where two photons interact, is notoriously difficult since the photons must be indistinguishable in all degrees of freedom. Time-reversed HOM interference also demands generation of quantum correlated photons from identical sources and high precision Mach-Zehnder interferometers (MZIs). Heralded multi-photon experiments necessitate combining many identical integrated sources of separable photons-pairs.

In this chapter we present the results demonstrating the first quantum interference in the mid-infrared. The results of the previous chapter confirmed the increased nonlinear refraction and reduced nonlinear absorption of the waveguide source, along with sensitive detectors and correlated photon-pairs. Now applying this infrastructure to a quantum integrated circuit remained as the final challenge to unleashing quantum optics to the mid-infrared (MIR). The results presented in this chapter formed the basis of an oral presentation, given at the postdeadline session at the CLEO Europe 2019. The results were published in a peer reviewed conference proceeding[199] and formed the final section of an article (Ref. 186).

5.1 Time reversed Hong-Ou-Mandel interference

The HOM effect causes two completely indistinguishable single photons, when injected into the two ports of a balanced beamsplitter, to strictly bunch at the outputs[43] producing the path-entangled output state $(|20\rangle - |02\rangle)/\sqrt{2}$. Here, instead of achieving two photon interference of identical photons at a beamsplitter, we achieve two-photon on-chip quantum interference using a time-reversed HOM experiment[46,133,200], interfering the photons in a Mach-Zehnder interferometer[49].

All quantum mechanical evolution can be described with a unitary operator $\hat{U}$. It should not be surprising that the Hermitian conjugate, or inverse of a unitary, applies time-reversed operation such that $\hat{U}\hat{U}^{\dagger} = \mathbb{1}$. The input to 'traditional' HOM interference

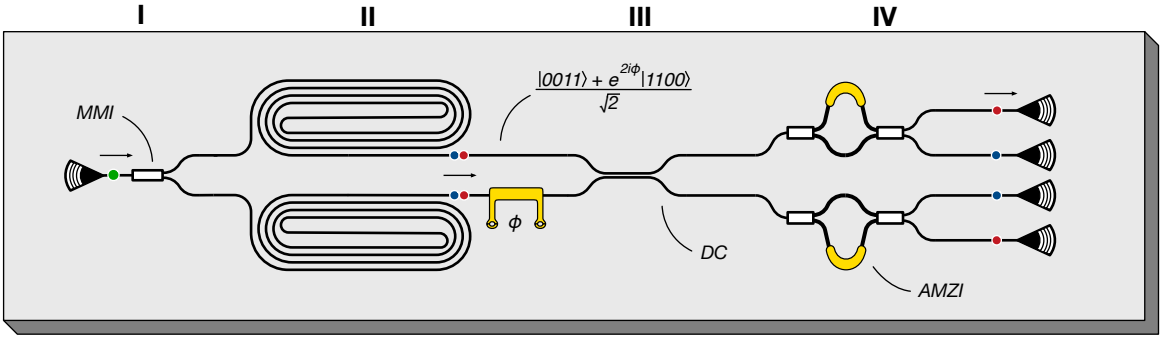

Figure 5.1: Operation of the time-reversed HOM circuit. **I**, The pump is split between waveguide sources with an MMI. **II**, Photon-pairs are coherently created in a superposition of both waveguide sources and a phase ϕ is applied to one waveguide. **III**, Both sources are interfered on a directional coupler (DC). **IV**, The single-photons are frequency demultiplexed with asymmetric Mach-Zehnder interferometers (AMZI).

is a pair of single-photons on a beamsplitter, outputting a path-entangled superposition. The time-reversed HOM effect generates a path-entangled superposition of photon-pairs in two coherently pumped waveguide sources, with a possible output state containing one photon at each output of the beamsplitter.

This interference effect between the sources can be further manipulated. Applying a phase shift to one source before the beamsplitter yields statistics where the photons are in a superposition of split and bunched, depending on the relative phase. Correctly choosing this phase can lead to the deterministic splitting or bunching of photons from such a waveguide circuit. It turns out that this effect can be used as a building block[60], and to characterise[37] larger-scale multiple source experiments.

We will now discuss the theory of the device operation, then show our experimental scheme and finally presents our results, analysis and discussion.

5.1.1 Theory

Here we give the quantum treatment for the time-reversed HOM interference effect. We start with a bright coherent state $|\alpha\rangle$ incident at the start of the waveguide circuit shown in Fig. 5.1. After the on-chip multimode interference coupler (MMI), the pump is split between the two waveguide sources A and B i.e. the coherent state undergoes the transformation

$$|\psi_{\text{in}}\rangle = |\alpha\rangle \mapsto |\frac{\alpha}{\sqrt{2}}\rangle_A \, |\frac{\alpha}{\sqrt{2}}\rangle_B = |0_s 0_i \bar{\alpha}\bar{\alpha}\rangle_A |0_s 0_i \bar{\alpha}\bar{\alpha}\rangle_B , \tag{5.1}$$

where the occupation number state is for the signal and idler Fock states and we make the substitution $\bar{\alpha} = \alpha/\sqrt{2}$. The Hamiltonian of spontaneous four-wave mixing (SFWM) is given by[195,201]

$$\hat{H}_{\text{SFWM}} = -\chi_0 \int \hat{a}_s^\dagger \hat{a}_i^\dagger \hat{a}_{p1} \hat{a}_{p2} e^{-i(k_s + k_i - k_{p1} - k_{p2})z} dk_s dk_i dk_{p1} dk_{p2} + \text{H.c.}, \tag{5.2}$$

where χ_0 is an effective nonlinear coefficient, k is the wavevector and subscripts $s, i, p1, p2$ denote the signal, idler and two pump photons, respectively. In the low squeeze limit (i.e. $\ll 1$ pair per pulse) regime and making the undepleted pump approximation, we

can expand the unitary operator $\hat{U}_{\text{SFWM}} = \exp(-i\hat{H}t/\hbar)$ to first order

$$\hat{U}_{\text{SFWM}} \approx \mathbb{1} + \frac{\chi_0'}{\sqrt{2}} \int \hat{a}_s^\dagger \hat{a}_i^\dagger \hat{a}_{p1} \hat{a}_{p2} e^{-i(k_s+k_i-k_{p1}-k_{p2})z} dk_s dk_i dk_{p1} dk_{p2} + \text{H.c.} \tag{5.3}$$

$$= \left[\mathbb{1} + \frac{\chi_0'}{\sqrt{2}} \int \Phi(k_s, k_i) \hat{a}_s^\dagger \hat{a}_i^\dagger \hat{a}_{p1} \hat{a}_{p2} dk_s dk_i \right] \tag{5.4}$$

$$= \mathbb{1} + \gamma \hat{a}_s^\dagger \hat{a}_i^\dagger \hat{a}_{p1} \hat{a}_{p2} \tag{5.5}$$

where $\Phi(k_s, k_i)$ is the energy and momentum conserving joint spectral amplitude function, $\chi_0' = i\chi_0 t/\hbar$ and $\gamma = (\chi_0'/\sqrt{2}) \int dk_s dk_i \Phi(k_s, k_i)$ is an effective signal-idler photon pair generation coefficient. Pair generation occurs in both waveguide sources, therefore

$$\hat{U}_{\text{SFWM,A}} |0_s 0_i \bar{\alpha}\bar{\alpha}\rangle_A \otimes \hat{U}_{\text{SFWM,B}} |0_s 0_i \bar{\alpha}\bar{\alpha}\rangle_B$$

$$= (\mathbb{1} + \gamma \bar{\alpha}^2 \hat{a}_s^\dagger \hat{a}_i^\dagger) |0_s 0_i \bar{\alpha}\bar{\alpha}\rangle_A \otimes (\mathbb{1} + \gamma \bar{\alpha}^2 \hat{b}_s^\dagger \hat{b}_i^\dagger) |0_s 0_i \bar{\alpha}\bar{\alpha}\rangle_B . \tag{5.6}$$

$$= (|0_s 0_i \bar{\alpha}\bar{\alpha}\rangle_A + \gamma \bar{\alpha}^2 |1_s 1_i \bar{\alpha}\bar{\alpha}\rangle_A) \otimes (|0_s 0_i \bar{\alpha}\bar{\alpha}\rangle_B + \gamma \bar{\alpha}^2 |1_s 1_i \bar{\alpha}\bar{\alpha}\rangle_B). \tag{5.7}$$

To illustrate the path entangled state, we discard the pump and look at only the single-photon Fock states in modes A and B

$$|0_s 0_i 0_s 0_i\rangle + \gamma \bar{\alpha}^2 |1_s 1_i 0_s 0_i\rangle + \gamma \bar{\alpha}^2 |0_s 0_i 1_s 1_i\rangle + \mathcal{O}((\gamma \bar{\alpha}^2)^2). \tag{5.8}$$

For the remainder of the calculation we keep track of the behaviour of one coherent state per spatial mode. Therefore, postselecting on one-pair events and normalising the state in Eqn. (5.7),

$$|\psi_{\text{source}}\rangle = \frac{1}{\sqrt{2}} (\hat{a}_s^\dagger \hat{a}_i^\dagger + \hat{b}_s^\dagger \hat{b}_i^\dagger) |0_s 0_i \bar{\alpha}\rangle_A |0_s 0_i \bar{\alpha}\rangle_B . \tag{5.9}$$

The light in mode B undergoes a phase shift ($\hat{U}_\phi = \exp(i\hat{n}\phi)$, where $\hat{n} = \hat{b}^\dagger \hat{b}$ is the number operator) transforming the state to

$$\hat{U}_\phi |\psi_{\text{source}}\rangle = \frac{1}{\sqrt{2}} (\hat{a}_s^\dagger \hat{a}_i^\dagger + e^{2i\phi} \hat{b}_s^\dagger \hat{b}_i^\dagger) |0_s 0_i \bar{\alpha}\rangle_A |0_s 0_i \bar{\alpha} e^{i\phi}\rangle_B . \tag{5.10}$$

Finally the state is incident on a directional coupler*, which transforms the mode operators according to $\hat{a}^\dagger \mapsto (\hat{c}^\dagger + i\hat{d}^\dagger)/\sqrt{2}$ and $\hat{b}^\dagger \mapsto (i\hat{c}^\dagger + \hat{d}^\dagger)/\sqrt{2}$, so that

$$|\psi_{\text{out}}\rangle = \frac{1}{2\sqrt{2}} \left[(\hat{c}_s^\dagger + i\hat{d}_s^\dagger)(\hat{c}_i^\dagger + i\hat{d}_i^\dagger) + e^{2i\phi} (i\hat{c}_s^\dagger + \hat{d}_s^\dagger)(i\hat{c}_i^\dagger + \hat{d}_i^\dagger) \right]$$

$$\times |0_s 0_i, \frac{\alpha + i\alpha e^{i\phi}}{2}\rangle_C |0_s 0_i, \frac{i\alpha + \alpha e^{i\phi}}{2}\rangle_D \tag{5.11}$$

$$= \frac{1}{2\sqrt{2}} \left[(\hat{c}_s^\dagger \hat{c}_i^\dagger - \hat{d}_s^\dagger \hat{d}_i^\dagger + i\hat{c}_s^\dagger \hat{d}_i^\dagger + i\hat{d}_s^\dagger \hat{c}_i^\dagger) + e^{2i\phi} (-\hat{c}_s^\dagger \hat{c}_i^\dagger + \hat{d}_s^\dagger \hat{d}_i^\dagger + i\hat{c}_s^\dagger \hat{d}_i^\dagger + i\hat{d}_s^\dagger \hat{c}_i^\dagger) \right]$$

$$\times |0_s 0_i, \frac{\alpha}{2}(1 + ie^{i\phi})\rangle_C |0_s 0_i, \frac{\alpha}{2}(i + e^{i\phi})\rangle_D , \tag{5.12}$$

we now make the substitution $i\exp(i\phi) = \exp(i\phi + i\pi/2) = \exp(i\bar{\phi})$

$$= ie^{i\phi} \left[\frac{1}{2i}(e^{-i\phi} - e^{i\phi}) \frac{|1_s 1_i 0_s 0_i\rangle - |0_s 0_i 1_s 1_i\rangle}{\sqrt{2}} + \frac{1}{2}(e^{i\phi} + e^{-i\phi}) \frac{|1_s 0_i 0_s 1_i\rangle + |0_s 1_i 1_s 0_i\rangle}{\sqrt{2}} \right]$$

$$\times |\alpha e^{i\bar{\phi}/2} \frac{1}{2}(e^{-i\bar{\phi}/2} + e^{i\bar{\phi}/2})\rangle_C |i\alpha e^{i\bar{\phi}/2} \frac{1}{2}(e^{-i\bar{\phi}/2} - e^{i\bar{\phi}/2})\rangle_D \tag{5.13}$$

$$= ie^{i\phi} \left(\sin\phi |\psi_{\text{bunch}}\rangle + \cos\phi |\psi_{\text{split}}\rangle \right) |\alpha e^{i\bar{\phi}/2} \cos(\bar{\phi}/2), \alpha e^{i\bar{\phi}/2} \sin(\bar{\phi}/2)\rangle_{CD} \tag{5.14}$$

*See Sec. B.4.1 for the action of the beamsplitter on the coherent state $|\bar{\alpha}\rangle$.

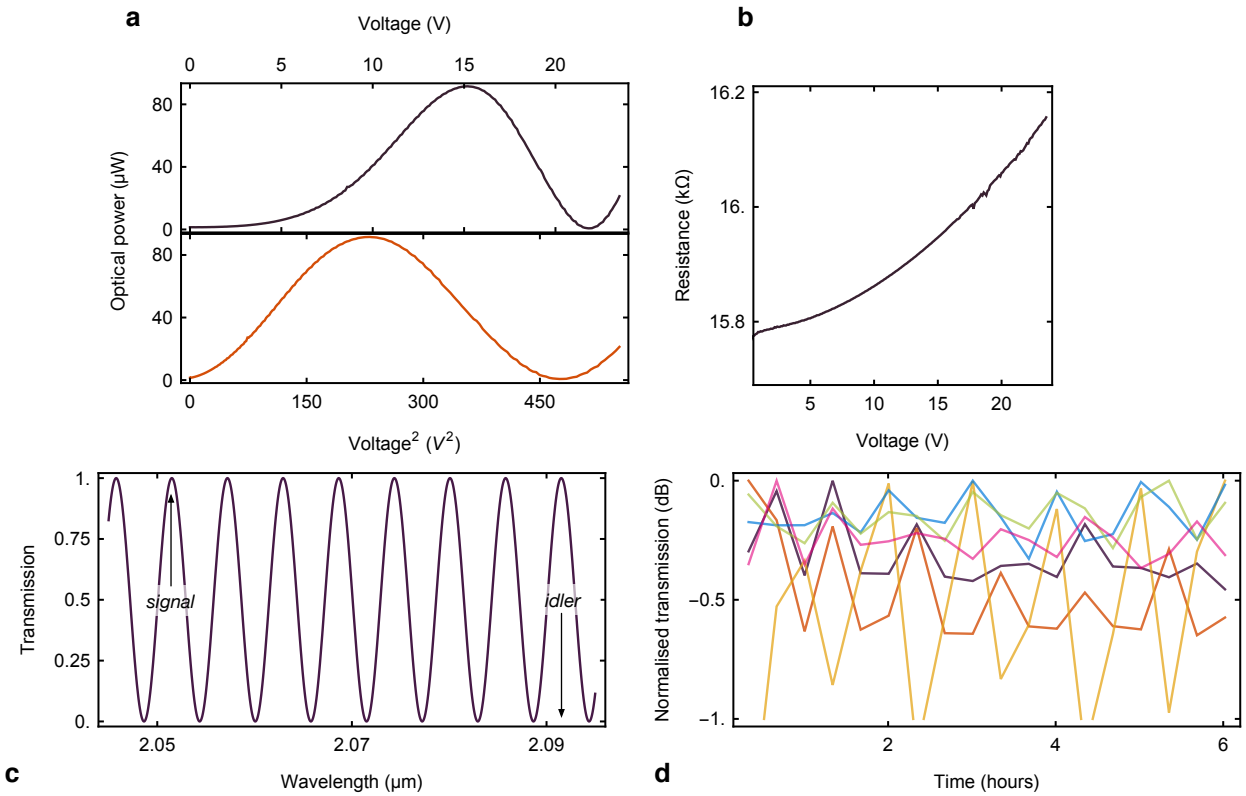

Figure 5.2: Characterisation of the time-reversed HOM waveguide circuit. **a**, Optical transmission of the source interferometer with swept voltage. A comparison between linear and squared voltage demonstrates that the resulting fringe is linearly sinusoidal with V^2. **b**, The change of the resistance of the source TOPM with varying voltage. **c**, Simulated wavelength transmission function of the on-chip demultiplexing asymmetric Mach-Zehnder interferometers, using the measured value of the group index from Sec. 3.5.1. **d**, Long term normalised coupling transmission stability for several measurements of the experiment. Fluctuations in the coupling have a period that is similar to the laboratory air conditioning cycles, strongly indicating that this effect is due to thermal expansion.

where we make the definition of the states[46]

$$|\psi_{\text{bunch}}\rangle = \frac{|0_s 0_i 1_s 1_i\rangle - |1_s 1_i 0_s 0_i\rangle}{\sqrt{2}} \tag{5.15}$$

$$|\psi_{\text{split}}\rangle = \frac{|1_s 0_i 0_s 1_i\rangle + |0_s 1_i 1_s 0_i\rangle}{\sqrt{2}}. \tag{5.16}$$

This yields the behaviour at the directional coupler output ports where the photon-pair interference fringe has half the period of the bright pump light varying the on-chip phase ϕ. Since we can only simultaneously measure two of the four outputs, we project onto the $|1001\rangle$ state, therefore reducing the maximum rate of coincidences by a factor of two.

5.1.2 Experiment

Characterising on-chip phase modulators

To characterise the on-chip phase modulators, we take the tuneable continuous wave (CW) laser and launch it at the pump frequency for the source interferometer. Launching into the source vertical grating coupler (VGC), the voltage for the thermo-optic phase

modulator (TOPM) is swept and the output transmission is monitored with a photodiode. We fit the resulting curve of the square-voltage against optical transmission (in linear units) to obtain the fitted phase-voltage relationship, which we show in Fig. 5.2a and the voltage-resistance profile in Fig. 5.2b. We find that 22 V are required for the full 2π phase shift.

The tuneable laser is then set to the signal/idler frequencies for the demultiplexing asymmetric Mach-Zehnder interferometers (AMZIs) at the chip output. Again, the transmission against voltage-squared curves are fit and used to determine the single voltage setting that is used to optimise transmission of the single-photon wavelengths for an the entire data set acquisition. The simulated wavelength response* of the wavelength demultiplexing AMZI is shown in Fig. 5.2c.

Experiment for on-chip quantum interference

To drive SFWM in our designed waveguide, we start with a picosecond-pulsed pump laser, centred at 2.0715 μm, which we filter to a width of 1.0 nm using a double-pass grating monochromator. Controlling polarisation, we inject this pump into the fundamental transverse electric (TE) mode of the 510×340 nm^2 waveguide via vertical grating couplers. The waveguide, shown in Fig. 5.3a (see Fig. F.12 for magnified view of the layout), is wrapped into a 7.4-mm nested square spiral with 10 μm radius Euler bends. Coherently pumping both waveguides creates a superposition of the signal and idler photons being generated in both sources (see Sec. 5.1.1). Varying the phase on one arm of the source yields statistics at the beamsplitter output of the form

$$|\psi_{\text{out}}\rangle = \sin\phi\,|\psi_{\text{bunch}}\rangle + \cos\phi\,|\psi_{\text{split}}\rangle\,, \tag{5.17}$$

where $|\psi_{\text{bunch}}\rangle, |\psi_{\text{split}}\rangle$ are defined in Eqns. (5.15) and (5.16). Single photons are then frequency demultiplexed with AMZIs and coupled back off chip. Both channels are filtered with back-to-back grating monochromators to achieve the $>$ 100 dB pump rejection required to attenuate the pump down to the single photon level[178]. The signal and idler photon collection filters are separated by 1.46 THz (20.8 nm) from the pump. The experimental scheme for the time-reversed HOM experiment is shown in Fig. 5.3b. Since we only have two detectors monitoring half of the outputs, we project onto the $|1_s 0_i\rangle_A |0_s 1_i\rangle_B$ half of the state in Eqn. (5.14). During acquisition of the results, we use the calibrated thermo-optic phase-shifters described in Sec. 5.1.2, and set 31 evenly spaced (voltage-squared) phases between 0-20 V. Each data point is integrated for a total of 120 seconds, divided into 20 second sub-integrations. Each data point is measured for 20 seconds before acquiring the next iteration of data collection. This is to ensure that long term measurement effects, such as coupling drift and variable transmission from lab air conditioning cycles (see Fig. 5.2d), are less correlated with the time that the data point was collected. Furthermore, it allows us to put error bars on the data .

5.1.3 Results

Setting the on chip pump power to be 0.32 W, corresponds to a coincidence to accidental ratio (CAR) of 19.3. This pump power is broadly in agreement with the power for the

*Using the mode solved and experimentally verified (Sec. 3.5.1) value of the group index.

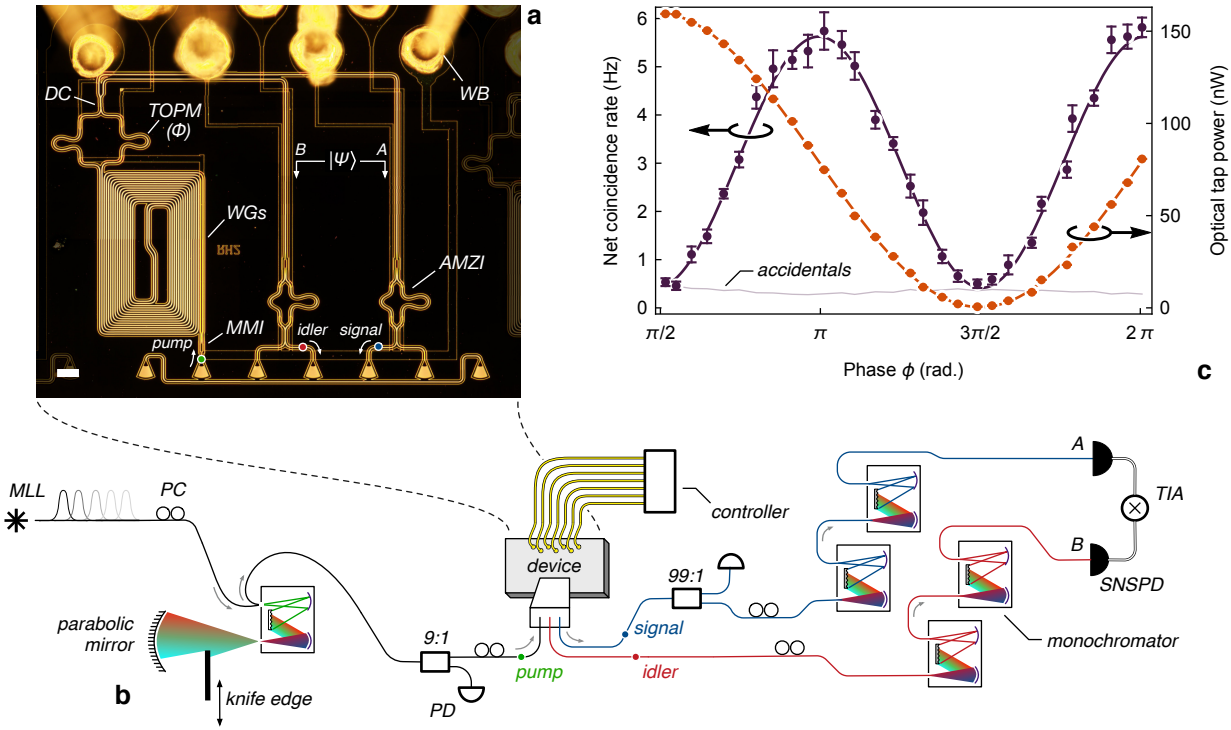

Figure 5.3: Experimental measurement of on-chip quantum interference. **a**, Dark-field optical micrograph of the time-reversed Hong-Ou-Mandel experiment. Multimode interference coupler (MMI), waveguides (WGs), thermo-optic phase modulator (TOPM), directional coupler (DC), asymmetric Mach-Zehnder interferometer (AMZI), wirebond (WB). Scale bar 50 μm. **b**, Experimental scheme. A pump laser is polarisation controlled (PC), filtered with a double-pass monochromator, and coupled into the waveguide circuit, with a monitor photodiode (PD) at the input tap (9:1). A controller provides DC-voltage manipulation of the on-chip quantum state. The signal and idler photons are demultiplexed, filtered and then detected with superconducting nanowire detectors (SNSPDs) and a time interval analyser (TIA). **c**, Quantum and classical interference fringes with varying on-chip phase ϕ, with fitted accidental-subtracted (net) visibility $V = 0.993 \pm 0.017$.

optimal CAR presented in Sec. 4.4.2*. We now present the main result of this section in Fig. 5.3c. Error bars are taken as the the standard deviation of the coincidence count rates in the 20 second sub-integration windows. We see that the quantum (coincidence) fringe has characteristic half-period interference fringes[46,47] relative to the bright light transmission, which agrees with the theoretical result predicted by Eqn. (5.14).

The visibility of the interference fringe determines the photon-number purity of the source. Here, we observe a net visibility of $V = 0.993 \pm 0.017$ (0.862 ± 0.014 raw), where we calculate the visibility of the fringe as[49]

$$V = \frac{X_{\max} - X_{\min}}{X_{\max} + X_{\min}}, \tag{5.18}$$

where $X_{\min}$ and $X_{\max}$ are the minimum and maximum coincidence count rates of the sinusoidal fit, equivalent to a HOM dip visibility of 0.993 (0.852 raw)[60]. The quoted errors

*The length of the spiral in this measurement was 7.2-mm, which is very close to the length of the time reverse HOM source.

of the visibility are from the standard error of the fitted nonlinear model parameters. These results compare favourably to a recently reported HOM interference dip with MIR photon-pairs from a bulk down-conversion crystal[202]. Projecting onto $|1_s 0_i\rangle_A |0_s 1_i\rangle_B$, we observe coincidence rates up to 5.5 ± 0.2 Hz at the interference peak. If we had two more detectors, simultaneously measuring all four chip outputs would double the observed rates.

5.1.4 Discussion

The first demonstration of on-chip interference between pair sources at 1.55 μm had pair rates of 16.6 Hz[46], which is comparable with our measurement if we could monitor all four outputs. From the grating coupler transmission spectra our grating insertion loss at the signal and idler wavelengths was approximately 5.1 and 4.7dB respectively. Current state-of-the-art grating couplers have a loss of 0.5 dB[203]. Implementing this photon-pair source with ultra-low-loss fibre-chip couplers, would improve this rate by more than 8 times. Furthermore, the dark count rate for both detectors was around 6 kHz, which limited the maximum attainable CAR and the bias settings for obtaining higher detection efficiencies. Developing a method to suppress the dark count rate (DCR) would significantly boost the maximum achievable count rates, which could be achieved with waveguide integrated superconducting nanowire single-photon detectors (SNSPDs). Applying an optical bandpass filter at low temperature has also been shown to suppress the dark count rate by 3 orders of magnitude[204] at 1.55 μm—employing this would greatly improve the dark count noise of our experiment.

A CW laser was used in the near infrared (NIR) experiment[46] while a pulsed laser was used for our MIR experiment. Additionally, the NIR implementation used fibre Bragg gratings at the chip output to suppress the narrow linewidth laser, followed by high-extinction wavelength division demultiplexing. Our approach employed two back-to-back grating monochromators at the chip output to achieve the same level of pump suppression, but at the cost of around 10 dB per single photon channel*; strongly motivating the challenge of developing low-loss off- or on-chip filters to boost coincidence count rates. We did attempt to use a double-pass monochromator on the single photon channels, but the extinction was insufficient and residual pump leakage was observed.

The degradation of the chip was evident over the run-time of this experiment. When the time-reversed HOM measurements were first collected, the count rates were significantly higher, indicating that an output grating coupler may have become damaged over the data acquisition period. A measurements summary of the net and raw visibility along with the peak coincidence and accidental rates are summarised in Figs. 5.4a and 5.4b.

A key point is that while the accidental-subtracted visibilities (net) are consistently above 97%, the raw visibility decreases rapidly with the launched peak power coupled to to the waveguide. During the analysis of the source performance, it is essential to check the raw uncorrected visibility. The performance at high power has larger pair-production rates, but the quality of the quantum interference is dramatically reduced.

For the time-reversed HOM interference, the $|\psi_{\text{bunch}}\rangle$ output states of the chip in the Fock basis produces a $N00N$ state-like entanglement where both photons occupy the same output mode. In fact, if degenerate SFWM is used to produce identical photon-

*Translating to a reduction of 100× in the coincidence rate.

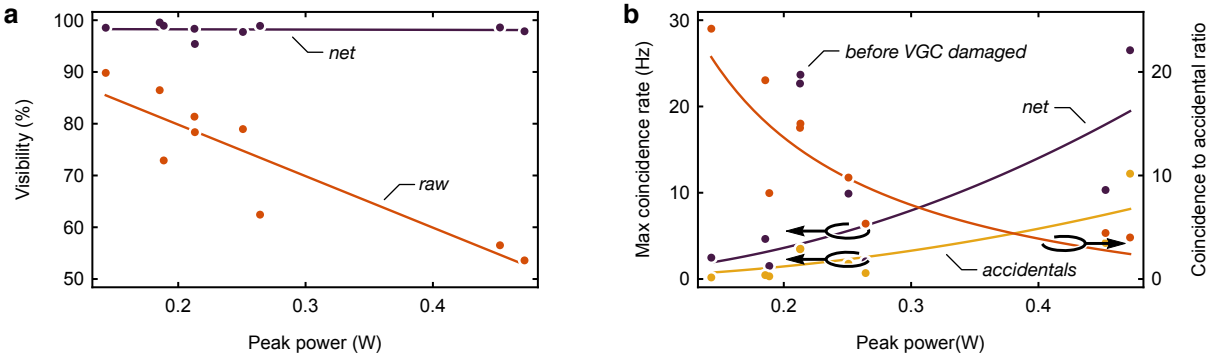

Figure 5.4: Effect of multi-pair emission on the fringe visibility and pair rates. **a**, Net and raw fringe visibilities with varying launched peak power in each waveguide source. **b**, Maximum net and accidental count rates and coincidence to accidental ratio, with different peak powers coupled to the waveguide source. Lines are to guide the eye.

pairs, then the output state $|\psi_{\text{bunch}}\rangle$ is essentially the same as the output path-entangled state from 'traditional' HOM interference[46]. An alternative representation of the entanglement of the source can be seen by inspecting the output states $|\psi_{\text{bunch}}\rangle$, $|\psi_{\text{split}}\rangle$, and writing these in the logical qubit basis using the relation from Eqns. (1.16) and (1.17). In this form they represent maximally entangled path-frequency Bell states

$$|\psi_{\text{bunch}}\rangle = \frac{|1_s1_i0_s0_i\rangle - |0_s0_i1_s1_i\rangle}{\sqrt{2}} = \frac{|00\rangle_{\mathbf{L}} - |11\rangle_{\mathbf{L}}}{\sqrt{2}} = |\Phi^-\rangle \tag{5.19}$$

$$|\psi_{\text{split}}\rangle = \frac{|0_s1_i1_s0_i\rangle + |1_s0_i0_s1_i\rangle}{\sqrt{2}} = \frac{|01\rangle_{\mathbf{L}} + |10\rangle_{\mathbf{L}}}{\sqrt{2}} = |\Psi^+\rangle\,, \tag{5.20}$$

where the subscript $\mathbf{L}$ denotes the path qubit logical encoding. This type of entanglement has been described as 'discrete colour entanglement' and originally was demonstrated with spontaneous parametric down-conversion (SPDC) polarisation-frequency qubits[205]. In our experiment this type of entanglement was not thoroughly tested with a CHSH inequality, thus further evidence is required to substantiate this result as a entanglement resource. We did however demonstrate high visibility quantum interference and the deterministic splitting of SFWM photon-pairs generated by a time-reversed HOM source. This is the essential first steps for establishing any quantum optics platform. The results shown here pave the way for a new generation of experimental MIR integrated quantum optics in silicon.

5.2 Summary

In this chapter, we showed the that the first quantum interference in the mid-infrared was on a silicon chip. For a first attempt, the performance of this device was comparable to the first on-chip quantum interference between photon pair sources in the NIR. We found the visibility of the interference critically depends on the pump power, as well as showing that the inevitable degradation in performance of the photonic waveguide chip with prolonged data collection. Nonetheless, the work presented in this chapter demonstrates the way forward for a new era of integrated photonic quantum information processing in the low-loss mid-infrared.

Statement of work

I designed the source and integrated optics structures presented in this chapter except the 1×2 MMI which was designed by Dr. Joshua Silverstone. I designed the circuit layout used in the time-reversed Hong-Ou-Mandel interference experiment. I performed all of the measurements and associated calibrations presented in this chapter with assistance from Dominic Sulway. The data analysis was performed by myself and Dr. Joshua Silverstone.

Chapter 6

Conclusions and outlook

Quantum optics in the mid-infrared (MIR) has made a new step forwards, pushing the boundaries of what was previously technologically possible. At the outset of the project, we aimed to generate a source of quantum correlated photons on a silicon chip in the 2.1 μm wavelength band, and show high visibility quantum interference. Solving a number of technical challenges along the way including bulk and integrated optics, on- and off-chip filtering, and single-photon detection, led to the successful demonstration of our end goals.

While this research is a critical first step of unleashing quantum optics onto the MIR. the work has only really just begun. This work unlocks a whole host of exciting MIR applications ranging from quantum sensing all the way to quantum information processing. Motivated by the small piece of the puzzle that this thesis addresses, the details of this final chapter answers the question, where do we go next?

6.1 Thesis summary

Information processing has shown to be arguably the most important advancement in all of human existence, leading to the current era forged in history as the 'information age'. The ubiquitous adoption of silicon information processing technologies in nearly every aspect of society has fuelled the search for technology to beat the fundamental limits that accompany the transistor on nanoscopic scales. Silicon has proved itself to be a fantastic optical material, boasting widespread applications from data centre optical interconnects[66], to nonlinear applications like frequency combs[173], parametric amplifiers[119] and lab-on-a-chip sensors[143].

Quantum optics in silicon is not far behind. For many classical implementations of information processing, quantum enhanced analogues exist, all requiring exquisite performance, and with low linear and nonlinear loss. For silicon to truly thrive, its intrinsic nonlinear loss must be curtailed[128], which we have addressed by translating to the MIR at silicon's two-photon band edge.

In chapter 2, we outlined the construction and characterisation of several pieces of

MIR hardware including: a pulsed laser source, variable optical attenuator, off-chip filters for pump filtering and rejection, and superconducting detectors. With the instrumentation developed, chapter 3 discussed the design and implementation of MIR silicon photonics components and circuits, such as the integrated ring filter. This ultimately led to the observation of stimulated four-wave mixing (FWM) from a silicon waveguide source.

Chapter 4, established the performance of our newly acquired MIR single-photon detectors, a detailed appraisal of the waveguide source nonlinear parameters, verifying reduced two-photon absorption (TPA) and enhanced nonlinear refraction, and a 'smoking gun' measurement of quantum-correlated photons produced from spontaneous four-wave mixing (SFWM). Finally, chapter 5 achieved the ambition of the project, realising quantum interference between two integrated waveguide photon-pair sources, with an accidental-subtracted visibility of $V = 0.985$.

The results presented in this thesis are the crucial first steps in integrated MIR quantum optics and pave the way towards truly scalable quantum information processing in silicon. Quantum optics sets the upper bound for performance, due to the stringent requirements for manipulating and measuring single-photons. The technologies we have developed, such as the integrated waveguides, sources, fibre-chip couplers, and integrated filtering circuits, are now readily applicable to the MIR classical photonics community. This work has therefore pushed the forefront of both classical and quantum optics, and has broken new ground in MIR integrated photonics. We now outline some possible directions to take for future research, unlocking the full potential of the platform.

6.2 Future research

Longer wavelengths

The nonlinear figure of merit (FOM), can be used to benchmark the performance of a platform, taking into account the ratio of useful to detrimental nonlinearities described by[121]

$$\mathrm{FOM} = \frac{1}{\lambda}\frac{n_2}{\beta_{\mathrm{TPA}}}. \tag{6.1}$$

We plot the dispersion of the nonlinear FOM in Fig. 6.1d, and see that the asymptotic scaling of performance as we translate to longer wavelengths, as the nonlinear TPA tends to zero at silicon's band edge. According to this metric, our approach already shows a large improvement over current implementations in the near infrared (NIR), with the dominant performance constraint from the efficiency and dark count rate of the superconducting detectors—with a modest time and monetary investment from academia or industry, these could be improved to rival the current state-of-the-art in the NIR. Venturing a little further into the MIR, at around 2.2 μm, TPA is completely extinguished at room temperature (see Fig. 4.3), and the potential of the platform for quantum nonlinear optics becomes unrivalled. The MIR promises to unlock scalable, TPA free integrated silicon photonics for quantum information purposes. Translating beyond the silica transparency region of 4 μm also presents exciting opportunities for gas sensing, but requires new cladding materials such as silicon-on-sapphire[206], or subwavelength gratings in conjunction with bottom cladding removal[61].

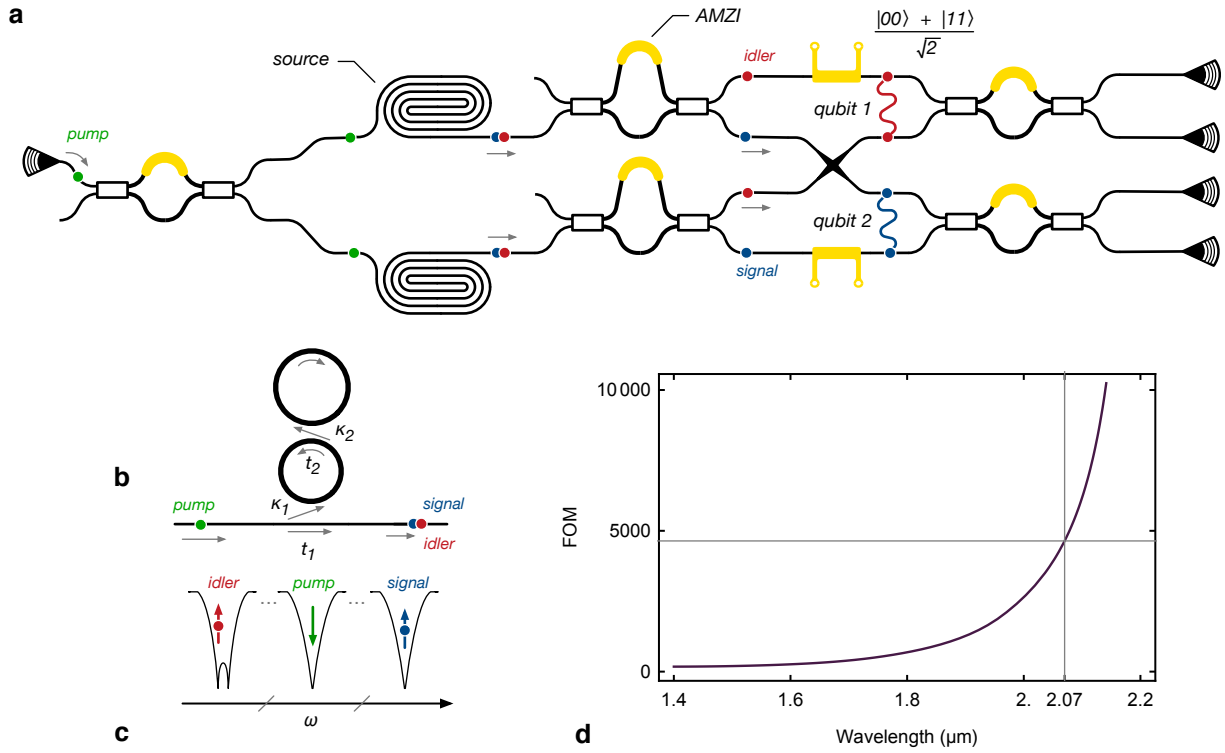

Figure 6.1: Photon pair sources. **a**, Experiment to generate and characterise on-chip entanglement, scheme from Ref. 207. **b**, Coupled ring cavity schematic for generating photon-pairs over a broadband range with dispersion tuning. **c**, Frequency-transmission diagram for the coupled ring cavity. The ring splitting, determined by the second coupling coefficient κ_2, is exploited to pump and collect photon-pairs in different resonances, allowing for energy conservation, even when the group index (i.e. the FSR) dispersion changes over large detunings. **d**, Nonlinear figure of merit (FOM) at room temperature, using a fit for data from Refs. 160,161.

Sources

In chapter 3 we described an integrated source that produced path entangled states, that could deterministically split or bunch the single photon-pairs into the output modes of a directional coupler[46]. An obvious first step into verifying this source of entanglement is to perform a Bell inequality test to prove the nonlocality of the state[207]. The experiment is only modestly more complex than the time-reversed Hong-Ou-Mandel (HOM) measurement and establishes the next step of generating of on-chip Bell states in the MIR. The design for this experiment is already realised on a phase-matched Cornerstone chip (CORN07, see Figs. 6.1a and F.8, page 167), and presents a natural choice for the next MIR quantum experiment in silicon.

So far, we have only shown silicon waveguide sources for photon-pair production. Another important route to explore is with SFWM generation in ring resonators[207], yielding improved footprint, source brightness and pair-production rates[102,103].

Generating photon-pairs far from the pump has attractive applications in gas sensing. Around 3.3 μm sharp absorption lines for methane (CH_4) exist[208] (Fig. 6.2a) and are still in the transparency region of the silica cladding. A source of single photons at this wavelength has an salient connection to environmental leak detection of CH_4, and would enable technologies to mitigate the impact of climate change. To produce photon-

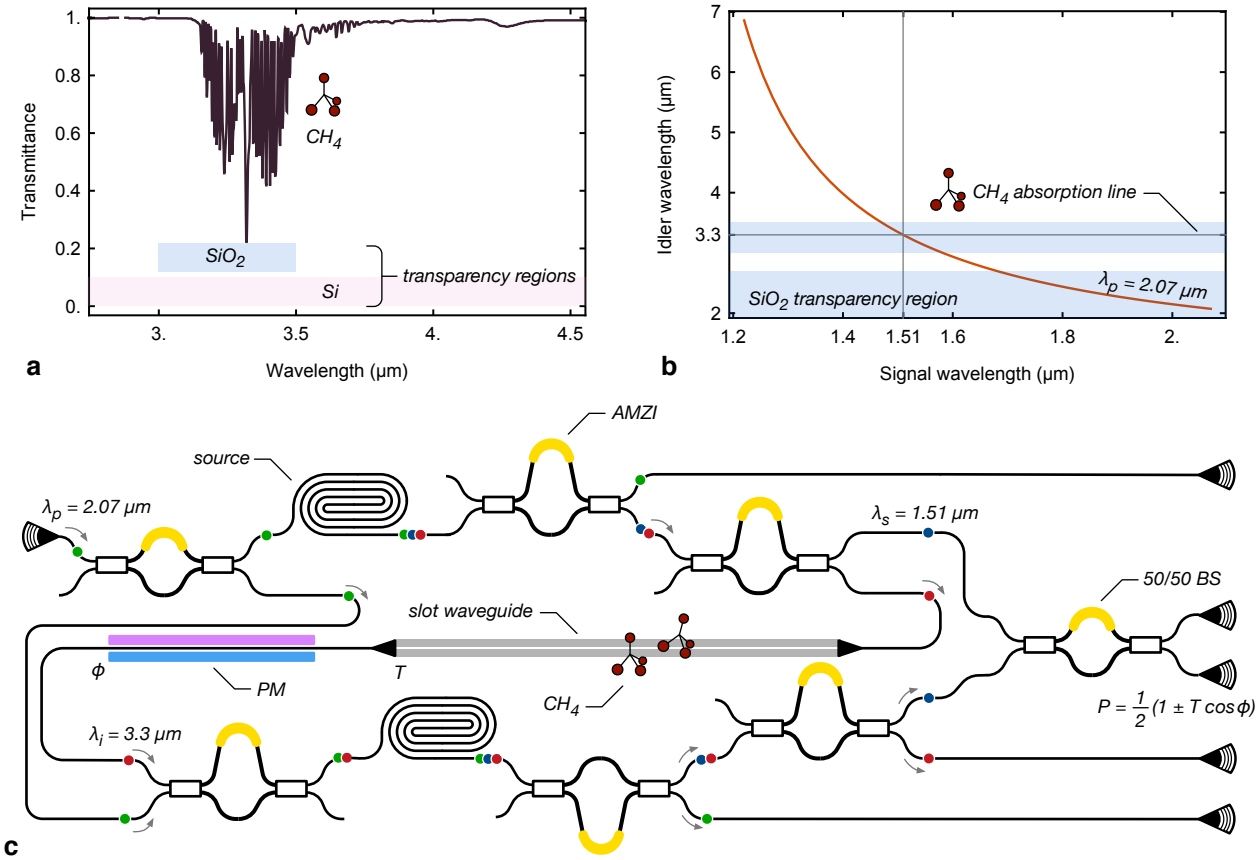

Figure 6.2: Methane gas detection experiment. **a**, Methane transmission spectrum, data from Ref. 208. **b**, Energy matching for the signal and idler photons, with a pump laser centred at $\lambda = 2.07$ μm. **c**, Experimental scheme for gas detection, measuring photons at telecom-band wavelengths. The pump laser (2.07 μm) pumps both sources, after demultiplexing (AMZI) the idler (3.3 μm) output from the first source passes through a slot waveguide and a phase-modulator (PM) before the second source. At the output of the second source, the which path information is erased leading to an interference fringe of the signal photon (1.51 μm) if and only the idler survives the gas detection. The fringe height is then used to calculate the methane concentration.

pairs hundreds of nanometers away from the pump, some extra dispersion engineering tricks are required, since contribution from the fourth-order dispersion starts to become significant at larger wavelength detunings (see appendix C.5). SFWM phase-matching techniques such as intermodal four-wave mixing [120], or coupled ring cavities [209] (see Figs. 6.1c, 6.1d and F.1 on page 160) could be used for producing photon-pairs over large detunings.

The energy-matching condition for signal and idler photons produced from our pulsed mode-locked laser indicates that a stimulating beam at 1.51 μm, would produce amplified emission in the 3.3 μm band—see Fig. 6.2b. The wide availability, and low cost of telecom-band instrumentation has the potential to unlock tuneable stimulated four-wave mixing from a chip in this spectral region.

Sensing

An interesting approach would be to exploit imaging photons without detection[210] for sensing. Here, two nonlinear sources are made to be indistinguishable, with the long-wavelength idler photon produced in the first source passing through a waveguide with transmission T and phase ϕ, and into the second source. At the output of the second source, the 'which source' information is erased leading to interference fringes at the signal wavelength with amplitude $P = (1 \pm T\cos\phi)/2$. For this experiment, the 3.3 μm idler photon could be discarded and the 1.51 μm signal photon, which is easy to detect, carries information about the idler photon, despite not interacting with the CH_4 itself. The presence or absence of a fringe[211], could thus be used to detect CH_4 using high efficiency 1.55 μm detectors, and without coincidences—see Fig. 6.2c for a proposed chip-scale experimental scheme.

In addition to the single photon discrete variable approach, the continuous variable approach to quantum information also benefits from high performance, and increased nonlinear FOM. The gain in precision of squeezing is counteracted by the optical loss*. Generation of integrated sub-shot-noise squeezed states has been shown in silicon nitride[213] and periodically polled lithium niobate waveguides[29], but has remains elusive in crystalline silicon. Hence squeezed coherent states using self-phase modulation (SPM) in the MIR is a promising direction for exploring quantum-enhanced gas detection with bright light. The intrinsically low loss and sensitivity to gas absorption lines in the MIR make silicon a primary candidate for developing compact squeezed light sources for sensing.

Consequently, an innovation of high quantum efficiency and fast MIR waveguide integrated photodiodes is still to be realised. It has been shown that alloying germanium photodiodes with tin extends the sensitivity wavelength range beyond 2 μm[214], although chip-scale foundry integration awaits. In principle, the development of the germanium-tin photodiodes could also see the rise of the integrated single-photon avalanche photodiode capable of detecting single photon.

Systems integration

Large scale single-photon quantum information processing relies on high efficiency detection. The holy grail for integrated quantum optics, and especially in the MIR, would be for large scale waveguide integration of superconducting nanowire single-photon detectors (SNSPDs) on a quantum information processing (QIP) chip[215]. Superconducting waveguide detectors would dramatically reduce the dark count rate from black-body radiation coupling into fibre that we encountered with our MIR detectors (see Sec. 4.3), and would mitigate output fibre-chip coupling loss.

Additionally, cyrogenic temperatures would further boost the nonlinear FOM of our approach at 2.1 μm. It has been shown that TPA significantly drops due to the phonon freeze-out at low temperature; n_2 also decreases, but by a smaller fraction of its room temperature value[121]. Full detector and cryogenic integration would come with associated challenges in complete pump rejection (> 120 dB) in the die.

Filtering on a single chip has historically been limited by a noise floor due to the coupling light into the silicon handle which cannot be spatially rejected with in plane

*See Eqn. (16) of Ref. 212.

waveguide filtering techniques. Recent work has shown coherency broken Bragg gratings[179], that have further improved the rejection to 80 dB. Currently, the only known implementation to achieve the full pump suppression has relied on the use of two-chip stages for filtering[178,180]. In principle, a spatial filter in the silicon slab using etched holes could also help push the performance of a single-chip stage filtering down to the single photon level.

Integration of photon-pair sources with on-chip filtering have been demonstrated in the NIR[180,216]. An important technological development for the MIR will therefore be to integrate sources, filters and eventually detectors onto the same chip. This will involve solving formidable problems, but is certainly within reach of current fabrication capabilities. It is worth reiterating that the prerequisites for quantum optics are particularly demanding. All the progress in developing the infrastructure will also have applications in classical photonics, with far-reaching, broad applications.

Quantum information processing

Small scale quantum information processing demonstrations will be necessary intermediate steps towards full blown quantum computation. We have designed a graph-state generation experiment with two photons, each encoded in four spatial modes (see Fig. F.5, page 164), with arbitrary $U(4)$ 'Clements' scheme interferometers[217] after the pair-sources. This qudit realisation is isomorphic to a four-qubit state, and provides an opportunity for the first MIR graph state quantum information processing experiment.

Linear optical quantum computing (LOQC) still has a large margin between the current and required performance for fault tolerance[32]. Some notable waypoints to achieving this end goal will be to produce ultra-low-loss waveguides, fast low-loss modulators[15] for time multiplexing probabilistic sources, and a bright source of three photon Greenberger-Horne-Zeilinger (GHZ) states[42]. At NIR wavelengths, the record loss is 0.08 dB/m[218] albeit with non-standard fabrication methods.

Proving ultra-low-loss MIR waveguides will be instrumental to the continued development of large scale MIR quantum optics in silicon. Silicon modulators typically suffer from being either high speed *or* low loss. In the MIR, plasma dispersion effects become stronger (see Eqn. (1.77)), facilitating fast and lower power consumption modulators. A way to implement low-loss electro-optic modulation in silicon is via the realisation of MIR DC Kerr effect PIN diodes[219]. These modulators in a multimode waveguide configuration, could provide high speeds and low loss required for multiplexing (see Fig. F.6, page 165). Finally, a source of three-photon GHZ states is of fundamental importance to linear optical quantum computing (LOQC)[42]. Schemes for generating on-chip three-photon path entangled GHZ states have been proposed[220], compelling a MIR integrated implementation.

6.3 Conclusions

In the journey to measure quantum-correlated photon pairs we found that to produce an efficient phase-matched sources of photon-pairs in the fundamental mode at 2.1 μm, silicon waveguide thicknesses must be greater than the industry standard 220 nm films. This also shows the importance of using thick silicon waveguides for long wavelength

applications, and also motivates using different transverse mode orders for achieving the correct dispersion for photon-pair sources in industry standard films.

While operating at 2.07 μm sees an enhanced nonlinear refraction and reduced two-photon absorption, residual TPA remains. Pumping beyond the room temperature two-photon band edge of silicon at 2.2 μm is necessary to eliminate TPA altogether and benefit from the full performance gains of translating to the MIR. While practical constraints in acquiring a pulsed light source was responsible for our wavelength choice, future MIR experiments should exploit any new developments of lasers in the 2.2 μm band to fully quench the effects of TPA.

The effect of blackbody radiation on the detector 'dark' counts were a large source of noise, detrimentally limiting the maximum coincidence to accidental ratio (CAR) for our experiment. A method to combat this noise with either full cryogenic integration of waveguides and detectors, or a cold bandpass filter are necessary to improve the CARs to state-of-the-art levels. Detection efficiencies still require engineering match the NIR SNSPDs, but could be only a few innovations away from achieving similar performance.

Linear propagation and optical coupling losses were quite high in our experiments. Improving the performance of these devices is an obvious target for boosting the measured pair generation rates in the 2.1 μm band. Ultimately, the auxiliary large bulk optics used for our experiments impact the miniaturisation aspect of chip-scale technology—waveguide integrated low-loss pump rejection filtering will greatly enhance pair rates and reduce footprint. If these aspects can be refined, it will present a compelling reason for the silicon quantum photonics community to adopt our approach.

We have shown the feasibility of the 2.1 μm band for quantum optics in silicon by demonstrating quantum interference between photon-pair sources on-chip with a high visibility. In doing so, we have enabled new single-photon technological applications and have taken the crucial first steps for chip-scale quantum nonlinear optics at novel wavelengths.

6.4 Closing remarks

With the genesis of silicon photonics came the inception of integrated silicon quantum photonics. Current experiments spearheading the field, with a handful of photons and postselection, are reaching the technological ceiling. For ultra-large, and ultimately useful implementations facilitated by integrated quantum optics, an approach that can scale is essential. In this work, we pioneered the first steps of MIR quantum information in silicon, producing a SFWM photon-pair source and demonstrating high visibility quantum interference in the 2.1 μm wavelength band, thereby curbing deleterious nonlinear absorption. The approach enables nonlinear, classical and quantum applications thus achieving a new apex of the silicon technology. This work illuminates a way forwards, enabling truly scalable quantum information processing in silicon, and unlocking a plethora of new applications for quantum optics in the MIR. The future is looking bright, because it's light work with long waves.

APPENDIX A

List of symbols, components and apparatus

Operators

Symbol	Meaning	Value	Comments
$\hat{a}_i$	annihilation operator	-	-
$\hat{a}_i^\dagger$	creation operator	-	-
δ_{ij}	Kronecker delta	0,1	-
$\hat{n}$	number operator	$\hat{a}^\dagger\hat{a}$	-
σ_i	Pauli operator	$\{x, y, z\}$	-
$R_i(\theta)$	rotation operator	$e^{i\theta\sigma_i/2}$	-
ρ	density matrix	-	-
$\mathbb{1}$	identity matrix	-	-
$\hat{D}(\alpha)$	displacement operator	-	-
$\hat{H}$	Hamiltonian	-	-
$\hat{U}$	unitary operator	-	-
Π_n	projection operator	-	-
Tr(.)	trace	$\sum_i A_{ii}$	-
∇	vector differential operator	$\{\partial_x, \partial_y, \partial_z\}$	-
E	electric field	-	-
D	displacement field	-	-
P	polarisation field	-	-
B	magnetic field	-	-
H	magnetic field strength	-	-

Table A.1: List of operator symbols.

Constants

Symbol	Meaning	Value	Comments
a_0	Bohr radius	5.292×10^{-11}	m

c	speed of light	2.998×10^{8}	ms^{-1}
e	elementary charge	1.602×10^{-19}	C
h	Planck constant	6.626×10^{-34}	Js
$\hbar$	reduced Planck constant	$h/2\pi$	Js
ϵ_0	vacuum permittivity	8.854×10^{-12}	Fm^{-1}
μ_0	vacuum permeability	$4\pi \times 10^{-7}$	Hm^{-1}
π	-	3.1416	-

Table A.2: List of physical constants.

Notation

Symbol	Meaning	Value	Comments
A_{eff}	effective area	-	m^2
$\mathbb{C}$	complex numbers	-	-
$\mathcal{F}(x,y)$	field profile	-	dimensionless
f	frequency	-	Hz
g	classical parametric gain	-	m^{-1}
I	intensity	P/A_{eff}	Wm^{-1}
k_0	wavevector	$2\pi/\lambda$	m^{-1}
L_{eff}	effective length	-	m
m	integer	-	-
m^*	effective mass	-	kg
n_2	nonlinear refraction	-	$\mathrm{m}^2\mathrm{W}^{-1}$
n_{eff}	effective refractive index	-	-
n_g	group index	-	-
N_c	carrier concentration	-	m^{-3}
$\mathcal{O}(x)$	of the order x	-	-
$\mathbb{N}_0$	natural numbers	0,1,2…	-
P	power	-	W
Q	quality factor	$\Delta\nu/\nu$	-
R	reflectivity	-	-
$\mathbb{R}$	real numbers	-	-
S	Poynting vector	-	-
$\hat{x},\hat{y},\hat{z}$	unit vector	-	-
V	visibility	-	-
X	counts	-	-
$\mathbb{Z}^+$	positive integers	1,2…	-
α	loss	-	m^{-1} or dBcm^{-1}
α_{TPA}	waveguide TPA coefficient	-	$\mathrm{m}^{-1}\mathrm{W}^{-1}$
β	propagation constant	$k_0 n$	m^{-1}
β_n	n^{th} order dispersion	$d^n\beta/d\omega^n$	-
β_{TPA}	bulk TPA coefficient	-	mW^{-1}
η	efficiency/transmission	-	-
$\chi^{(n)}$	n^{th} order electric susceptibility	-	$(\mathrm{mV}^{-1})^{n-1}$
γ	waveguide nonlinearity	$k_0 n_2/A_{\mathrm{eff}}$	Wm^{-1}
θ	angle	-	rad
Θ	phase matching efficiency	-	-

ϕ	phase	-	rad
λ	wavelength	-	m
λ_n	eigenvalue	-	-
Λ	grating pitch	-	m
ξ	squeeze parameter	-	-
τ_c	free carrier lifetime	~ 1	ns
$\Delta\tau$	pulse duration	-	s
ω	angular frequency	$2\pi f$	rad s^{-1}

Table A.3: Frequently used notation.

Components and apparatus

Component name	Abbreviation	Symbol
Grating coupler	VGC	
Waveguide source	WG	
Ring	-	
Directional coupler	DC	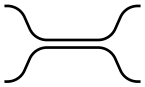
Multimode interference coupler	MMI	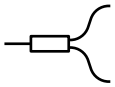
Crosser	-	
Slot waveguide	slot WG	
Electro optic modulator	EOM	
Phase modulator	TOPM	
Mach-Zehnder interferometer	MZI	
Asymmetric Mach-Zehnder interferometer	AMZI	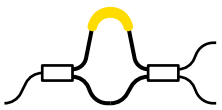

Table A.4: Integrated optics. The original design of these components is credited to Joshua Silverstone[221].

Apparatus name	Abbreviation	Symbol
Quantum cascade laser	QCL	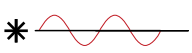
Tuneable CW laser	Lion	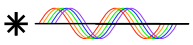
Mode-locked laser	MLL	
Supercontinuum laser	SuperK	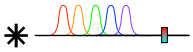
Fibre	-	
Fibre delay	-	
Polarisation controller	polarisation controller (PC)	
50/50 fibre beamsplitter (1 × 2)	1:1	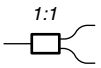
50/50 fibre beamsplitter (2 × 2)	1:1	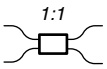
90/10 fibre beamsplitter	9:1	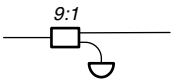
99/1 fibre beamsplitter	99:1	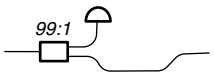
Bandpass filter	BPF	
Knife edge	-	
Curved mirror and knife edge	-	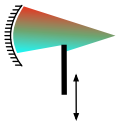
Half waveplate	$\lambda/2$	
Quarter waveplate	$\lambda/4$	

Linear polariser	LP	
Neutral density filter	NDF	
Fibre bench	FB	
Variable optical attenuator	VOA	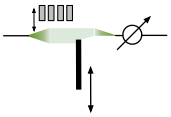
Device under test	DUT	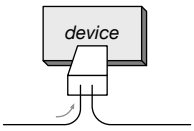
Computer controller	controller	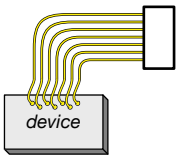
Monochromator	MC	
Photodiode	PD	
Superconducting single-photon detectors	SNSPDs	
Time interval analyser	TIA	
Optical spectrum analyser	OSA	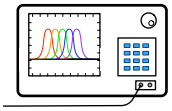
Oscilloscope	-	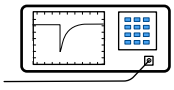

Table A.5: Experimental apparatus.

APPENDIX B

Quantum optics

B.1 Quantum states

A Hilbert space $\mathcal{H}$ is a complex vector space that generalises the notion of Euclidean space to an arbitrary number of (and even infinite) dimensions. We start with defining the bra-ket notation of vectors which will be used to represent quantum states

$$\langle\psi| = \begin{pmatrix} a_1^* & a_2^* & \cdots \end{pmatrix} \qquad |\psi\rangle = \begin{pmatrix} a_1 \\ a_2 \\ \vdots \end{pmatrix}, \tag{B.1}$$

where elements $a_i \in \mathbb{C}$ and the $*$ denotes complex conjugation. Therefore, the bra vector $\langle\psi|$ is the conjugate-transpose or 'Hermitian conjugate', denoted by †, of the ket vector $|\psi\rangle$

$$\langle\psi|^\dagger = |\psi\rangle\,, \qquad |\psi\rangle^\dagger = \langle\psi|\,. \tag{B.2}$$

The inner product of two vectors is a scalar number that determines the similarity between them, and maintains the notion of orthogonality in higher dimensions

$$\langle\psi|\phi\rangle = \begin{pmatrix} a_1^* & a_2^* & \cdots \end{pmatrix} \begin{pmatrix} b_1 \\ b_2 \\ \vdots \end{pmatrix} = \sum_i a_i^* b_i. \tag{B.3}$$

The outer product of two vectors forms a matrix

$$|\psi\rangle\langle\phi| = \begin{pmatrix} b_1 \\ b_2 \\ \vdots \end{pmatrix} \begin{pmatrix} a_1^* & a_2^* & ... \end{pmatrix} = \begin{pmatrix} a_1 b_1^* & a_1 b_2^* & \cdots & a_1 b_N^* \\ a_2 b_1^* & a_2 b_2^* & \cdots & a_2 b_N^* \\ \vdots & \vdots & \ddots & \vdots \\ a_N b_1^* & a_N b_2^* & \cdots & a_N b_N^* \end{pmatrix}. \tag{B.4}$$

For normalised vectors of unit length, orthogonal (orthonormal) basis vectors obey the rule

$$\langle n|m\rangle = \delta_{nm}, \qquad \text{where } \delta_{nm} \begin{cases} 1 \text{ if } n = m \\ 0 \text{ if } n \neq m \end{cases} \tag{B.5}$$

here, δ_{nm} is the Kronecker delta function. Tensors are generalisations of scalars (rank 0), vectors (rank 1) and matrices (rank 2) to arbitrary rank, and are generally represented as a multi-dimensional arrays. For a composite quantum system that is described by multiple subsystems, such as two photon in different spatial locations, the total combined Hilbert space is formed through the tensor product of the subspaces i.e.

$$|\psi_{AB}\rangle = |\psi_A\rangle \otimes |\psi_B\rangle\,, \tag{B.6}$$

throughout this thesis we use the short hand notation for the tensor product of quantum states

$$|a\rangle \otimes |b\rangle \otimes |c\rangle = |a\rangle\,|b\rangle\,|c\rangle = |a, b, c\rangle\,. \tag{B.7}$$

An arbitrary discrete quantum state can be decomposed into to a superposition of its basis vectors

$$|\psi\rangle = \sum_n c_n\,|\phi_n\rangle\,, \tag{B.8}$$

which has complex probability amplitudes that are normalised $\sum_n |c_n|^2 = 1$ and a spectrum of eigenvalues λ_n that is also discrete.

B.2 Operators, measurements and evolution

For a vector in a Hilbert space we now introduce the concept of operators, which map a vector to another. Operators can also mathematically be thought of as matrices leading to the expression

$$A_{ij} = \langle\phi_i|\hat{A}|\phi_j\rangle\,, \tag{B.9}$$

corresponding to the to the matrix elements of the operator. The expectation value of an operator for a given quantum state is similarly given by

$$\langle\hat{A}\rangle = \langle\psi|\hat{A}|\psi\rangle\,. \tag{B.10}$$

For a physical quantity that can be measured—also known as an observable—the matrix must be Hermitian or self-adjoint such that

$$\hat{A} = \hat{A}^\dagger. \tag{B.11}$$

This results in Hermitian matrices having real eigenvalues ($\lambda_n \in \mathbb{R}$), eigenvectors with different eigenvalues are orthogonal, and the eigenvectors can be chosen such that they form a complete orthonormal basis. Any observable has a spectral decomposition

$$\hat{A} = \sum_n \lambda_n \hat{\Pi}_n, \tag{B.12}$$

where if the eigenvalues λ_n are nondegenerate, they have corresponding orthonormal basis vector $|\lambda_n\rangle$ that so that $\langle\lambda_n|\lambda_m\rangle = \delta_{nm}$, that form projectors $\hat{\Pi}_n = |\lambda_n\rangle\langle\lambda_n|$. In measuring a quantum state, the outcome will always be in one of the eigenvalues of the observable. The probability of measuring a quantum state $|\psi\rangle$ existing in the state $|\lambda_n\rangle$ is given by the projection onto the basis states

$$P(\lambda_n) = \langle\psi|\,\hat{\Pi}_n\,|\psi\rangle\,. \tag{B.13}$$

In general, the Born rule describes the probability of finding the quantum state prepared as $|\psi\rangle$ in state $|\phi\rangle$

$$P(|\phi\rangle) = \langle\psi|\phi\rangle\langle\phi|\psi\rangle = |\langle\psi|\phi\rangle|^2. \tag{B.14}$$

A type of operator that is of key importance is the unitary operator. Unitary matrices have the property

$$\hat{U}^\dagger\hat{U} = \hat{U}\hat{U}^\dagger = \mathbb{1} \qquad \longrightarrow \qquad \hat{U}^\dagger = \hat{U}^{-1}, \tag{B.15}$$

or more verbosely, the Hermitian conjugate of a unitary matrix is the matrix inverse. The significance here is that the unitary operation preserves the norm of a vector in Hilbert space and therefore the probability amplitudes of a quantum state. Any unitary matrix can be represented as the matrix exponential of a Hermitian matrix because

$$\hat{U}\hat{U}^\dagger = \exp(i\hat{A})\exp(-i\hat{A}^\dagger) = \exp(i\hat{A})\exp(-i\hat{A}) = \mathbb{1}. \tag{B.16}$$

In fact, all operations that do not destroy probability amplitudes i.e. the set of operations that map a pure quantum state to another are unitary. This means the time evolution of a quantum state for a time-independent Hamiltonian is governed by

$$|\psi_{\text{out}}\rangle = \exp(-i\hat{H}t/\hbar)\,|\psi_{\text{in}}\rangle\,, \tag{B.17}$$

where $\hat{H}$ is the Hamiltonian of the system.

B.3 Quantisation of the electromagnetic field

We now give an overview of the quantisation of the electromagnetic field, closely following the derivation presented in Gerry and Knight[33]. Consider a polarised single mode electromagnetic field in a 1D cavity with perfectly conducting walls at $z = 0$ and $z = L$, shown in Fig. B.1a. The solutions of this model is a standing wave with vanishing field at the boundaries. In vacuum, a Maxwell's equation in SI units are given by

$$\nabla \times \mathbf{E} = \frac{\partial \mathbf{B}}{\partial t} \tag{B.18a}$$

$$\nabla \times \mathbf{B} = \mu_0\epsilon_0\frac{\partial \mathbf{E}}{\partial t} \tag{B.18b}$$

$$\nabla \cdot \mathbf{E} = 0 \tag{B.18c}$$

$$\nabla \cdot \mathbf{B} = 0, \tag{B.18d}$$

where $\nabla = (\partial/\partial x, \partial/\partial y, \partial/\partial z)$, ϵ_0 is the permittivity of free space, μ_0 is the permeability of free space.

We summarise the physical interpretations of these equations. Equation (B.18a) is known as Faraday's law, that states that magnetic fields changing in time produce an electric field, and is the fundamental principle behind electromagnetic induction. Equation (B.18b) is Ampères law, which is interpreted that time varying electric fields with constant currents produce magnetic fields. Equation (B.18c) states that the electric field flux across a surface is proportional to the electrical charges confined within*. Finally, Eqn. (B.18d) states that there are no magnetic monopoles or in other words, the magnetic flux around a closed region is necessarily zero.

*in this case of the vacuum, the charge enclosed in a volume is $\rho_f = 0$, see Sec. E.1.

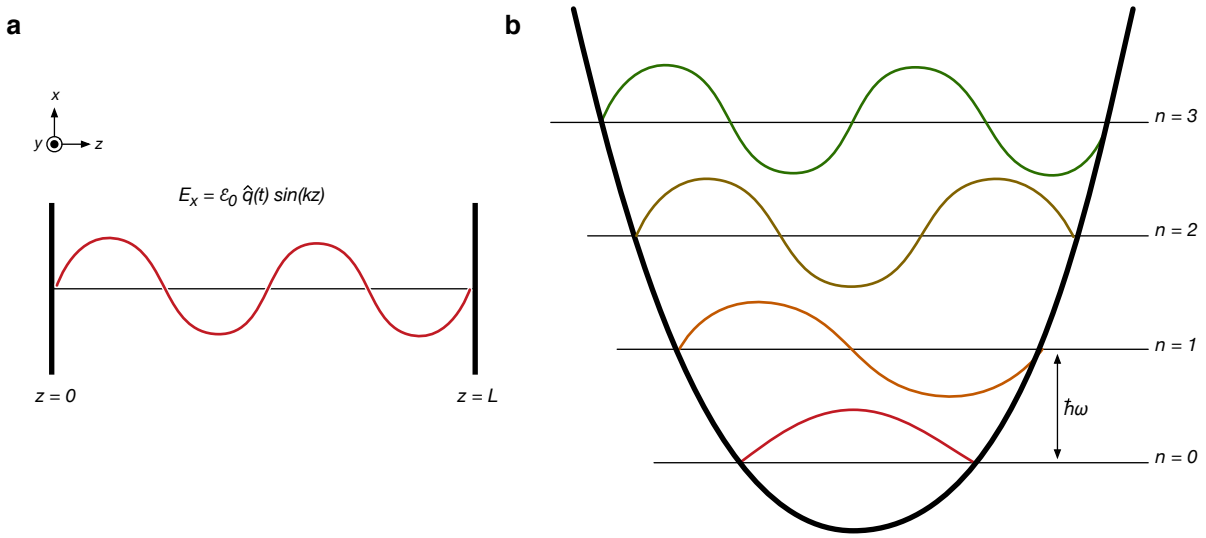

Figure B.1: Quantum harmonic oscillator. **a**, Problem construction, a 1D cavity of length L with perfectly conducting walls. **b**, Energy ladder diagram of the quantum harmonic oscillator. Each level is related by n quanta of energy $(n+1/2)\hbar\omega$.

Since we have a transverse field that is polarised we have $\mathbf{E}(\mathbf{r},t) = \hat{x}E_x(z,t)$ and $\mathbf{B}(\mathbf{r},t) = \hat{y}B_y(z,t)$ are the electric and magnetic fields, polarised along the $\hat{x}$ and $\hat{y}$ unit vectors, respectively. A solution of the electric and magnetic fields that satisfies Eqns. (B.18a) and (B.18b) are

$$E_x(z,t) = \sqrt{\frac{2\omega^2}{V\epsilon_0}}\,q(t)\sin(kz) \tag{B.19a}$$

$$B_y(z,t) = \frac{\mu_0\epsilon_0}{k}\sqrt{\frac{2\omega^2}{V\epsilon_0}}\,\partial_t q(t)\cos(kz), \tag{B.19b}$$

where V is the mode volume, ω is the frequency of the field, k is the wavenumber and the variables $q(t)$ is analogous to the canonical position of a unit mass particle, and $\partial_t q(t) = p(t)$, is therefore the canonical momentum. The Hamiltonian of the classical field is found by integrating the energy densities of the electric and magnetic field over all space

$$H = \frac{1}{2}\iiint\left[\epsilon_0\mathbf{E}^2(\mathbf{r},t) + \frac{1}{\mu_0}\mathbf{B}^2(\mathbf{r},t)\right]d\mathbf{r} \tag{B.20}$$

$$= \frac{1}{2}\int \epsilon_0 E_z^2(z,t) + \frac{1}{\mu_0}B_y^2(z,t)\,dV, \tag{B.21}$$

whose solution using Eqns. (B.19a) and (B.19b), along with the identities $\omega = ck$, and $c^2 = 1/(\mu_0\epsilon_0)$ gives

$$H = \frac{1}{2}(p^2 - \omega^2 q^2). \tag{B.22}$$

To quantise the electromagnetic field, we simply replace the classical canonical position and momentum with their corresponding operators[222] $q \mapsto \hat{q}$ and $p \mapsto \hat{p} = -i\hbar\partial/\partial x$, which obey the commutation relation

$$[\hat{q},\hat{p}] = i\hbar, \tag{B.23}$$

leading to

$$\hat{E}_x(z,t) = \mathcal{E}_0 \hat{q}(t)\sin(kz) \tag{B.24}$$

$$\hat{B}_y(z,t) = \mathcal{B}_0 \hat{p}(t)\cos(kz) \tag{B.25}$$

$$\hat{H} = \frac{1}{2}(\hat{p}^2 + \omega^2 \hat{q}^2), \tag{B.26}$$

where we define $\mathcal{E}_0 = \sqrt{2\omega^2/(V\epsilon_0)}$ and $\mathcal{B}_0 = (\mu_0\epsilon_0/k)\sqrt{2\omega^2/(V\epsilon_0)}$ which are the electric and magnetic fields 'per photon'. Since the operators $\hat{q}$ and $\hat{p}$ are Hermitian (by virtue of the Hamiltonian corresponding to the energy eigenstate observable), they are also observables. We can define these in terms of non-observable creation (raising) and annihilation (lowering) operators $\hat{a}^\dagger$ and $\hat{a}$ which add or remove one quanta of energy $\hbar\omega$

$$\hat{p} = \sqrt{\frac{\hbar}{2\omega}}(\hat{a} + \hat{a}^\dagger) \tag{B.27}$$

$$\hat{q} = i\sqrt{\frac{\hbar\omega}{2}}(\hat{a}^\dagger - \hat{a}). \tag{B.28}$$

We can express the creation and annihilation operators in terms of $\hat{p}$ and $\hat{q}$ as

$$\hat{a} = \sqrt{\frac{1}{2\hbar\omega}}(\omega\hat{q} + i\hat{p}) \tag{B.29}$$

$$\hat{a}^\dagger = \sqrt{\frac{1}{2\hbar\omega}}(\omega\hat{q} - i\hat{p}). \tag{B.30}$$

The bosonic creation ($\hat{a}^\dagger$) and annihilation ($\hat{a}$) operators obey the commutation relation

$$[\hat{a}, \hat{a}^\dagger] = \mathbb{1}. \tag{B.31}$$

Substituting Eqns. (B.27) and (B.28) into (B.26) and using the bosonic commutation relations leads to the quantised Hamiltonian, written in terms of these operators

$$\hat{H} = \hbar\omega\left(\hat{a}^\dagger\hat{a} + \frac{1}{2}\right). \tag{B.32}$$

A schematic illustrating the approximate shape of the wavefunctions for the first four energy eigenstates of the quantum harmonic oscillator is shown in Fig. B.1b.

B.4 Coherent states

Lasers are essential for any quantum optics experiment, as they provide coherent light that is necessary for control, manipulation and generation of quantum states. The coherent state for a laser can be described as the unique eigenstate of the annihilation operators described in the previous section[33]

$$\hat{a}|\alpha\rangle = \alpha|\alpha\rangle. \tag{B.33}$$

To understand the form of $|\alpha\rangle$, without loss of generality take this as the linear superposition of all Fock basis states

$$|\alpha\rangle = \sum_{n=0}^{\infty} c_n |n\rangle. \tag{B.34}$$

Applying the annihilation operator to this state gives

$$\hat{a}\,|\alpha\rangle = \sum_{n=1}^{\infty} c_n \sqrt{n}\,|n-1\rangle\,. \tag{B.35}$$

By comparing coefficients of $|n\rangle$ in Eqns. (B.34) and (B.35) gives the recursive relationship

$$\sqrt{n}\,c_n = \alpha c_{n-1} \tag{B.36}$$

$$c_n = \frac{\alpha}{\sqrt{n}} c_{n-1} = \frac{\alpha^2}{\sqrt{n(n-1)}} c_{n-2} = \ldots \tag{B.37}$$

$$= \frac{\alpha^n}{\sqrt{n!}} c_0. \tag{B.38}$$

All that remains is to normalise the state so that $\langle\alpha|\alpha\rangle = 1$, which implies that $c_0 = \exp(-|\alpha|^2/2)$ giving our final expression

$$|\alpha\rangle = e^{-|\alpha|^2/2} \sum_n \frac{\alpha^n}{\sqrt{n!}} |n\rangle = e^{\alpha\hat{a}^\dagger - \alpha^*\hat{a}}\,|0\rangle\,. \tag{B.39}$$

The last form of this formula can also be thought of as a unitary displacement operator, displacing the vacuum $|0\rangle$ to some amplitude $|\alpha\rangle$

$$\hat{D}(\alpha) = e^{\alpha\hat{a}^\dagger - \alpha^*\hat{a}}. \tag{B.40}$$

The statistics of the coherent state is Poissonian since the probability of detecting a Fock state containing exactly n photons is given by

$$P(|n\rangle) = |\,\langle n|\alpha\rangle\,|^2 = e^{-|\alpha|^2}\frac{|\alpha|^{2n}}{n!}, \tag{B.41}$$

where the mean number of photons in the field $\bar{n} = \langle\alpha|\hat{n}|\alpha\rangle = |\alpha|^2$.

B.4.1 Action of a beamsplitter

Under a beamsplitter transformation with reflectivity η, $\hat{a}^\dagger \mapsto \sqrt{\eta}\,\hat{c}^\dagger + i\sqrt{1-\eta}\,\hat{d}^\dagger$ the displacement operator transforms according to

$$\hat{D}_A(\alpha) \xrightarrow{BS} \exp\left(\alpha(\sqrt{\eta}\,\hat{c}^\dagger + i\sqrt{1-\eta}\,\hat{d}^\dagger) - \alpha^*(\sqrt{\eta}\,\hat{c} - i\sqrt{1-\eta}\,\hat{d})\right) \tag{B.42}$$

$$= \exp\left(\sqrt{\eta}(\alpha\hat{c}^\dagger - \alpha^*\hat{c}) + i\sqrt{1-\eta}(\alpha\hat{d}^\dagger - \alpha^*\hat{d})\right) \tag{B.43}$$

$$= \hat{D}_C(\eta\alpha)\hat{D}_D(\sqrt{1-\eta}\,i\alpha) \tag{B.44}$$

$$\hat{D}_A(\alpha)\,|0\rangle_A\,|0\rangle_B \xrightarrow{BS} |\sqrt{\eta}\,\alpha\rangle_C\,|\sqrt{1-\eta}\,i\alpha\rangle_D\,. \tag{B.45}$$

B.5 Two-mode squeezed vacuum

In general, a two-mode squeezed vacuum produces photons with the two-mode squeezing operator[33]

$$\hat{S}_{II}(\xi) = \exp(\xi\,\hat{a}^\dagger\hat{b}^\dagger - \xi^*\hat{a}\hat{b}) \tag{B.46}$$

$$\hat{S}_{II}(\xi)\,|\text{vac}\rangle = |\xi_{II}\rangle\,. \tag{B.47}$$

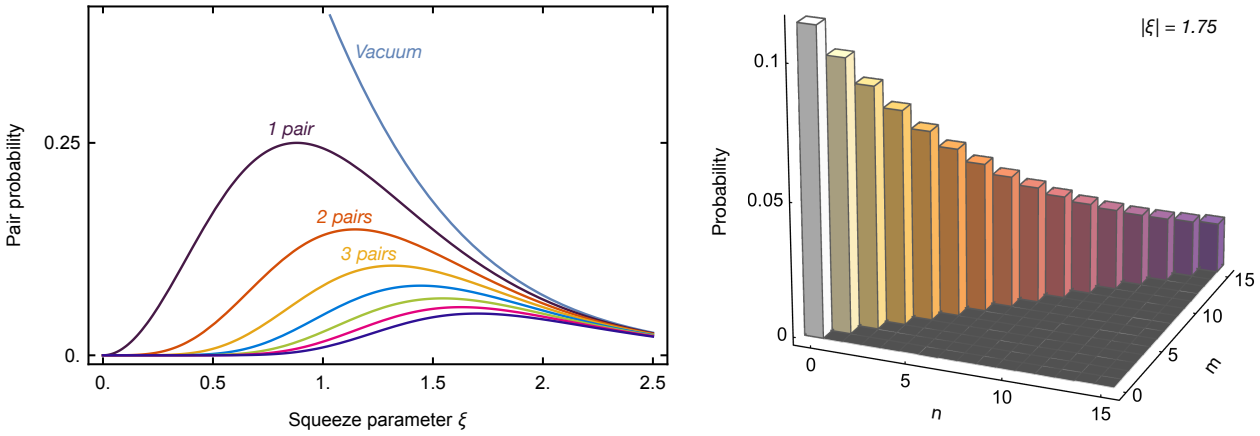

Figure B.2: Two-mode squeezed vacuum pair production probability

Using the Baker-Campbell-Hausdorff lemma, the annihilation operators transform with the two-mode squeezing operator as

$$\hat{S}_{II}(\xi)\hat{a}\hat{S}^{\dagger}_{II}(\xi) = \hat{a}\cosh|\xi| + e^{i\theta}\hat{b}^{\dagger}\sinh|\xi| \tag{B.48}$$

$$\hat{S}_{II}(\xi)\hat{b}\hat{S}^{\dagger}_{II}(\xi) = \hat{b}\cosh|\xi| + e^{i\theta}\hat{a}^{\dagger}\sinh|\xi| \tag{B.49}$$

where we express $\xi = |\xi|e^{i\theta}$. Since the annihilation operator acting on the vacuum gives

$$\hat{a}|00\rangle = 0, \tag{B.50}$$

we can insert the identity after the operator, and action of an operator before the annihilation operator also gives the zero giving us

$$\hat{a}\hat{S}^{\dagger}_{II}(\xi)\hat{S}_{II}(\xi)|00\rangle = 0 \tag{B.51}$$

$$\hat{S}_{II}(\xi)\hat{a}\hat{S}^{\dagger}_{II}(\xi)\hat{S}_{II}(\xi)|00\rangle = 0 \tag{B.52}$$

$$\hat{S}_{II}(\xi)\hat{a}\hat{S}^{\dagger}_{II}(\xi)|\xi_{II}\rangle = 0 \tag{B.53}$$

$$(\hat{a}\cosh|\xi| + e^{i\theta}\hat{b}^{\dagger}\sinh|\xi|)|\xi_{II}\rangle = 0 \tag{B.54}$$

$$(\mu\hat{a} + \nu\hat{b}^{\dagger})|\xi_{II}\rangle = 0, \tag{B.55}$$

where $\mu = \cosh|\xi|$ and $\nu = e^{i\theta}\sinh|\xi|$. Expanding the state in terms of its coefficients $|\xi_{II}\rangle = \sum_{nm} c_{nm}|nm\rangle$ and applying the mode operators to the state turns Eqn. (B.55) into

$$\sum_{nm} c_{nm}\left(\mu\sqrt{n}\,|n-1,m\rangle + \nu\sqrt{m+1}\,|n,m+1\rangle\right) = 0 \tag{B.56}$$

$$\sum_{nm} c_{nm}\mu\sqrt{n}\,|n-1,m\rangle = -\sum_{n'm'} c_{n'm'}\nu\sqrt{m'+1}\,|n',m'+1\rangle\,. \tag{B.57}$$

Equating coefficients of the states, we see that the relationship $n' = n-1$ and $m' = m-1$ must hold therefore

$$c_{nm}\mu\sqrt{n}\,|n-1,m\rangle = -c_{n-1,m-1}\nu\sqrt{m-1+1}\,|n-1,m-1+1\rangle \tag{B.58}$$

$$c_{nm}\mu\sqrt{n}\,|n-1,m\rangle = -c_{n-1,m-1}\nu\sqrt{m}\,|n-1,m\rangle \tag{B.59}$$

$$c_{nm} = c_{n-1,m-1}(-1)\left(\frac{\nu}{\mu}\right)\left(\frac{\sqrt{m}}{\sqrt{n}}\right) = c_{n-2,m-2}(-1)^2\left(\frac{\nu}{\mu}\right)^2\left(\frac{\sqrt{m}}{\sqrt{n}}\right)^2 = \ldots. \tag{B.60}$$

We are only interested in the state containing the the two-mode vacuum, so from the recursive relationship in the last line, we infer

$$c_{nm} = c_{00}(-1)^n \left(\frac{\nu}{\mu}\right)^n \left(\frac{\sqrt{m}}{\sqrt{n}}\right)^n \delta_{nm} \tag{B.61}$$

$$c_{nn} = c_{00}(-1)^n e^{in\theta} \tanh^n |\xi|. \tag{B.62}$$

Enforcing the state is normalised yields $c_{00} = \text{sech}|\xi|$ giving our two mode squeezed vacuum state

$$|\xi_{II}\rangle = \text{sech}|\xi| \sum_n e^{in\theta} \tanh^n |\xi| \, |nn\rangle \, . \tag{B.63}$$

The probability distributions for the two-mode squeezing operator is presented in Fig. B.2

APPENDIX C

Integrated optics and design methods

C.1 Slab waveguides

It is possible to analytically derive the modes supported in the slab waveguide, where we now follow a similar treatment of Ref. 66. For a symmetrical waveguide where the top and bottom cladding has the same refractive index, as shown in Fig. C.1, the propagation of light is facilitated by total internal reflection at the upper and lower interfaces. Recall that the critical angle for total internal reflection $\theta_c = \sin^{-1}(n_2/n_1)$, thus for all angles of propagation greater than the critical angle, light is guided. The wavevector of the light propagating in the slab is given by $k = n_1 k_0$ and propagates at some angle θ_1 to the normal of the interface. By simple trigonometry, the z and y components of wavevector are

$$k_y = n_1 k_0 \cos\theta_1 \tag{C.1}$$

$$k_z = n_1 k_0 \sin\theta_1. \tag{C.2}$$

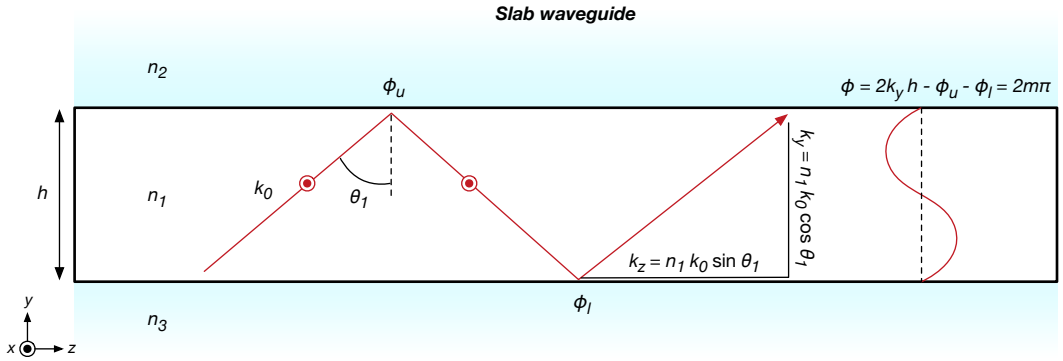

Figure C.1: Slab waveguide construction. A field polarised in the x direction propagates in the z direction. The allowed modes propagation angles θ_1 correspond to a standing wave between the two interfaces with a round trip of $\phi = 2m\pi$.

Consider a wave that travels exclusively in the y-direction, which is reflected at the interfaces of the slab waveguide forming a standing wave. For one round trip of this wave (for a slab of height h) the phase acquired is then

$$\phi_t = 2k_y h = 2k_0 n_1 h \cos\theta_1 - \phi_u - \phi_l, \tag{C.3}$$

where the additional phase shift terms ϕ_u, ϕ_l arise from reflections at the upper and lower interfaces. Since this is a standing wave, the total phase for one round trip must be a multiple of 2π, i.e. $\phi_t = 2m\pi$ for $m \in \mathbb{N}_0$. Note that for this eigenvalue equation, there are discrete values of θ_1 that lead to this condition, leading to our labelled modes of propagation m (indexed from 0). In this construction, the phase induced from reflection at the upper and lower boundaries are the same due to the symmetric cladding index. The Fresnel reflection coefficient for transverse electric (TE) polarised light is

$$r_{\mathrm{TE}} = \frac{n_1 \cos\theta_1 - \sqrt{n_2^2 - n_1^2 \sin^2\theta_1}}{n_1 \cos\theta_1 + \sqrt{n_2^2 - n_1^2 \sin^2\theta_1}}, \tag{C.4}$$

where for total internal reflection, the light is completely reflected implying that $|r| = 1 \rightarrow r_{\mathrm{TE}} = \exp(i\phi_{\mathrm{TE}})$, is complex and has imparted a phase shift on the reflected wave. Solving for the angle ϕ_{TE} gives*

$$\phi_{TE} = 2\tan^{-1} \frac{\sqrt{\sin^2\theta_1 - \left(\frac{n_2}{n_1}\right)^2}}{\cos\theta_1}. \tag{C.5}$$

Finally, substituting Eqn. (C.5) into Eqn. (C.3) and rearranging yields

$$\tan\left[\frac{k_0 n_1 h \cos\theta_1 - m\pi}{2}\right] = \frac{\sqrt{\sin^2\theta_1 - (n_1/n_2)^2}}{\cos\theta_1}. \tag{C.6}$$

C.2 Grating couplers

To understand how to design gratings we now outline the theory of their operation, where we follow the derivation from Ref. 66. For an incident light wave, with wavevector k, the component in the propagation z-direction of the slab waveguide, with propagation constant $\beta_{\mathrm{wg}} = n_{\mathrm{eff}} k_0$, is given by

$$k_z = n_{\mathrm{clad}} k_0 \sin\theta_i, \tag{C.7}$$

and the grating has a wavevector $k_\Lambda = 2m\pi/\Lambda$, for $m \in \{\pm 1, \pm 2, \ldots\}$ which modulates the propagation constant of the slab, corresponding to different diffraction orders m of the grating with a grating period Λ—shown in Fig. C.2. The phase-match condition is simply when the incident wavevector matches the grating modulated propagation constant i.e.

$$k_z = \beta_{\mathrm{wg}} + k_\Lambda \tag{C.8}$$

$$n_{\mathrm{clad}} k_0 \sin\theta_i = n_{\mathrm{eff}} k_0 + \frac{2m\pi}{\Lambda}. \tag{C.9}$$

For a guided waveguide mode, the cladding index must be lower than effective index and $\sin\theta_i \leq 1$, meaning the sign of m must be negative to ensure phase-matching. Most

*and use of the trigonometric identity $\tan^{-1}(z) = \frac{i}{2}\log\left(\frac{1-iz}{1+iz}\right)$.

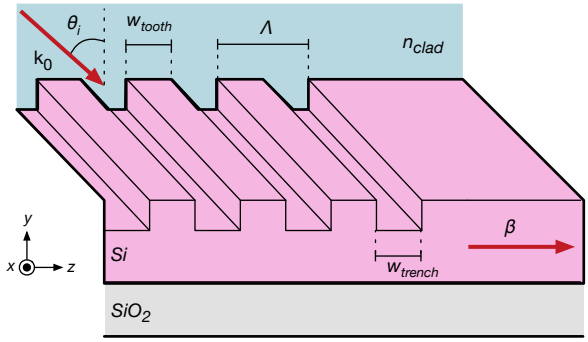

Figure C.2: Grating couplers overview. In plane isometric view of the grating, with incident light at angle θ_i, period Λ, tooth and trench widths $w_{\text{tooth}}, w_{\text{trench}}$ and top cladding with index n_{clad}.

grating couplers are designed for the $m = -1$ diffraction order. Rearranging Eqn. (C.9) for the grating period Λ yields

$$\Lambda = \frac{\lambda}{n_{\text{eff}} - n_{\text{clad}} \sin\theta_i}. \tag{C.10}$$

When designing a uniform grating coupler, usually the parameters that define our desired structure will be the incident angle and the central wavelength of the coupler. To make an efficient grating coupler, the effective index of the grating is the free parameter allowing the phase-matching condition to be satisfied. Typically, foundries fix the partial etch depth so the effective indices of the tooth and trench slab modes must be calculated. This is evaluated numerically or analytically with the asymmetric slab waveguide eigenvalue equation for TE modes*

$$[k_0 n_{\text{core}} h \cos\theta_1 - m\pi] = \tan^{-1}\left[\frac{\sqrt{\sin^2\theta_i - (n_{\text{core}}/n_{\text{box}})^2}}{\cos\theta_i}\right] + \tan^{-1}\left[\frac{\sqrt{\sin^2\theta_i - (n_{\text{core}}/n_{\text{clad}})^2}}{\cos\theta_i}\right]. \tag{C.11}$$

This equation must be solved graphically or numerically—I used the Python programming language to numerically calculate the solutions of this for the fundamental TE slab modes. To determine the refractive index to use as the input for Eqn. (C.11) of the silicon and the silica cladding, the Sellmeier equation can be used[73]

$$n(\lambda) = \sqrt{1 + \sum_{i=1}^{3} \frac{B_i \lambda^2}{\lambda^2 - C_i}}, \tag{C.12}$$

where n is the refractive, and coefficients for B_i and C_i are determined by the material. For silicon and silica the refractive index at room temperature† given by[224,225] the following table:

To compute the effective index of the slab modes, the value of refractive index from the Sellmeier model should be input into Eqn. (C.11), giving two effective indices for the

*as opposed to Eqn. (C.6), here the top and bottom cladding may have different refractive indices. See Ref. 66 for the TM eigenvalue equations.

†For the temperature dependent Sellmeier models see Refs. 74,223

Material	B_1	B_2	B_3	C_1	C_2	C_3
Silicon	10.6684293	0.003043475	1.54133408	0.301516485	1.13475115	1104.0
Silica	0.6961663	0.4079426	0.8974794	0.0684043	0.1162414	9.896161

Table C.1: Sellmeier coefficients of silicon and fused silica from Refs 74,224.

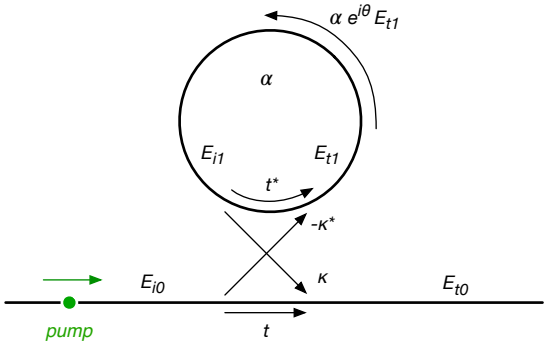

Figure C.3: Schematic of the single bus ring resonator.

tooth and trenches of the grating. The fill factor d (ratio of tooth width to grating period) determines the grating effective index, taken as the weighted average of the tooth and trench slab modes

$$n_{\text{eff}} = d \cdot n_{\text{tooth}} + (1 - d) \cdot n_{\text{trench}}. \tag{C.13}$$

Finally, for any designed incident angle θ_i, wavelength λ, cladding and grating slab modes, the grating period Λ can be calculated inserting these into Eqn. (C.9).

C.3 Ring resonators

We now give the background of a single bus ring resonator operation. A pictorial representation of the system is shown in Fig. C.3. Light enters the system from the left hand side through the input waveguide, and is incident on the coupling bus—see Fig. C.3 for a schematic. The transfer matrix for the electric fields of the device is given by[107]

$$\begin{pmatrix} E_{t0} \\ E_{t1} \end{pmatrix} = \begin{pmatrix} t & \kappa \\ -\kappa^* & t^* \end{pmatrix} \begin{pmatrix} E_{i0} \\ E_{i1} \end{pmatrix}, \tag{C.14}$$

where κ is cross coupling coefficient and t is the reflectivity of the coupler. Consequently, the coefficients obey

$$|\kappa|^2 + |t|^2 = 1. \tag{C.15}$$

To simplify the algebra, we set the input field equal to unity. The input field to the coupler after one round trip of the ring is described by

$$E_{i1} = \alpha \cdot e^{i\theta} E_{t1}, \tag{C.16}$$

where the phase from a round trip of the ring is given by $\theta = \beta L = \frac{2\pi n_{\text{eff}}}{\lambda} L$, where β is the propagation constant and L is the cavity length. From the previous equations we can describe the electric field at the output bus

$$E_{t1} = \frac{t - \alpha e^{i\theta}}{1 - \alpha t^* e^{i\theta}}. \tag{C.17}$$

Making the substitution $t = |t|e^{i\phi}$, where $|t|$ is the coupling loss and ϕ is the phase of the coupler, the power with some algebra at the output is then described by

$$P_{t1} = |E_{t1}|^2 = \frac{|t|^2 - \alpha^2 - 2\alpha|t|\cos(\theta+\phi)}{1+\alpha^2|t|^2 - 2|t|\cos(\theta+\phi)}. \tag{C.18}$$

When the light in the ring completes an integer number of wavelengths i.e. $\theta+\phi = 2m\pi$,this reduces to

$$P_{t1} = \frac{(\alpha - |t|)^2}{(1-\alpha|t|)^2}. \tag{C.19}$$

In the case where $|t| = \alpha$, i.e. the coupling losses of the ring balance the round trip losses, the transmitted power at the output waveguide drops to zero. This phenomena, known as critical coupling, is due to the destructive interference. When a ring is critically coupled, the light propagates indefinitely inside the ring until it's field has decayed from scattering and propagation losses.

Resonators give a cavity enhancement on the pair-generation rates by a factor[201]

$$F = \left|\frac{E_{t1}}{E_{i0}}\right| = \left|\frac{\kappa}{\alpha t e^{i(\theta+\phi)} - 1}\right|. \tag{C.20}$$

For critical coupling on resonance and a low loss ring, this simplifies to

$$F = \frac{1}{\kappa} \approx \sqrt{\frac{Q}{m\pi}}, \tag{C.21}$$

where Q is the quality factor that determines the resonance linewidth

$$Q = \frac{\Delta\nu}{\nu} = \frac{\Delta\lambda}{\lambda}. \tag{C.22}$$

C.4 Mach-Zehnder interferometers

C.4.1 Derivation of the free spectral range

Asymmetric Mach-Zehnder interferometers (AMZIs) provide a method for frequency demultiplexing on a chip. A path length difference between two waveguides in the AMZI results in a sinusoidal frequency dependent response at the output. The spacing in frequency or wavelength between minima or maxima of the AMZI spectrum is known as the free spectral range (FSR).

The derivation of the FSR is now given. The phase accumulated from propagating through one arm of an AMZI is given by

$$\phi = \frac{2\pi n_{\text{eff}} L}{\lambda}, \tag{C.23}$$

where L is the length and λ is the wavelength of light. Assuming the waveguides propagation constants are identical and lossless, for a single given wavelength of light, the phase difference between the two arms is given by

$$\Delta\phi = \frac{2\pi n_{\text{eff}} L_1}{\lambda} - \frac{2\pi n_{\text{eff}} L_2}{\lambda} = \beta\Delta L = 2m\pi, \tag{C.24}$$

where constructive interference occurs when round trip phase is an integer multiple of $2m\pi$ where $m \in \mathbb{Z}^+$. Since we are concerned with the wavelength spacing between resonances, these occur when different wavelength (and therefore propagation constants) have $\Delta m = 1$. In a waveguide, the round trip depends on the propagation constant at the two different wavelength for which the resonances occur so that

$$(\beta_m - \beta_{m+1})\Delta L = 2\pi(m - (m+1)) \tag{C.25}$$

$$\Delta\beta\Delta L = -2\pi. \tag{C.26}$$

We can now introduce the FSR $\Delta\lambda$ in wavelength units

$$\Delta L\frac{\Delta\beta}{\Delta\lambda} = -\frac{2\pi}{\Delta\lambda}. \tag{C.27}$$

If we assume that the dispersion of the propagation constant isn't too large, we can approximate that the slope of the fit is linear, we can make the expression with $\Delta\beta$ into a derivative

$$\Delta L\frac{d\beta}{d\lambda} = -\frac{2\pi}{\Delta\lambda}. \tag{C.28}$$

Substituting the expression for the propagation constant $\beta = 2\pi n_{\text{eff}}/\lambda$

$$\Delta L\frac{d}{d\lambda}\left(\frac{2\pi n_{\text{eff}}(\lambda)}{\lambda}\right) = 2\pi\Delta L\left(\frac{1}{\lambda}\frac{dn}{d\lambda} - \frac{n}{\lambda^2}\right) = -\frac{2\pi}{\Delta\lambda} \tag{C.29}$$

$$\frac{\Delta L}{\lambda^2}n_g = \frac{1}{\Delta\lambda}, \tag{C.30}$$

where we make the substitution on the left hand side for $n_g = n - \lambda dn/d\lambda$ which we define as the group index. Taking the reciprocal of both sides, gives our expression for the free spectral range

$$\text{FSR}_\lambda = \frac{\lambda^2}{n_g\Delta L} \tag{C.31}$$

$$\text{FSR}_\nu = \frac{c}{n_g\Delta L}, \tag{C.32}$$

where c is the speed of light, n_g is the group index ΔL is the cavity length, λ is the wavelength and $\text{FSR}_{\nu,\lambda}$ are the free spectral range in frequency and wavelength units, respectively.

C.4.2 Designing asymmetric Mach-Zehnder interferometers

Asymmetric Mach-Zehnders (Fig. C.4b) are commonly used in integrated optics circuits for frequency demultiplexing[226]. In integrated quantum optics this is used to demultiplex the pump from the copropagating signal and idler photons[178], as well as separating the signal and idler into different waveguides. When designing photonic chips, an easy mistake to make* is to get the FSR of the AMZI wrong. To save future generations from making this critical error we give a verbose formula for designing the AMZI FSR. For non-degenerate four-wave mixing (FWM), there are three frequencies involved for the pump, signal and idler: ν_p, ν_s, ν_i. Note that the pump-signal frequency detuning is the same as

*I unfortunately made this mistake more than once!

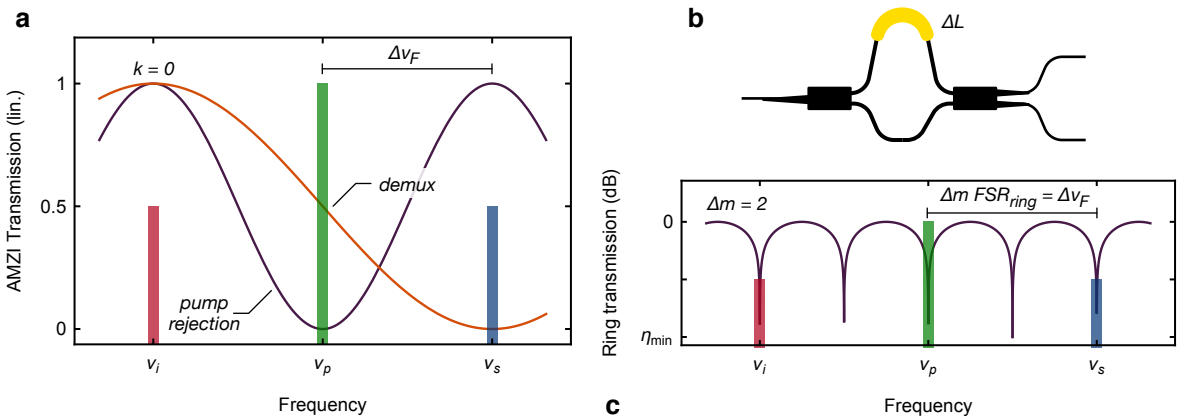

Figure C.4: Asymmetric Mach-Zehnders AMZIs for filtering. **a**, Transmission spectrum of a pump rejection and signal-idler demultiplexing AMZIs, for the lowest ($k = 0$) order filter. **b**, Schematic of a AMZI with path length difference ΔL. **c**, Transmission spectrum of a ring resonator, with the selected signal and idler two resonance ($\Delta m = 2$) away from the pump.

the pump-idler detuning. Defining our target separation of the FWM pump-signal detuning as $\Delta\nu_F \equiv \nu_s - \nu_p$, for a waveguide source the pump-rejection stage should have the relationship

$$\Delta\nu_{\text{pump reject}} = \frac{\Delta\nu_F}{k+\frac{1}{2}} \qquad \text{for } k \in \mathbb{N}_0, \tag{C.33}$$

and the signal-idler demultiplexing stage should have the relationship

$$\Delta\nu_{\text{demux}} = \frac{\Delta\nu_F}{k+\frac{1}{4}} \qquad \text{for } k \in \mathbb{N}_0. \tag{C.34}$$

For the lowest order, and hence largest collection bandwidth response of the AMZI filter, $k = 0$ should be chosen. In terms of AMZI path length differences, these equations may be written

$$\Delta L_{\text{pump reject}} = \frac{c}{n_g \Delta\nu_F}\left(k+\frac{1}{2}\right) \tag{C.35}$$

$$\Delta L_{\text{demux}} = \frac{c}{n_g \Delta\nu_F}\left(k+\frac{1}{4}\right). \tag{C.36}$$

The transmission function of the lowest order pump rejection and demultiplexing AMZIs is illustrated in Fig. C.4a. If a ring resonator is being used as a source, the signal and idler photons are emitted in resonances spaced by an integer number of FSRs, Δm, away from the resonance that is being pumped. The pump-signal detuning is then fixed by an integer number of the rings FSR, i.e. $\Delta\nu_F = \Delta m \text{FSR}_{\text{ring}}$. The Eqns. (C.33) and (C.34) can then be used to choose the FSR of the AMZIs. In the case where the ring resonator has the same waveguide (and hence n_g) as the AMZIs, the path length difference for the AMZIs is given by

$$\Delta L_{\text{pump reject}} = \frac{L_{\text{ring}}}{\Delta m}\left(k+\frac{1}{2}\right) \tag{C.37}$$

$$\Delta L_{\text{demux}} = \frac{L_{\text{ring}}}{\Delta m}\left(k+\frac{1}{4}\right). \tag{C.38}$$

To clarify this, a ring source with an AMZI possessing an identical waveguide is depicted in Fig. C.4c, with a side resonance spacing of $\Delta m = 2$.

C.5 Phase-matching and the GVD

We start with momentum matching condition described by Eqn. (1.74), and apply the series expansion about the pump frequency ω_p

$$\Delta k = 2\beta_p - \beta_s - \beta_i \tag{C.39}$$

$$= 2\left(\beta_0 + \beta_1(\omega_p - \omega_p) + \frac{\beta_2}{2}(\omega_p - \omega_p)^2 + \ldots\right) - \left(\beta_0 + \beta_1(\omega_p - \omega_s) + \frac{\beta_2}{2}(\omega_p - \omega_s)^2 + \ldots\right) - \left(\beta_0 + \beta_1(\omega_p - \omega_i) + \frac{\beta_2}{2}(\omega_p - \omega_i)^2 + \ldots\right). \tag{C.40}$$

First we note that all terms in pump expansion except β_0 cancel and that using the energy matching constraint from Eqn. (1.73) we can express $\omega_p - \omega_s = -(\omega_p - \omega_i)$ which leads to

$$\Delta k = 2\beta_0 - \left(\beta_0 + \beta_1(\omega_p - \omega_s) + \frac{\beta_2}{2}(\omega_p - \omega_s)^2 + \ldots\right) - \left(\beta_0 + (-1)\beta_1(\omega_p - \omega_s) + (-1)^2\frac{\beta_2}{2}(\omega_p - \omega_s)^2 + \ldots\right). \tag{C.41}$$

The lowest order term β_0 cancels, and we note that for β_n with n odd also cancel leaving only even terms of the expansion

$$\Delta k = -\beta_2(\omega_p - \omega_s)^2 - \frac{\beta_4}{12}(\omega_p - \omega_s)^4 + \ldots \tag{C.42}$$

$$\approx -\beta_2(\omega_p - \omega_s)^2. \tag{C.43}$$

C.6 FDTD simulation methodology

Finite-difference time-domain (FDTD) simulations were used to validate integrated optics components in Lumerical FDTD solutions. The design parameters were usually calculated from mode solving simulations with a corresponding analysis. In the case of grating couplers (see appendix C.2), numerical techniques for calculating the slab modes were employed to find the target design parameters. Some generic initial steps that were performed in both grating coupler and beamsplitter FDTD simulations are now given, with more detail on the specific structures presented in the following subsections.

The first step before starting any simulations is ensuring the material dispersion parameters are appropriately fitted. In the Lumerical software, the materials 'Si (Silicon) - Palik' and 'SiO2 (Glass) - Palik'[227] are opened in the material explorer, and the simulation bandwidth set from 1.2–2.5 μm to ensure a smooth fit as seen in Figs. C.5a and C.5b. These are fit with a passive fit multi-coefficient model with 3 coefficients, a fit tolerance of 0.01, and an imaginary weight of 0.001. This often leads to very small (i.e. 10^{-9}) imaginary values with a bad fit, but due its small magnitude the material is essentially lossless as required.

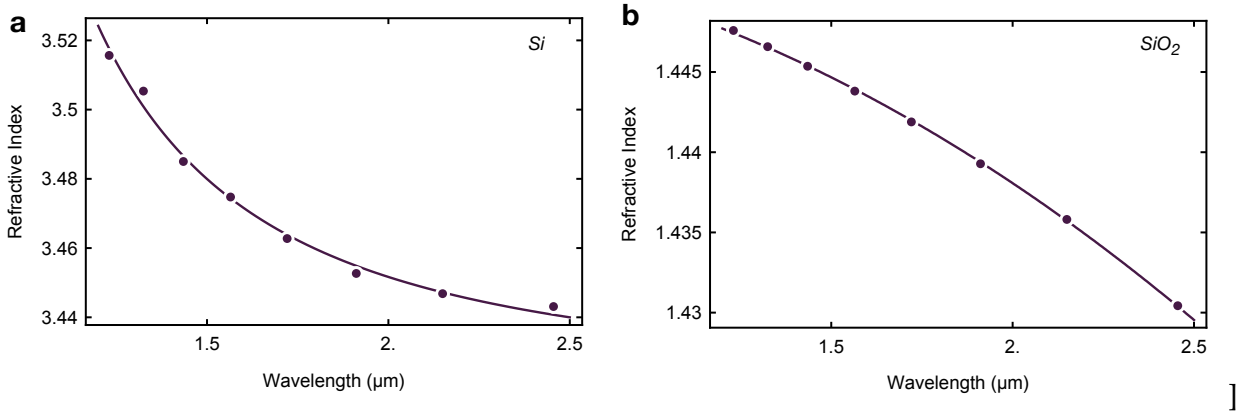

Figure C.5: Fitted material dispersion for FDTD simulations. **a**, Dispersion of bulk silicon, fit with a multi-coefficient model. **b**, Dispersion of bulk Silica, fit with a multi-coefficient model, experimental data from Palik[227].

Once the material dispersion is satisfactorily fit, the FDTD simulation region must be added. Typically the simulation boundary conditions are set to be the perfectly matched layer (PML) on every minimum and maximum Cartesian axis. The mesh size also is critically dependent on the structure being simulated. I found that the Lumerical conformal mesh (variant 0) gave reasonably accurate results with a mesh accuracy greater than 5, although the runtime of these simulations grows rapidly at high mesh levels. Care should be taken to ensure that the calculated grid cells correctly overlap with the device—see Fig. C.6a. This can be addressed by adding an override mesh at the structure interfaces or in design sensitive regions such as a directional coupler gap. Finally the structure, top and bottom cladding, and silicon handle must be drawn and set as the fitted multi-coefficient materials.

C.6.1 Grating couplers

To verify the target grating couplers designs 2D FDTD simulations were performed. With the materials and simulations boundaries setup as previously mentioned, the grating structure, cladding and handle are added viewed as a cross section through the chip as shown in Figs. C.6a and C.6c.

The source is chosen as a Gaussian source with the required set polarisation, direction and beam waist. Care must be taken that the geometric span of the source is greater than the mode-field diameter (MFD) to avoid clipping, and that the source does not overlap with the PML boundaries as shown in Fig. C.6c.

A transmission and mode-expansion monitor are placed on the output waveguide to calculate transmission into the output waveguide (Fig. C.6b). Additionally, an electric field monitor (Fig. C.6d) and/or a movie monitor are often useful for diagnosing any problems with the simulation. Finally, the source x-position should be swept over a range of values across the grating to optimise the transmission into the waveguide.

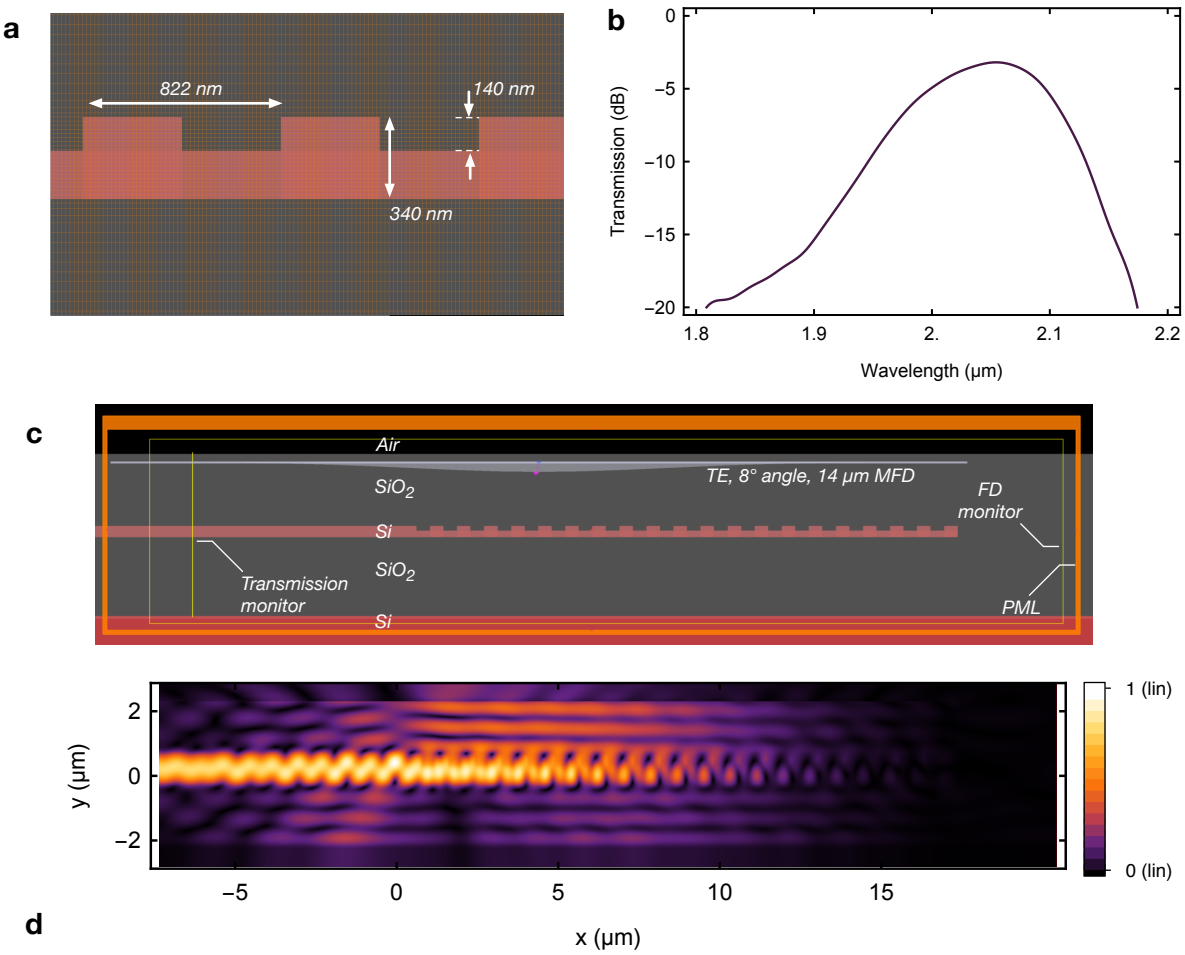

Figure C.6: Typical grating coupler 2D FDTD simulation setup. **a**, The magnified view with the FDTD simulation mesh of the grating cross section with the key grating parameters labelled. This grating coupler was used as the pump grating in Sec. 3.5.1. **b**, Transmission spectrum of light coupled from the Gaussian source into the waveguide. **c**, The FDTD simulation construction for the results in parts **b** and **d**. A Gaussian mode source is launched from above a grating with a transmission into the waveguide monitored. Label key: Perfectly matched layer (PML), frequency domain monitor (FD monitor), Silicon (Si), Silica (SiO_2), Transverse electric (TE), Mode field diameter (MFD). **d**, Normalised frequency domain real part of the electric field at $\lambda = 2.05$ μm.

C.6.2 Beamsplitters

MMIs

The strategy for determining the multimode interference coupler (MMI) length is described in Sec. 1.4.5 and Fig. 1.14. To verify the target design 3D FDTD was employed. The materials and simulation boundaries must be set up appropriately.

The source is chosen as a mode source and overlapped on the input waveguide by setting the suitable span limits. The mode that is launched into the simulation should be selected by the user. Simulating the mode profiles of the input waveguide, the TE fundamental mode is selected, and the electric field in the propagation direction is verified to be approximately zero. To sanity check the mode is correctly set, the mode profile is viewed on a logarithmic scale and visually inspected to ensure the electric field has

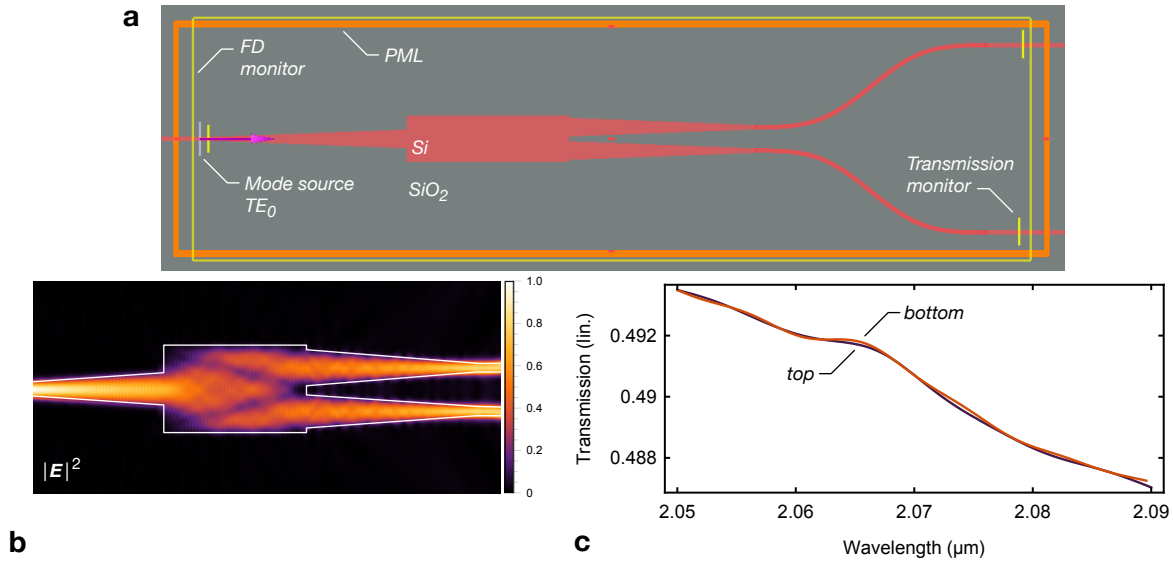

Figure C.7: Typical MMI FDTD simulation. **a**, FDTD simulation setup for an 1×2 MMI. A mode source with the fundamental mode is launched into in input waveguide, with the outputs monitored with transmission monitors. Label key: Perfectly matched layer (PML), frequency domain monitor (FD monitor), Silicon (Si), Silica (SiO_2), Transverse electric (TE). **b**, The simulated normalised electric field profile magnitude. **c**, The linear transmission measured in the top (purple) and bottom (orange) linear transmission monitors.

sufficiently decayed to -100 dB at the source boundary. If this is not satisfied numerical artefacts can be introduced making the launched effective index incorrect. The mode source should be placed at least one wavelength away from the PML boundary otherwise the simulation can become unstable and diverge—see Fig. C.7a for a FDTD simulation construction for a 1×2 MMI.

A transmission monitor and a mode expansion monitor are placed at the output waveguides (see Fig. C.7a) to calculate the MMI transmission and reflectivity of the coupler, as shown in Fig. C.7c. Additionally a 2D frequency-domain profile monitor (Fig. C.7b) intersects the middle of the plane of the device giving additional information of how the electric field propagates through the structure.

Directional couplers

The setup and construction of the simulation settings for the directional coupler is identical to the MMI in the previous subsection—see Fig. C.8a for a typical FDTD setup. The straight coupling region of a directional coupler can be well simulated with mode solving. An additional consideration for directional couplers is to calculate the effective coupling length from the bending region leading up to the straight coupling section. To do this, the directional coupler with a zero length coupling region is simulated i.e. the only coupling contribution is from the bending regions.

Once the 3D FDTD simulation is completed, the effective reflectivity of the bending region (see Figs. C.8b and C.8c) can be calculated. From this, the difference in the length of the coupling region where the waveguides are parallel estimated from the mode solving simulations is modified to achieve the desired reflectivity. Finally to validate the design, the full directional coupler geometry is simulated.

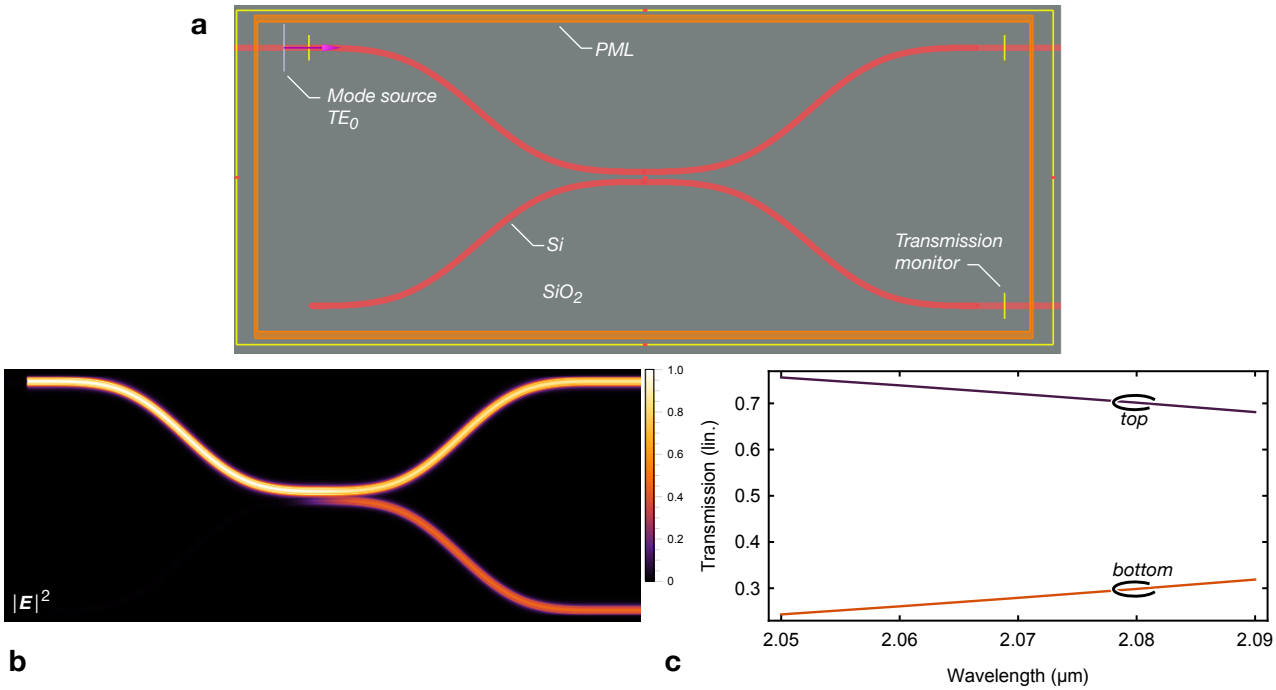

Figure C.8: Typical directional coupler FDTD simulation. **a**, FDTD simulation setup for a zero length coupling region directional coupler. A mode source with the fundamental mode is launched into in input waveguide, with the outputs monitored with transmission monitors. Label key: Perfectly matched layer (PML), Silicon (Si), Silica (SiO_2), Transverse electric (TE). **b**, The simulated normalised electric field profile magnitude of the directional coupler. **c**, The linear transmission spectrum measured in the top and bottom output transmission monitors.

APPENDIX D

Experimental techniques

D.1 Loss independent reflectivity measurements

To measure the reflectivity R (which is equivalent to the splitting ratio) of an integrated beamsplitters, independently of the transmission losses of the grating couplers and waveguides leading up to the beamsplitter, the following method can be employed. We denote transmission from port i to j by

$$t_{ij} = t_i t_j x_{ij}, \tag{D.1}$$

where t_{ij} is the measured optical transmission (in linear units) from port i to j, t_i is the channel transmission up to input port i of the coupler, t_j is the transmission after the coupler from port j up to the measurement apparatus, and x_{ij} is the true transmission from ports i to j on the coupler. Injecting light into port 1 of the coupler (see Fig. D.1 for port labels), and measuring on 3 and 4, and similarly repeating measuring the outputs

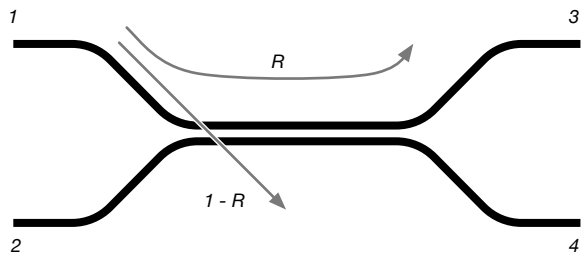

Figure D.1: Beamsplitter port labelling for reflectivity measurements

when light is injected into port 2 gives rise the to the following equations

$$t_{13} = t_1 t_3 x_{13} \tag{D.2a}$$
$$t_{14} = t_1 t_4 x_{14} \tag{D.2b}$$
$$t_{23} = t_2 t_3 x_{23} \tag{D.2c}$$
$$t_{24} = t_2 t_4 x_{24}. \tag{D.2d}$$

Assuming that the coupler is lossless, we can replace the x_{ij} with the reflectivity R when going from ports $1 \rightarrow 3$ and $2 \rightarrow 4$ or $(1-R)$ when going from ports $1 \rightarrow 4$ and $2 \rightarrow 3$. This gives rise to

$$t_{13} = t_1 t_3 R \tag{D.3a}$$
$$t_{14} = t_1 t_4 (1-R) \tag{D.3b}$$
$$t_{23} = t_2 t_3 (1-R) \tag{D.3c}$$
$$t_{24} = t_2 t_4 R. \tag{D.3d}$$

Taking a product of these terms gives

$$\frac{t_{13} t_{24}}{t_{14} t_{23}} = \frac{t_1 t_3 t_2 t_4 R^2}{t_1 t_4 t_2 t_3 (1-R)^2} = \frac{R^2}{(1-R)^2}. \tag{D.4}$$

Make the substitution $b = (t_{13} t_{24})/(t_{14} t_{23})$ and rearranging

$$b = \frac{R^2}{(1-R)^2} \tag{D.5a}$$
$$b(1-R)^2 = R^2 \tag{D.5b}$$
$$b - 2bR + bR^2 = R^2 \tag{D.5c}$$
$$(b-1)R^2 - (2b)R + b = 0, \tag{D.5d}$$

can now be solved using the quadratic formula giving

$$R = \frac{2b \pm \sqrt{4b^2 - 4(b-1)b}}{2(1-b)} = \frac{b \pm \sqrt{b}}{(1-b)}, \tag{D.6}$$

which yields a channel loss independent measurement of the coupler reflectivity from measuring all transmission from input to output ports. Note that only one of the two solutions to Eqn. (D.6) is physical (due to the $\pm$), with one of values outside of the range $0 < R < 1$.

D.2 Automated alignment strategy

For the grating coupler measurements presented in Sec. 3.2, I wrote code to automatically align and measure the set of test structures. The initial step in the measurement routine required manual coupling of light to the top right grating loopback of the array (DP-938). To measure the structures, first a crude positioning shifted between adjacent gratings. A coupling optimisation was then performed. The nanopositioner would first sweep over the x-axis and record the output power reading and move to the optimum

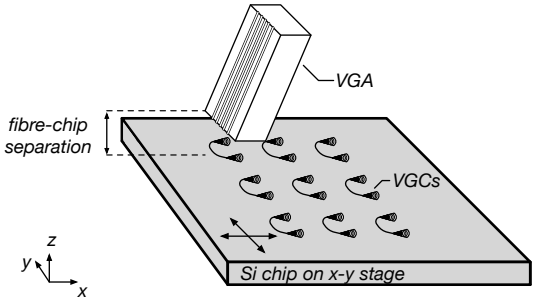

Figure D.2: Automatic alignment setup. A fibre array (VGA) couples light into a pair of grating couplers (VGC) from the top. The silicon chip is actuated in the x-y plane to move between adjacent grating pairs.

position (which is essentially a convex function in the absence of noisy behaviour such as polarisation drift and laser power fluctuations). The position was then optimised using the same routine in the y-axis. Repeating these two steps several times would achieve optimal coupling for a pair of gratings, and the best transmission from the device would be recorded. The algorithm would move onto the next pair of gratings, defined by the crude alignment step that had all of the positions of the grating coupler array encoded.

This measurement technique did suffer problems. The main issue in achieving optimal coupling is that the fibre V-groove array (VGA) needs to be as close to the chip surface as possible (see Fig. D.2). However, there is a trade off between the ease of coupling light into a chip and the height of the VGA above the chip: If the VGA is too close the chip, the chance of the emission cone of the grating coupler overlapping with the fibre acceptance angle is small. Conversely, if the VGA is too far away there is a better chance of grating coupler emission coupling light into the fibre, but the signal may be sufficiently diffuse for the photodiode to register. Additionally, the Nanomax positioning stage had a variable z-position as the x-y axes were actuated. Increased fibre-chip separation was required to ensure that the VGA did not crash into the chips top oxide and damage it.

D.3 Measuring spectra without an OSA

The following set of measurements give a rough idea of the spectral dependence of integrated optics. It should be stressed that this measurement technique is only useful in the absence of an optical spectrum analyser (OSA), which provides a quicker, more accurate and precise data. The spectral characterisation of the integrated optics was performed with a supercontinuum source, a monochromator and superconducting detectors. To tune the monochromator passband we used a customised metal chassis built by the university mechanical workshop. Mounting a chassis on the device meant the calibrated wavelength counter was removed and the mechanical drive shaft attached to a gear, actuated with a computer controlled stepper motor. The voltage pulses to drive the stepper motor were generated by an old heater driver module customised to be the input of a Geckodrive G201X stepper motor controller. The strategy for measuring spectra is outlined in the next subsection.

This experimental method had many limitations, predominately that it was not possible to extract the exact transmission of the device, only the general wavelength depen-

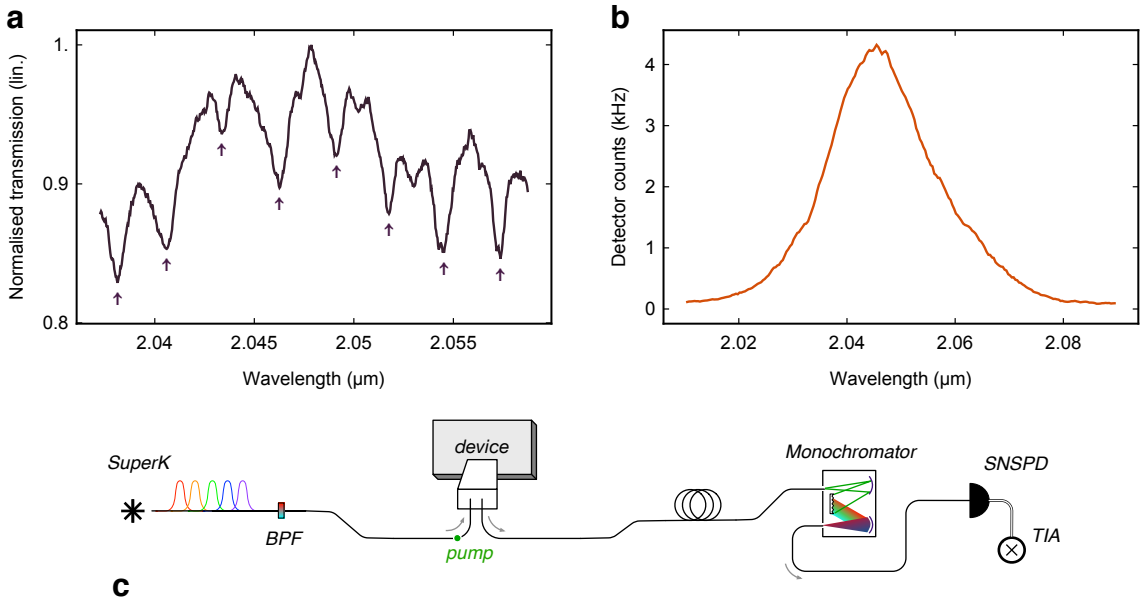

Figure D.3: Original spectral characterisation method. **a**, Microring resonator transmission spectrum, with the grating coupler profile removed. Ring resonances are labelled with an arrow. **b**, Grating coupler transmission spectrum of the deep etch grating with period $\Lambda = 1.008$ μm.

dence. Since the light was too dim to register on a photodiode, but too bright for the superconducting detectors, if the bright light transmission from a device was sufficiently large, the maximum count rate as measured on the superconducting detectors would saturate at 25 kHz at the repetition rate of the laser. For integrated devices with high transmission, the central wavelength had to be approximated by a fit.

In spite of these limiting factors, this method was regularly used in the early days of the project as it was the only way of understanding the spectral behaviour of the devices before we acquired an OSA.

Measuring transmission spectra

To characterise the spectral dependence of the integrated optics the measurement procedure used the following steps:

1. Set the quantum cascade laser (QCL) laser controller at 16°C and 100 mA to ensure that the output was centred on $\lambda = 2.049$ μm as a reference wavelength.

2. Couple the QCL through the monochromator directly into a photodiode and optimise the grating position to maximise transmission, thus calibrating the start position to the laser reference wavelength.

3. Transmit the QCL through the chips' integrated optics and optimise coupling on a photodiode.

4. Bandpass filter (BPF) the supercontinuum source to reduce the spectrum of the optical output to 2.25 ± 0.25 μm and the danger of naked eye exposure to the class 4 laser.

5. Route the supercontinuum light at the output of the chip through the monochromator and finally to superconducting detectors.

6. From the computer, step the monochromator across the wavelength region of interest, at each step recording the transmitted photon flux.

Using the experimental configuration shown in Fig. D.3c, a sample spectrum of a ring and grating coupler measured with this technique is shown in Figs. D.3a and D.3b, respectively.

D.4 Coupling strategy for two independent fibres

Coupling into the waveguides was challenging as the grating couplers were at opposite ends of the waveguide, requiring control of two independent single fibres, each with 4 degrees of freedom (x, y, z, θ) and polarisation. Furthermore, the optimal incident angle for coupling light into the grating coupler was also unknown since these devices were designed for operating at 2.29 μm. Using the QCL laser and photodiode with a noise floor of −40 dBm, the process of successfully measuring transmitted light through the chip took almost two weeks before a repeatable measurement strategy and a significant optical coupling was recorded. The strategy for optimising the coupling was as follows:

1. Adjust both fibres to a set angle using a rotation mount with angular markers on it.

2. Move the fibre away from the grating nearby to an area with no optical structures.

3. Lower the fibre towards the surface of the chip until it impacts, leaving a visual small mark in the surface.

4. Raise the fibre away from the chip surface by a small enough distance so that it does not scratch the surface as it is moved towards the reference grating.

5. Move the fibre so that it just occludes the target grating coupler.

6. Repeat the previous three steps for the second fibre.

7. Walk one fibre around looking for any sign of optical transmission.

8. Try walking around with the other fibre.

9. If any optical throughput achieved, optimise signal until it is maximised.

10. Record maximum transmission, then elevate fibres from chip surface and go back to step 1 for a new angle.

D.5 Monochromator coupling routine

The coupling strategy to reach the global optimum for the monochromator is as follows:

1. Optimise coupling in both directions with red alignment laser between two opposing fibre launches approximately separated by 30 cm, where the focus through the lens centres the beam waist in the mid point of the two fibre launches.

2. Insert the monochromator into the beam path, adjusting the position so that the red laser spot hits the middle of the slit.
3. Adjust the focus in both directions so that the visibility of red laser spot is minimised since the laser should now enter the slit.
4. Optimise coupling with red alignment laser by first iterating each sides x, then y then z axis before swapping sides.
5. Now optimise the coupling walking the beam with pairs of axes on each fibre coupler.
6. Swap the red alignment laser and photodiode for the QCL and mid-infrared (MIR) photodiode and adjust monochromator wavelength to transmit 2.049 μm.
7. Repeat Steps 7-8 until coupling is optimal
8. Now walk the x, z axes on the monochromator, and the corresponding axes in pairs on the fibre couplers until the global maximum is achieved.

D.6 Deconvolution factor for a hyperbolic secant pulse shape

Since our laser is mode-locked, we assume an hyperbolic secant pulse ansatz of the form $\text{sech}^2(\tau/t_p)$, where t_p is the characteristic time of the pulse. To calculate the actual pulse duration from our oscilloscope, we must find the deconvolution factor. The autocorrelation trace width is then related to the full width at half maximum full width at half maximum (FWHM) by

$$\Delta\tau = 2t_p \text{arccosh}(\sqrt{2}). \tag{D.7}$$

The autocorrelation function of our ansatz is given by

$$A(t') = \int_{-\infty}^{\infty} \text{sech}^2\left(\frac{\tau}{t_p}\right)\text{sech}^2\left(\frac{\tau - t'}{t_p}\right)d\tau\ , \tag{D.8}$$

$$= 4\left[t'\coth\left(\frac{t'}{t_p}\right) - t_p\right]\text{csch}^2\left(\frac{t'}{t_p}\right), \tag{D.9}$$

where t' is time units as measured on the oscilloscope trace. This function is not valid at $t' = 0$ since $\coth(0)$ is undefined, so we taking the limit $A(0) \lim_{t'\to 0} = \frac{4t_p}{3}$. We make the substitution $T = t'/t_p$ and numerically solve for the value at half maximum i.e. $A(t') = A(0)/2$

$$\frac{1}{6} = (T\coth(T) - 1)\text{csch}^2(T), \tag{D.10}$$

where we find $T \approx 1.36$. Finally, to obtain the actual pulse duration FWHM, the oscilloscope trace FWHM width is $\Delta t' = 2t' = 2.72t_p$. Finally substituting Eqn. (D.7) into this result, we find the actual pulse width is related to the FWHM of the oscilloscope trace by

$$\Delta\tau = \frac{2\ \text{arccosh}\left(\sqrt{2}\right)}{2.72}\Delta t' \approx 0.648\Delta t'. \tag{D.11}$$

APPENDIX E

Nonlinear wave propagation

E.1 The wave equation

The proceeding derivation of the pulse propagation in nonlinear media follows the treatment from Agrawal[73]. Maxwell's equations describe the phenomena of electromagnetism, in dielectric media are given by the following formulae

$$\nabla \times \mathbf{E} = -\frac{\partial \mathbf{B}}{\partial t} \tag{E.1a}$$

$$\nabla \times \mathbf{H} = \mathbf{J} + \frac{\partial \mathbf{D}}{\partial t} \tag{E.1b}$$

$$\nabla \cdot \mathbf{D} = \rho_f \tag{E.1c}$$

$$\nabla \cdot \mathbf{B} = 0, \tag{E.1d}$$

where **E** and **H** are the electric and magnetic fields, **D** and **B** are the electric and magnetic field flux densities. Finally, **J** is the current density and ρ_f is the charge density.

The quantities **E**, **H** are related to flux densities **D** and **B** with the following relationship

$$\mathbf{D} = \epsilon_0 \mathbf{E} + \mathbf{P} \tag{E.2}$$

$$\mathbf{B} = \mu_0 \mathbf{H} + \mathbf{M}, \tag{E.3}$$

where the quantities **P** and **M** are the polarisation and magnetisation fields and ϵ_0 and μ_0 are physical constants of the permittivity and permeability in vacuum. The electric and magnetic polarisation fields are defined by the microscopic bound charges and currents within a material. This is the density of permanent or induced electric and magnetic dipole moments in dielectric and magnetic materials, respectively. Typically, waveguides and fibres media are not magnetic and therefore $\mathbf{M} = 0$. Taking the curl of Eqn. (E.1a) gives the wave equation:

$$\nabla \times \nabla \times \mathbf{E} = \frac{1}{c^2}\frac{\partial^2 \mathbf{E}}{\partial t^2} - \mu_0 \frac{\partial \mathbf{P}}{\partial t^2} \tag{E.4}$$

where c is the vacuum speed of light and the relationship $c = 1/\sqrt{\mu_0 \epsilon_0}$ is defined.

The polarisability **P** can be decomposed into the linear and nonlinear parts

$$\mathbf{P}(\mathbf{r},t) = \mathbf{P}_{\mathrm{L}}(\mathbf{r},t) + \mathbf{P}_{\mathrm{NL}}(\mathbf{r},t) \tag{E.5}$$

where we assume the dominant nonlinear effects are induced by the third order nonlinearity of silicon $\chi^{(3)}$. The linear and nonlinear polarisation parts are then related back to the electric field with the relations

$$\mathbf{P}_{\mathrm{L}}(\mathbf{r},t) = \epsilon_0 \int_{-\infty}^{\infty} \chi^{(1)}(t-t') \cdot \mathbf{E}(\mathbf{r},t')\,dt' \tag{E.6}$$

$$\mathbf{P}_{\mathrm{NL}}(\mathbf{r},t) = \epsilon_0 \iiint_{-\infty}^{\infty} \chi^{(3)}(t-t_1, t-t_2, t-t_3) \times \mathbf{E}(\mathbf{r},t_1)\mathbf{E}(\mathbf{r},t_2)\mathbf{E}(\mathbf{r},t_3)\,dt_1\,dt_2\,dt_3 \tag{E.7}$$

which are valid under the dipole approximation where the induced polarisation from the electromagnetic field is local in the material. To solve the general formulae Eqns. (E.4)-(E.7), further approximation is required. Assuming that the contribution from the nonlinear polarisation is small relative to the total induced polarisation, we can set $\mathbf{P}_{\mathrm{NL}} = 0$. Using the Fourier transform of **E**

$$\tilde{\mathbf{E}}(\mathbf{r},\omega) = \int_{-\infty}^{\infty} \mathbf{E}(\mathbf{r},t) e^{i\omega t}\,dt, \tag{E.8}$$

with $\mathbf{P}_{\mathrm{NL}} = 0$, Eqn. (E.4) can be rewritten as

$$\nabla \times \nabla \times \tilde{\mathbf{E}}(\mathbf{r},\omega) = \epsilon(\omega)\frac{\omega^2}{c^2}\tilde{\mathbf{E}}. \tag{E.9}$$

Here we have defined the dielectric permittivity $\epsilon(\omega)$ as

$$\epsilon(\omega) = 1 + \tilde{\chi}^{(1)}(\omega), \tag{E.10}$$

where $\tilde{\chi}^{(1)}(\omega)$ is the Fourier transform of $\chi^{(1)}(t)$. In general $\epsilon(\omega)$ is complex, we can write this as

$$\epsilon(\omega) = [n(\omega) + i\kappa(\omega)]^2, \tag{E.11}$$

where $n(\omega)$ is the frequency dependent linear refractive index and $\kappa(\omega)$ is the frequency dependent linear attenuation coefficient. Assuming that the linear losses of the material is small, we set $\kappa(\omega) = 0$, meaning that $\epsilon \approx n(\omega)^2$. Furthermore, assuming we have a step index profile for the waveguiding structure, the core and cladding refractive index is uniform the vector identity can be used

$$\nabla \times \nabla \times \mathbf{A} \equiv \nabla(\nabla \cdot \mathbf{A}) - \nabla^2(\mathbf{A}), \tag{E.12}$$

to simplify Eqn. (E.9) to become the wave equation in guided media

$$\nabla^2 \tilde{\mathbf{E}} + n(\omega)^2 \frac{\omega^2}{c^2}\tilde{\mathbf{E}} = 0. \tag{E.13}$$

This wave equation can be solved to understand waveguide modes and pulse propagation in the context of the nonlinear Schrodinger equation described in Sec E.2.

E.2 Nonlinear pulse propagation

In our silicon waveguides, the optical nonlinearity gives rise to several nonlinear effects which requires a method of understanding pulse propagation. We now derive the result of the nonlinear Schrödinger equation (NLSE), using the treatment of Ref. 73. To understand the effects of nonlinear media on ultrashort and intense laser pulses, we must revisit the wave equation described by Eqn. (E.4) and include the nonlinear polarisation terms. The formula may be written as

$$\nabla^2\mathbf{E} - \frac{1}{c^2}\frac{\partial^2\mathbf{E}}{\partial t^2} = \mu_0\frac{\partial^2\mathbf{P}_\mathrm{L}}{\partial t^2} + \mu_0\frac{\mathbf{P}_\mathrm{NL}}{\partial t^2}. \tag{E.14}$$

Under the assumptions that the nonlinearity is a small perturbation to the linear polarisability, the electric field is quasi monochromatic, the envelope is slowly varying and can be separated from the rapidly oscillating part of the electric field, the field is linearly polarised and the optical nonlinear response from the material is instantaneous, the time dependence in Eqn. (E.7) reduces to

$$\mathbf{P}_\mathrm{NL}(\mathbf{r},t) = \epsilon_0\chi^{(3)}\mathbf{E}(\mathbf{r},t)\mathbf{E}(\mathbf{r},t)\mathbf{E}(\mathbf{r},t) \tag{E.15}$$

$$\approx \epsilon_0\epsilon_\mathrm{NL}E(\mathbf{r},t), \tag{E.16}$$

where we define the nonlinear dielectric coefficient

$$\epsilon_\mathrm{NL} = \frac{3}{4}\chi^{(3)}_{xxxx}|E(\mathbf{r},t)|^2. \tag{E.17}$$

Defining the Fourier transform of pulse with the stated approximations

$$\tilde{E}(\mathbf{r},\omega-\omega_0) = \int_{-\infty}^{\infty} E(\mathbf{r},t)\ e^{i(\omega-\omega_0)t}dt, \tag{E.18}$$

is a solution to the Helmholtz equation

$$\left(\nabla^2 + \epsilon(\omega)k_0^2\right)\tilde{E} = 0 \tag{E.19}$$

where $k_0 = \omega/c = 2\pi/\lambda$ and

$$\epsilon(\omega) = 1 + \tilde{\chi}^{(1)}_{xx}(\omega) + \epsilon_\mathrm{NL}. \tag{E.20}$$

The dielectric constant defined in Eqn. (E.11) is now a function of optical intensity where $\epsilon = (\tilde{n} + i\tilde{\kappa})^2$ and $\tilde{\kappa} = \frac{\tilde{\alpha}}{2k_0}$ and we define

$$\tilde{n} = n + n_2|E|^2 \tag{E.21}$$

$$\tilde{\alpha} = \alpha + \alpha_2|E|^2. \tag{E.22}$$

Here n_2 and α_2 are the nonlinear refraction and the nonlinear two-photon absorption coefficients of the waveguide.

A solution to Eqn. (E.19) can be solved assuming a solution with separated variables of the form

$$\tilde{E}(\mathbf{r},\omega-\omega_0) = \mathcal{F}(x,y)\tilde{A}(z,\omega-\omega_0)e^{i\beta_0 z}, \tag{E.23}$$

where β_0 is the wavenumber. Here, we must assume that the envelope $\tilde{A}$ is a slowly varying function of z and β_0. The following solutions for F and A are

$$\frac{\partial^2\mathcal{F}}{\partial x^2} + \frac{\partial^2\mathcal{F}}{\partial y^2} + [\epsilon(\omega)k_0^2 - \tilde{\beta}^2]\mathcal{F} = 0 \tag{E.24}$$

$$2i\beta_0\frac{\partial\tilde{A}}{\partial z} + (\tilde{\beta}^2 - \beta_0^2)\tilde{A} = 0, \tag{E.25}$$

where the second derivative with respect to $\tilde{A}$ was neglected due to the slowly varying approximation. Approximating $\epsilon(\omega)$ with

$$\epsilon = (n + \Delta n)^2 \approx n^2 + 2n\Delta n, \tag{E.26}$$

with Δn being a small perturbation

$$\Delta n = n_2 |E|^2 + \frac{i\tilde{\alpha}}{2k_0} \tag{E.27}$$

and the eigenvalue $\tilde{\beta}$ becomes

$$\tilde{\beta}(\omega) = \beta(\omega) + \Delta\beta, \tag{E.28}$$

where

$$\Delta\beta = \frac{k_0 \iint_{-\infty}^{\infty} \Delta n |F(x,y)|^2 dxdy}{\iint_{-\infty}^{\infty} |F(x,y)|^2 dxdy}. \tag{E.29}$$

We may write the electric field $\mathbf{E}(\mathbf{r}, t)$ as

$$\mathbf{E}(\mathbf{r}, t) = \frac{1}{2}\hat{x}\left(\mathcal{F}(x,y)A(z,t)e^{i(\beta_0 z - \omega_0 t)} + c.c\right), \tag{E.30}$$

where the Fourier transform of this equation satisfies Eqn. (E.25) with the approximation that $\tilde{\beta}^2 - \beta_0^2 \approx 2\beta_0(\tilde{\beta} - \beta_0)$

$$\frac{\partial \tilde{A}}{\partial z} = i\left[\beta(\omega) + \Delta\beta - \beta_0\right]\tilde{A}. \tag{E.31}$$

This equation gives physical intuition on the pulses envelopes evolution propagating through the nonlinear material—each frequency components in the pulse accumulates a phase shift that is dependent on its frequency and intensity.

In general it is not possible to know the exact form of the propagation constant so usually a Taylor expansion about the central frequency ω_0 is taken

$$\beta(\omega) = \beta_0 + \beta_1(\omega - \omega_0) + \frac{\beta_2}{2}(\omega - \omega_0)^2 + \frac{\beta_3}{6}(\omega - \omega_0)^3 + \ldots \tag{E.32}$$

where $\beta_n = d^n\beta/d\omega^n$ for $n \in \mathbb{Z}^+$. Finally, substituting this result into Eqn. (E.31), taking the inverse Fourier transform using

$$A(z,t) = \frac{1}{2\pi}\int_{-\infty}^{\infty} \tilde{A}(z, \omega - \omega_0)e^{-i(\omega-\omega_0)t}d\omega \tag{E.33}$$

and replacing $\omega - \omega_0$ with the differential operator $\mathrm{i}(\partial/\partial t)$ we obtain the final result

$$\frac{\partial A}{\partial z} + \beta_1\frac{\partial A}{\partial t} + \frac{i\beta_2}{2}\frac{\partial^2 A}{\partial t^2} + \frac{\alpha}{2}A = i\gamma|A|^2 A, \tag{E.34}$$

where we define the effective waveguide nonlinear parameter

$$\gamma = \frac{k_0 n_2}{A_{\text{eff}}}, \tag{E.35}$$

and A_{eff} is the effective modal area. This key result is also known as the NLSE and can be an invaluable tool to perform numerical pulse evolution in nonlinear media using the split-step Fourier method—more information about the this is found in the following section.

E.3 Split-step Fourier method

The split-step Fourier method is a pseudospectral method for computationally implementing the NLSE. Inspecting Eqn (E.34), we find that it can be written in the form[73]

$$\frac{\partial A}{\partial z} = (\hat{D} + \hat{N})\, A, \tag{E.36}$$

where $\hat{D}$ is an operator that encompasses the effects of linear absorption and dispersion, and $\hat{N}$ is a nonlinear operator that determines the effects of optical nonlinearities on the pulse. Formally, these operators are defined

$$\hat{D} = -\frac{i\beta_2}{2}\frac{\partial^2}{\partial T^2} + \frac{\beta_3}{6}\frac{\partial^3 A}{\partial T^3} - \frac{\alpha}{2}, \tag{E.37}$$

$$\hat{N} = i\gamma\left(|A|^2 A + \frac{i}{\omega_0}\frac{\partial}{\partial T}(|A|^2 A) - T_R A\frac{\partial |A|^2}{\partial T}\right). \tag{E.38}$$

In reality the two operators act simultaneously on the optical pulse as it propagates through the nonlinear medium, however as the operators do not commute it is not possible to apply them simultaneously. Instead, across a short distance of z to $z + \Delta z$, the operators are treated to act independently so that the dispersion operator is applied on its own in the time domain and the nonlinearity operator on its own in the frequency domain. Choice of the step size Δz* is important here, since it determines the accuracy of the simulation. Given a numerical input description of the pulse shape in time and frequency, modelling its nonlinear behaviour propagating in waveguide can be simulated.

E.4 Self-phase modulation

In the mid-infrared (MIR), silicon has a large nonlinear refractive coefficient n_2, which gives rise to a host of useful nonlinear effects such as stimulated and spontaneous FWM, self-phase modulation (SPM) and cross-phase modulation. Self-phase modulation is an effect where a phase shift of each frequency component in an optical pulse is proportional to its intensity, giving rise to frequency spectra with broadened envelopes as shown in Fig. E.1c. Following Ref. 73, in general the refractive index of a material is given by

$$n = n_0 + n_2|E|^2, \tag{E.39}$$

where n_0 is the linear part of the refractive index, and $|E|^2$ is the optical intensity. The NLSE in the retarded frame where we transform into the coordinates moving at the group velocity of the pulse $T = t - z/v_g = t - \beta_1 z$, simplifies to

$$i\frac{\partial A}{\partial z} = -\frac{i\alpha}{2}A + \frac{\beta_2}{2}\frac{\partial^2 A}{\partial T^2} - \gamma|A|^2 A. \tag{E.40}$$

Introducing a new time scale which is normalised to the input pulse width T_0

$$\tau = \frac{T}{T_0} = \frac{t - \beta_1 z}{T_0}, \tag{E.41}$$

*The dominant error term means this method is accurate to Δz^2

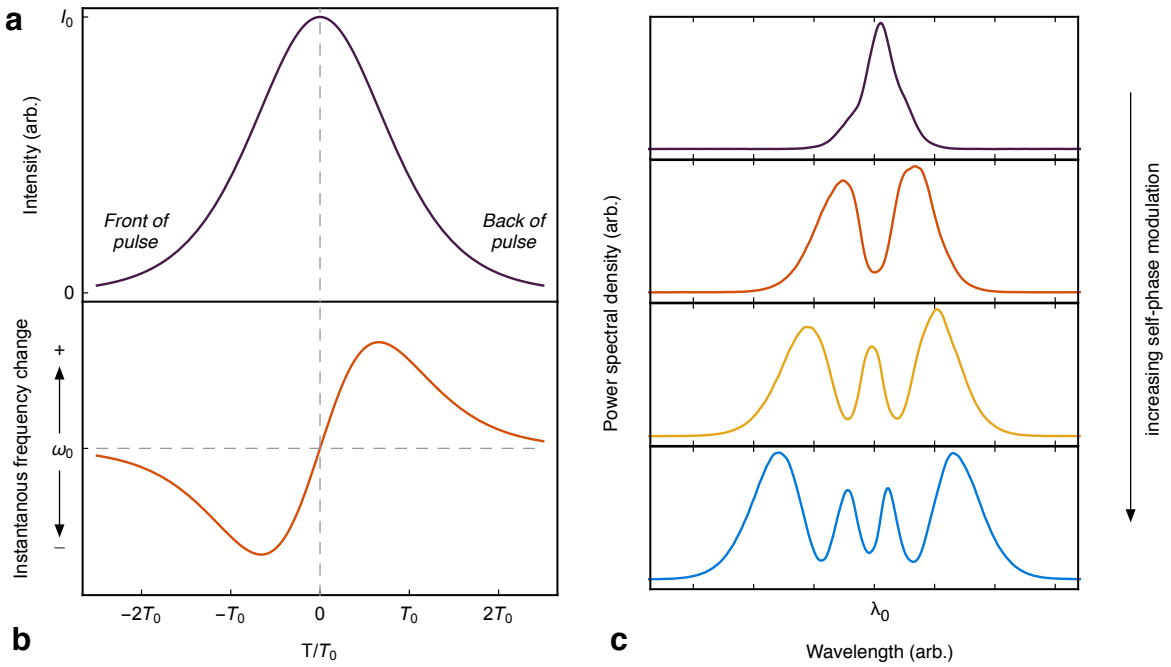

Figure E.1: An overview of self-phase modulation effect. **a**, Time normalised intensity envelope of a hyperbolic secant shaped pulse. **b**, The instantaneous frequency change for the pulse. **c**. Typical spectral broadening of an optical pulse due to self-phase modulation. The power launched into the nonlinear media increases from top to bottom of the plots.

means we can now introduce an amplitude normalised pulse envelope U

$$A(z,\tau) = \sqrt{P_0}\, e^{-\alpha z/2} U(z,\tau), \tag{E.42}$$

where P_0 is the initial peak power of the pulse. Inserting this solution into Eqn. (E.40) yields

$$i\frac{\partial U}{\partial z} = \frac{\beta_2}{2}\frac{\partial U}{\partial \tau^2} - e^{-\alpha z}\gamma P_0 |U|^2 U. \tag{E.43}$$

To illustrate the effect of SPM, we set the group velocity dispersion $\beta_2 = 0$ which gives

$$\frac{\partial U}{\partial z} = i\gamma P_0 e^{-\alpha z}|U|^2 U. \tag{E.44}$$

Writing U in polar form $U = |U|e^{i\phi}$

$$\frac{\partial}{\partial z}\left(|U|e^{i\phi}\right) = \frac{\partial |U|}{\partial z}e^{i\phi} + |U|e^{i\phi}\left(i\frac{\partial \phi}{\partial z}\right) = |U|e^{i\phi}\left(i\gamma P_0 e^{-\alpha z}|U|^2\right) \tag{E.45}$$

Comparing the real and imaginary coefficients of Eqns. (E.44) and (E.45), we see that the real part is zero implying that the amplitude of $|U|$ is invariant along z. The imaginary part is given by

$$\frac{\partial \phi}{\partial z} = \gamma P e^{-\alpha z}|U|^2. \tag{E.46}$$

Integrating both sides obtains

$$\phi_{\mathrm{NL}} = |U|^2\gamma P_0 \int_0^L e^{-\alpha z} dz = |U|^2\gamma P\left(\frac{1-e^{-\alpha L}}{\alpha}\right) = |U|^2\gamma P L_{\mathrm{eff}}, \tag{E.47}$$

where we define the effective length of the waveguide L_{eff}. In general the envelope therefore evolves according to

$$U(L,T) = U(0,T)e^{i\phi_{\text{NL}}(L,T)}. \tag{E.48}$$

SPM spectral broadening is a result of the time dependence of the nonlinear phase ϕ_{NL}. The physical intuition of this can be realised if each optical frequency component has instantaneously varying phase in time, the frequency has then changed as the period has also been modified. The instantaneous frequency change in time is therefore given by

$$\delta\omega(T) = -\frac{\partial\phi_{\text{NL}}}{\partial T} = -\gamma P L_{\text{eff}}\frac{\partial}{\partial T}|U(0,T)|^2 \tag{E.49}$$

An example is shown in Fig. E.1a and E.1b, where we take the envelope U to be a hyperbolic secant shaped pulse of the form $U(0,T) = \text{sech}^2(T/T_0)$, giving rise to an instantaneous frequency change

$$\delta\omega(T) = -\gamma P L_{\text{eff}}\frac{2\tanh(T/T_0)}{T_0}\text{sech}^2(T/T_0). \tag{E.50}$$

APPENDIX F

Photonic chip overview

Layer	Abbreviation	Symbol
Waveguide	WG	
Rib waveguide	RIB	
Grating coupler etch	GRAT	
Metal layer 1	MT1	
Metal layer 2	MT2	
Heater	HTR	
Bondpad	BPAD	
Positive type doping	P	
Heavy positive type doping	P++	
Negative type doping	N	
Heavy negative type doping	N++	
Via	VIA	
Bounding box	BBOX	
Cleave	CLEAVE	
None	NONE	

Table F.1: Mask design layer symbology.

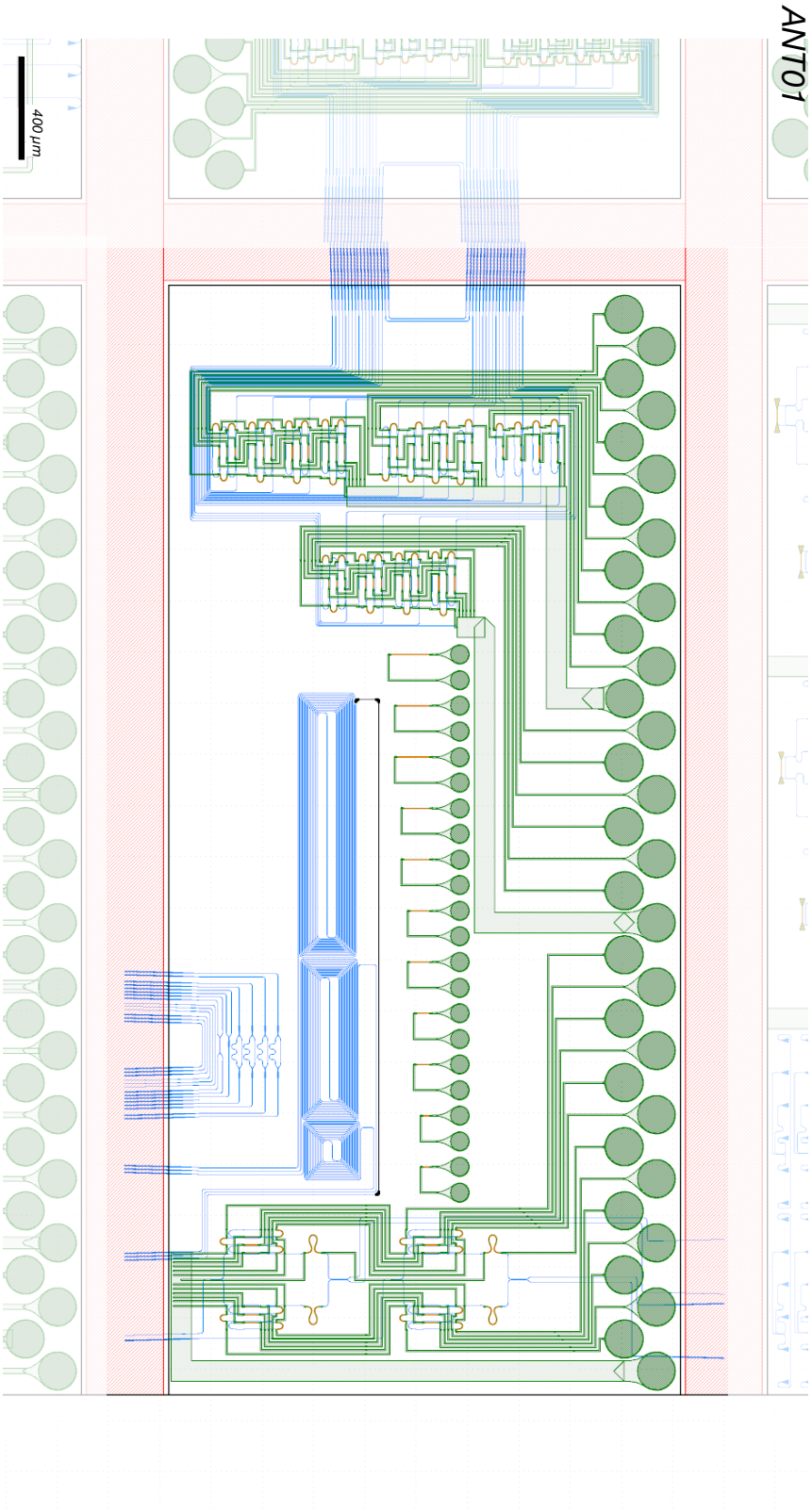

Figure F.1: Applied Nanotools: ANT01. Design credit: Lawrence Rosenfeld, Joshua Silverstone. Received April 2018.

Figure F.2: Institute of Microelectronics: IME02. Design credit: Joshua Silverstone. Received October 2015. Other designers experiments on the die have intentionally been blurred out.

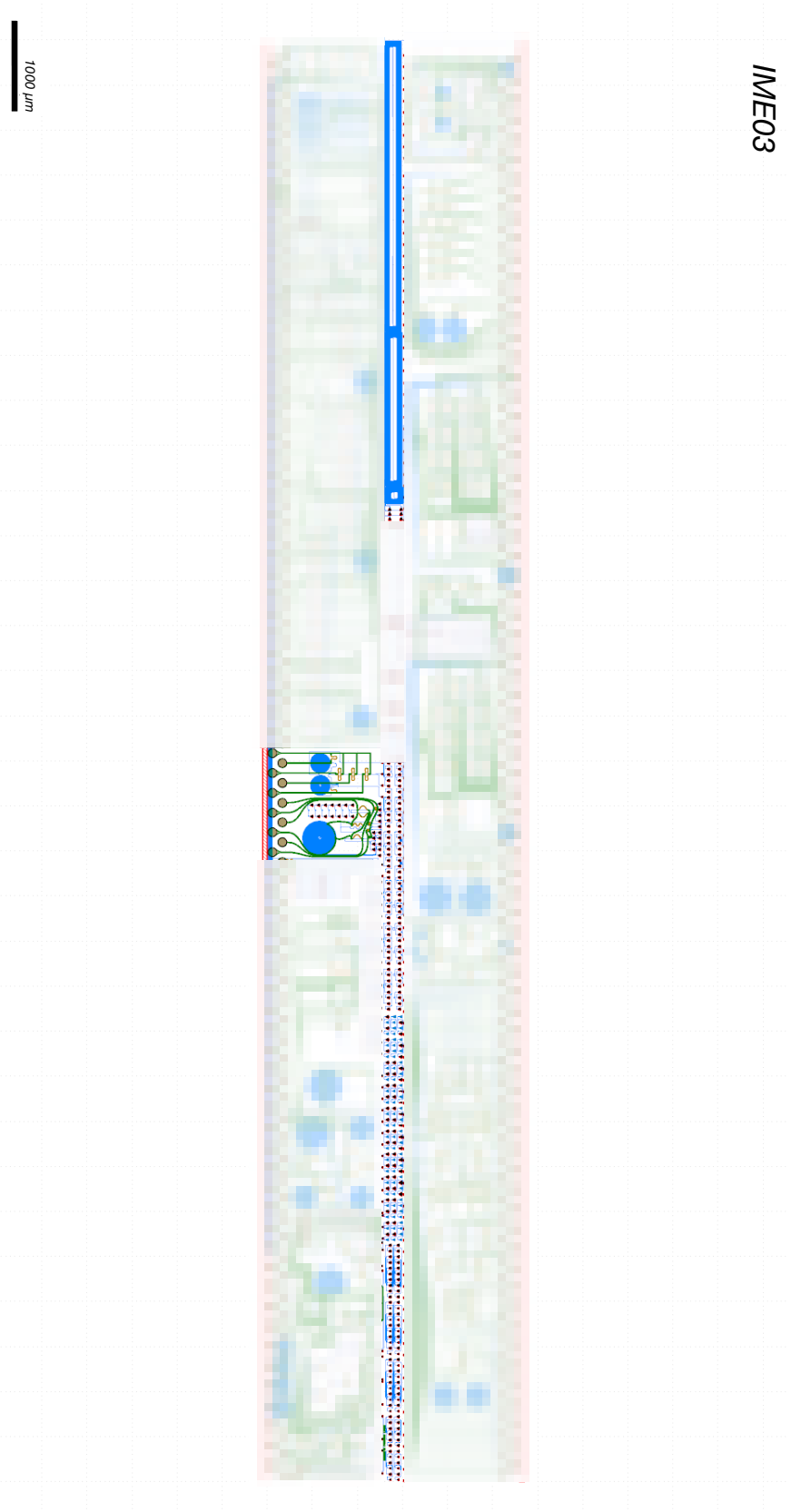

Figure F.3: Institute of Microelectronics: IME03. Design credit: Joshua Silverstone, Lawrence Rosenfeld. Received November 2016.

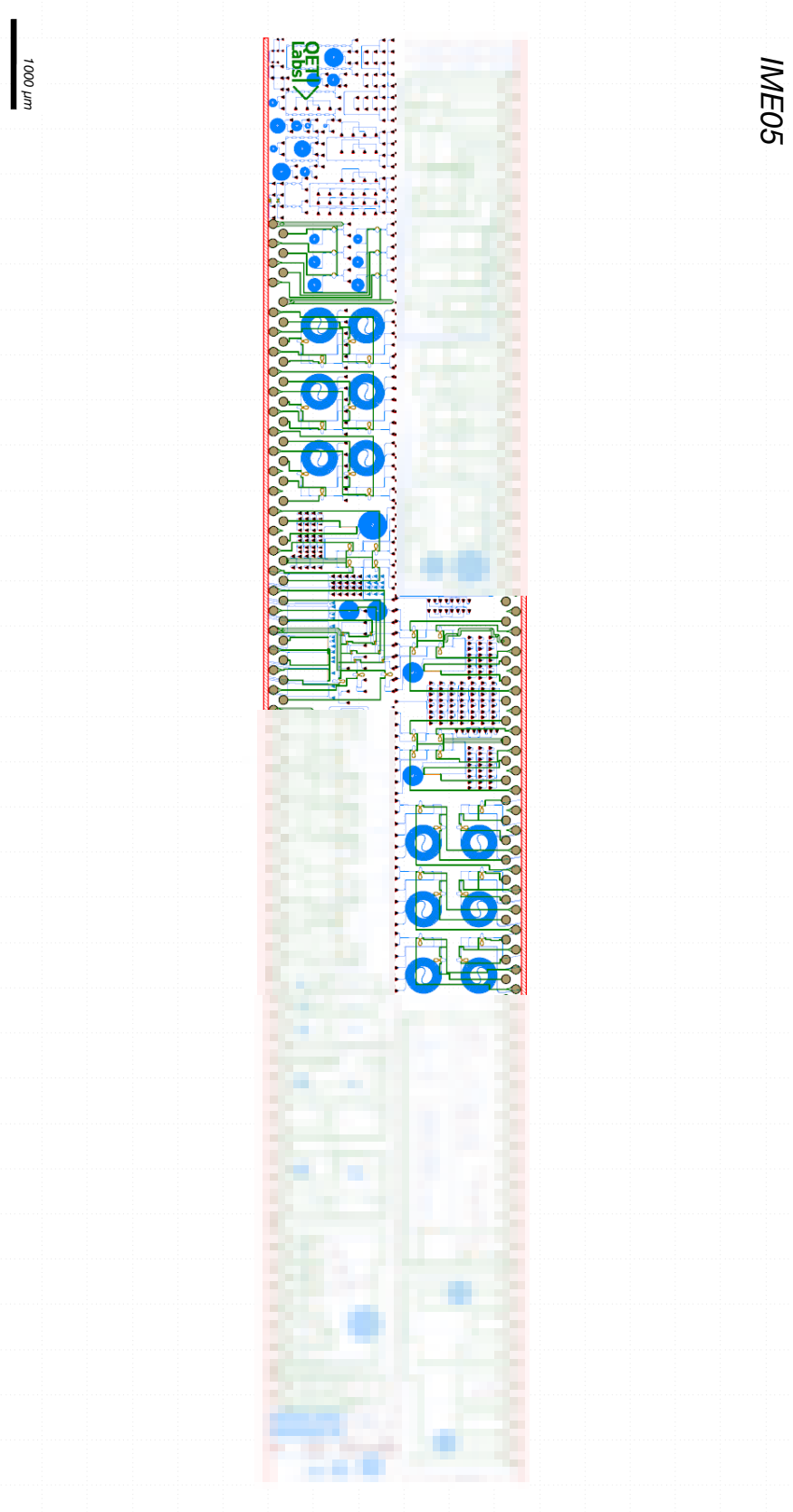

Figure F.4: Institute of Microelectronics: IME05. Design credit: Lawrence Rosenfeld, Joshua Silverstone. Received July 2017.

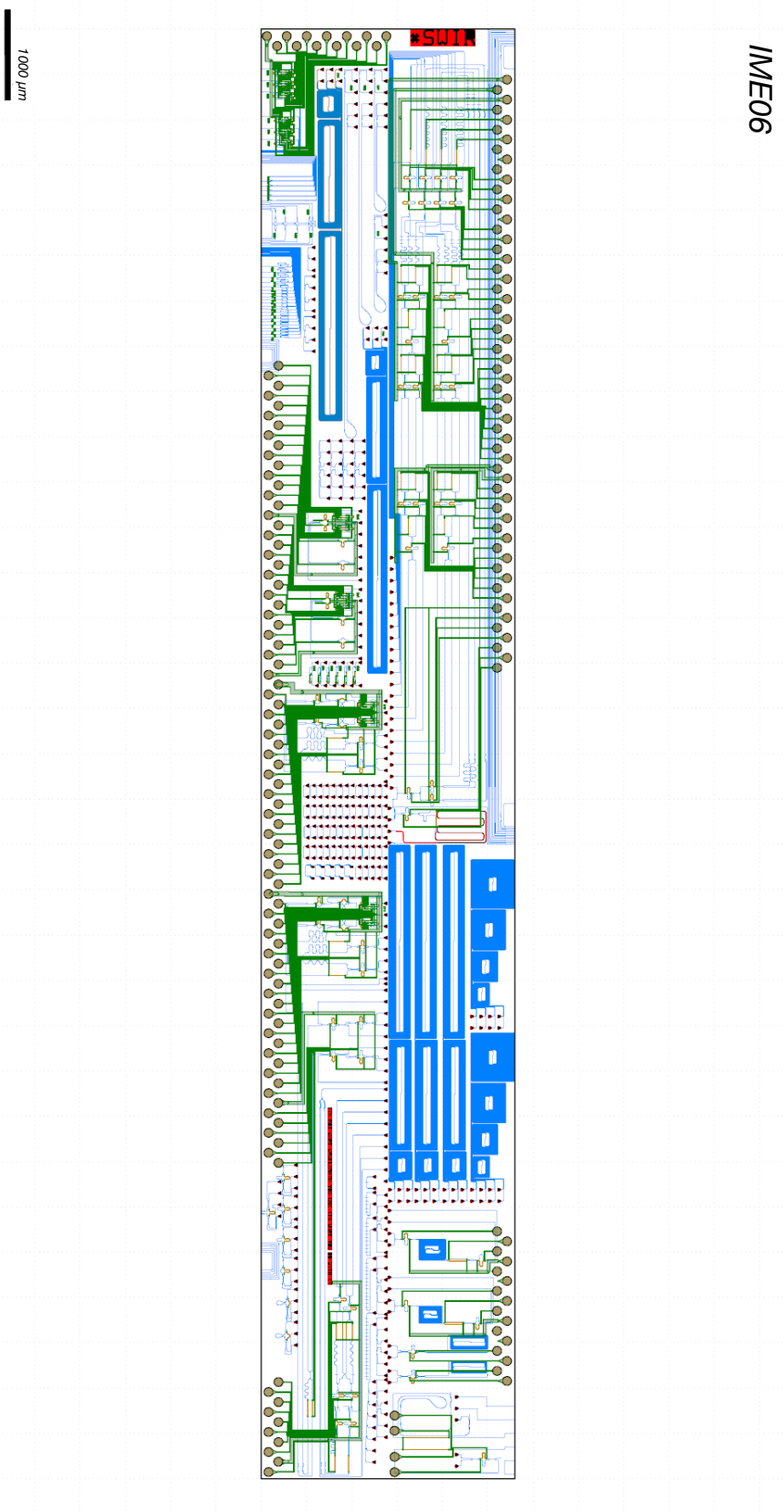

Figure F.5: Institute of Microelectronics: IME06. Design credit: Lawrence Rosenfeld, Dominic Sulway, Jake Biele. Received May 2019.

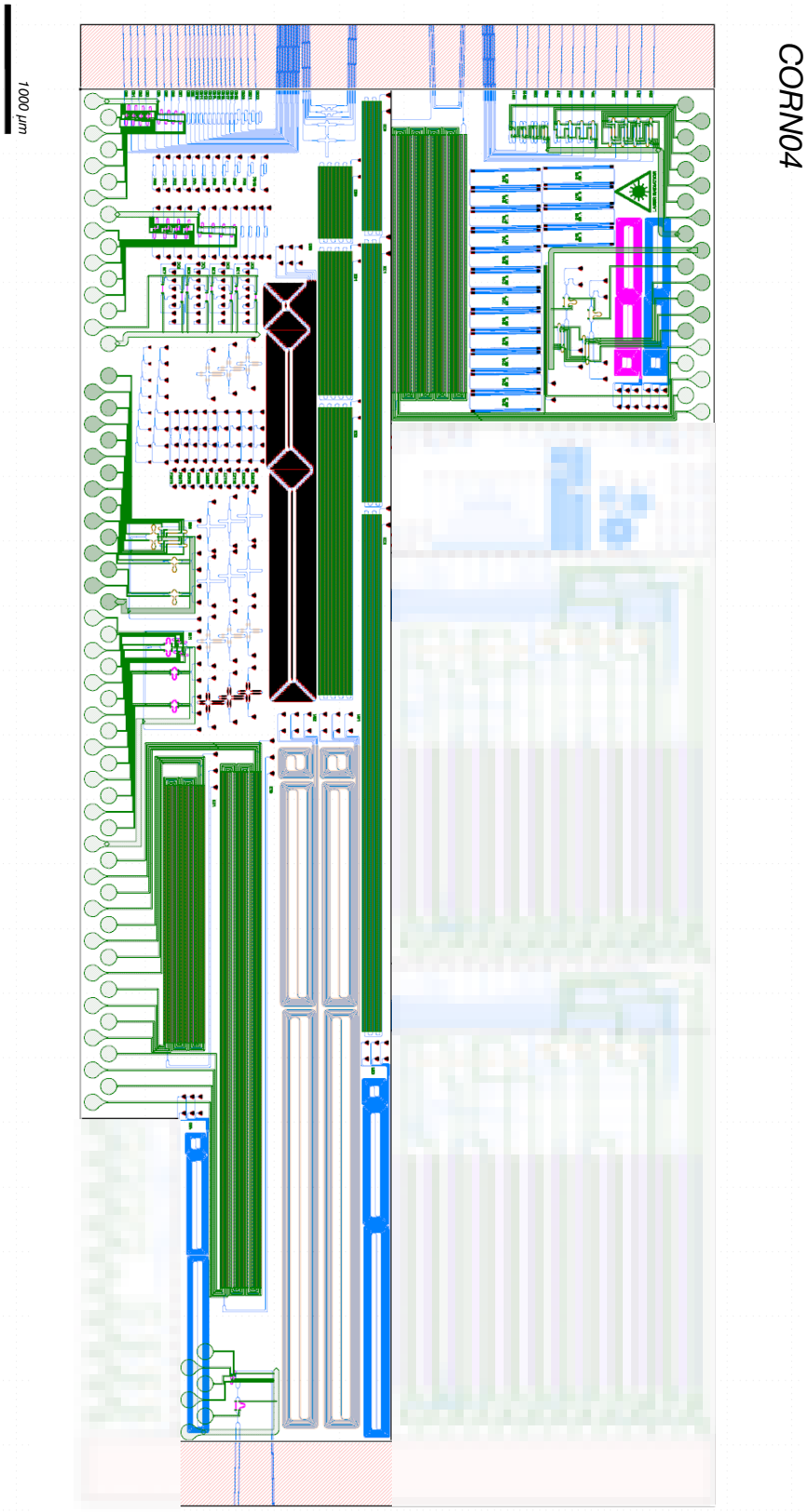

Figure F.6: Cornerstone: CORN04. Design credit: Lawrence Rosenfeld, Joshua Silverstone.

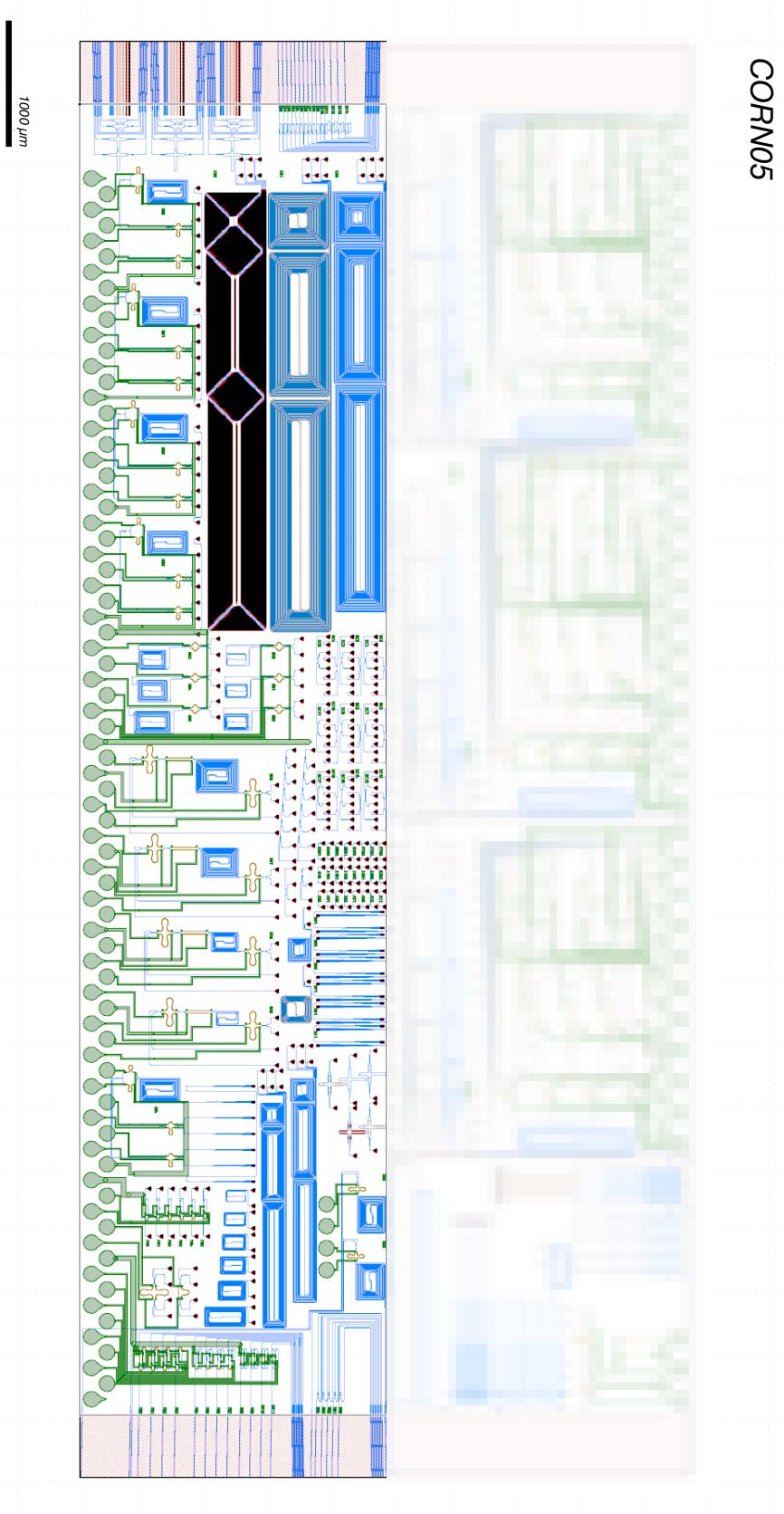

Figure F.7: Cornerstone: CORN05. Design credit: Lawrence Rosenfeld, Joshua Silverstone. Received September 2018.

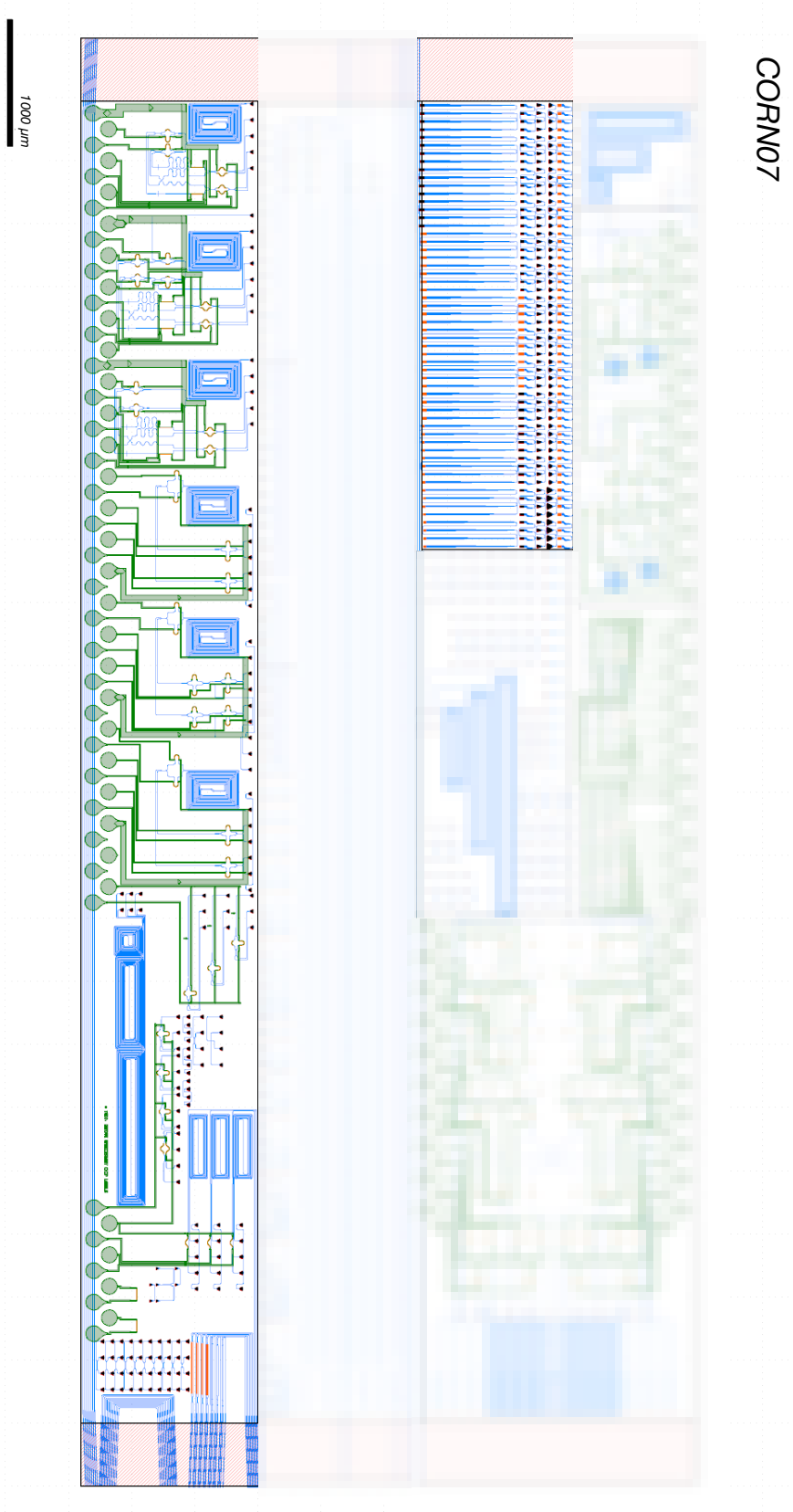

Figure F.8: Cornerstone: CORN07. Design credit: Lawrence Rosenfeld, Joshua Silverstone. Received February 2019.

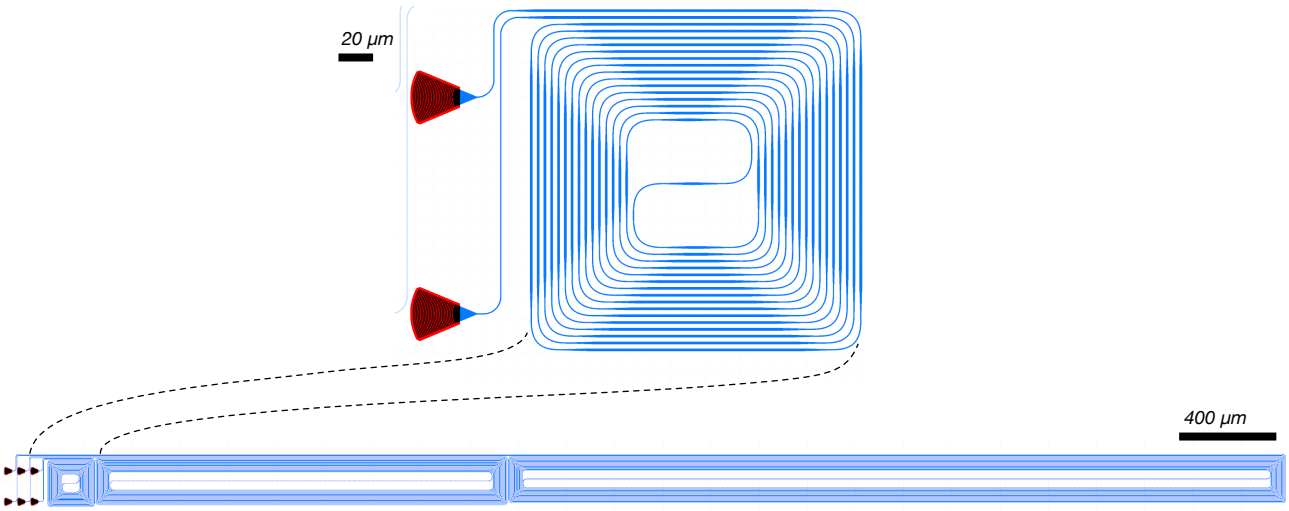

Figure F.9: IME03 (generation 2) waveguide delay line presented in Sec. 3.2.

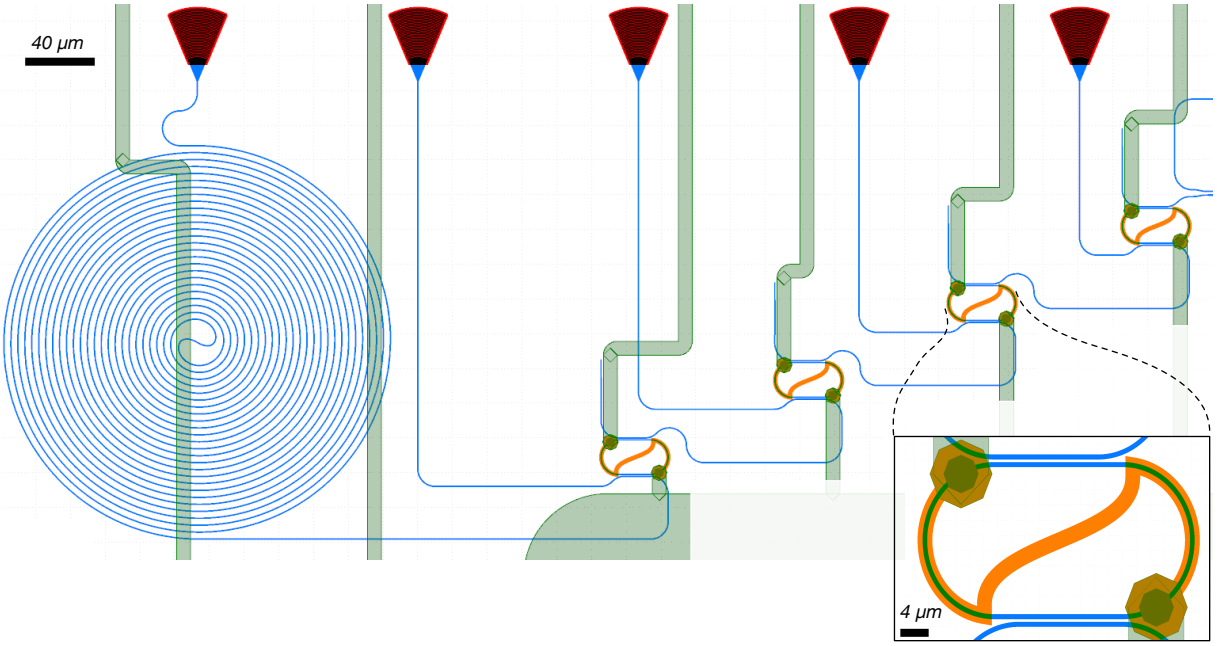

Figure F.10: IME05 (generation 4) cascaded ring filter presented in Sec. 3.4.3.

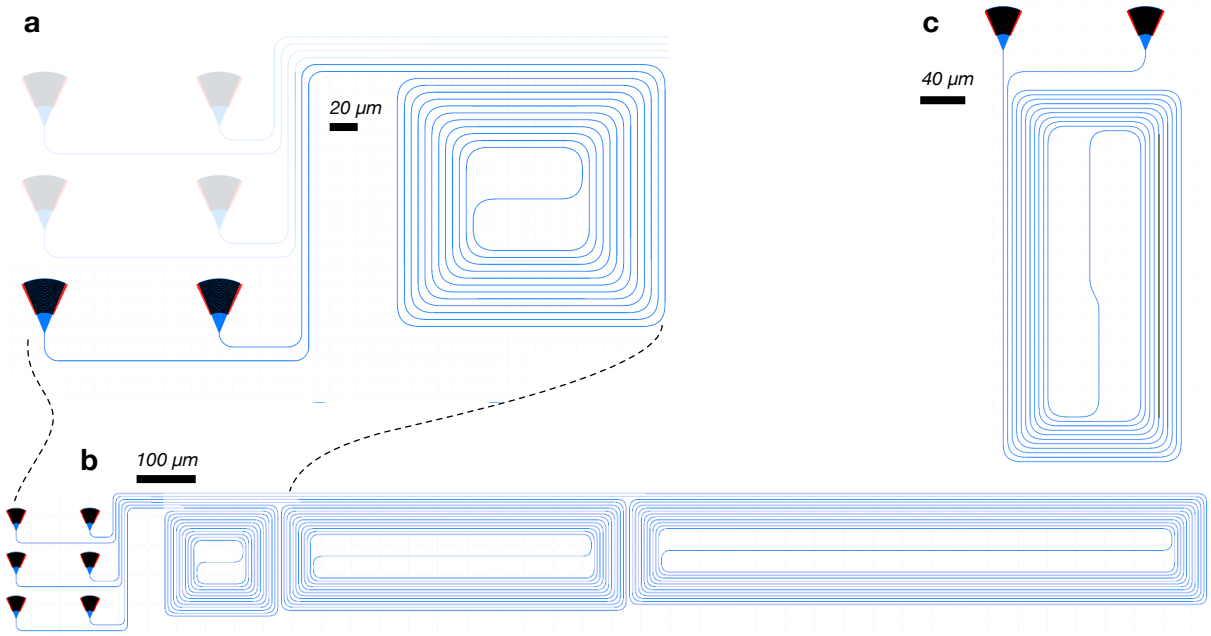

Figure F.11: CORN05 (generation 5) waveguides sources. **a,** The waveguide source producing quantum correlated photon pairs in Sec. 4.4.1. **b,** The set of waveguides for the cutback measurement presented in Fig. 3.12. **c,** The waveguide source for measuring stimulated four-wave mixing in Sec. 3.5.2.

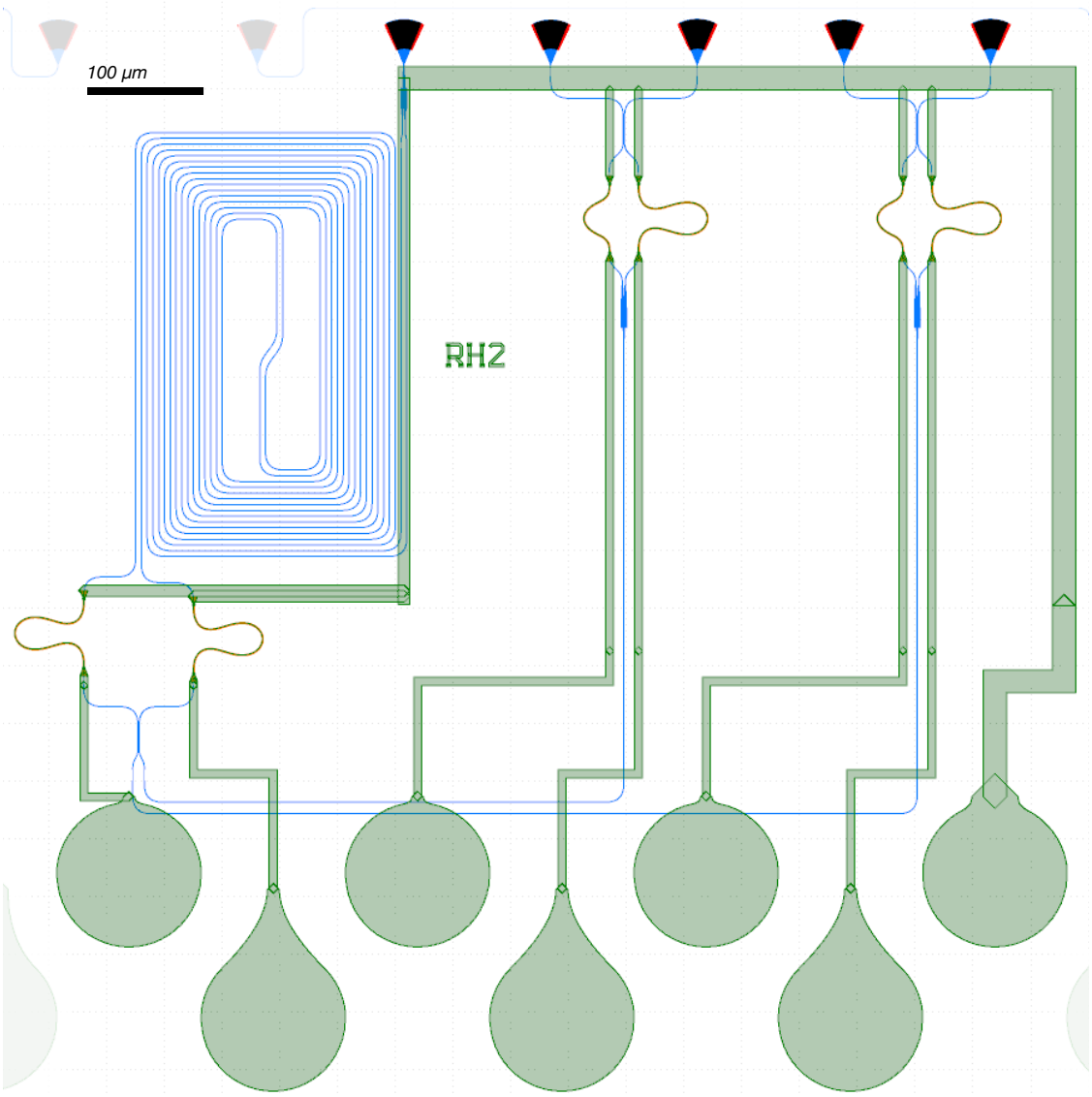

Figure F.12: CORN05 (generation 5) time-reversed Hong-Ou-Mandel circuit from Sec. 5.1.2.

APPENDIX G

Miscellaneous

G.1 Thesis timeline

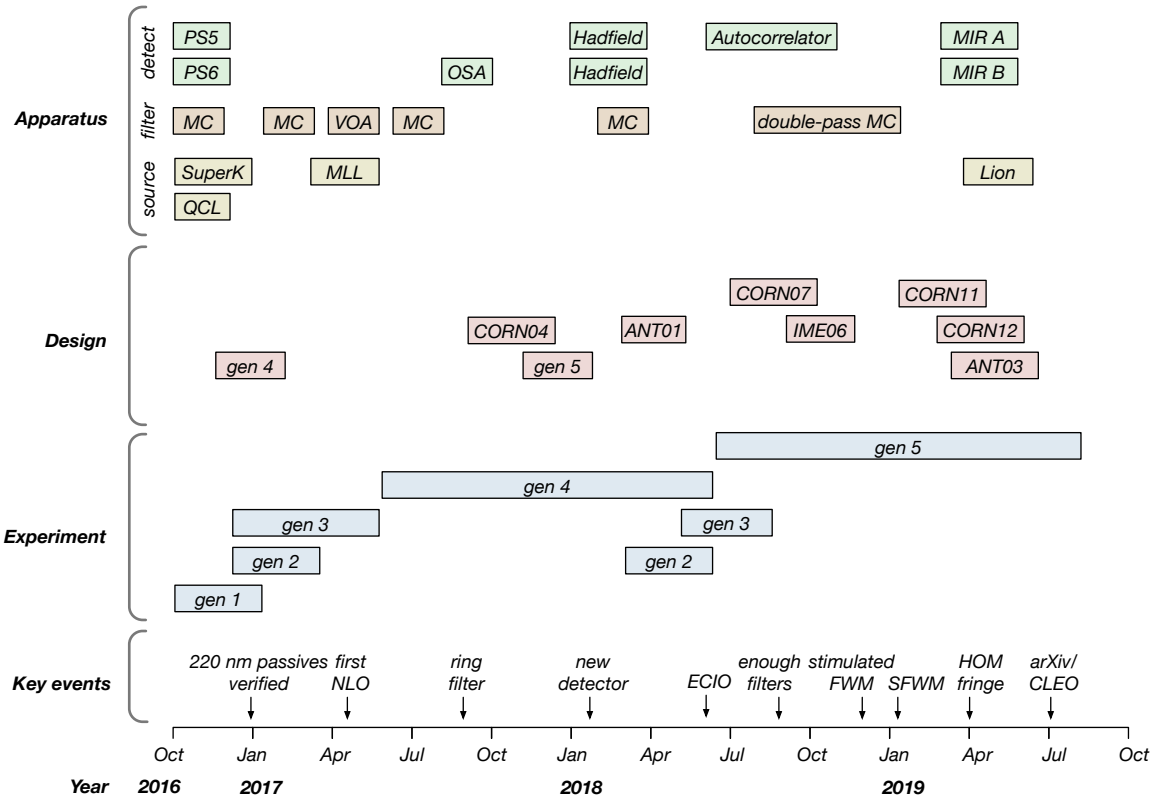

Figure G.1: Timeline of the experiments, design, and apparatus construction over the 3 years of the project. Note gen and number combination denotes chip generation from chapter 3.

Figure G.2: Some marvellous dark field optical micrographs of directional and grating couplers. Image credit: Lawrence Rosenfeld, Josh Silverstone.

References

[1] O'Brien, J. L., Furusawa, A. & Vučković, J. Photonic quantum technologies. *Nature Photonics* **3**, 687 (2009). ⟨1, 3, 10, 38⟩.

[2] Silverstone, J. W. *Entangled light in silicon waveguides*. Ph.D. thesis, University of Bristol (2015). ⟨1, 32, 35⟩.

[3] Planck, M. K. E. L. Zur theorie des gesetzes der energieverteilung im normalspectrum. *Verhandl. Dtsc. Phys. Ges.* **2**, 237 (1900). ⟨1⟩.

[4] Einstein, A. Über einen die erzeugung und verwandlung des lichtes betreffenden heuristischen gesichtspunkt. *Annalen der physik* **322**, 132–148 (1905). ⟨2⟩.

[5] Rutherford, E. Lxxix. the scattering of α and β particles by matter and the structure of the atom. *The London, Edinburgh, and Dublin Philosophical Magazine and Journal of Science* **21**, 669–688 (1911). ⟨2⟩.

[6] Heisenberg, W. Über quantentheoretische umdeutung kinematischer und mechanischer beziehungen. *Zeitschrift für Physik* **33**, 879–893 (1925). ⟨2⟩.

[7] Schrödinger, E. An undulatory theory of the mechanics of atoms and molecules. *Physical Review* **28**, 1049 (1926). ⟨2⟩.

[8] Transistor count (2019). URL `https://en.wikipedia.org/wiki/Transistor_count`. ⟨2⟩.

[9] Evolution of the silicon wafer infographic. URL `https://f450c.org/infographic/`. ⟨2⟩.

[10] Turing, A. M. On computable numbers, with an application to the entscheidungsproblem. *Proceedings of the London Mathematical Society* **2**, 230–265 (1937). ⟨2⟩.

[11] Kilby, J. S. Miniaturized electronic circuits (1959). US Patent 3,138, 743. ⟨2⟩.

[12] Moore, G. E. Cramming more components onto integrated circuits. *Proceedings of the IEEE* **86**, 82–85 (1998). ⟨2⟩.

[13] Samsung successfully completes 5nm euv development to allow greater area scaling and ultra-low power benefits. URL `https://news.samsung.com/global/samsung-successfully-completes-5nm-euv-development-to-allow-greater-area-scaling-and-ultra-low-power-benefits`. ⟨2⟩.

[14] Shen, Y. *et al.* Deep learning with coherent nanophotonic circuits. *Nature Photonics* **11**, 441 (2017). ⟨2⟩.

[15] Reed, G. T., Mashanovich, G., Gardes, F. Y. & Thomson, D. Silicon optical modulators. *Nature Photonics* **4**, 518 (2010). ⟨2, 17, 116⟩.

[16] Kaminow, I. & Carruthers, J. Optical waveguiding layers in LiNbO3 and LiTaO3. *Applied Physics Letters* **22**, 326–328 (1973). ⟨2⟩.

[17] Izawa, T. Deposited silica waveguide for integrated optical circuits. *Applied Physics Letters* **38**, 483–485 (1981). ⟨2⟩.

[18] Knights, A. P. & Doylend, J. Silicon photonics—recent advances in device development. *Advances in Information Optics and Photonics* **1** (2008). ⟨2⟩.

[19] Liu, A. *et al.* A high-speed silicon optical modulator based on a metal–oxide–semiconductor capacitor. *Nature* **427**, 615 (2004). ⟨3⟩.

[20] Cheng, Q., Bahadori, M., Glick, M., Rumley, S. & Bergman, K. Recent advances in optical technologies for data centers: a review. *Optica* **5**, 1354–1370 (2018). ⟨3, 14⟩.

[21] Feynman, R. P. Simulating physics with computers. *International Journal of Theoretical Physics* **21**, 467–488 (1982). ⟨3⟩.

[22] Cho, A. Google claims quantum computing milestone. *Science* **365**, 1364–1364 (2019). ⟨3⟩.

[23] Gibney, E. Quantum gold rush: the private funding pouring into quantum start-ups. *Nature* **574**, 22 (2019). ⟨3⟩.

[24] Montanaro, A. Quantum algorithms: an overview. *npj Quantum Information* **2**, 15023 (2016). ⟨3⟩.

[25] Gidney, C. & Ekerå, M. How to factor 2048 bit rsa integers in 8 hours using 20 million noisy qubits. *arXiv preprint arXiv:1905.09749* (2019). ⟨3⟩.

[26] Peruzzo, A. *et al.* A variational eigenvalue solver on a photonic quantum processor. *Nature communications* **5**, 4213 (2014). ⟨3, 11⟩.

[27] Knill, E., Laflamme, R. & Milburn, G. J. A scheme for efficient quantum computation with linear optics. *Nature* **409**, 46 (2001). ⟨3⟩.

[28] Lloyd, S. & Braunstein, S. L. Quantum computation over continuous variables. *Physical Review Letters* **82**, 1784 (1999). ⟨3⟩.

[29] Mondain, F. *et al.* Chip-based squeezing at a telecom wavelength. *Photonics Research* **7**, A36–A39 (2019). ⟨3, 115⟩.

[30] Wang, H. *et al.* Boson sampling with 20 input photons in 60-mode interferometers at 10^{14} state spaces. *arXiv preprint arXiv:1910.09930* (2019). ⟨3, 11, 32⟩.

[31] Corning. Corning SMF-28 ultra optical fibre. Accessed: 18-10-2019 `https://www.corning.com/media/worldwide/coc/documents/Fiber/SMF-28%20Ultra.pdf`. ⟨3⟩.

[32] Rudolph, T. Why I am optimistic about the silicon-photonic route to quantum computing. *APL Photonics* **2**, 030901 (2017). ⟨3, 11, 12, 13, 116⟩.

[33] Gerry, C., Knight, P. & Knight, P. L. *Introductory quantum optics* (Cambridge University Press, 2005). ⟨4, 5, 33, 93, 127, 129, 130⟩.

[34] Crespi, A. *et al.* Integrated photonic quantum gates for polarization qubits. *Nature communications* **2**, 566 (2011). ⟨5⟩.

[35] Humphreys, P. C. *et al.* Linear optical quantum computing in a single spatial mode. *Physical Review Letters* **111**, 150501 (2013). ⟨5⟩.

[36] Lukens, J. M. & Lougovski, P. Frequency-encoded pho-

tonic qubits for scalable quantum information processing. *Optica* **4**, 8–16 (2017). ⟨5⟩.

[37] Wang, J. *et al.* Multidimensional quantum entanglement with large-scale integrated optics. *Science* **360**, 285–291 (2018). ⟨5, 32, 38, 102⟩.

[38] Kok, P. & Lovett, B. W. *Introduction to optical quantum information processing* (Cambridge University Press, 2010). ⟨6⟩.

[39] Santagati, R. *et al.* Silicon photonic processor of two-qubit entangling quantum logic. *Journal of Optics* **19**, 114006 (2017). ⟨9⟩.

[40] Kok, P., Lee, H. & Dowling, J. P. Creation of large-photon-number path entanglement conditioned on photodetection. *Physical Review A* **65**, 052104 (2002). ⟨9⟩.

[41] Pan, J.-W., Bouwmeester, D., Daniell, M., Weinfurter, H. & Zeilinger, A. Experimental test of quantum nonlocality in three-photon Greenberger–Horne–Zeilinger entanglement. *Nature* **403**, 515 (2000). ⟨9⟩.

[42] Gimeno-Segovia, M., Shadbolt, P., Browne, D. E. & Rudolph, T. From three-photon Greenberger-Horne-Zeilinger states to ballistic universal quantum computation. *Physical Review Letters* **115**, 020502 (2015). ⟨10, 13, 116⟩.

[43] Hong, C.-K., Ou, Z.-Y. & Mandel, L. Measurement of subpicosecond time intervals between two photons by interference. *Physical Review Letters* **59**, 2044 (1987). ⟨10, 101⟩.

[44] Burnham, D. C. & Weinberg, D. L. Observation of simultaneity in parametric production of optical photon pairs. *Physical Review Letters* **25**, 84 (1970). ⟨10⟩.

[45] Harada, K.-i. *et al.* Indistinguishable photon pair generation using two independent silicon wire waveguides. *New Journal of Physics* **13**, 065005 (2011). ⟨10⟩.

[46] Silverstone, J. W. *et al.* On-chip quantum interference between silicon photon-pair sources. *Nature Photonics* **8**, 104 (2014). ⟨10, 28, 32, 101, 104, 106, 107, 108, 113⟩.

[47] Matthews, J. C. F., Politi, A., Stefanov, A. & O'Brien, J. L. Manipulation of multiphoton entanglement in waveguide quantum circuits. *Nature Photonics* **3**, 346 (2009). ⟨11, 106⟩.

[48] Semenenko, H., Sibson, P., Thompson, M. G. & Erven, C. Interference between independent photonic integrated devices for quantum key distribution. *Optics Letters* **44**, 275–278 (2019). ⟨11⟩.

[49] Rarity, J. G. *et al.* Two-photon interference in a Mach-Zehnder interferometer. *Physical Review Letters* **65**, 1348 (1990). ⟨11, 101, 106⟩.

[50] Sepiol, M. *et al.* Probing qubit memory errors at the part-per-million level. *Physical Review Letters* **123**, 110503 (2019). ⟨11⟩.

[51] Arute, F. *et al.* Quantum supremacy using a programmable superconducting processor. *Nature* **574**, 505–510 (2019). ⟨11⟩.

[52] Fruchtman, A. & Choi, I. Technical roadmap for fault-tolerant quantum computing (2016). ⟨11⟩.

[53] Reck, M., Zeilinger, A., Bernstein, H. J. & Bertani, P. Experimental realization of any discrete unitary operator. *Physical review letters* **73**, 58 (1994). ⟨12⟩.

[54] Carolan, J. *et al.* Universal linear optics. *Science* **349**, 711–716 (2015). ⟨12, 14⟩.

[55] Nielsen, M. A. & Chuang, I. Quantum computation and quantum information (2002). ⟨12⟩.

[56] Raussendorf, R. & Briegel, H. J. A one-way quantum computer. *Physical Review Letters* **86**, 5188 (2001). ⟨12⟩.

[57] Walther, P. *et al.* Experimental one-way quantum computing. *Nature* **434**, 169 (2005). ⟨12⟩.

[58] Browne, D. E. & Rudolph, T. Resource-efficient linear optical quantum computation. *Physical Review Letters* **95**, 010501 (2005). ⟨13⟩.

[59] Robinson, J. T., Chen, L. & Lipson, M. On-chip gas detection in silicon optical microcavities. *Optics Express* **16**, 4296–4301 (2008). ⟨14⟩.

[60] Adcock, J. C., Vigliar, C., Santagati, R., Silverstone, J. W. & Thompson, M. G. Programmable four-photon graph states on a silicon chip. *Nature Communications* **10**, 1–6 (2019). ⟨14, 38, 102, 106⟩.

[61] Penades, J. S. *et al.* Suspended silicon mid-infrared waveguide devices with subwavelength grating metamaterial cladding. *Optics Express* **24**, 22908–22916 (2016). ⟨15, 56, 112⟩.

[62] McNab, S. J., Moll, N. & Vlasov, Y. A. Ultra-low loss photonic integrated circuit with membrane-type photonic crystal waveguides. *Optics Express* **11**, 2927–2939 (2003). ⟨15⟩.

[63] Marcatili, E. A. Dielectric rectangular waveguide and directional coupler for integrated optics. *Bell System Technical Journal* **48**, 2071–2102 (1969). ⟨16⟩.

[64] Hagan, D. E. & Knights, A. P. Mechanisms for optical loss in soi waveguides for mid-infrared wavelengths around 2 mum. *Journal of Optics* **19** (2017). ⟨17, 18, 39⟩.

[65] Payne, F. & Lacey, J. A theoretical analysis of scattering loss from planar optical waveguides. *Optical and Quantum Electronics* **26**, 977–986 (1994). ⟨17⟩.

[66] Reed, G. T. & Knights, A. P. *Silicon photonics: an introduction* (John Wiley & Sons, 2004). ⟨17, 21, 111, 133, 134, 135⟩.

[67] Rukhlenko, I. D., Premaratne, M. & Agrawal, G. P. Effective mode area and its optimization in silicon-nanocrystal waveguides. *Optics Letters* **37**, 2295–2297 (2012). ⟨18, 88⟩.

[68] Baker-Finch, S. C., McIntosh, K. R., Yan, D., Fong, K. C. & Kho, T. C. Near-infrared free carrier absorption in heavily doped silicon. *Journal of Applied Physics* **116**, 063106 (2014). ⟨18⟩.

[69] Gnan, M., Thoms, S., Macintyre, D., De La Rue, R. & Sorel, M. Fabrication of low-loss photonic wires in silicon-on-insulator using hydrogen silsesquioxane electron-beam resist. *Electronics Letters* **44**, 115–116 (2008). ⟨18⟩.

[70] Vlasov, Y. A. & McNab, S. J. Losses in single-mode silicon-on-insulator strip waveguides and bends. *Optics Express* **12**, 1622–1631 (2004). ⟨18⟩.

[71] Horikawa, T., Shimura, D. & Mogami, T. Low-loss silicon wire waveguides for optical integrated circuits. *MRS Communications* **6**, 9–15 (2016). ⟨18⟩.

[72] Cardenas, J. *et al.* Low loss etchless silicon photonic waveguides. *Optics Express* **17**, 4752–4757 (2009). ⟨18, 38⟩.

[73] Agrawal, G. P. *Nonlinear Fiber Optics* (Academic Press, San Diego, 2001), 3 edn. ⟨18, 28, 29, 30, 36, 37, 62, 135, 151, 153, 155⟩.

[74] Frey, B. J., Leviton, D. B. & Madison, T. J. Temperature-dependent refractive index of silicon and germanium. In *Optomechanical Technologies for Astronomy*, vol. 6273, 62732J (International Society for Optics and Photonics, 2006). ⟨19, 135, 136⟩.

[75] Li, M., Wang, L., Li, X., Xiao, X. & Yu, S. Silicon intensity mach–zehnder modulator for single lane 100 gb/s applications. *Photonics Research* **6**, 109–116 (2018). ⟨19⟩.

[76] Harris, N. C. *et al.* Efficient, compact and low loss thermo-optic phase shifter in silicon. *Optics Express* **22**, 10487–10493 (2014). ⟨19⟩.

[77] Ice Oxford. ICE completes development of a High Cooling Power (2015). URL `https://www.iceoxford.com/News/Nov-2015---ICE-completes-development-of-a-High-Cooling-Power-(230mW-@-1.0K)-Cryostat-for-MIT/309.htm`. ⟨19⟩.

[78] Hinkelmann, M., Wandt, D., Morgner, U., Neumann, J. & Kracht, D. Mode-locked Ho-doped laser with subsequent diode-pumped amplifier in an all-fiber design operating at 2052 nm. *Optics Express* **25**, 20522–20529 (2017). ⟨20, 43⟩.

[79] Vermeulen, D. *et al.* Reflectionless grating couplers for silicon-on-insulator photonic integrated circuits. *Optics express* **20**, 22278–22283 (2012). ⟨21⟩.

[80] Chen, X., Li, C., Fung, C. K., Lo, S. M. & Tsang, H. K. Apodized waveguide grating couplers for efficient coupling to optical fibers. *IEEE Photonics Technology Letters* **22**, 1156–1158 (2010). ⟨21, 74⟩.

[81] Marchetti, R. *et al.* High-efficiency grating-couplers: demonstration of a new design strategy. *Scientific Reports* **7**, 16670 (2017). ⟨21, 74⟩.

[82] Benedikovic, D. *et al.* High-directionality fiber-chip grating coupler with interleaved trenches and subwavelength index-matching structure. *Optics Letters* **40**, 4190–4193 (2015). ⟨21, 57, 58⟩.

[83] Wang, Y. *et al.* O-band sub-wavelength grating coupler. In *2017 IEEE Photonics Conference (IPC)*, 429–430 (IEEE, 2017). ⟨21, 56, 65⟩.

[84] Benedikovic, D. *et al.* Subwavelength index engineered surface grating coupler with sub-decibel efficiency for 220-nm silicon-on-insulator waveguides. *Optics Express* **23**, 22628–22635 (2015). ⟨21, 38⟩.

[85] Tuma, M. L. & Beheim, G. Calculated coupling efficiency between an elliptical-core optical fiber and a silicon oxynitride rib waveguide. In *Micro-Optics/Micromechanics and Laser Scanning and Shaping*, vol. 2383, 199–210 (International Society for Optics and Photonics, 1995). ⟨22⟩.

[86] Almeida, V. R., Panepucci, R. R. & Lipson, M. Nanotaper for compact mode conversion. *Optics Letters* **28**, 1302–1304 (2003). ⟨22⟩.

[87] Cheben, P. *et al.* Broadband polarization independent nanophotonic coupler for silicon waveguides with ultra-high efficiency. *Optics express* **23**, 22553–22563 (2015). ⟨22⟩.

[88] Tiecke, T. *et al.* Efficient fiber-optical interface for nanophotonic devices. *Optica* **2**, 70–75 (2015). ⟨22⟩.

[89] Zeilinger, A. General properties of lossless beam splitters in interferometry. *Am. J. Phys* **49**, 882–883 (1981). ⟨22, 96⟩.

[90] Chrostowski, L. & Hochberg, M. *Silicon photonics design: from devices to systems* (Cambridge University Press, 2015). ⟨22⟩.

[91] Chen, G. F. *et al.* Broadband silicon-on-insulator directional couplers using a combination of straight and curved waveguide sections. *Scientific Reports* **7**, 7246 (2017). ⟨23⟩.

[92] Lu, Z. *et al.* Broadband silicon photonic directional coupler using asymmetric-waveguide based phase control. *Optics Express* **23**, 3795–3808 (2015). ⟨23⟩.

[93] Greenberg, M. & Orenstein, M. Multimode add-drop multiplexing by adiabatic linearly tapered coupling. *Optics Express* **13**, 9381–9387 (2005). ⟨23⟩.

[94] Ding, Y. *et al.* On-chip two-mode division multiplexing using tapered directional coupler-based mode multiplexer and demultiplexer. *Optics Express* **21**, 10376–10382 (2013). ⟨23⟩.

[95] Luo, L.-W. *et al.* WDM-compatible mode-division multiplexing on a silicon chip. *Nature Communications* **5**, 3069 (2014). ⟨23⟩.

[96] Soldano, L. B. & Pennings, E. C. Optical multi-mode interference devices based on self-imaging: principles and applications. *Journal of Lightwave Technology* **13**, 615–627 (1995). ⟨24, 25, 56⟩.

[97] Sun, X., Aitchison, J. S. & Mojahedi, M. Realization of an ultra-compact polarization beam splitter using asymmetric MMI based on silicon nitride/silicon-on-insulator platform. *Optics Express* **25**, 8296–8305 (2017). ⟨25⟩.

[98] Maese-Novo, A. *et al.* Wavelength independent multimode interference coupler. *Optics Express* **21**, 7033–7040 (2013). ⟨25⟩.

[99] Shen, B., Wang, P., Polson, R. & Menon, R. An integrated-nanophotonics polarization beamsplitter with 2.4× 2.4 μm 2 footprint. *Nature Photonics* **9**, 378 (2015). ⟨25⟩.

[100] Zhang, Y. *et al.* A compact and low loss Y-junction for submicron silicon waveguide. *Optics Express* **21**, 1310–1316 (2013). ⟨25⟩.

[101] Turner, A. C., Foster, M. A., Gaeta, A. L. & Lipson, M. Ultra-low power parametric frequency conversion in a silicon microring resonator. *Optics Express* **16**, 4881–4887 (2008). ⟨26, 30⟩.

[102] Azzini, S. *et al.* Ultra-low power generation of twin photons in a compact silicon ring resonator. *Optics Express* **20**, 23100–23107 (2012). ⟨26, 113⟩.

[103] Engin, E. *et al.* Photon pair generation in a silicon micro-ring resonator with reverse bias enhancement. *Optics Express* **21**, 27826–27834 (2013). ⟨26, 32, 35, 113⟩.

[104] Baba, T. *et al.* 50-Gb/s ring-resonator-based silicon modulator. *Optics express* **21**, 11869–11876 (2013). ⟨26⟩.

[105] Dong, P. *et al.* GHz-bandwidth optical filters based on high-order silicon ring resonators. *Optics Express* **18**, 23784–23789 (2010). ⟨26⟩.

[106] Yebo, N. A., Lommens, P., Hens, Z. & Baets, R. An integrated optic ethanol vapor sensor based on a silicon-on-insulator microring resonator coated with a porous ZnO film. *Optics Express* **18**, 11859–11866 (2010). ⟨26⟩.

[107] Rabus, D. G. Ring resonators: Theory and modeling. *Integrated Ring Resonators: The Compendium* 3–40 (2007). ⟨26, 136⟩.

[108] Natarajan, C. M., Tanner, M. G. & Hadfield, R. H. Superconducting nanowire single-photon detectors: physics and applications. *Superconductor Science and Technology* **25**, 063001 (2012). ⟨27, 28⟩.

[109] Semenov, A. D. *et al.* Vortex-based single-photon response in nanostructured superconducting detectors. *Physica C: Superconductivity and its applications* **468**, 627–630 (2008). ⟨27⟩.

[110] Cooper, L. N. Bound electron pairs in a degenerate Fermi gas. *Physical Review* **104**, 1189 (1956). ⟨27⟩.

[111] Marsili, F. *et al.* Detecting single infrared photons with 93% system efficiency. *Nature Photonics* **7**, 210 (2013). ⟨28⟩.

[112] Marsili, F. *et al.* Efficient single photon detection from 500 nm to 5 μm wavelength. *Nano letters* **12**, 4799–4804 (2012). ⟨28, 98⟩.

[113] Leuthold, J., Koos, C. & Freude, W. Nonlinear silicon photonics. *Nature Photonics* **4**, 535 (2010). ⟨28⟩.

[114] Boyd, R. W. *Nonlinear optics* (Elsevier, 2003). ⟨29, 36⟩.

[115] Mollenauer, L. F., Stolen, R. H. & Gordon, J. P. Experimental observation of picosecond pulse narrowing and solitons in optical fibers. *Physical Review Letters* **45**, 1095 (1980). ⟨30⟩.

[116] Bergman, K. & Haus, H. Squeezing in fibers with optical pulses. *Optics Letters* **16**, 663–665 (1991). ⟨30⟩.

[117] Ranka, J. K., Windeler, R. S. & Stentz, A. J. Visible continuum generation in air–silica microstructure optical fibers with anomalous dispersion at 800 nm. *Optics Letters* **25**, 25–27 (2000). ⟨30, 42⟩.

[118] Matsuda, N., Shimizu, R., Mitsumori, Y., Kosaka, H. & Edamatsu, K. Observation of optical-fibre kerr nonlinearity at the single-photon level. *Nature Photonics* **3**, 95 (2009). ⟨30⟩.

[119] Liu, X., Osgood Jr, R. M., Vlasov, Y. A. & Green, W. M. Mid-infrared optical parametric amplifier using silicon nanophotonic waveguides. *Nature Photonics* **4**, 557 (2010). ⟨30, 37, 68, 77, 111⟩.

[120] Signorini, S. *et al.* Intermodal four-wave mixing in silicon waveguides. *Photonics Research* **6**, 805–814 (2018). ⟨31, 114⟩.

[121] Sinclair, G. F., Tyler, N. A., Sahin, D., Barreto, J. & Thompson, M. G. Temperature dependence of the Kerr nonlinearity and two-photon absorption in a silicon waveguide at 1.55 μm. *Physical Review Applied* **11**, 044084 (2019). ⟨31, 86, 87, 88, 89, 99, 112, 115⟩.

[122] Tsang, H. & Liu, Y. Nonlinear optical properties of silicon waveguides. *Semiconductor Science and Technology* **23**, 064007 (2008). ⟨31⟩.

[123] Soref, R. & Bennett, B. Electrooptical effects in silicon. *IEEE Journal of Quantum Electronics* **23**, 123–129 (1987). ⟨31⟩.

[124] Liu, Y. & Tsang, H. Nonlinear absorption and Raman gain in helium-ion-implanted silicon waveguides. *Optics Letters* **31**, 1714–1716 (2006). ⟨32⟩.

[125] Xu, Q. & Lipson, M. Carrier-induced optical bistability in silicon ring resonators. *Optics Letters* **31**, 341–343 (2006). ⟨32⟩.

[126] Shao, H. *et al.* Performance influence of FCA and nonlinear FCD to the Mach-Zehnder-Interference based silicon DPSK generation. *Optics Express* **20**, 23527–23534 (2012). ⟨32⟩.

[127] Husko, C. A. *et al.* Multi-photon absorption limits to heralded single photon sources. *Scientific Reports* **3**, 3087 (2013). ⟨32, 34, 36, 37, 97⟩.

[128] Silverstone, J. W., Bonneau, D., O'Brien, J. L. & Thompson, M. G. Silicon quantum photonics. *IEEE Journal of Selected Topics in Quantum Electronics* **22**, 390–402 (2016). ⟨32, 38, 39, 99, 100, 111⟩.

[129] Gajda, A., Zimmermann, L., Bruns, J., Tillack, B. & Petermann, K. Design rules for pin diode carriers sweeping in nano-rib waveguides on soi. *Optics Express* **19**, 9915–9922 (2011). ⟨32⟩.

[130] Smith, J., Monroy-Ruz, J., Rarity, J. G. & Balram, K. C. Single photon emission and single spin coherence of a nitrogen vacancy centre encapsulated in silicon nitride. *arXiv preprint arXiv:1909.09383* (2019). ⟨32⟩.

[131] Mancinelli, M. *et al.* Mid-infrared coincidence measurements on twin photons at room temperature. *Nature Communications* **8**, 15184 (2017). ⟨32, 38, 84, 98⟩.

[132] Fiorentino, M., Voss, P. L., Sharping, J. E. & Kumar, P. All-fiber photon-pair source for quantum communications. *IEEE Photonics Technology Letters* **14**, 983–985 (2002). ⟨32⟩.

[133] Jin, H. *et al.* On-chip generation and manipulation of entangled photons based on reconfigurable lithium-niobate waveguide circuits. *Physical Review Letters* **113**, 103601 (2014). ⟨32, 101⟩.

[134] Ramelow, S. *et al.* Silicon-nitride platform for narrowband entangled photon generation. *arXiv preprint arXiv:1508.04358* (2015). ⟨32, 38⟩.

[135] Gimeno-Segovia, M. *Towards practical linear optical quantum computing*. Ph.D. thesis, Imperial College London (2015). ⟨32⟩.

[136] Riedmatten, H. D. *et al.* Two independent photon pairs versus four-photon entangled states in parametric down

conversion. *Journal of Modern Optics* **51**, 1637–1649 (2004). ⟨33⟩.

[137] Clemmen, S. *et al.* Continuous wave photon pair generation in silicon-on-insulator waveguides and ring resonators. *Optics Express* **17**, 16558–16570 (2009). ⟨34⟩.

[138] Yin, L. & Agrawal, G. P. Impact of two-photon absorption on self-phase modulation in silicon waveguides. *Optics letters* **32**, 2031–2033 (2007). ⟨34, 87, 88, 97⟩.

[139] Zielnicki, K. *et al.* Joint spectral characterization of photon-pair sources. *Journal of Modern Optics* **65**, 1141–1160 (2018). ⟨34⟩.

[140] Liscidini, M. & Sipe, J. Stimulated emission tomography. *Physical Review Letters* **111**, 193602 (2013). ⟨34, 77, 85⟩.

[141] Rarity, J. G., Ridley, K. D. & Tapster, P. Absolute measurement of detector quantum efficiency using parametric downconversion. *Applied Optics* **26**, 4616–4619 (1987). ⟨35⟩.

[142] Ma, C. *et al.* Silicon photonic entangled photon-pair and heralded single photon generation with car> 12,000 and g (2)(0)< 0.006. *Optics Express* **25**, 32995–33006 (2017). ⟨35, 84, 94⟩.

[143] Sieger, M. & Mizaikoff, B. Toward on-chip mid-infrared sensors. *Analytical Chemistry* **88**, 5562 (2016). ⟨37, 111⟩.

[144] Corrigan, P., Martini, R., Whittaker, E. A. & Bethea, C. Quantum cascade lasers and the Kruse model in free space optical communication. *Optics Express* **17**, 4355–4359 (2009). ⟨37⟩.

[145] Prost, M. *et al.* MWIR solid-state optical phased array beam steering using germanium-silicon photonic platform. In *Optical Fiber Communication Conference*, M4E–3 (Optical Society of America, 2019). ⟨37⟩.

[146] Milošević, M. M. *et al.* Silicon waveguides and devices for the mid-infrared. *Applied Physics Letters* **101**, 121105 (2012). ⟨37⟩.

[147] Nedeljkovic, M. *et al.* Silicon photonic devices and platforms for the mid-infrared. *Optical Materials Express* **3**, 1205–1214 (2013). ⟨59⟩.

[148] Miller, S. A. *et al.* Low-loss silicon platform for broadband mid-infrared photonics. *Optica* **4**, 707–712 (2017).

[149] Hattasan, N. *et al.* High-efficiency SOI fiber-to-chip grating couplers and low-loss waveguides for the short-wave infrared. *IEEE Photonics Technology Letters* **24**, 1536–1538 (2012). ⟨37⟩.

[150] Jalali, B. Silicon photonics: Nonlinear optics in the mid-infrared. *Nature Photonics* **4**, 506 (2010). ⟨37⟩.

[151] Griffith, A. G. *et al.* Silicon-chip mid-infrared frequency comb generation. *Nature Communications* **6**, 6299 (2015). ⟨37, 86⟩.

[152] McCracken, R. A., Graffitti, F. & Fedrizzi, A. Numerical investigation of mid-infrared single-photon generation. *JOSA B* **35**, C38–C48 (2018). ⟨38⟩.

[153] Sua, Y. M., Fan, H., Shahverdi, A., Chen, J.-Y. & Huang, Y.-P. Direct generation and detection of quantum correlated photons with 3.2 μm wavelength spacing. *Scientific Reports* **7**, 17494 (2017). ⟨38, 98⟩.

[154] Harris, N. C. *et al.* Linear programmable nanophotonic processors. *Optica* **5**, 1623 (2018). ⟨38⟩.

[155] Lee, D. H. *et al.* Low-loss silicon waveguides with sidewall roughness reduction using a SiO2 hard mask and fluorine-based dry etching. *Journal of Micromechanics and Microengineering* **25**, 015003 (2014). ⟨38⟩.

[156] Sheng, Z. *et al.* A compact and low-loss MMI coupler fabricated with CMOS technology. *IEEE Photonics Journal* **4**, 2272–2277 (2012).

[157] Rouifed, M.-S. *et al.* Low loss SOI waveguides and MMIs at the MIR wavelength of 2 μm. *IEEE Photonics Technology Letters* **28**, 2827–2829 (2016). ⟨38, 39⟩.

[158] Ji, X. *et al.* Ultra-low-loss on-chip resonators with sub-milliwatt parametric oscillation threshold. *Optica* **4**, 619–624 (2017). ⟨38⟩.

[159] Gardeniers, J. G., Tilmans, H. & Visser, C. Lpcvd silicon-rich silicon nitride films for applications in micromechanics, studied with statistical experimental design. *Journal of Vacuum Science & Technology A: Vacuum, Surfaces, and Films* **14**, 2879–2892 (1996). ⟨38⟩.

[160] Bristow, A. D., Rotenberg, N. & Van Driel, H. M. Two-photon absorption and Kerr coefficients of silicon for 850–2200 nm. *Applied Physics Letters* **90**, 191104 (2007). ⟨39, 62, 64, 88, 89, 100, 113⟩.

[161] Wang, T. *et al.* Multi-photon absorption and third-order nonlinearity in silicon at mid-infrared wavelengths. *Optics Express* **21**, 32192–32198 (2013). ⟨39, 62, 64, 89, 113⟩.

[162] Garcia, H. & Kalyanaraman, R. Phonon-assisted two-photon absorption in the presence of a DC-field: the nonlinear Franz-Keldysh effect in indirect gap semiconductors. *Journal of Physics B: Atomic, Molecular and Optical Physics* **39**, 2737 (2006). ⟨39, 89⟩.

[163] Grillot, F., Vivien, L., Laval, S., Pascal, D. & Cassan, E. Size influence on the propagation loss induced by sidewall roughness in ultrasmall SOI waveguides. *IEEE Photonics Technology Letters* **16**, 1661–1663 (2004). ⟨39⟩.

[164] Cheben, P., Halir, R., Schmid, J. H., Atwater, H. A. & Smith, D. R. Subwavelength integrated photonics. *Nature* **560**, 565 (2018). ⟨39⟩.

[165] Varshni, V. P. Temperature dependence of the energy gap in semiconductors. *Physica* **34**, 149–154 (1967). ⟨39, 98, 99⟩.

[166] Faist, J. *et al.* Quantum cascade laser. *Science* **264**, 553–556 (1994). ⟨41⟩.

[167] Rosfjord, K. M., Villalaz, R. A. & Gaylord, T. K. Constant-bandwidth scanning of the Czerny–Turner monochromator. *Applied Optics* **39**, 568–572 (2000). ⟨42⟩.

[168] Martinelli, R. U., Zamerowski, T. J. & Longeway, P. A. 2.6 μm InGaAs photodiodes. *Applied Physics Letters* **53**, 989–991 (1988). ⟨42⟩.

[169] Yasa, Z. A. & Amer, N. M. A rapid-scanning autocorrelation scheme for continuous monitoring of picosecond laser pulses. *Optics Communications* **36**, 406–408 (1981).

⟨47⟩.

[170] Takagi, Y., Kobayashi, T., Yoshihara, K. & Imamura, S. Multiple-and single-shot autocorrelator based on two-photon conductivity in semiconductors. *Optics Letters* **17**, 658–660 (1992). ⟨47⟩.

[171] Yamashita, T. *et al.* Temperature dependent performances of superconducting nanowire single-photon detectors in an ultralow-temperature region. *Applied physics express* **3**, 102502 (2010). ⟨51⟩.

[172] Rosenfeld, L. *et al.* A new platform for integrated quantum optics: the short-wave infrared. In *20th Eur. Conf. Integr. Opt.-ECIO* (2018). ⟨55, 64⟩.

[173] Kuyken, B. *et al.* An octave-spanning mid-infrared frequency comb generated in a silicon nanophotonic wire waveguide. *Nature Communications* **6**, 6310 (2015). ⟨56, 61, 111⟩.

[174] Allen, E. *Suppression of Noise in Classical and Quantum Optics*. Ph.D. thesis, University of Bristol (2018). ⟨60⟩.

[175] Cherchi, M., Ylinen, S., Harjanne, M., Kapulainen, M. & Aalto, T. Dramatic size reduction of waveguide bends on a micron-scale silicon photonic platform. *Optics Express* **21**, 17814–17823 (2013). ⟨60⟩.

[176] Selvaraja, S. K., Bogaerts, W., Absil, P., Van Thourhout, D. & Baets, R. Record low-loss hybrid rib/wire waveguides for silicon photonic circuits. *Group IV Photonics* **2010** (2010). ⟨61⟩.

[177] Fisher, R. A. & Bischel, W. K. Numerical studies of the interplay between self-phase modulation and dispersion for intense plane-wave laser pulses. *Journal of Applied Physics* **46**, 4921–4934 (1975). ⟨62⟩.

[178] Piekarek, M. *et al.* High-extinction ratio integrated photonic filters for silicon quantum photonics. *Optics Letters* **42**, 815–818 (2017). ⟨68, 71, 94, 105, 116, 138⟩.

[179] Oser, D. *et al.* Coherency-broken bragg filters: Overcoming on-chip rejection limitations. *Laser & Photonics Reviews* **13**, 1800226 (2019). ⟨116⟩.

[180] Harris, N. C. *et al.* Integrated source of spectrally filtered correlated photons for large-scale quantum photonic systems. *Physical Review X* **4**, 041047 (2014). ⟨68, 71, 116⟩.

[181] Little, B. E. *et al.* Ultra-compact Si-SiO 2 microring resonator optical channel dropping filters. *IEEE Photonics Technology Letters* **10**, 549–551 (1998). ⟨68⟩.

[182] Cubeddu, R., Polloni, R., Sacchi, C. & Svelto, O. Self-phase modulation and "rocking" of molecules in trapped filaments of light with picosecond pulses. *Physical Review A* **2**, 1955 (1970). ⟨71⟩.

[183] Khudus, M. I. A. *et al.* Phase matched parametric amplification via four-wave mixing in optical microfibers. *Optics Letters* **41**, 761–764 (2016). ⟨77⟩.

[184] Rosenfeld, L. M., Sulway, D. A., Thompson, M. G., Rarity, J. G. & Silverstone, J. W. Short-wave infrared correlated photons from silicon waveguides. In *2019 Conference on Lasers and Electro-Optics Europe and European Quantum Electronics Conference*, ea_p_4 (Optical Society of America, 2019). ⟨83⟩.

[185] Silverstone, J. W., Rosenfeld, L. M. *et al.* Silicon quantum photonics in the short-wave infrared: A new platform for big quantum optics. In *2019 Conference on Lasers and Electro-Optics Europe and European Quantum Electronics Conference*, ea_6_2 (Optical Society of America, 2019). ⟨83⟩.

[186] Rosenfeld, L. M. *et al.* Mid-infrared quantum optics in silicon. *arXiv preprint arXiv:1906.10158* (2019). ⟨83, 101⟩.

[187] Stry, S. *et al.* Widely tunable diffraction limited 1000 mw external cavity diode laser in littman/metcalf configuration for cavity ring-down spectroscopy. *Applied Physics B* **85**, 365–374 (2006). ⟨84⟩.

[188] Eckstein, A. *et al.* High-resolution spectral characterization of two photon states via classical measurements. *Laser & Photonics Reviews* **8**, L76–L80 (2014). ⟨85⟩.

[189] Reintjes, J. F. & McGroddy, J. C. Indirect two-photon transitions in Si at 1.06 μm. *Physical Review Letters* **30**, 901 (1973). ⟨86⟩.

[190] Pernice, W. H., Li, M. & Tang, H. X. Time-domain measurement of optical transport in silicon micro-ring resonators. *Optics express* **18**, 18438–18452 (2010). ⟨86⟩.

[191] Pernice, W. H., Schuck, C., Li, M. & Tang, H. X. Carrier and thermal dynamics of silicon photonic resonators at cryogenic temperatures. *Optics express* **19**, 3290–3296 (2011).

[192] Dimitropoulos, D., Jhaveri, R., Claps, R., Woo, J. & Jalali, B. Lifetime of photogenerated carriers in silicon-on-insulator rib waveguides. *Applied Physics Letters* **86**, 071115 (2005). ⟨86⟩.

[193] Turner-Foster, A. C. *et al.* Ultrashort free-carrier lifetime in low-loss silicon nanowaveguides. *Optics express* **18**, 3582–3591 (2010). ⟨86⟩.

[194] W, G. R. & O, S. W. A practical algorithm for the determination of phase from image and diffraction plane pictures. *Optik* **34**, 227–284 (1972). ⟨88⟩.

[195] Yang, Z., Liscidini, M. & Sipe, J. Spontaneous parametric down-conversion in waveguides: a backward heisenberg picture approach. *Physical Review A* **77**, 033808 (2008). ⟨93, 102⟩.

[196] Savanier, M., Kumar, R. & Mookherjea, S. Photon pair generation from compact silicon microring resonators using microwatt-level pump powers. *Optics Express* **24**, 3313–3328 (2016). ⟨94⟩.

[197] Guo, K. *et al.* High coincidence-to-accidental ratio continuous-wave photon-pair generation in a grating-coupled silicon strip waveguide. *Applied Physics Express* **10**, 062801 (2017). ⟨98⟩.

[198] Cardona, M., Meyer, T. & Thewalt, M. Temperature dependence of the energy gap of semiconductors in the low-temperature limit. *Physical Review Letters* **92**, 196403 (2004). ⟨98⟩.

[199] Rosenfeld, L. M., Sulway, D. A., Thompson, M. G., Rarity, J. G. & Silverstone, J. W. The first quantum interference

in the mid-infrared is on a silicon chip. In *2019 Conference on Lasers and Electro-Optics Europe and European Quantum Electronics Conference*, pd_2_2 (Optical Society of America, 2019). ⟨101⟩.

[200] He, J. *et al.* Ultracompact quantum splitter of degenerate photon pairs. *Optica* **2**, 779–782 (2015). ⟨101⟩.

[201] Helt, L. G., Yang, Z., Liscidini, M. & Sipe, J. E. Spontaneous four-wave mixing in microring resonators. *Optics Letters* **35**, 3006–3008 (2010). ⟨102, 137⟩.

[202] Prabhakar, S. *et al.* Two-photon quantum interference and entanglement at 2 μm. *arXiv preprint arXiv:1906.02082* (2019). ⟨107⟩.

[203] Hoppe, N. *et al.* Ultra-efficient silicon-on-insulator grating couplers with backside metal mirrors. *IEEE Journal of Selected Topics in Quantum Electronics* **26**, 1–6 (2019). ⟨107⟩.

[204] Shibata, H., Shimizu, K., Takesue, H. & Tokura, Y. Ultimate low system dark-count rate for superconducting nanowire single-photon detector. *Optics letters* **40**, 3428–3431 (2015). ⟨107⟩.

[205] Ramelow, S., Ratschbacher, L., Fedrizzi, A., Langford, N. & Zeilinger, A. Discrete tunable color entanglement. *Physical Review Letters* **103**, 253601 (2009). ⟨108⟩.

[206] Zou, Y., Chakravarty, S., Chung, C.-J., Xu, X. & Chen, R. T. Mid-infrared silicon photonic waveguides and devices. *Photonics Research* **6**, 254–276 (2018). ⟨112⟩.

[207] Silverstone, J. W. *et al.* Qubit entanglement between ring-resonator photon-pair sources on a silicon chip. *Nature Communications* **6**, 7948 (2015). ⟨113⟩.

[208] Society, C. & Craver, C. *The Coblentz Society desk book of infrared spectra* (The Society, 1980). ⟨113, 114⟩.

[209] Gentry, C. M., Zeng, X. & Popović, M. A. Tunable coupled-mode dispersion compensation and its application to on-chip resonant four-wave mixing. *Optics letters* **39**, 5689–5692 (2014). ⟨114⟩.

[210] Lemos, G. B. *et al.* Quantum imaging with undetected photons. *Nature* **512**, 409 (2014). ⟨115⟩.

[211] Zou, X., Wang, L. J. & Mandel, L. Induced coherence and indistinguishability in optical interference. *Physical Review Letters* **67**, 318 (1991). ⟨115⟩.

[212] Schnabel, R. Squeezed states of light and their applications in laser interferometers. *Physics Reports* **684**, 1–51 (2017). ⟨115⟩.

[213] Cernansky, R. & Politi, A. Nanophotonic source of broadband quadrature squeezing. *arXiv preprint arXiv:1904.07283* (2019). ⟨115⟩.

[214] Dong, Y. *et al.* Two-micron-wavelength germanium-tin photodiodes with low dark current and gigahertz bandwidth. *Optics Express* **25**, 15818–15827 (2017). ⟨115⟩.

[215] Kahl, O. *et al.* Waveguide integrated superconducting single-photon detectors with high internal quantum efficiency at telecom wavelengths. *Scientific Reports* **5**, 10941 (2015). ⟨115⟩.

[216] Oser, D. *et al.* High quality photon pair generation with on-chip filtering. In *Frontiers in Optics*, FTu1E–2 (Optical Society of America, 2019). ⟨116⟩.

[217] Clements, W. R., Humphreys, P. C., Metcalf, B. J., Kolthammer, W. S. & Walmsley, I. A. Optimal design for universal multiport interferometers. *Optica* **3**, 1460–1465 (2016). ⟨116⟩.

[218] Lee, H., Chen, T., Li, J., Painter, O. & Vahala, K. J. Ultra-low-loss optical delay line on a silicon chip. *Nature Communications* **3**, 867 (2012). ⟨116⟩.

[219] Timurdogan, E., Poulton, C. V., Byrd, M. & Watts, M. Electric field-induced second-order nonlinear optical effects in silicon waveguides. *Nature Photonics* **11**, 200 (2017). ⟨116⟩.

[220] Bergamasco, N., Menotti, M., Sipe, J. & Liscidini, M. Generation of path-encoded Greenberger-Horne-Zeilinger states. *Physical Review Applied* **8**, 054014 (2017). ⟨116⟩.

[221] Silverstone.science (2018). URL `http://qontrol.co.uk/josh/data/Integrated%20Optics.gstencil`. ⟨121⟩.

[222] Sakurai, J. & Napolitano, J. *Modern Quantum Mechanics* (Addison-Wesley, 2011). ⟨128⟩.

[223] Leviton, D. B. & Frey, B. J. Temperature-dependent absolute refractive index measurements of synthetic fused silica. In *Optomechanical Technologies for Astronomy*, vol. 6273, 62732K (International Society for Optics and Photonics, 2006). ⟨135⟩.

[224] Bass, M. *et al. Handbook of Optics, Third Edition Volume IV: Optical Properties of Materials, Nonlinear Optics, Quantum Optics (set)*. Handbook of optics (McGraw-Hill Education, 2009). ⟨135, 136⟩.

[225] Malitson, I. Interspecimen comparison of the refractive index of fused silica. *JOSA* **55**, 1205–1209 (1965). ⟨135⟩.

[226] Horst, F. *et al.* Cascaded Mach-Zehnder wavelength filters in silicon photonics for low loss and flat pass-band WDM (de-) multiplexing. *Optics Express* **21**, 11652–11658 (2013). ⟨138⟩.

[227] Palik, E. D. *Handbook of optical constants of solids*, vol. 3 (Academic press, 1998). ⟨140, 141⟩.